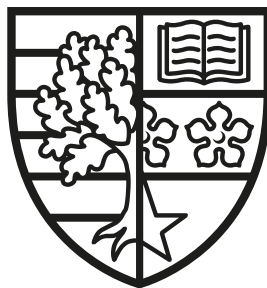


Reconfigurable Quasi-Optical Beamformers for Next-Generation Satellite Applications: Electromagnetic Modeling and Design

Thomas Ströber

SUBMITTED FOR THE DEGREE OF
DOCTOR OF PHILOSOPHY



HERIOT-WATT UNIVERSITY
Institute of Signals, Sensors and Systems
School of Engineering & Physical Sciences

AWARDED JOINTLY WITH
UNIVERSITÉ DE RENNES 1

December, 2020

The copyright in this thesis is owned by the author. Any quotation from the thesis or use of any of the information contained in it must acknowledge this thesis as the source of the quotation or information.

THÈSE DE DOCTORAT DE

L'UNIVERSITÉ DE RENNES 1
Comue Université Bretagne Loire

École Doctorale N° 601
*Mathématiques et Sciences et Technologies
de l'Information et de la Communication*
Spécialité : Électronique

Par

Thomas Ströber

Reconfigurable Quasi-Optical Beamformers for Next-Generation Satellite Applications: Electromagnetic Modeling and Design

Thèse présentée et soutenue à Rennes, le 11 Décembre 2020
Institut d'Electronique et des Technologies du Numérique (IETR) – UMR 6164

Rapporteurs avant soutenance :

Matteo ALBANI Associate Professor, Università degli Studi di Siena
Eva RAJO IGLESIAS Professor, Universidad Carlos III de Madrid

Composition du Jury :

Examineurs :	Matteo ALBANI	Associate Professor, Università degli Studi di Siena
	Eva RAJO IGLESIAS	Professor, Universidad Carlos III de Madrid
	Nuria LLOMBART	Professor, Delft University of Technology
	Oscar QUEVEDO TERUEL	Associate Professor, KTH Royal Institute of Technology, Stockholm
	Hervé LEGAY	Docteur Ingénieur, Thales Alenia Space, Toulouse
Dir. de thèse :	Mauro ETTORRE	Chercheur CNRS, HDR, IETR – UMR 6164, Rennes
Co-dir. de thèse :	George GOUSSETIS	Professor, Heriot-Watt University, Edinburgh

Acknowledgments

I am most grateful to my advisor, Mauro Ettore, for his mentorship, his confidence in me, and his outstanding commitment. His passion for research and the many tricks he shared with me have made this thesis an exciting experience, and will undoubtedly shape my future career.

I would also like to thank my co-advisor Prof. George Goussetis for his constant support and guidance throughout my Ph.D. studies. I remember well our first chat at Heriot-Watt in 2017, which eventually turned out to be my job interview for this project and the beginning of a fruitful collaboration.

I would like to express my deep gratitude to Hervé Legay for his unwavering dedication and the warm welcome during my stay at Thales Alenia Space. His expert knowledge and can-do attitude have greatly contributed to the success of this project.

I am grateful to Etienne Girard who closely followed my research work. His positive attitude, creativity and kind help in networking gave momentum to the whole project. I want to thank Ségolène Tubau for her valuable advice during the design phase. I also had great pleasure of working with Xavier Morvan and Laurent Le Coq. Their expertise and skills greatly facilitated the prototyping process and following the final measurements was my personal moon landing. I would like to extend my sincere gratitude to Prof. Matteo Albani and Prof. Eva Rajo-Iglesias for reviewing this thesis and for providing me with very valuable feedback. I also wish to thank Prof. Nuria Llombart and Prof. Oscar Quevedo-Teruel who accepted to be part of my thesis committee.

I would like to thank my Revolve fellow colleagues with who I had the pleasure to work in this project and spend many memorable moments together. Wherever my secondments brought me over the past three years, it felt good to know that at least one of you is going to be around. A heartfelt thanks to Andrea, Claire, Florian, Haris, Louis and Petros, who went through the ups and downs with me while working on our theses.

I want to extend my gratitude to the people at IETR, who made my time in Rennes very enjoyable. To my conference companion Michele, to Alvaro, Srđan, Nicola, Denys, Jorge, Antoine and Tuyen. Our fun nights out, market visits and trips to the coast provided a cheerful diversion from work and I will never forget them. I wish to extend a special thank you to François for his invaluable help despite being in the final stage of his thesis preparation. I would like to thank also Nathalie, Noëlle, Martine, David and Benjamin who always had an open ear for me and lent a helping hand when I needed it.

I have been very fortunate over the years to have had the support and friendship of many people outside the lab. I am grateful to my friends back home, Sebi, Christian, Franz, Julian, Regina, Elli, Flo and Dani who visited me on various occasions. I also want to thank Alex, Patrick and Christopher, with who I can always pick up right where we left off.

I am deeply grateful to my family for their constant love and support. Thank you to my parents Martin and Claudia for encouraging me in all of my pursuits. Thank you to my brother Simon and my sister Maria for always cheering me up and standing by me.

Last, and most importantly, I want to thank Silvia for her love and patience, for always believing in me and making me happy.

Résumé

Les constellations de satellites en orbite basse (LEO) et intermédiaire (MEO) devraient étendre la connectivité dans les zones difficiles d'accès. La nécessité d'avoir un large secteur angulaire (environ $\pm 20^\circ$ pour les satellites MEO et jusqu'à plus de $\pm 60^\circ$ pour les satellites LEO), ainsi que la possibilité d'utiliser des plus larges bandes de fréquence en bande Ka a créé de nouveaux défis dans la conception d'antennes. De plus, des solutions à bas coût sont nécessaires, en particulier pour les constellations LEO pour lesquelles le nombre d'antennes nécessaires dans le segment spatial et sol est important. Pour atteindre des débits élevés et des communications stables, les antennes satellite doivent pouvoir générer des faisceaux étroits, orientables, et à gain élevé. En l'absence de liens inter-satellites, plusieurs antennes de poursuite avec une précision de pointage élevée sont également nécessaires pour les stations sols.

Les réseaux de formateurs de faisceaux passifs offrent de bonnes performances en balayage et des faisceaux multiples à faible coût. Cependant, les pertes et la complexité du réseau augmentent rapidement avec le nombre de faisceaux et la taille de l'ouverture rayonnante. Des formateurs de faisceaux quasi-optiques ont été développés pour diverses applications afin de surmonter ce problème. Dans le domaine des communications par satellite à large bande, ces dispositifs ont reçu une attention croissante en raison de leur caractéristique de retard en temps réel. De plus, les progrès en fabrication antenne ont ouvert de nouvelles voies pour des implémentations efficaces à faible coût aux longueurs d'onde millimétriques. Le concept proposé précédemment de lentilles continues en guide d'ondes à plans parallèles semble particulièrement prometteur pour les applications spatiales. Le principe de fonctionnement est similaire à celui d'une lentille contrainte bidimensionnelle, sauf que la compensation du trajet optique est obtenue à l'aide d'une cavité verticale de guide d'ondes à plans parallèles. Ses principaux avantages sont la réduction des pertes de dépointage par rapport aux systèmes pillbox à réflecteur parabolique, la facilité de fabrication par rap-

port aux lentilles contraintes exclusivement constituées en métal, et enfin leur intégrabilité par rapport aux lentilles géodésiques. La principale limitation des précédentes solutions est le secteur angulaire d'environ $\pm 30^\circ$. De plus, les applications LEO nécessitent des systèmes d'alimentation compacts qui fournissent une reconfigurabilité des faisceaux. Ces deux aspects sont traités dans cette thèse, et ont conduit au développement de deux nouvelles architectures d'antenne, d'outils numériques permettant la caractérisation et la synthèse efficace des réseaux de sources, ainsi que d'une nouvelle solution pour l'implémentation en PCB des lentilles continues en guide d'ondes à plans parallèles.

Plan de la Thèse

Dans le chapitre 1, les exigences spécifiques sur les antennes pour les systèmes de communications par satellites LEO/MEO sont identifiées, tout en soulignant la nécessité des dispositifs quasi-optiques. Les principes de conception et un état de l'art sur les réalisations technologiques sont présentés.

Le chapitre 2 traite des limites théoriques des antennes multifaisceaux. Des solutions pratiques au problème de non-orthogonalité de faisceaux dans les systèmes quasi-optiques sont passées en revue. L'accent est mis sur deux approches qui ont été suivies dans cette thèse: le balayage mécanique du faisceau et l'excitation par des clusters superposés.

Dans ce qui suit, les travaux de recherche effectués au cours de cette thèse et ses contributions principales sont résumés.

Sujet 1: Balayage mécanique du faisceau sur une large couverture angulaire

Dans le chapitre 3, un nouveau système d'alimentation mécanique basé sur la caractéristique sans contact des guides d'ondes en technologie gap waveguide est présenté. Les principaux avantages du concept d'alimentation proposé par rapport aux solutions conventionnelles basées sur des câbles coaxiaux flexibles et des joints tournants sont une bande passante plus large, un profil réduit et une grande robustesse mécanique. La structure peut être réalisée pour effectuer un mouvement linéaire ou circulaire rapide. De plus, le système de balayage est efficace pour diverses solutions de formateurs de faisceaux en guide d'ondes à plans parallèles.

La procédure de conception d'un système d'alimentation fonctionnant en bande Ka (liaison montante) est présentée. De plus, des modèles analytiques approximatifs facilitant ce processus sont expliqués. Une simple lentille en guide d'ondes à plans parallèles compatible avec le système d'alimentation développé est proposée. Une routine d'optimisation basée sur une procédure de tracé de rayons proposée précédemment est utilisée pour contrôler l'amplitude et la distribution de phase sur l'ouverture rayonnante en façonnant les différents contours de la lentille. Les résultats calculés démontrent la couverture d'un secteur angulaire de $\pm 35^\circ$. Ensuite, un système compact à deux lentilles est introduit, permettant de dépointer sur un secteur angulaire plus large. La structure finale de l'antenne, composée du dispositif quasi-optique et du système d'alimentation mécanique, est détaillée. Le processus de fabrication et la caractérisation expérimentale d'un prototype exclusivement constitué de métal sont décrits. Les résultats de mesure démontrent de bonnes performances de balayage sur un secteur angulaire d'environ $\pm 50^\circ$.

Sujet 2: Méthodes numériques pour l'analyse des formateurs de faisceaux en guide d'ondes à plans parallèles

Dans le chapitre 4, des modèles asymptotiques pour l'analyse des formateurs de faisceaux en guide d'ondes à plans parallèles en réception sont présentés. Une combinaison d'optique géométrique et optique physique est utilisée pour déterminer la distribution du champ dans la région focale des lentilles continues en guide d'ondes à plans parallèles. Les méthodes sont validées par comparaison avec un solveur électromagnétique classique. En appliquant la réciprocité, les modèles décrits permettent une caractérisation rapide et rigoureuse des réseaux de sources primaires. Un avantage de cette approche se traduit par le fait que le couplage entre le système quasi-optique et les sources peut être entièrement décrit au moyen d'une quantité scalaire, appelée efficacité de transfert.

La procédure proposée est ensuite utilisée pour déterminer les contours de gain maximum des réflecteurs paraboliques cylindriques et pour évaluer leurs limites sur les performances de balayage. De plus, la dérivation d'un arc focal amélioré est démontrée pour un modèle simplifié d'une lentille contrainte.

Une extension de la formulation permettant la synthèse de cluster de sources est décrite. Un exemple de conception est présenté pour démontrer l'utilité de cette approche. Les limitations de sa validité pour des sources électriquement petites sont mises en évidence.

Sujet 3: Lentille en guide d'ondes à plans parallèles alimentés par des clusters superposés en PCB

Dans le chapitre 5, une lentille multifaisceaux utilisant des clusters de sources superposés est proposée. Une nouvelle caractéristique de cette conception est sa réalisation en technologie PCB multicouches. Le concept de double lentilles présenté au chapitre 3 est appliqué pour obtenir les propriétés de focalisation souhaitées et un profil réduit. La méthode présentée dans le chapitre 4 est utilisée pour optimiser l'arc focal et pour déterminer les pondérations complexes de l'excitation des clusters. La conception d'une transition de sortie permettant l'utilisation de la lentille comme dispositif à rayonnement direct est présentée. Les résultats de simulations d'une antenne fonctionnant en bande Ka (liaison descendante) démontrent des bonnes performances en dépointage sur un large secteur angulaire d'environ $\pm 60^\circ$.

Le profil réduit, la légèreté et la réduction du coût de fabrication font de ce formateur de faisceaux un candidat très attractif pour des architectures d'antennes actives soumises à des exigences strictes de couverture et d'encombrement.

Abstract

Reconfigurable Quasi-Optical Beamformers for Next-Generation
Satellite Applications: Electromagnetic Modeling and Design

by

Thomas Ströber

Emerging satellite constellations at low- and medium earth orbits are expected to revolutionize the expansion of broadband connectivity into rural areas. The requirements of wide field of view and the availability of larger bandwidths in the Ka-band have opened new challenges in antenna design. At the same time, highly cost-effective solutions are needed. The main objective of this thesis is to investigate and develop quasi-optical millimeter-wave antennas with enhanced beam scanning and beam reconfiguration capabilities that answer these needs. High-frequency models are developed for the analysis of different parallel-plate beamformers in reception. It is shown that these models can be used efficiently for the design of feed systems with stringent requirements on scanning range. Two novel lens beamformers, operating in the uplink and downlink Ka-band, respectively, are presented. The first is a shaped parallel-plate lens combined with a mechanical scanning feed based on gap waveguide technology. Equivalent circuit models that aid in the design of the feed structure are addressed. The resulting design and experimental results from an all-metal demonstrator are presented. The second corresponds to a lens beamformer implemented in multilayer PCB technology. The developed numerical procedure is applied to the synthesis of overlapping feed clusters. Both designs represent significant advances in terms of scanning performance and low-cost implementation.

Keywords: gap waveguide technology, high-frequency techniques, multiple-beam antennas, parallel-plate optics, quasi-optical systems

Research Thesis Submission

Name:	Thomas Ströber		
School:	School of Engineering & Physical Sciences		
Version: <i>(i.e. First, Resubmission, Final)</i>	Final	Degree Sought:	Ph.D.

Declaration

In accordance with the appropriate regulations I hereby submit my thesis and I declare that:

1. The thesis embodies the results of my own work and has been composed by myself
2. Where appropriate, I have made acknowledgement of the work of others
3. The thesis is the correct version for submission and is the same version as any electronic versions submitted*.
4. My thesis for the award referred to, deposited in the Heriot-Watt University Library, should be made available for loan or photocopying and be available via the Institutional Repository, subject to such conditions as the Librarian may require
5. I understand that as a student of the University I am required to abide by the Regulations of the University and to conform to its discipline.
6. I confirm that the thesis has been verified against plagiarism via an approved plagiarism detection application e.g. Turnitin.

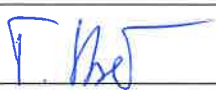
ONLY for submissions including published works

7. Where the thesis contains published outputs under Regulation 6 (9.1.2) or Regulation 43 (9) these are accompanied by a critical review which accurately describes my contribution to the research and, for multi-author outputs, a signed declaration indicating the contribution of each author (complete)
8. Inclusion of published outputs under Regulation 6 (9.1.2) or Regulation 43 (9) shall not constitute plagiarism.

* Please note that it is the responsibility of the candidate to ensure that the correct version of the thesis is submitted.

Signature of Candidate:		Date:	03/02/2021
-------------------------	---	-------	------------

Submission

Submitted By <i>(name in capitals)</i> :	THOMAS STRÖBER
Signature of Individual Submitting:	
Date Submitted:	03/02/2021

For Completion in the Student Service Centre (SSC)

Limited Access	Requested	Yes	<input type="checkbox"/>	No	<input type="checkbox"/>	Approved	Yes	<input type="checkbox"/>	No	<input type="checkbox"/>
<i>E-thesis Submitted (mandatory for final theses)</i>										
Received in the SSC by <i>(name in capitals)</i> :						Date:				

Contents

1	Introduction	1
1.1	Background	1
1.2	The Need for Quasi-Optical Beamformers	2
1.3	Overview of Existing Solutions	4
1.3.1	Pillbox Systems	4
1.3.2	Constrained Lenses	5
1.3.3	Radially Symmetric Lenses	10
1.3.4	Continuous Parallel-Plate Waveguide Lenses	14
1.4	Novel Contributions in this Thesis	16
1.5	Thesis Structure	17
2	Beam Reconfigurability in Quasi-Optical Systems	19
2.1	Fundamental Limitations of Multibeam Antennas	20
2.2	High-Crossover Low-Sidelobe Designs	26
2.2.1	Lossy Networks	26
2.2.2	Split Aperture Decoupling Method	27
2.2.3	Stacked Feed Structure	28
2.2.4	Fabry-Perot Feed System	29
2.2.5	Modified Optics	30
2.2.6	Variable Phase Shifters	30
2.3	Mechanical Beam Scanning	31
2.3.1	Design Considerations for Quasi-Optical Systems	31
2.3.2	Existing Feed Designs	35
2.4	Multiple-Feed-per-Beam Operation	39
2.5	Chapter Summary	40
3	A Parallel-Plate Lens for Mechanical Wide-Angle Beam Steering	41
3.1	Low-Profile Mechanical Feed System	42
3.1.1	Basic Principle and Advantages of Gap Waveguides	42

3.1.2	Unit Cell Design for Ka-Band	44
3.1.3	Proposed Feed System	47
3.1.4	Analysis and Design of Waveguide Building Blocks	48
3.2	Quasi-Optical Design	61
3.2.1	Basic Design Principles	61
3.2.2	Single-Ridge Lens with Moderate Scanning Range	64
3.2.3	Dual-Ridge Lens with Enhanced Scanning Range	66
3.3	Antenna Manufacturing and Assembly	69
3.4	Experimental Results	73
3.4.1	Return Loss	73
3.4.2	Radiation Performance at Broadside	73
3.4.3	Scanning Performance	74
3.5	Comparison with State-of-the-Art Solutions and Discussion	76
3.6	Chapter Summary	81
4	Analysis of Integrated Quasi-Optical Beamformers	83
4.1	Overview of Relevant High-Frequency Techniques	84
4.2	Modeling of Quasi-Optical Systems	87
4.2.1	Pillbox Reflector	88
4.2.2	Bootlace Lens	89
4.2.3	Continuous Parallel-Plate Waveguide Lens	92
4.3	Power Transfer Characterization	95
4.4	Single-Feed Study	97
4.4.1	Pillbox Reflector	98
4.4.2	Rotman Lens	101
4.5	Feed Cluster Synthesis	103
4.5.1	Numerical Procedure	104
4.5.2	Cluster Example	105
4.6	Chapter Summary	112
5	A Multilayer PCB Lens Beamformer for Active Antenna Architectures	117
5.1	Motivation	117
5.2	Proposed Design Concept	119
5.3	Quasi-Optical Design	121
5.4	Feed System Design	124
5.4.1	Beam Port Contour	124
5.4.2	Feed Dimensioning	125

5.4.3	Input Transition	128
5.5	Output Transition	129
5.6	Final Designs and Simulation Results	133
5.6.1	Single-Feed-per-Beam Design	133
5.6.2	Multiple-Feed-per-Beam Design	136
5.7	Comparison with State-of-the-Art Solutions and Discussion . . .	139
5.8	Chapter Summary	139
6	Conclusion	143
6.1	Summary and Discussion	143
6.2	Future Directions	146
Appendix A Effects of Primary Aberrations on the Radiation Pattern of a Line Source		149
Appendix B Phase Error Analysis of Bifocal Lens Model		157
Appendix C Geometrical Optics Analysis of a Two-Lens System		159
Bibliography		163

List of Figures

1.1	Double-layer pillbox system with (a) circular reflector, (b) parabolic reflector.	5
1.2	Schematic view of a metal-plate lens with straight front face. . .	6
1.3	Schematic view of a Rotman lens.	7
1.4	Schematic view of an (a) R - $2R$ lens, (b) R - KR lens.	9
1.5	Schematic view of a (a) Maxwell fisheye lens, (b) classical Luneburg lens, (c) modified Luneburg lens.	11
1.6	Cross-sectional view of a (a) Rinehart lens, (b) modulated geodesic lens.	13
1.7	(a) Schematic view of a multiple-beam continuous PPW lens, (b) constrained lens model.	14
1.8	(a) Schematic view of a spatial amplifier stage, (b) tray amplifiers.	15
2.1	Schematic view of a transmitting beamforming network.	21
2.2	(a) Beam coupling (—), radiation efficiency (--) and (b) crossover level for uniform illumination.	25
2.3	(a) Beam coupling (—), radiation efficiency (--) and (b) crossover level for cosine-type illumination.	26
2.4	Constrained lens beamformer with (a) resistive tapering, (b) passive beam port overlap network.	27
2.5	Pillbox system with (a) split aperture decoupling, (b) stacked feed structure.	28
2.6	Fabry-Perot feed system with reduced mutual coupling.	30
2.7	Mechanical beam scanning with a circularly symmetric lens. . .	33
2.8	Rotman lens contours for (a) $\beta = 1.0$, (b) $\beta = 0.88$	35
2.9	Normalized RMS phase error of a Rotman lens with $\beta = 1.0$ (—) and $\beta = 0.88$ (--) for (a) $\zeta_{\max} = 0.6$, (b) $\zeta_{\max} = 0.7$	36
2.10	Coaxial-to-waveguide transition using a (a) current probe, (b) ridge waveguide section.	37

2.11	Cross-sectional view of a waveguide rotary joint.	38
3.1	(a) Stopband structure, (b) equivalent boundary value problem. .	43
3.2	Basic structure of (a) ridge gap waveguides, (b) groove gap waveguides with vertical polarization.	43
3.3	Calculated dispersion characteristic of TM (—), TE modes (--) and corresponding simulation results (\diamond) for a unit cell with $d = 3.5$ mm, $h = 0.5$ mm, $r = 0.2$ mm and $p = 0.8$ mm.	45
3.4	Simulated dispersion characteristic of an optimized unit cell with $d = 2.7$ mm, $h = 0.5$ mm, $r = 0.5$ mm and $p = 3.0$ mm.	46
3.5	Simulated dispersion characteristic of a basic groove gap waveguide cell (—) and of TE ₁₀ mode in a WR-28 waveguide (--). . . .	47
3.6	Perspective view of the proposed feed system.	48
3.7	Simulated reflection coefficient of groove gap waveguide structure (—), calculation based on waveguide equivalent circuit model (--). . . .	49
3.8	Simulated reflection coefficient of a groove gap waveguide H -plane corner compensated by one pin (--) and three pins (....), of an optimized mitered WR-28 waveguide bend (—).	50
3.9	Ideal transition from rectangular to groove gap waveguide. . . .	52
3.10	(a) Cross-sectional view of a conventional choke-flange coupling, (a) circular-groove choke flange.	52
3.11	Choke flange based on (a) gap waveguide technology, (b) holey EBG structures.	54
3.12	(a) Side view of a non-contacting choke coupling, (b) front view of the gap waveguide choke flange.	55
3.13	(a) Perspective view, (b) front view and (c) cross-sectional view of the proposed choke flange (all dimensions in mm).	57
3.14	Simulated S parameters of a non-contacting gap waveguide joint (--) and of the proposed choke joint (....), calculation based on simplified equivalent circuit model for a circular choke joint (—).	58
3.15	Simulated reflection coefficient of a vertical transition from rectangular to groove gap waveguide (—), calculation based on waveguide equivalent circuit model (--).	59
3.16	(a) Perspective view of a matched vertical transition from WR-28 waveguide to groove gap waveguide, (b) geometry of the top plate (all dimensions in mm).	60

3.17 Simulated S parameters of an optimized transition from rectangular to groove gap waveguide.	60
3.18 (a) Cross-sectional view of a continuous PPW lens, (b) constrained bifocal lens model.	61
3.19 Normalized RMS phase error versus scan angle of a constrained bifocal lens with $g = 1.0$ (---), $g = 1.27$ (---), and of an optimized non-focal design (—) with $F/D = 0.7$	63
3.20 Calculated (—), simulated (---) and ideal (....) phase front along the lens aperture.	65
3.21 (a) All-metal implementation of single-ridge lens beamformer, (b) cross-sectional view.	65
3.22 Calculated (—) and simulated (---) radiation patterns at the design frequency (29.25 GHz).	66
3.23 (a) Cross-sectional view of a dual-ridge lens, (b) first-order optics model.	67
3.24 Rays passing through a dual-lens system in transmission (—) and rays describing the virtual image formation (---) for (a) $\phi_0 = 0^\circ$, (b) $\phi_0 = 25^\circ$	68
3.25 Calculated (—) and simulated (\diamond) focal surfaces for $\phi_i = [-30\dots30^\circ]$, imposed focal arc (---).	69
3.26 Normalized RMS phase error versus scan angle of an optimized dual-ridge (—) and single-ridge design (---).	69
3.27 Calculated (—), simulated (---) and ideal (....) phase front along the lens aperture.	70
3.28 Calculated (—) and simulated (---) radiation patterns at the design frequency (29.25 GHz).	70
3.29 (a) All-metal implementation of dual-ridge lens beamformer, (b) cross-sectional view.	71
3.30 Top view of the final gap waveguide feed structure.	71
3.31 Top and back view of the prototype lens beamformer.	72
3.32 Front and back view of 3D printed non-contacting choke flange.	73
3.33 Simulated input reflection coefficient for various feed positions.	74
3.34 Measured input reflection coefficient for various feed positions.	75
3.35 Measurement setup in the compact antenna test range (a) without and (b) with additional absorber. (c) Angular adjustment of the feed position.	75

3.36	Broadside radiation pattern at 29.25 GHz in the (a) H plane and (b) E plane.	76
3.37	Measured (—) and simulated (--) H -plane radiation patterns for $\phi_0 = [-50^\circ, -40^\circ, \dots, 50^\circ]$ at (a) 29.25 GHz, (b) 27.5 GHz and (c) 31 GHz.	77
3.38	Measured H -plane radiation pattern as a function of frequency for various feed angular positions.	78
3.39	Measured (—) and simulated (--) (a) scan angle and (b) half-power beamwidth, (c) measured maximum sidelobe level in the H plane as a function of frequency.	79
3.40	(a) Measured (—) and simulated (--) maximum directivity, (b) maximum gain.	80
3.41	Measured 3D co- and cross-polarized pattern at 29.25 GHz for (a) $\phi_0 = 0^\circ$, (b) $\phi_0 = 30^\circ$ and (c) $\phi_0 = 50^\circ$	80
3.42	Perspective view of a mechanical scanning lens beamformer with CTS array.	81
4.1	Schematic view of a two-dimensional scattering problem.	87
4.2	Schematic view of a receiving pillbox reflector.	89
4.3	Calculated (—) and simulated (--) electric field along the focal plane of a reflector with $D = 20\lambda$, $F/D = 0.4$ for (a) $\phi_i = 0^\circ$, (b) $\phi_i = 20^\circ$	90
4.4	Calculated (—) and simulated (--) electric field along the focal plane of a reflector with $D = 20\lambda$, $F/D = 1.0$ for (a) $\phi_i = 0^\circ$, (b) $\phi_i = 20^\circ$	90
4.5	Calculated (—) and simulated (\diamond) maximum-field intensity points resulting from $\phi_i = [0\dots 40^\circ]$ for (a) $F/D = 0.4$, (b) $F/D = 1.0$	91
4.6	Schematic view of a receiving bootlace lens.	92
4.7	Schematic view of a receiving continuous PPW lens.	93
4.8	Simplified cross-sectional view of a receiving lens modeled by ray tracing.	93
4.9	Calculated (—) and simulated (--) magnetic field along the inner lens contour for $\phi_i = 0^\circ$	94
4.10	Calculated (—) and simulated (--) magnetic field along the inner lens contour for $\phi_i = 30^\circ$	94
4.11	Calculated (—) and simulated (--) electric field in proximity of the focal-region maximum for $\phi_i = 0^\circ$	95

4.12	Calculated (—) and simulated (--) electric field in proximity of the focal-region maximum for $\phi_i = 30^\circ$	95
4.13	Calculated (—) and simulated (\diamond) maximum-field intensity points resulting from $\phi_i = [-35\dots35^\circ]$, feed curve optimized with a phase-only model (....).	96
4.14	Power transfer in a quasi-optical system (a) from an incoming wave to a feed terminated with a matched load (receive mode), (b) from a radiating feed to an outgoing wave (transmit mode). . . .	96
4.15	Comparison of Petzval surface (....) and maximum scan-gain contours of an isotropic feed (—) and feeds with 10 dB (--) and 20 dB edge taper (---) for (a) $F/D = 0.4$, (b) $F/D = 1.0$	99
4.16	Maximum T factor with different feed configurations for (a) $F/D = 0.4$, (b) $F/D = 1.0$	100
4.17	Calculated and simulated (\diamond) gain loss versus beamwidths scanned for (a) $F/D = 0.4$, (b) $F/D = 1.0$	101
4.18	Original focal arc [13] (....), maximum-field locus (—) and improved focal curve [15] (--) of (a) original Rotman lens design, (b) lens design for enhanced scan range.	102
4.19	RMS phase error for original focal arc [13] (....), maximum-field locus (—) and improved focal curve [15] (--).	103
4.20	Comparison of original focal arc [13] (....) and optimal contour of 10-dB edge taper feed (—) in terms of (a) T factor, (b) radiation patterns.	104
4.21	Calculated (—) and simulated (--) focal-region field for $\phi_i = 0^\circ$ with cosine illumination.	106
4.22	Calculated (—) and simulated transfer efficiency (--) versus feed size.	106
4.23	Comparison of the assumed field distribution (—) and the simulated tangential fields (--) on the aperture plane for a feed of (a) 0.7λ , (b) 2λ	107
4.24	Magnitude of the received electric field (—) and the assumed amplitude distribution of the feed system (--).	108
4.25	Comparison of the assumed field distribution (—) and the simulated tangential fields (--) on the aperture plane of a cluster with $3 \times 0.67\text{-}\lambda$ elements.	109

4.26	Calculated (—) and simulated (--) illumination of the inner lens contour, cosine illumination (⋯).	110
4.27	Comparison of calculated (—) and simulated (--) radiation pattern with prescribed pattern mask (⋯).	110
4.28	Schematic view of the studied feed configurations for a scan range of $\pm 35^\circ$.	111
4.29	T factor versus scan angle for a feed system with 2λ - (—) and 0.67λ -apertures (⋯).	111
4.30	Simulated radiation patterns for (a) single-feed-per-beam excitation, (b) three-feeds-per-beam excitation.	112
5.1	Schematic view of an active quasi-optical beamforming device.	118
5.2	(a) Schematic cross section of a PPW lens beamformer implemented in multilayer PCB technology. (b) machined PCB stack-up	120
5.3	Estimated attenuation for the TEM mode of a parallel-plate waveguide in Rogers RT/duroid 5880 with thickness $H = 3.175$ mm.	121
5.4	Height-to-diameter ratio versus focal ratio.	122
5.5	Perspective view of a dual-ridge lens with five optimized beam port positions.	123
5.6	Calculated (—) and simulated (--) radiation patterns of single-ridge lens.	124
5.7	Calculated (—) and simulated (--) focal surface for $\phi_i = [-40\dots 40^\circ]$, optimized feed positions (o).	125
5.8	Calculated (—) and simulated (--) electric field in proximity of focal-region maximum for $\phi_i = 0^\circ$.	126
5.9	Calculated (—) and simulated (--) (a) beam crossover level, (b) spillover efficiency, and (c) mutual coupling versus feed size for single-feed-per-beam operation.	126
5.10	Schematic view of lens beamformer with (a) single-feed-per-beam operation, (b) two-feed-per-beam operation.	127
5.11	Calculated (—) and simulated (--) (a) beam crossover level and (b) spillover efficiency versus feed size for two-feed-per-beam operation.	128
5.12	Top and side view of input transition (all dimensions in mm).	129
5.13	Simulated S parameters of optimized transition from SMA end launch connector (port 1) to SIW (port 2).	129

5.14	Reflection coefficient of a TE-polarized plane wave in Rogers RT/duroid 5880 obliquely incident upon a substrate-air interface with (--) and without (—) ideal quarter-wave matching layer. . .	130
5.15	Reflection coefficient of a TE-polarized plane wave in Rogers RT/duroid 5880 obliquely incident upon a substrate-air interface with quarter-wave matching layer.	131
5.16	Side and top view of a chamfered substrate-air transition inside a parallel-plate waveguide.	132
5.17	Simulated reflection coefficient of a TE-polarized plane wave incident upon optimized chamfered substrate-air transition.	132
5.18	Perspective view of lens-flare interface.	132
5.19	Top and cross-sectional view of PCB lens model with single-feed-per-beam excitation (all dimensions in mm).	134
5.20	Simulated input reflection coefficient for the single-feed-per-beam configuration.	135
5.21	Simulated mutual coupling between conjugate input ports for the single-feed-per-beam configuration.	135
5.22	Simulated H -plane radiation pattern at (a) 18.75 GHz, (b) 17.3 GHz and (c) 20.2 GHz.	136
5.23	Simulated (a) scan angle and (b) sidelobe level in the H plane as a function of frequency.	137
5.24	Simulated (a) realized gain, (b) radiation efficiency for the broad-side beam as a function of frequency.	138
5.25	Top view of PCB lens model with multiple-feed-per-beam excitation (all dimensions in mm).	139
5.26	Simulated input reflection coefficient for the two-feed-per-beam configuration.	140
5.27	Simulated mutual coupling between conjugate input ports for the two-feed-per-beam configuration.	140
5.28	Simulated H -plane radiation pattern at (a) 18.75 GHz, (b) 17.3 GHz and (c) 20.2 GHz.	141
5.29	Simulated H -plane radiation pattern at 18.75 GHz for two-feed-per-beam excitation.	141
A.1	Effect of linear phase error on radiation pattern.	151
A.2	Effect of quadratic phase error on radiation pattern.	152
A.3	Effect of cubic phase error on radiation pattern.	153

A.4	Effect of quartic phase error on radiation pattern.	154
A.5	Gain loss and sidelobe level due to quadratic (—), cubic (--) and quartic (---) phase error.	155
A.6	Beam tilt due to linear (....) and cubic (--) phase error.	155
B.1	Constrained bifocal model of a continuous PPW lens.	158
C.1	Image formation in a system formed by (a) two converging lenses, (b) one converging and one diverging lens.	160

List of Tables

2.1	Multiple-beam parameters for different illuminations.	25
3.1	Comparison of non-contacting waveguide joints.	57
3.2	Comparison of mechanical scanning antenna designs.	78
4.1	Maximum transfer efficiency and optimal cluster weights (calculated/simulated).	109
4.2	Comparison of pattern mask and synthesized patterns (calculated/simulated).	109
5.1	Comparison of quasi-optical beamformers based on PCB technology.	142

CHAPTER 1

Introduction

1.1 Background

A recent report by the World Economic Forum, cooperating with the International Telecommunication Union (ITU), states that as of 2016, about 53% of the world's population is without access to the Internet [1]. While some may not see personal benefits in being connected, the main reason for limited internet penetration is the fact that many live in hard-to-reach or remote areas which often lack of access to transport and energy infrastructure. Major technological advancements in optical communications over the past two decades have driven the deployment of fiber optic backbones, which is steadily moving forward also in developing countries. Nevertheless, the expansion of fiber optic networks into rural areas often involves prohibitive costs, such that these services are mainly limited to urban agglomerations. At the same time, cellular networks providing last-mile broadband access continue to expand. However, despite the existing network footprint, savings in backhaul infrastructure in sparsely populated areas limit the capacity per user [2]. The next-generation cellular technology, 5G, promises significantly increased data rates, but current studies are focused on high-density scenarios and early deployments are therefore likely to impact mainly urban areas. The technology that is expected to revolutionize the expansion of broadband access into difficult-to-reach areas is satellite communication or, more specifically, satellite constellations operating at low (LEO) and medium earth orbits (MEO). Given the advantages of ubiquitous coverage and low latency in such networks, operators are committed to entirely close the digital divide by 2027. As in any modern wireless application, the ever-growing demand for reliable data communications implies increasingly stricter performance requirements and at the same time, inexpensive solutions

are needed to facilitate the development of infrastructure in all parts of the world. The trend towards smaller satellites has enabled dramatically reduced costs for manufacturing and launch costs; however, also user terminals and installations for the control segment need to be cost-effective to provide world-wide affordable services. In each segment, the antenna system is of particular importance as it largely determines the overall capacity and costs. The complex dynamics of LEO/MEO satellites, due to the relative motion with respect to the ground station, and the availability of larger bandwidths in the Ka-band have opened new design challenges. Hence, further research on the electromagnetic analysis and the design of broadband antennas with enhanced multibeam and scanning capabilities is essential to meet the demands of this rapidly evolving technology.

1.2 The Need for Quasi-Optical Beamformers

Due to the availability of higher bandwidths and the possibility to use smaller apertures on board the spacecraft and for user terminals, Ka-band satellite communications have become well established over the past decade. In the vast majority of scenarios, these advantages outweigh the drawback of increased susceptibility to atmospheric interference compared with lower bands in the microwave spectrum.

According to the ITU radio regulations, the frequency bands from 17.7 to 20.2 GHz and from 27.5 to 30.0 GHz are allocated to the downlink and uplink, respectively, of commercial fixed-satellite services. In addition, the bands from 20.2 to 21.2 GHz and from 30.0 to 31.0 GHz are assigned for military use. Considering the reduction in size, mass and cost, antenna systems capable of operating in both the uplink and downlink band are of great interest. However, this requires antenna designs with a fractional bandwidth of more than 50% and adequate external circuitry.

In low earth orbit (at an altitude of about 500 to 2000 km) satellites move fast with respect to ground terminals. To reduce the number of satellites in a constellation, antennas with a large field of view of up to $\pm 60^\circ$ are required. For example, at an altitude of 1450 km, satellite antennas must cover an angular range of about $\pm 50^\circ$ for a minimum elevation angle of 20° to the user terminal [3, p. 40]. Fan beams produced by such antennas result in highly elliptical footprints on earth, which often provide sufficient flexibility to cover the ser-

vice zone. Moreover, moderate antenna gains (20...30 dB) are needed to meet the requirements on G/T (gain-to-noise temperature ratio) and EIRP (effective isotropic radiated power) of receive and transmit systems, respectively. Directive antennas with wide-angle performance are therefore essential for future satellite communications.

Direct radiating arrays offer the advantage of rapid electronic beam scanning and shaping. Traditional phased array solutions provide high functionality but they require complex and costly corporate feed networks. In most cases, each array element is connected to an amplifier stage. The distributed amplification offers high reliability, since a single-point failure in the array results in graceful degradation of antenna performance. Due their lower manufacturing costs and power consumption, passive beamforming networks such as Blass [4] or Butler [5] matrices are an attractive alternative. However, the complexity and insertion loss of such networks also increases rapidly as the number of beams or array elements is increased. Moreover, the beams produced by matrix-fed arrays squint with frequency, with the result that the field of view decreases as frequency increases. While the feed network itself may operate only over a certain frequency band, the bandwidth of a matrix beamformer is also limited by the onset of grating lobes.

In recent years, quasi-optical beamforming architectures have received increasing attention in the field of space applications. Besides the more compact construction, the major advantage of quasi-optical systems over multiple-beam matrices is their true time delay, which removes bandwidth limitations. Since the operating principle is based on electrical path length compensation, the beam pointing angle remains stationary as frequency changes. In fact, the concept of beam-scanning reflector and lens antennas has been subject of continuous research since the 1940s. Early development efforts focused on mechanically steerable antennas for radar applications. Furthermore, quasi-optical multibeam designs providing discrete beam scanning or multiple simultaneous beams were introduced. The latter solution is nowadays widely used for antenna systems on board geostationary satellites providing fixed spot beam coverage over a limited angular range (less than $\pm 10^\circ$). In contrast, LEO/MEO satellite applications call for multiple-beam antennas with wide field of view in the space segment and highly maneuverable antennas in the ground segment, capable of steering narrow beams continuously to provide near-constant communication links. Considering this set of requirements, there is a great need for innovative

quasi-optical beamforming solutions and accurate numerical models that aid in the analysis and design of such.

The following section provides an overview of the state of the art of quasi-optical beamformers. Their operating principle will be briefly described and examples of practical implementations are given. Emphasis is placed on the potentials and shortcomings of existing solutions with regard to the design requirements discussed in this section.

1.3 Overview of Existing Solutions

The following overview focuses on integrated quasi-optical beamformers which provide fan-beam scanning in one plane. Three-dimensional (3D) reflector and lens antennas (e.g. formed by a body of revolution) are widely used for pencil beam scanning; especially the former is the standard solution in antenna systems for geostationary satellites with spot beam coverage. The involved scan mechanisms are readily apparent from the two-dimensional (2D) designs discussed in the following. Moreover, from an integration point of view, a stack of such low-profile beamformers appears to be more attractive than single 3D designs if steering in the azimuth and elevation plane is desired.

1.3.1 Pillbox Systems

Pillbox antennas, typically formed by a reflector system integrated into a parallel-plate waveguide (PPW), can be seen as the most basic type of quasi-optical beamformer. Scanning is achieved by displacement [6] or rotation [7] of a single feed or by using multiple feeds placed in the focal region of the reflector [8, 9]. Due to the symmetrical geometry, circular reflectors are free of off-axis phase aberrations and therefore lend themselves to mechanical wide-angle scanning. However, such configurations suffer from spherical aberrations, meaning that a cylindrical wave emanating from the paraxial focus is not converted into a plane wave. This effect may be overcome, for example, by placing a correcting lens in the object or image space of the reflector or by shaping the reflector contour. As indicated in Fig. 1.1(a), the feed contour is concentric with respect to the reflector and the maximum scan range is limited by spillover and shadowing effects. The designs presented in [7] demonstrate scan ranges up to $\pm 55^\circ$ but their overall performance is limited by relatively high mismatch losses due to

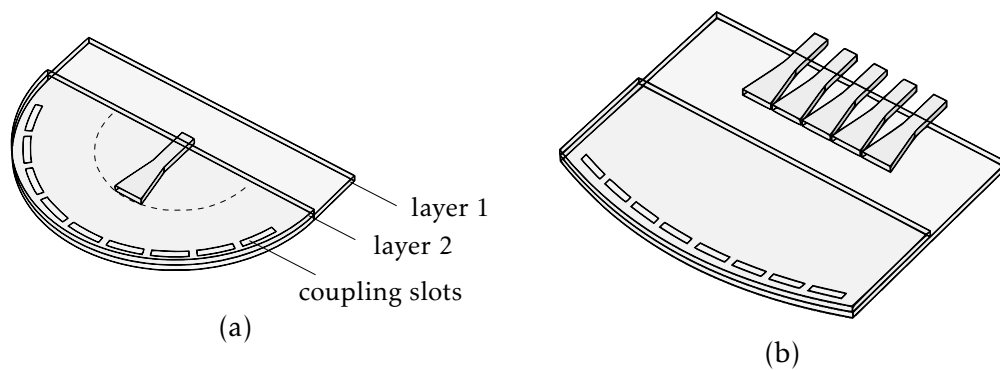


Figure 1.1: Double-layer pillbox system with (a) circular reflector, (b) parabolic reflector.

internal reflections.

Parabolic reflectors, on the other hand, exhibit one perfect focus and have been widely used in more recent pillbox designs [6, 8, 9]. The lateral feed displacement required for scanning the beam leads to the following conflict: feed offset angle and beam pointing direction are closely related and therefore reflectors with small F/D (focal-length-to-diameter ratio), subtending a larger angle, are preferable to minimize spillover loss at wide scan angles. On the other hand, a larger F/D value is needed to mitigate the degradation of the far-field pattern with the number of beamwidths scanned. As a consequence, a compromise needs to be found taking into account size limitations and the requirements on radiation performance. To avoid aperture blockage by the feed, multilayer structures have been widely adopted. In this case, the fields reflected by the mirror are coupled to a layer above where they are guided to the radiating part of the beamformer. Different low-profile radiating systems, including leaky-wave slot arrays [8], resonant slotted waveguides [6] and continuous transverse stub arrays [9] have been proposed in conjunction with pillbox couplers. Nevertheless, the useful scan range of parabolic reflectors is typically limited to several numbers of beamwidth (< 10) due to the emergence of high coma lobes.

1.3.2 Constrained Lenses

In contrast to dielectric lenses (regardless of whether homogeneous or inhomogeneous), where propagation is governed by Snell's law of refraction, constrained lenses refer to focusing devices in which waves are confined to discrete paths which may have different propagation properties. The geometry and length of

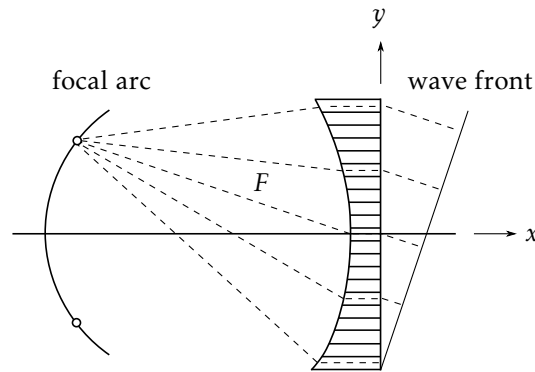


Figure 1.2: Schematic view of a metal-plate lens with straight front face.

the guiding structures are designed such that the desired amplitude and phase distribution is generated along the aperture of the lens for various feed positions. Metal-plate optics, as described in [10] and [11], can be seen as the origin of constrained lenses. In the conventional metal-lens design, waves are confined between conducting plates oriented parallel to the electric field vector, i.e., the delay mechanism is based on the dispersion characteristic of the first transverse electric (TE_1) mode of a parallel-plate waveguide. Such a lens obeys Snell's law and the focusing behavior is comparable to that of its dielectric counterparts. In constrained metal lenses, by contrast, electromagnetic waves are guided by the plates but their direction is not affected by the refractive index. Since Snell's law does not need to be satisfied at the boundaries, other conditions along with path length constraints can be specified. This yields additional degrees of freedom in the design, and consequently a number of unique features can be obtained with constrained lenses. The design discussed in [11] allows to impose three independent conditions, which results in lenses with two symmetrical off-axis focal points and different mechanical layouts. Scanning of a one-degree beam over an angular range of 100 beamwidths has been demonstrated with such a lens having $F/D = 1.5$. The phase error analysis of different designs shows that highest scan performance can be achieved with lenses having a straight front face and proper refocusing of the focal arc. Metal-plate lenses are uniquely defined by three independent variables: the shape of the inner lens profile, the variation of the refractive index and the thickness of the lens. Due to the parallel plate arrangement, the aperture of the lens is confined along the y axis according to the inner lens contour. Using flexibly routable transmission lines, such as coaxial cables, an extra degree of freedom is obtained, namely the relative positions of outer lens contour points with respect to their counterparts on the inner contour.

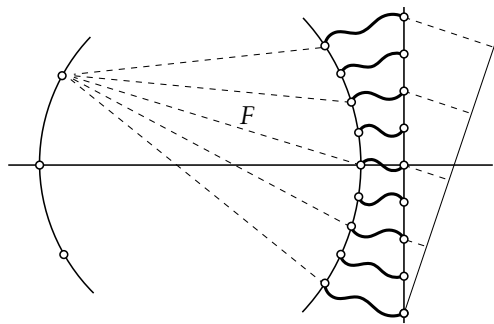


Figure 1.3: Schematic view of a Rotman lens.

This corresponds to the basic design principle of bootlace lenses as introduced by Gent [12]. Two of the most popular designs will be discussed in the following.

1.3.2.1 Rotman Lens

The design proposed by Rotman [13] is by far the most commonly implemented bootlace lens. In this case, the available degrees of freedom are used to specify one on-axis and two symmetrical off-axis focal points. Moreover, following the conclusions in [11], a straight front face is imposed. As shown in Fig. 1.3, the points on the outer contour are equidistant such that the lens can be used for phasing a linear array. One particularity of the original Rotman lens with respect to the more general class of trifocal lenses is the fact that feeds at angular positions between the focal points lie on a circular arc passing through these. The optimum configuration, i.e., the ratio of on- to off-axis focal distance (G/F) ensuring a minimum of phase errors over a wide range of feed positions is found using the refocusing condition established in [11]. Several modifications to the original Rotman lens concept have been proposed. The method described in [14] allows a significant reduction of phase errors for lenses with suboptimal G/F . The improved feed arc is determined through numerical integration. Moreover, the ratio of beam pointing angle to feed position angle is used as an additional design parameter. More recently, another design method for reducing the phase error of suboptimal Rotman lenses has been proposed [15]. The described approach allows enhanced scan ranges while maintaining a convenient focal-curve shape with respect to the inner lens contour. A reduction in scan loss by 2 dB for a scanning range of $\pm 50^\circ$ (about ± 16 beamwidths) has been demonstrated with a phase-only model.

The original design proposed by Rotman [13] is based on a parallel-plate structure with a separation of less than a half wavelength and flexible coaxial cables,

used to connect the probes on the inner lens contour with the array elements. The lens relies therefore entirely on transverse electromagnetic (TEM) propagation and offers wideband performance. The use of coaxial transmission lines allows fine discretization but involves complex manufacturing and assembly processes. Implementations based on planar transmission lines such as microstrip or stripline allow a significant reduction in size and cost while maintaining bandwidths as large as 3:1. As with probes, a half-wavelength port spacing can be readily achieved. The efficiency of the lens is subject to common printed circuit board (PCB) design conflicts: the miniaturization of circuitry calls for thin high-permittivity substrates which ensure tightly bound fields. However, due to the greater resistance in narrow strips, conductor losses increase rapidly in such designs. In addition, significant bandwidth limitations may arise if the radiating elements are to be integrated on the same substrate. For reduced losses at millimeter-wave frequencies, Rotman lenses may be implemented using rectangular waveguide feeds and delay lines. Two different concepts, based on TEM [16] and TE propagation [17] inside the parallel-plate guide, have been proposed. In the first case, feeds and parallel-plate cavity are identical to the design presented by Rotman, i.e., vertically polarized horns are used to excite the fundamental PPW mode. The rectangular waveguides forming the delay paths are oriented with their broad wall horizontal. To ensure that the waveguides operate well above cutoff, an array port spacing larger than a half wavelength is required; this affects the placement of feeds and array elements [16]. Waveguides oriented with their broad wall vertical may be used to overcome this complication. In this case, the electric field inside the parallel-plate region is polarized horizontally and feeds must be designed carefully to excite only the TE_1 mode. Clearly, the involved modes introduce dispersion which counteracts the true-time delay characteristic of the lens. More recently, equivalent PCB implementations based on substrate integrated waveguides have been proposed [18, 19]. The design in [18] is based on a multilayer structure which allows a reduction in footprint by a factor of two. Parallel-plate cavity and SIW delay lines are realized on two different substrate layers and coupled to each other using a reflector and multibranch slots.

1.3.2.2 *R-2R* and *R-KR* Lens

While Rotman lenses are mainly used in combination with linear arrays, the *R-2R* and *R-KR* lenses provide appropriate feeding for circular beam-scanning arrays.

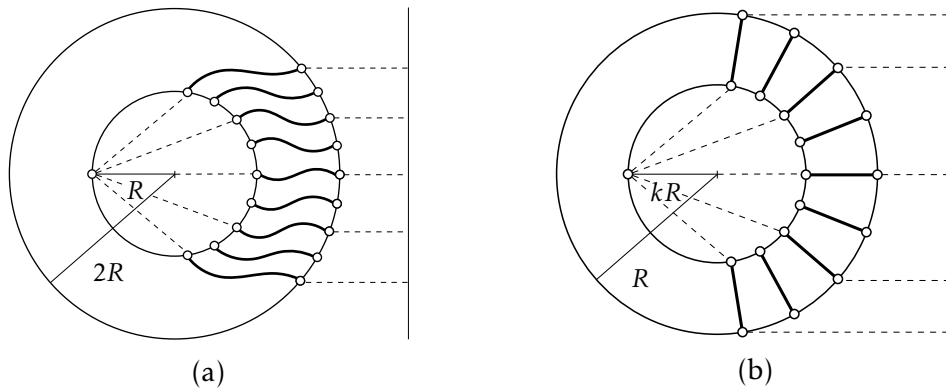


Figure 1.4: Schematic view of an (a) $R-2R$ lens, (b) $R-KR$ lens.

As shown in Fig. 1.4, the geometry of such lenses is based on two circles (not necessarily concentric), one of which used as feed arc and array port contour and the other on which the array elements lie. The $R-2R$ lens uses a radiating array placed on a circle with a radius twice that of the lens periphery. Transmission lines of equal length are used to connect the array elements with the ports on the lens contour. The remarkable and among bootlace lenses unique feature of this design is that perfect focusing is provided for all points on the focal arc. Interestingly, the limitation on the scan range is due to the same feature that enables the superior focusing properties of $R-2R$ lenses, namely the array port placement with respect to the radiating elements. More specifically, the radius ratio implies that a circular array subtending an angle ϕ requires an array port contour extending out to 2ϕ ; likewise, steering the main beam to ϕ requires an angular feed position of 2ϕ . The $R-KR$ lens, shown in Fig. 1.4(b), also uses equal-length delay lines and offers the advantage of one-to-one mapping between the lens contour and the circular array. However, the lens geometry does not allow perfect focusing on the focal arc. Hence, the fields generated by a feed are transformed into a nearly planar wave emerging in the diametrically opposite direction. Also in this case, the portion available for the feed arc is reduced as the portion of the lens periphery connected to array elements is increased. As a consequence, all elements on the lens contour need to be used as both feed and array ports if coverage of 360° is desired. Additional components such as switches or circulators are required to alternate the operating mode of each port. Since circulators are nonreciprocal devices, typically realized using anisotropic materials such as ferrites, it is generally not possible to use such a lens antenna for both transmission and reception. A dual-lens structure which

overcomes this limitation has been proposed in [20].

Using PCB technologies, integrated active designs can be realized where lens and power amplifiers are integrated with the radiating elements on the same substrate. Due to the discretization at the input and output, constrained lenses can be readily used as low- and high-level beamforming networks (BFN). The discretization which gives such lenses their improved focusing characteristics, when compared to conventional dielectric lenses, has two drawbacks. First, while the lens itself provides true time delay, the selected array port spacing sets an upper limit on the frequency of operation. It should be noted that in practice, limitations on the achievable bandwidth rather arise from the components that are used to construct the lens, such as feed ports or waveguide transitions. The main disadvantage of constrained lenses is, as with matrix beamforming networks, their high integration complexity, especially for large apertures. Typically, a trade-off needs to be found between compact design and high efficiency.

1.3.3 Radially Symmetric Lenses

As with semicircular reflectors, the symmetry of cylindrical homogeneous lenses makes them natural candidates for wide-angle scanning. However, also the refractor suffers from inherent spherical aberrations which increase with aperture size. Another disadvantage of this type of lens is that the step in refractive index at the dielectric surface is generally large enough to require a matching layer for eliminating reflections [21].

When introducing inhomogeneous refractive index materials, lenses with unique focusing properties can be formed. Solutions to the differential ray equation in spherical coordinates have lead to several distinct designs, including two types of lenses suitable for wide-angle beam scanning. The spherical lens introduced by Maxwell represents an example of an absolute optical instrument and offers perfect imaging from one point on the lens surface into a diametrically opposite point. Its performance is based on a gradient index profile of

$$n(\rho) = \frac{n_0}{1 + (\rho/R)^2} \quad (1.1)$$

where n_0 is the refractive index at the center of the lens and R the radius of the lens. As shown in Fig. 1.5(a), the ray trajectories within the lens are circular arcs. By cutting the lens in half, a collimated beam can be formed. Since rotational symmetry no longer holds, the scanning performance is clearly affected by this

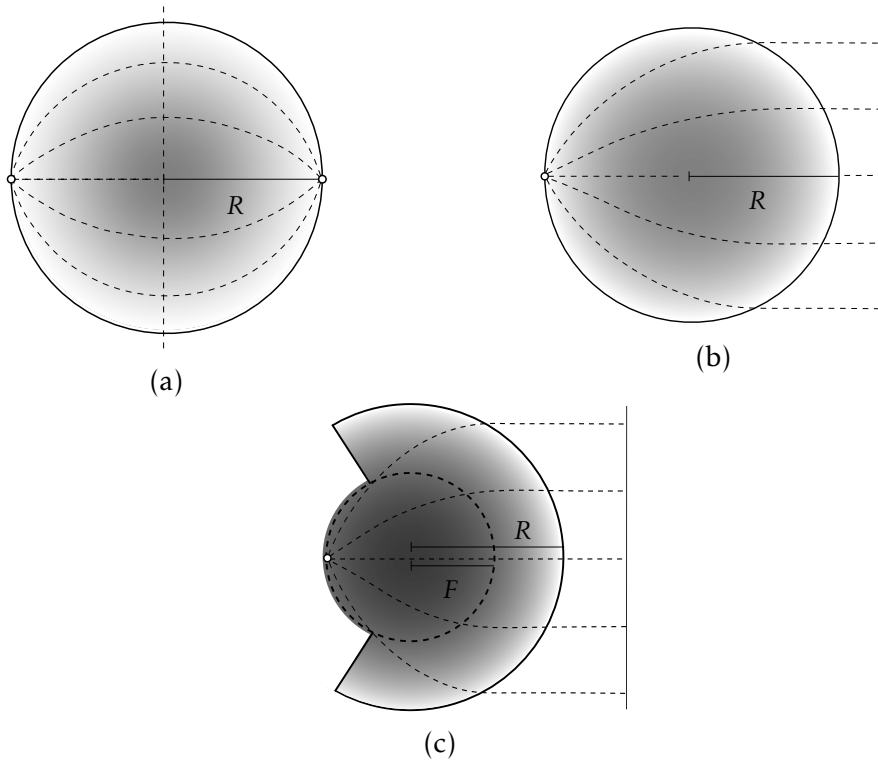


Figure 1.5: Schematic view of a (a) Maxwell fisheye lens, (b) classical Luneburg lens, (c) modified Luneburg lens.

modification. Moreover, the lens suffers from reflections at the transition to free space.

The two-dimensional Luneburg lens corresponds to a cylindrical design in which the variation of the refractive index with radial distance ρ is described by

$$n(\rho) = \sqrt{2 - (\rho/R)^2}. \quad (1.2)$$

As a result, the refractive index ranges from $\sqrt{2}$ at the center to 1 at the periphery; the latter is of particular advantage since no reflections occur at the transition to free space. In theory, the focal arc is formed by the entire perimeter of the lens, i.e., a cylindrical wave emanating from any point on the border is transformed into a plane wave emerging at the opposite of the lens. Due to the circular symmetry, the scanning performance is independent of the beam direction. In practice, the field of view is usually restricted by blockage due to the lens support, including the radiating aperture and the feed structure. Furthermore, it has been shown that the focus of a Luneburg lens may be shifted onto a circle of

smaller radius F inside the lens by using a refractive index profile given by [22]

$$n(\rho) = \sqrt{\frac{1 + (F/R)^2 - (\rho/R)^2}{(F/R)^2}}. \quad (1.3)$$

As a result, a refractive index of 1 at the periphery is maintained while the value required at the center of the lens increases as the focal arc radius is decreased. Since at the focal arc $n = R/F > 1$, feeds need to be designed carefully to ensure proper impedance match. To accommodate the feeding structure, a sector of the cylindrical lens needs to be removed as illustrated in Fig. 1.5(c), and therefore a significant reduction in weight is achieved.

For manufacturing reasons, Luneburg lenses are typically constructed of nested shells with uniform refractive index, which provides a discretized approximation to the continuous gradient. The number of required layers increases with the size of the lens; typically, a threshold is found beyond which the aperture efficiency does not improve significantly. Due to inaccuracies in the construction process, the existence of air gaps between the shells may be unavoidable. Such gaps give rise to reflections between the dielectric layers, thus degrading the overall radiation performance of the lens [23]. To address this problem and the ease of manufacturing, numerous alternative solutions based on different propagation mechanisms have been proposed. These include parallel-plate structures and dielectric slabs with varying height [24–26] as well as printed periodic structures [27] approximating the required refractive index profile. To overcome the increasing losses in dielectric media at higher frequencies, lens designs based on fully metallic metasurfaces have been developed [28], [29].

The geodesic realization of two-dimensional graded-index lenses is obtained using a pair of non-planar parallel plates as shown in Fig. 1.6. In this case, the third dimension, orthogonal to the scan plane, is exploited to obtain the optical properties of flat gradient-index media. The parallel-plate spacing is such that only the TEM mode will propagate. Rays emanating from the feed are guided between the plates toward the radiating aperture on the diametrically opposite side. The ray paths inside the lens are governed by Fermat's principle of least time and follow geodesic lines [30]. Due to their all-metal design, geodesic lenses present a particularly attractive solution for space-segment antennas. Moreover, they offer the advantage of mechanical simplicity and stable performance at millimeter-wave frequencies. The geodesic equivalent of the Luneburg lens is known as Rinehart lens [31]. A clear drawback of the original design is its large

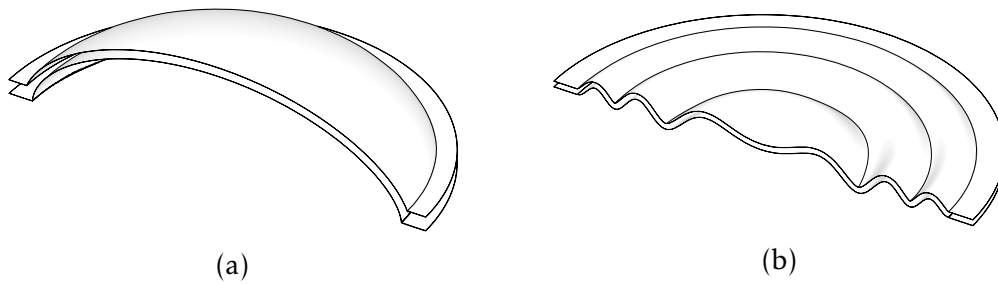


Figure 1.6: Cross-sectional view of a (a) Rinehart lens, (b) modulated geodesic lens.

vertical dimension (about 0.6 times its radius) which complicates the integration of the lens into a stack of beamformers for pencil-beam steering. The approach proposed in [32] addresses this problem by reflecting parts of the lens profile across a horizontal plane intersecting the lens. However, the resulting contours exhibit sharp edges, described by a discontinuous derivative, which are expected to negatively affect the propagation inside the lens. Recently, this concept has been revisited by introducing optimized bends at the mirroring points, which allows a reduction in height by a factor of 2.5 while maintaining a smooth shape [33]. Similar to the design of non-focal constrained lenses [34], recent development efforts were focused on shaping the lens profile as a whole through optimization processes for controlling amplitude and phase distribution in the radiating aperture, rather than altering the original geodesic configuration [35]. The focusing performance of graded-index lenses and their geodesic analogues is unsurpassed when compared to other quasi-optical systems. Rapid advancements in manufacturing technology and in the research on metamaterials have opened the way for efficient low-cost implementations at millimeter-wave frequencies. Perhaps the only drawback of this type of lens is its overall size and shape, which limit its range of applications. Radially symmetric lenses may be used as direct radiating devices or in conjunction with circular arrays. However, they are inefficient for feeding linear arrays since the illumination becomes asymmetric as the beam is scanned. The so called Myers lens [30, 36] does not suffer from this drawback, meaning that all feeds generate equivalent field distributions along the linear aperture; however, due to its high profile, a more detailed discussion is outside the scope of this chapter.

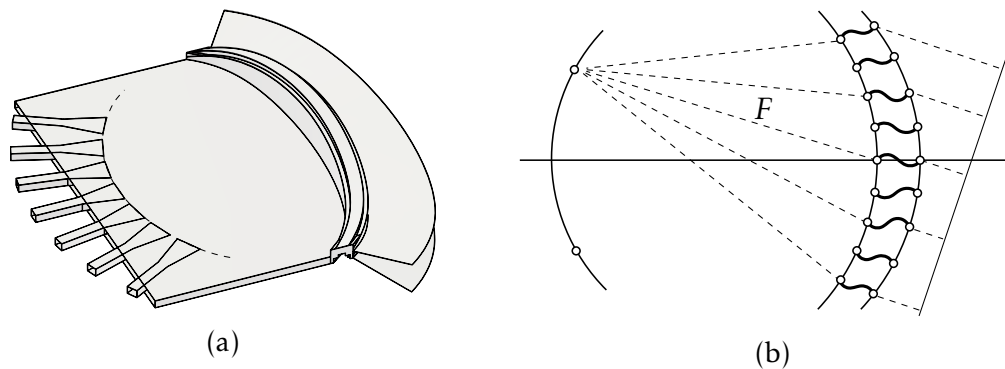


Figure 1.7: (a) Schematic view of a multiple-beam continuous PPW lens, (b) constrained lens model.

1.3.4 Continuous Parallel-Plate Waveguide Lenses

More recently, lens designs based on continuously shaped parallel-plate waveguide sections have been introduced [37–39]. In this case, the true time delay is accomplished by a transversal delay section as shown in Fig. 1.7(a). The beamformer can be divided into two main parts: a horizontal PPW section forming the focal region of the quasi-optical system and a continuously shaped vertical PPW section which constitutes the actual lens. Also here the plate spacing is small enough such that only the dominant mode propagates. If the lens is to be used as a direct-radiating antenna, a flared is added to interface the structure to free space.

The available degrees of freedom are comparable to that of conventional bifocal lenses, thus yielding excellent scan performance for a moderate range of angles. Due to the uniform parallel-plate waveguide forming the quasi-optical system, the continuous lens can be viewed as the *constant-refractive-index design* discussed in [11], with the difference that inner and outer lens profile are identical and theoretically collocated. The latter property is also the key difference with respect to the classical Rotman lens where the lens contours can be defined rather independently. Starting from the bifocal model, the beam ports are placed along a focal arc which intersect the foci. As with the constrained lenses discussed previously, inter-focal feed positions do not provide perfect focusing and result in phase errors along the outer lens surface. However, as in [11] an optimum refocusing condition for the feed arc can be found.

Just as geodesic PPW lenses, such beamformers provide a continuous aperture and therefore overcome bandwidth limitations due to the emergence of grating

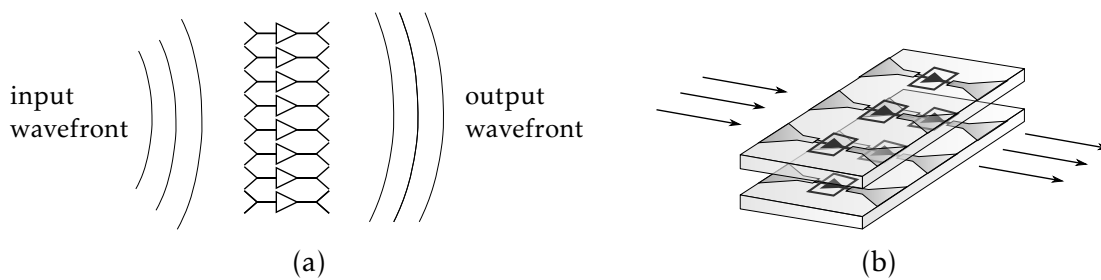


Figure 1.8: (a) Schematic view of a spatial amplifier stage, (b) tray amplifiers.

lobes. Since the delay mechanism involves only TEM propagation, there is no beam squint with frequency. In theory, the bandwidth of the quasi-optical system is limited by the onset of the first set of higher-order modes. This implies that both downlink and uplink frequency bands could be covered as long as the plate spacing is chosen such that the cutoff frequency lies well above the latter frequency range. However, designing a suitable feed system presents the main challenge. Compared with constrained lenses, the construction and assembly are greatly simplified due to the fact that no discrete delay lines are employed. The lens concept is compatible with a fully metallic implementation, offering high radiation efficiency, enhanced power-handling capacity and mechanical ruggedness. Since the design does not involve dielectric media, it may operate in extreme environments without compromising performance. Most importantly, the quasi-optical system offers a high degree of design flexibility, meaning that its geometry can be formed to fit into various beamforming structures. Like pill-box couplers, the lens can be combined with more advanced radiating parts such as continuous transverse stub arrays [40]. A continuous aperture, as shown in Fig. 1.7(a), can be maintained when integrating the amplifier stage with the feeds. In this configuration, the lens acts as a high-level BFN. For an air-filled PPW, the insertion loss of the lens is low (< 0.3 dB for a lens diameter of 20λ [39]), such that antenna gain performance is not significantly compromised. However, the failure of one amplifier can cause the total loss of one beam, unless redundancy is provided. Alternatively, amplification can be introduced at aperture level using spatial power-combining techniques [41]. In this amplification scheme, power is combined coherently in free space by an array of active devices coupled to antennas. As shown in Fig. 1.8(a), each array element is designed to receive energy through an input antenna and, after amplification, retransmit the signal from a second antenna. Since the energy is distributed in guided beams or waveguide modes, rather than planar transmission lines, spatial power combining is

an efficient solution to achieve relatively high power from solid-state devices at millimeter-wave frequencies. An array with tray geometry, as shown in Fig. 1.8(b), is more complex to integrate than a planar grid, but compatible with traveling-wave antennas and therefore ideally suited to broadband applications. Previously presented continuous PPW lens designs make use of fixed feed horns, which allow multiple simultaneous beams or discrete beam scanning. The proof-of-concept design presented in [37] operates at Ku-band and produces six equally spaced beams in the range $\pm 30^\circ$. A more advanced Ka-band configuration for a similar scan range has been proposed more recently in [39]. Using two stacked delay sections, a beam crossover of -3 dB and relatively low sidelobe levels are achieved. Radiation efficiencies of more than 95% are reported for a structure of 20λ in diameter. Moreover it is shown that the beamformer can be made from only two complementary blocks.

So far, the concept of continuous parallel-plate lenses has addressed a number of important needs of satellite antenna systems. Nevertheless, previous lens designs show two main limitations in terms of scanning performance. One shortcoming is the moderate scan range, especially when compared to circularly symmetric devices. This means that for LEO satellite applications, lenses with large F/D and therefore large axial dimensions would be required to limit scan losses across the field of view. The second limitation of previous studies is the fact that only basic multiple-beam configurations have been considered, in which complete coverage of the field of view is achieved at the expense of an additional quasi-optical system [39].

1.4 Novel Contributions in this Thesis

This thesis addresses the need for integrated beamforming devices with enhanced scanning performance, which is essential for continuous communication in next-generation satellite networks. Starting from numerical tools available at the beginning of the study, this work further develops the analytical modeling of parallel-plate lenses. A ray-tracing technique previously developed to determine the far-field patterns is extended to investigate the focal-region distribution in reception. These methods are used for the practical design of two lens beamformers. The novel aspects elaborated in this thesis include the following:

- The design of a continuous parallel-plate waveguide lens with enhanced

field of view of $\pm 50^\circ$, operating at Ka-band and suitable for use in both ground and space segment of LEO/MEO satellite networks.

- The design of a mechanically reconfigurable feed system based on gap waveguide technology which, in conjunction with the developed beamformer, enables continuous scanning over a large angular range. The proposed concept is validated with a prototype.
- A rigorous analysis of parallel-plate lenses in reception. The resulting numerical method constitutes a powerful tool for the characterization and synthesis of advanced feed configurations.
- The design of a lens beamformer with overlapping feed clusters, using the developed numerical tool. The beamformer is designed toward complete coverage of a wide angular range of $\pm 60^\circ$.
- The cost-effective implementation of such a lens beamformer in multilayer PCB technology.

1.5 Thesis Structure

This thesis can be divided into three main parts. In the first part, corresponding to Chapter 2, the theoretical limitations of multiple-beam antennas are revisited and previous approaches to overcome these are discussed. In the second part, including Chapter 3 and 5, the design and implementation of two beamformers, relying on different feed mechanisms and technological solutions, are presented. The third part, Chapter 4, is focused on the analysis of integrated quasi-optical systems on receive and the systematic use of the insights gained for the design of efficient feed systems.

The manuscript is organized as follows:

Chapter 2 discusses inherent limitations of beamforming networks and gives an overview of practical solutions to the problem of orthogonality loss in quasi-optical designs. Two approaches particularly suited for parallel-plate lenses are discussed: mechanical beam scanning for continuous coverage and multiple-feed-per-beam operation providing high-crossover low-sidelobe patterns.

Chapter 3 presents the development of a mechanically reconfigurable gap waveguide structure, used to feed a continuous PPW lens with enhanced scan range. Analytical models which aid in the design of both the feed structure and the quasi-optical system are discussed in detail. The manufacturing and experimental characterization of a prototype operating in the uplink Ka-band are reported.

Chapter 4 focuses on the analysis of quasi-optical systems, in particular of PPW lenses, in reception. An asymptotic technique, based on a previously proposed ray-tracing procedure and on physical optics, for determining the field distribution in the focal region for arbitrary incident fields is presented. The use of reciprocity in the focal-region domain for characterizing the coupling to a given feed distribution is described. The developed numerical tool is used to study the beam scanning limitations of the quasi-optical system and for the derivation of improved feed contours. Furthermore, the procedure is extended to the synthesis of overlapping feed clusters.

Chapter 5 focuses on the design of a lens beamformer with multiple-feed-per-beam operation. A major part of the design process is based on the numerical tool detailed in Chapter 4. The PCB implementation of a lens operating in the downlink Ka-band is described.

Chapter 6 reviews the key developments achieved in this work. Suggestions for future research activities are identified.

CHAPTER 2

Beam Reconfigurability in Quasi-Optical Systems

Ka-band satellite communications call for antenna systems with increased functionality. Given the need for compact light-weight and low-power devices, reconfigurable antennas can be seen as a solution to this problem. In the broad sense, the reconfiguration of an antenna refers to a deliberate change of its operating frequency band, polarization or radiation characteristic. Most of the quasi-optical systems discussed in the previous chapter are based on guided wave propagation and the effect of higher-order modes often prevents covering or switching between Tx and Rx band. Dual polarization allows doubling the communication capacity by transmitting separate signals on orthogonal polarizations over the same physical link and at the same frequency. Modern satellite communications rely on circularly polarized antennas to reduce the interference from multipath signals and the impact of misalignment between transmitter and receiver. In the context of 2D quasi-optical beamformers, recent developments have been concentrated on low-profile linear-to-circular polarization converters [42, 43] placed in proximity of the radiating aperture. Following this modular approach, the requirement of polarization diversity is addressed separately from the design of the actual beamformer. This work focuses on the radiation characteristics that need to be provided by quasi-optical systems in order to meet the essential coverage requirements of future satellite communications.

2.1 Fundamental Limitations of Multibeam Antennas

Similar to high-performance radar systems, satellite communications require low sidelobe levels in order to mitigate interferences. For ground-segment antennas, sidelobes mainly determine the level of interference with other orbiting satellites. On the other hand, the sidelobe level of spaceborne antennas does not only determine the interference outside the intended coverage area but also the scattering from the satellite body and solar panels. Another important requirement is that the antenna system provides high beam crossing levels such that nearly the full gain is available at any point within the field of view.

The design of the feed system depends on whether a beamforming device is used for beam scanning or fixed-beam operation. In a beam-scanning antenna system using multiple feeds, the key performance parameters are peak gain, gain ripple and sidelobe levels. The gain ripple results from the crossover of two discrete beams produced by adjacent feed elements. In an antenna system generating simultaneous fixed beams, also the minimum gain within the field of view and the interference between beams need to be taken into account. In both cases, the feed design is typically concerned with the conflicting requirements of small element spacing to raise beam crossing levels, and large feed apertures to reduce sidelobe levels and spillover losses. The first formal treatment of this problem has been developed in the context of beamforming matrices [44–46] but can be readily applied to quasi-optical devices. As an example, the Butler matrix [5] is used to feed in parallel a linear array that produces a beam for every input port. The feed network is passive, lossless and provides uniform illumination along the array resulting in $\sin x/x$ type beams with sidelobes at about -13 dB. The generated patterns squint with frequency, thus forming a contiguous set of beams that cross each at -3.9 dB. In many applications, much lower sidelobes or even higher crossover levels may be required. However, soon after the emergence of multiple-beam matrices it has been demonstrated that, due to the principle of energy conservation, beams must be mutually orthogonal over one period of the pattern in order to be formed by a lossless network [44]. Based on the symmetry and unitary properties of the scattering matrix of a lossless reciprocal network, it can be shown that this region is given by $-\lambda/(2Nd) < u < \lambda/(2Nd)$ in sine space, where d is the element spacing of the array and N the number of elements. For a uniformly illuminated array the angular spacing of orthogonal beams is then

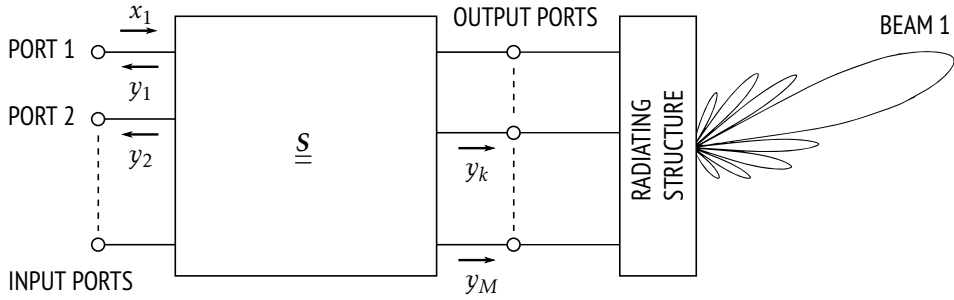


Figure 2.1: Schematic view of a transmitting beamforming network.

given by $\Delta u = \lambda/(Nd)$, while for a cosine amplitude taper it increases to $2\lambda/(Nd)$. The generation of multiple independent beams from a common aperture means that the radiation resulting from a simultaneous excitation of two or more of the input ports is simply a linear superposition of the radiated fields obtained when exciting these ports separately. However, beam orthogonality also implies that crossover levels and beam shapes cannot be specified independently, unless network losses are accepted [45]. In view of this major limitation, the question of optimal multiple-beam antennas has been addressed in [46], which will be outlined in the following. Using the notation of Fig. 2.1, waves incident at the antenna ports are represented by x_m and related to the reflected waves y_k by

$$y_k = \sum_{m=1}^M S_{km} x_m \quad \text{or} \quad \mathbf{y} = \underline{\underline{\mathbf{S}}}\mathbf{x}. \quad (2.1)$$

If the power incident at the k th port is equal to unity, the radiated field at a distance R from the antenna can be described by a spherical wave of the form

$$\mathbf{E}_k(\theta, \phi) = q_k \mathbf{R}_k(\theta, \phi) \frac{e^{jk_0 R}}{R}, \quad (2.2)$$

where k_0 is the wavenumber of free space. The vector $\mathbf{R}_k(\theta, \phi)$ is referred to as beam pattern and normalized conveniently so that

$$\frac{1}{2\eta_0} \int_0^{2\pi} \int_0^{\pi} \mathbf{R}_k(\theta, \phi) \cdot \mathbf{R}_k^*(\theta, \phi) \sin \theta \, d\theta \, d\phi = 1 \quad (2.3)$$

where η_0 is the intrinsic impedance of free space. As a result, the total radiated power for the k th beam is

$$P_k = \frac{R^2}{2\eta_0} \int_0^{2\pi} \int_0^\pi \mathbf{E}_k(\theta, \phi) \cdot \mathbf{E}_k^*(\theta, \phi) \sin \theta \, d\theta d\phi = |q_k|^2. \quad (2.4)$$

Since unit power is incident at the input port, $|q_k|^2$ represents the radiation efficiency for the k th beam, while $1 - |q_k|^2$ describes the insertion loss and the power reflected back into the feed lines.

The coupling between different beams is described by the coefficients

$$\beta_{kj} = \frac{1}{2\eta_0} \int_0^{2\pi} \int_0^\pi \mathbf{R}_k(\theta, \phi) \cdot \mathbf{R}_j^*(\theta, \phi) \sin \theta \, d\theta d\phi \quad (2.5)$$

where $\beta_{kk} = 1$, $\beta_{kj} = \beta_{jk}^*$ and $|\beta_{kj}| \leq 1$. The terms β_{kj} form a square matrix, also referred to as beam coupling matrix, whose off-diagonal entries represent the coupling between the different beams and, if zero, define an orthogonality relationship between them. Due to the Fourier transform relation between far-field pattern and source distribution, the beam coupling matrix may also be determined directly from the aperture fields using Parseval's theorem [47]. Assuming that all input ports are excited with arbitrary complex amplitude, the total radiated power is found as

$$P_{\text{rad}} = \frac{R^2}{2\eta_0} \int_0^{2\pi} \int_0^\pi \mathbf{E}(\theta, \phi) \cdot \mathbf{E}^*(\theta, \phi) \sin \theta \, d\theta d\phi = \sum_{k=1}^M \sum_{j=1}^M x_k^* q_k^* \beta_{kj} x_j q_j \quad (2.6)$$

or, in more compact notation,

$$P_{\text{rad}} = \mathbf{x}^H \underline{\underline{\Gamma}} \mathbf{x} \quad (2.7)$$

where \mathbf{x}^H denotes the Hermitian transpose of the excitation vector and

$$\Gamma_{kj} = q_k^* \beta_{kj} q_j. \quad (2.8)$$

The matrix defined above has eigenvalues γ_k that satisfy

$$\underline{\underline{\Gamma}} \mathbf{x} = \gamma \mathbf{x}. \quad (2.9)$$

Since $\beta_{kj} = \beta_{jk}^*$, it is apparent from (2.8) that the matrix is Hermitian. Moreover, as the total radiated power must be positive real or zero, it follows from (2.7) that the matrix is also positive semidefinite, thus having N non-negative eigenvalues. The important conclusion reached in [46], also referred to as Stein's limit, is the fact that the largest eigenvalue of the matrix cannot exceed unity, i.e.,

$$(\gamma_k)_{\max} \leq 1. \quad (2.10)$$

The far-reaching implications of (2.10) can be demonstrated by considering the simple case of all beams having equal radiation efficiencies, that is, $q_k = q$ for all k . The matrix is then given by

$$\Gamma_{kj} = |q|^2 \beta_{kj}. \quad (2.11)$$

and the eigenvalue problem simplifies to

$$|q|^2 \beta \mathbf{x} = \gamma \mathbf{x}. \quad (2.12)$$

The eigenvalues γ_k are then directly related to the set of eigenvalues β_k of the beam coupling matrix by

$$\gamma_k = |q|^2 \beta_k. \quad (2.13)$$

As a result, Stein's limit may be written as

$$|q|^2 \leq \frac{1}{(\beta_k)_{\max}} \quad (2.14)$$

which expresses the inherent limitations on radiation efficiency in terms of the beam coupling. As all the diagonal elements β_{kk} are unity, the trace of the beam coupling matrix is equal to N . Since for any square matrix the trace equals the sum of the eigenvalues, the dominant eigenvalue cannot be smaller than the average of the diagonal elements, i.e., $(\beta_k)_{\max} \geq 1$. As a consequence, $|q|^2 \leq 1$ and $|q|^2 = 1$ is possible only if all the eigenvalues β_k are equal to unity. The general beam coupling matrix is Hermitian and therefore diagonalizable; this implies that if all eigenvalues are equal, the beam coupling matrix becomes the identity matrix. In this case, no beam coupling occurs and all beams are mutually orthogonal. Assuming the simple case of two beams with equal radiation efficiency, the

eigenvalues of the beam coupling matrix are found from

$$\begin{vmatrix} 1 - \beta & \beta_{12} \\ \beta_{12}^* & 1 - \beta \end{vmatrix} = 0 \quad (2.15)$$

which gives $\beta_1 = 1 - \beta_{12}$ and $\beta_2 = 1 - \beta_{12}$. The maximum radiation efficiency is then given by

$$|q_{\max}|^2 = \frac{1}{1 + |\beta_{12}|}. \quad (2.16)$$

The array factor of a large one-dimensional array with elements spaced a half wavelength or less apart may be approximated by the pattern of a continuous line source of length $D = Nd$, so that for uniform excitation

$$F_k(u) = \frac{\sin(N\pi(u - u_k)d/\lambda)}{N \sin(\pi(u - u_k)d/\lambda)} \approx \frac{\sin(\pi(u - u_k)D/\lambda)}{\pi(u - u_k)D/\lambda} \quad (2.17)$$

where $u = \sin \theta$, and $u_k = \sin \theta_k$ with θ_k being the pointing angle of the k th beam. The beam pattern corresponding to (2.17) is then given by

$$R_k(u) = \sqrt{\frac{2\eta_0 D}{\lambda}} F_k(u) \quad (2.18)$$

Considering a second beam pointing in the direction $u_j = u_k + \Delta u$, the resulting beam coupling coefficient is

$$\beta_{kj} = \frac{\sin(\pi\Delta u D/\lambda)}{\pi\Delta u D/\lambda}. \quad (2.19)$$

For a cosine amplitude distribution, the array factor is approximately

$$F_k(u) \approx \frac{\cos(\pi(u - u_k)D/\lambda)}{1 - 4[(u - u_k)D/\lambda]^2} \quad (2.20)$$

and the beam pattern becomes

$$R_k(u) = \sqrt{\frac{16\eta_0 D}{\pi^2 \lambda}} F_k(u). \quad (2.21)$$

The beam overlap factor is then found as

$$\beta_{kj} = \frac{1}{2} \left[2 \frac{\sin(\pi\Delta u D/\lambda)}{\pi\Delta u D/\lambda} + \frac{\sin(\pi(1 + \Delta u D/\lambda))}{\pi(1 + \Delta u D/\lambda)} + \frac{\sin(\pi(1 - \Delta u D/\lambda))}{\pi(1 - \Delta u D/\lambda)} \right]. \quad (2.22)$$

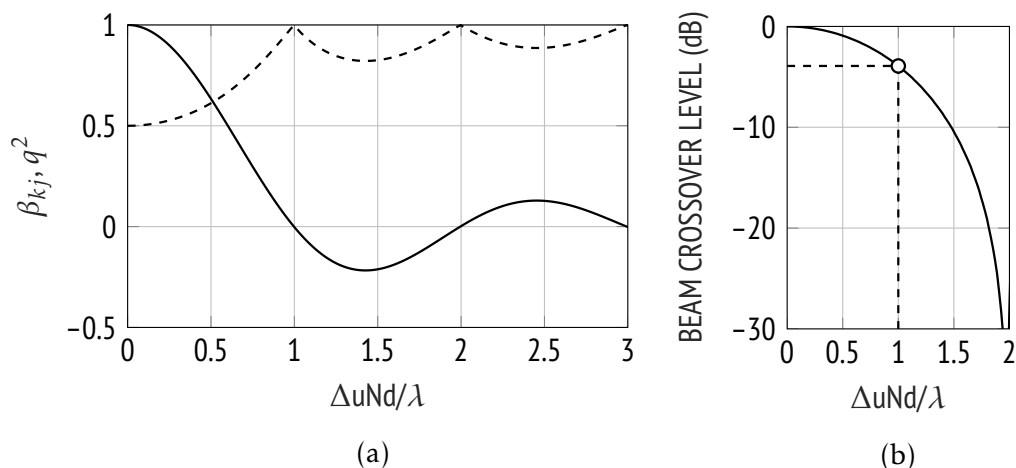


Figure 2.2: (a) Beam coupling (—), radiation efficiency (--) and (b) crossover level for uniform illumination.

Table 2.1: Multiple-beam parameters for different illuminations.

Illumination	Orthogonal spacing Δu	Crossover (dB)	SLL (dB)
Uniform	λ/D	-3.9	-13.3
Cosine	$2\lambda/D$	-9.5	-23.0
Cosine-squared	$3\lambda/D$	-15.4	-31.7
Cosine on a pedestal			
ET = 5 dB	$1.3\lambda/D$	-5.8	-17
10 dB	$1.6\lambda/D$	-8.0	-20
15 dB	$1.8\lambda/D$	-9.3	-22

Figures 2.2 and 2.3 show the beam coupling factor and radiation efficiency for uniform and cosine illumination as a function of the normalized beam spacing, along with the resulting crossover level. For the latter illumination, it is seen that the crossover point drops to about -9.5 dB at the smallest orthogonal beam separation. The pattern and orthogonality parameters are summarized in Table 2.1 for several common amplitude distributions. The cosine on a pedestal illumination is found in most practical quasi-optical beamformers, since it is usually not possible to generate a taper along a lens or reflector surface that goes to zero at the edges. Such beamforming devices show a few differences compared to constrained networks. As mentioned earlier, for a quasi-optical system the beam peak directions essentially remain fixed in space independent of frequency.

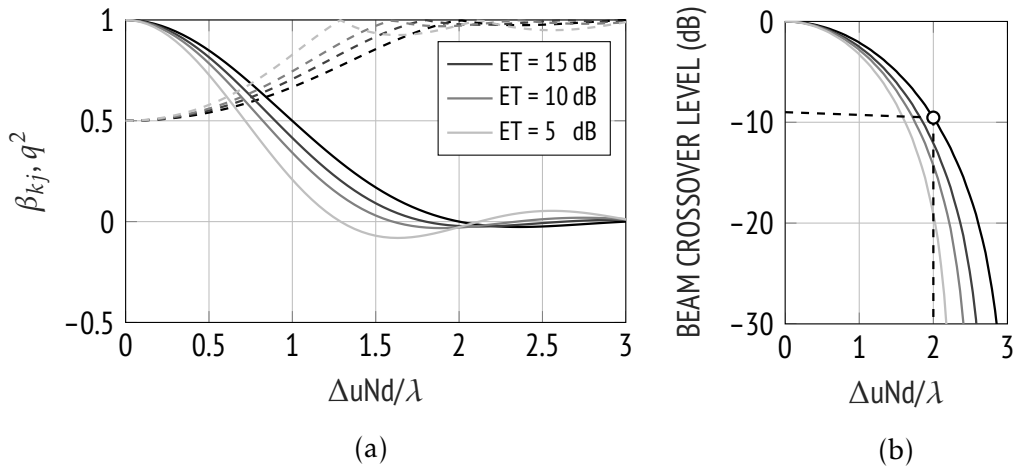


Figure 2.3: (a) Beam coupling (—), radiation efficiency (--) and (b) crossover level for cosine-type illumination.

However, as frequency decreases, the beamwidth broadens and thereby the crossover levels rise. As a consequence, exact beam orthogonality only holds at a single frequency. In multiple-beam matrices, the price paid for forming a set of non-orthogonal beams is usually dissipative loss between the antenna ports. It should be noted that this mechanism, along with the intended amplitude tapering, accounts for gain reduction. Quasi-optical beamformers involve an additional loss mechanism in the form of spillover. Moreover, most practical lenses and reflector systems suffer from beam broadening due to inherent phase errors at large scan angles.

2.2 High-Crossover Low-Sidelobe Designs

As demonstrated in the previous section, low-sidelobe patterns with high crossover levels require a departure from beam orthogonality. The advantages and limitations of previously proposed design methods are discussed in the following.

2.2.1 Lossy Networks

One flexible solution is the use of matched attenuators, which can be placed close to the radiating aperture [48] or inside the beamforming network [19] in order to produce the desired amplitude taper. Alternatively, a passive beam port overlap network may be used [16, 49, 50]. In this case, the tapered illumination is created

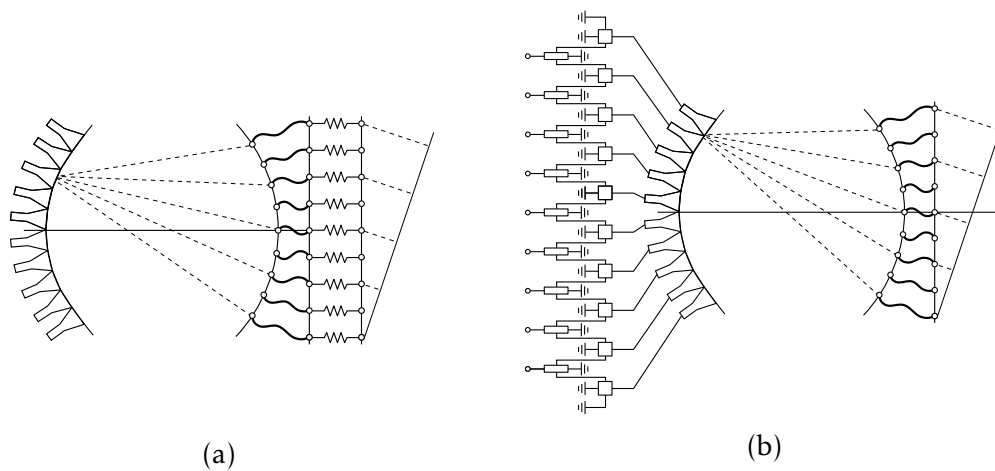


Figure 2.4: Constrained lens beamformer with (a) resistive tapering, (b) passive beam port overlap network.

by simultaneous excitation of adjacent feeds; the orthogonality loss occurs, for example, in the resistive terminations that are needed to form passive feed networks. One advantage of these two techniques is that they may be used for a wide range of beamforming devices. However, for the common requirements on sidelobe levels (< -20 dB) and crossover (≥ -3 dB), network losses may be as high as 3 dB. The Rotman lens design presented in [16] uses overlapping feed pairs as shown in Fig. 2.4(b), resulting in sidelobe levels lower than -20 dB and crossovers of about -2 dB over a scan range of $\pm 30^\circ$. This is achieved at the expense of a 3-dB network loss, occurring in the resistive terminations of the power distribution network. Two alternative trade-off designs are proposed in [49], offering similar sidelobe levels and crossovers of -4 and -4.5 dB over the same scan range, with insertion losses of 1.76 dB and 1.25 dB, respectively. Three feeds per beam are employed, with beam port centers at alternate elements. An overview of alternative approaches, particularly suited for quasi-optical beamformers, is given in the following.

2.2.2 Split Aperture Decoupling Method

The previous discussion has been limited to beams formed from a single aperture. If two beam patterns have different phase centers, the integrand in (2.5) contains a phase factor which will affect the resulting beam coupling coefficient. If the entire apertures generating the two beams are disjoint, the orthogonality integral becomes zero; this result is readily evident when evaluating the cross-coupling

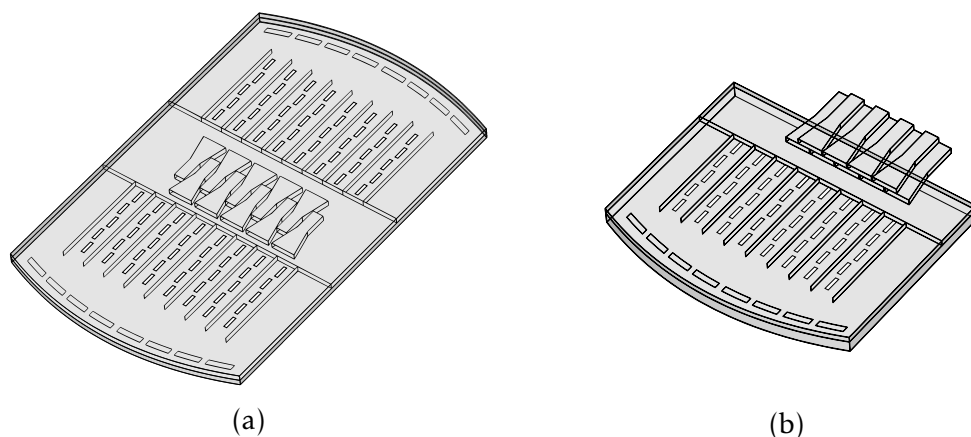


Figure 2.5: Pillbox system with (a) split aperture decoupling, (b) stacked feed structure.

based on the aperture fields. Hence, two beams radiated from physically separate apertures may be spaced arbitrarily close in space without mutual coupling [45]. This technique has been applied in [47] by using a pair of opposite pillbox couplers, each exciting a different aperture as shown in Fig. 2.5(a). The quasi-optical systems are fed by two complementary sets of feeds whose displacement corresponds to half a beamwidth. A fractional bandwidth of about 2.5% is achieved for the majority of feeds. At the design frequency, the antenna provides crossovers of -3 dB within a field of view of $\pm 40^\circ$, with sidelobe levels of about -11 dB for the extreme beams. A similar approach has been adopted for the design in [39]. The proposed beamformer consists of two stacked lenses, each fed by a set of beam ports, and provides beam patterns with a crossover of -3 dB and sidelobe levels of about -18 dB covering an angular range of $\pm 31.5^\circ$.

The split aperture decoupling method offers ease of design and construction, as well as high radiation efficiencies. However, its main drawback is the increase in cost and size, typically a factor of 2 along one dimension compared with the original beamformer.

2.2.3 Stacked Feed Structure

For two-dimensional quasi-optical beamformers, typically fed by sectoral horns, the third dimension can be used to accommodate intermediate feeds providing the desired beam overlap. This leads to a stack of feeds as shown in Fig. 2.5(b) for a parabolic pillbox system. The lower layer of the pillbox coupler is subdivided into two layers, each of which containing a set of contiguous feeds. The major

advantage of this solution is its compact construction since no complementary aperture or quasi-optical system is needed. However, due to the high level of integration, the feed system is more complicated to manufacture. Moreover, the feed apertures must be dimensioned carefully in order to minimize mutual coupling between closely spaced elements; this can also limit the control of the amplitude taper.

2.2.4 Fabry-Perot Feed System

Overlapping feeds can be realized on a single layer using Fabry-Perot structures [51]. An SIW implementation of this concept is shown in Fig. 2.6. The basic structure consists of two coaxial probe feeds (S_1 and S_2) placed between a totally reflecting wall (G_0) and a partially reflecting grid (G_1). The former acts as a ground plane inside the parallel-plate structure, while the latter is designed to support a leaky-wave mode. The grid parameters are then tuned such that the radiation from the leaky-wave structure provides the desired illumination over the quasi-optical system. The position of the probe along the traveling-wave structure determines the phase center of the feed. In this way, directive primary patterns can be formed from closely spaced beam ports. One disadvantage of this solution is that mutual coupling and the resulting reduction in radiation efficiency become unacceptable for small probe separations. It has been demonstrated in [51] that this effect can be mitigated significantly by introducing a second partially reflecting grid (G_2) parallel to the original one. Moreover, with this modification the structure supports a second leaky-wave mode which provides an additional degree of freedom for shaping the illumination pattern. The estimated fractional bandwidth of such a structure is about 5%. The main advantage of this overlapping feed concept is its low-profile and low-cost realization. However, coaxial probe transitions are sensitive to fabrication tolerances which give rise to performance degradation at millimeter-wave frequencies. Due to its rectangular geometry, the leaky-wave structure is particularly suited for feeding parabolic pillbox systems. However, for lens beamformers with highly curved feed profiles this concept is probably not feasible.

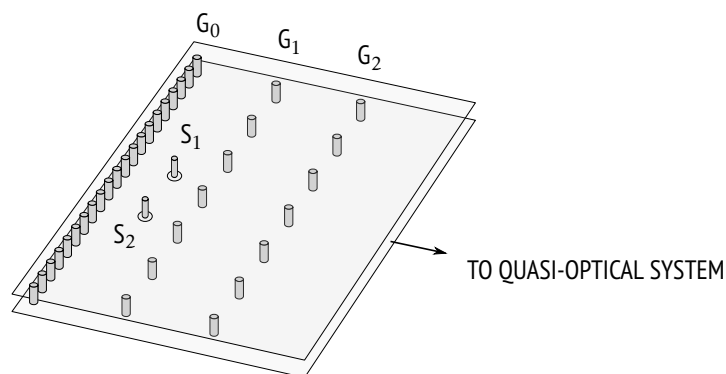


Figure 2.6: Fabry-Perot feed system with reduced mutual coupling.

2.2.5 Modified Optics

The techniques discussed previously are limited to modifications of the feed elements. Instead, the quasi-optical system can be modified in such a way that low-sidelobe high-crossover patterns can be provided with an ordinary feed structure. A method that has been used successfully in the design of 3D multibeam reflector antennas [52] is to oversize the radiating aperture and to broaden the beams by deliberately introducing a certain amount of phase error. In this case, the phase distribution is controlled by shaping the reflector surface, typically through the use of optimization techniques. To maintain low sidelobe levels, the reflector must be shaped such that sharp discontinuities in the phase profile are avoided. Since the appropriate feed size and the resulting beam separation are mainly determined by the F/D value of the reflector rather than by its shape, the beam widening leads to higher crossover. This approach offers the advantage of a simple feed structure, avoiding additional circuitry. Furthermore, it may be applied to various 2D quasi-optical beamformers, such as constrained lenses which offer additional degrees of freedom. However, previous studies have shown that the oversizing required for reflectors tends to be significant, leading to diameters twice that of the original configuration [52].

2.2.6 Variable Phase Shifters

Another solution for improved coverage is the use of variable phase shifters. Compared with previously described methods, this approach offers the additional possibility of scanning multiple simultaneous beams. Since all beams are moved to the same extent when varying the phase shifters, the crossover level between adjacent beams remains essentially constant. By proper choice of the

feeds, the entire field of view can be covered by several orthogonal beams, each of which scanning within a limited sector. In the case of constrained lenses, for example, the beam generated by a conventional input horn can be scanned by introducing a linearly progressive phase delay in the transmission lines. The design reported in [13] uses coaxial phase shifter to scan a beam over an angular sector of $\pm 12^\circ$ around its pointing angle. The advantages and disadvantages of different types of variable phase shifters are discussed in [53]. The main drawback of using individual phase shifters is the increased cost and complexity, especially for large apertures and fine discretization. For pillbox systems and continuous PPW lenses, the use of a single electromechanical phase shifter seems to be most suitable [54].

2.3 Mechanical Beam Scanning

The multibeam designs discussed in the previous section are either bulky, difficult to manufacture, or involve relatively high insertion losses. In this dissertation, two different approaches are investigated. The first is based on a movable feed system for applications where continuous beam scanning is required. In fact, such a configuration no longer falls into the category of the multiple-beam systems addressed in [46]. The advantages of this solution in the context of LEO/MEO satellite communications and previous related developments will be discussed in the following.

2.3.1 Design Considerations for Quasi-Optical Systems

A variety of quasi-optical beamforming devices has been proposed in conjunction with a single movable feed [7, 30, 55–57]. Most of these were originally intended for microwave radar applications where high gain and high angular resolution are required. Future satellite constellations with highly dynamic link geometries call for continuous beam scanning (i.e., a maximum of crossover) in order to provide near-constant communication. Due to the relatively small size and weight of millimeter-wave antennas, rapid mechanical scanning becomes a promising option. Obviously, for spaceborne antennas mechanically steerable solutions become impractical when larger aperture sizes are needed to satisfy the spot beam gain requirements, or when the number of simultaneous spot beams is relatively large. However, this approach appears to be particularly

suiting for gateway antennas which will be operated in large numbers to track highly populated LEO constellations [58]. Moreover, continuous beam steering is required for low-profile terminal antennas onboard fast-moving platforms such as vehicles, trains and aircrafts. In this case, robust communication links are ensured by a combination of electronic beam-switching in elevation and mechanical scanning in azimuth.

One major concern in mechanical scanning solutions is the fact that for actuation to be simple, the feed motion must be either linear or circular. Parabolic pillbox antennas with mechanical scanning scheme have been presented in [9] and [51]. Beam scanning is achieved by moving a compact feed horn along the focal plane of an integrated reflector. It has been shown in [59] that second-order phase errors of paraboloid reflectors can be eliminated by axial refocusing of the feed, thus mitigating the gain loss and leading to sharper nulls in the pattern of off-axis beams. A more extensive study [60] has shown that the feed contours producing maximum gain are in fact a function of edge taper and F/D . The derived feed profiles are, as scalar optics suggests, generally curved. It will be demonstrated in Chapter 4 for the two-dimensional case that depending on the focal length-to-diameter ratio and the edge taper of the feed, the maximum scan-gain contours may lie close to the focal plane. If the maximum possible scan gain can be achieved over a large portion of the focal plane, the penalty for employing a feed with simple lateral displacement is small. Purely geometrical considerations suggest that displaced feeds should be tilted back to aim at the vertex of the reflector in order to reduce spillover and to ensure a more symmetric illumination. However, analyses have shown that for low and moderate F/D , a higher gain is achieved when retaining the feed in straight-ahead orientation [60]. In contrast, for reflectors with higher F/D value, scan losses can be reduced by tilting the feed, especially for large displacement. In practice, this would require additional actuation for rotating the feed and is therefore often avoided. It should be noted that for maximum broadside gain, feeds are typically designed to produce an edge illumination of -11 dB. However, spillover may become significant if the same feed is placed at an extreme scan position. Hence, when using a single horn feed, a compromise aperture dimension needs to be selected. In a semicircular pillbox system, the beam can be scanned mechanically by moving the feed along a circle whose center coincides with the center of curvature of the reflector. Correcting lenses used for reflectors with large

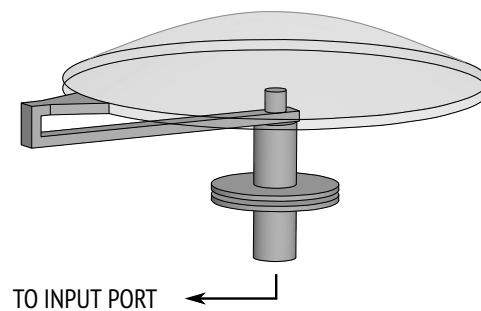


Figure 2.7: Mechanical beam scanning with a circularly symmetric lens.

effectively utilized aperture need to be moved with the feed.

Due to their circular shape and rotational symmetry, the two-dimensional Luneburg lens and its geodesic analogues are particularly well suited for mechanical scanning schemes. Since the required feed motion path is circular, a simple rotary actuator can be used to displace the feed. This greatly reduces the complexity of the mechanical design, just as the movement along a straight line in parabolic pillbox antennas. The designs presented in [55] and [56] are based on a waveguide feed moving around the periphery of a Luneburg-like lens as illustrated in Fig. 2.7. Naturally, the focusing performance is not compromised when compared to the configuration with multiple fixed feeds. Moreover, the refractive index profile can be modified to support linear feed motion [61, 62].

The situation is different for most lenses with linear aperture. Classical designs employ feeds that are placed on a circular contour [11, 13]. In the seminal study of constrained bifocal lenses [11], a focal arc with a radius equal to the focal length has been considered initially. It has been found that lenses with straight front face provide the best wide-angle scanning performance. However, this requires refocusing of the feeds by a certain amount, leading to a focal arc with smaller radius that is no longer centered at the vertex of the lens. The same principle has been applied for defining the optimum position of the third (on-axis) focal point in the original Rotman lens design [13]. Furthermore, it has been demonstrated that phase errors for non-focal feed positions can be reduced when resorting to non-canonical feed curves [14, 15]. However, in practice, such configurations are only useful when multiple stationary feeds are used. For mechanical beam steering, it is desirable to retain a circular feed motion path since a simple rotary drive can be used to move the feed along

the focal surface of the lens. Another substantial constraint is the fact that at every scan position, the feed should be pointing toward the center of the lens in order to minimize spillover and to produce a symmetrical illumination. This is particularly important if no absorbing sidewalls or dummy ports are used since internal reflections may lead to disturbed radiation patterns and increased reflection losses. Unless an additional actuator is used, this can be achieved only if the center of the focal arc coincides with the apex of the inner lens profile, i.e., the radius of the focal arc needs to be equal to the focal distance. Clearly, this structural simplification limits the scanning performance of the lens. The expected penalty can be demonstrated by examining the RMS phase errors of a classical Rotman lens. The contours depicted in Fig. 2.8 are normalized by the on-axis focal distance F_1 and correspond to lens designs with parameters $\zeta_{\max} = 0.6$ and $\alpha = \pm 30^\circ$ as specified in [63]; the focal arc is defined by the parameter β . The RMS error in Fig. 2.9 is given in degrees and normalized by F_1/λ . In the required configuration with $\beta = 1.0$, that is, with a focal arc centered at the vertex of the lens, the RMS phase error increases much more rapidly beyond the focal points than in the optimum case proposed by Rotman ($\beta = 0.88$). As pointed out in the original paper, the optimum focal ratio minimizes the scan losses for moderate ratios of focal distance to lens aperture width; in the present example $F/D = 1/(2\zeta_{\max}) \approx 0.83$. Nevertheless, if phase error requirements are relaxed, so that a lower F/D can be selected, values of β higher than the optimum may lead to better results. This is demonstrated by the RMS error in Fig. 2.9(b) for a lens with $\zeta_{\max} = 0.7$ ($F/D \approx 0.71$) and otherwise unchanged design parameters. As can be seen, the phase errors for $\beta = 1$ are lower for feed positions between the focal points. The new optimum β can be expected to lie between the two values considered. On the other hand, it can be seen from Fig. 2.8 that a proper illumination of the lens contour, especially at extreme scan angles, is more difficult to achieve due to the strong curvature of the inner lens contour. It should be noted that, although providing a compact representation of the focusing performance, the RMS phase error of a lens does not allow direct conclusions on the pattern quality. The expected pattern degradation is typically inferred from the maximum phase error, occurring in most cases at the edges of the lens aperture. As demonstrated in Appendix B, a purely quadratic or cubic quarter-wavelength error leads to sidelobe levels in the order of -8 dB for uniform illumination. An edge taper of 10 dB helps to reduce these to about -13 dB. This effect becomes even more severe for lower F/D .

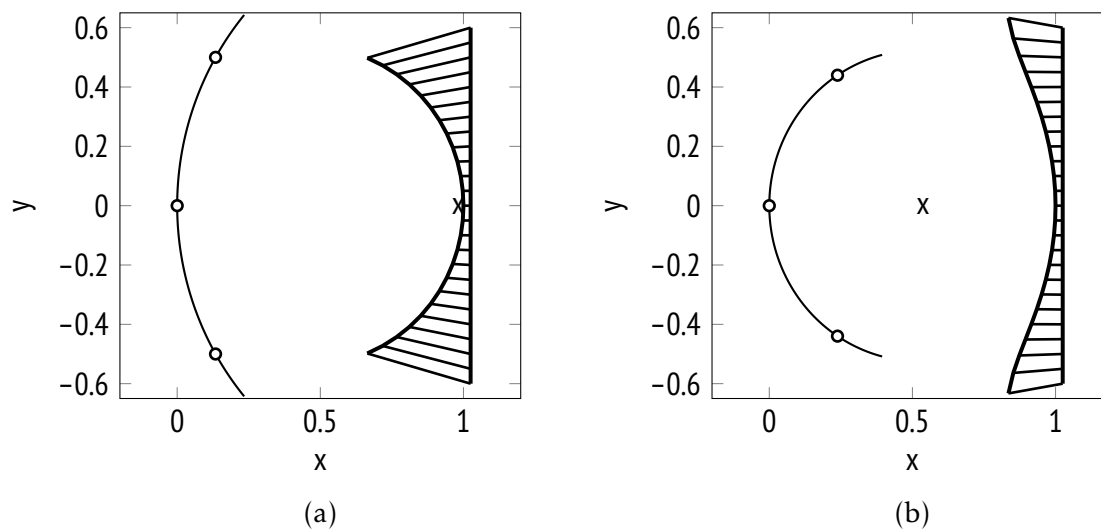


Figure 2.8: Rotman lens contours for (a) $\beta = 1.0$, (b) $\beta = 0.88$.

It is worth mentioning that mechanical scanning can be accomplished in various other ways without rotating the entire beamforming system. In the case of pillbox antennas, the most popular approach consists in employing a movable subreflector. For example, the fan-beam imaging systems proposed in [64, 65] enable rapid continuous scanning with one 360° rotation of a small secondary or tertiary reflector. Furthermore, beam steering can be achieved by rotational movement between stacked antenna parts, generating a phase gradient across the radiating aperture [66, 67]. Both concepts result in a relatively compact design and provide high scanning speed. However, they cannot be readily adopted for a wide range of devices such as lens beamformers.

2.3.2 Existing Feed Designs

In mechanical beam-scanning systems, it is usually necessary to provide relative motion between different guiding structures. This requires motional joints in the coaxial lines or waveguides forming the feed network. The design of such transitions is concerned with two electrical considerations. First, the joint needs to maintain a good impedance match for all required displacements. For the waveguide-type, this often involves the problem of mode purity, since the presence of undesired field distributions can lead to resonant behavior at the junction setting up pure standing waves. Second, precautions need to be taken in the design to minimize energy leakage from finite air gaps. Unwanted

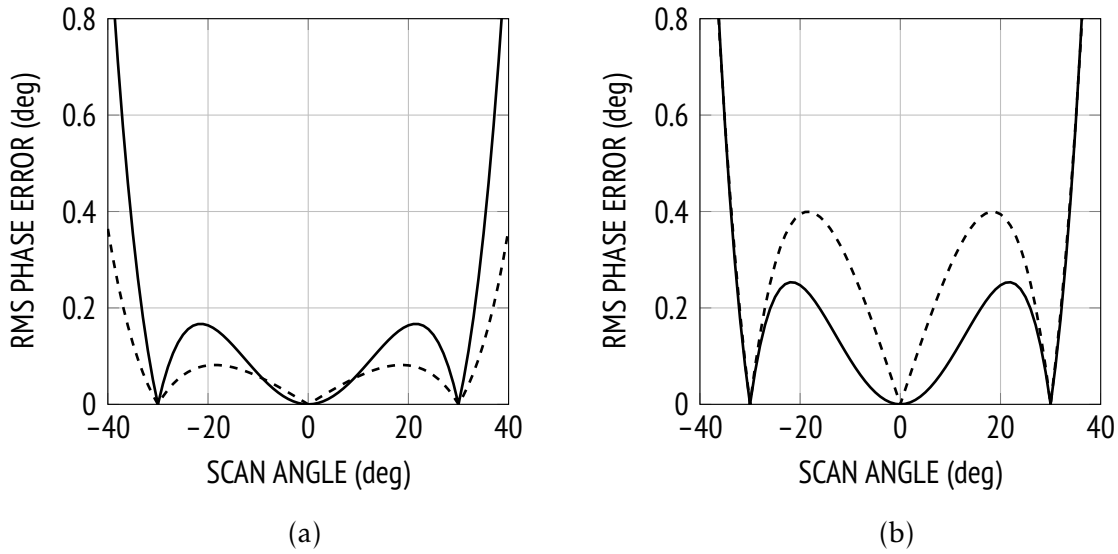


Figure 2.9: Normalized RMS phase error of a Rotman lens with $\beta = 1.0$ (—) and $\beta = 0.88$ (--) for (a) $\zeta_{\max} = 0.6$, (b) $\zeta_{\max} = 0.7$.

radiation needs to be prevented in order to ensure high-efficiency transmission and compliance with electromagnetic compatibility (EMC) specifications.

2.3.2.1 Flexible Coaxial Cables

The use of flexible cables to connect the transmitter/receiver circuitry to a movable feed is perhaps the most intuitive solution for mechanical beam scanning. Coaxial cables are light weight and can track virtually any form of motion, therefore providing great design flexibility. One limitation is the lower peak power capacity when compared to other types of transmission lines. Moreover, the cable must be robust enough to withstand continuous movement and flexure during scan operation, and exposure to environmental conditions. The cable assembly needs to be designed such that a sufficiently large bending radius is maintained during feed motion. Flexing forces the inner conductor to one side, thus disturbing the concentric arrangement with respect to the shield; this produces a change in impedance and as a result reflection losses will occur. Moreover, sharp bends may cause damage to the shield. While cable assemblies can be designed to endure repetitive or constant motion [68], the impact on transitions in the feed system is potentially more of a concern. Typically, the coaxial cable is used as a current probe to couple the transmission line mode to the dominant mode of a rectangular waveguide structure, such as a sectoral feed horn [6]. Tuning the separation between probe and conducting walls in an

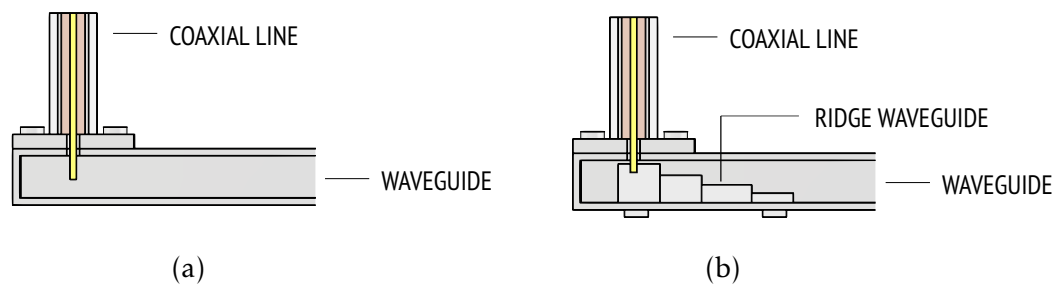


Figure 2.10: Coaxial-to-waveguide transition using a (a) current probe, (b) ridge waveguide section.

ordinary coaxial-to-waveguide transition yields only narrowband matching [69, pp. 318–322], [70, pp. 481–483], and therefore such a transition often limits the impedance bandwidth of the beamforming device. Broadband matching can be achieved by various means, such as reactive diaphragms or tapered ridge waveguide sections as shown in Fig. 2.10(b), at the expense of increased complexity and potentially lower breakdown figures [69]. Coaxial-to-waveguide transitions with good matching over a sufficiently wide frequency range at Ka-band have been reported [29]. However, even for stationary waveguide structures, precise machining and assembly is required to ensure a proper positioning of the probe. Hence, it can be expected that recurrent mechanical stress on the adapter will eventually affect its performance.

2.3.2.2 Rotary Joints

For mechanical beam scanning with bootlace lenses, radially symmetric lenses or semicircular pillboxes, a continuous rotation of the feed about one axis is required. In the millimeter-wave region, waveguide rotary joints are typically used for connecting a movable feed to stationary rectangular waveguide structures. As shown in Fig. 2.11, such joints are formed by two sections of circular waveguide connected by a choke-to-flange junction that is free to rotate. Basic principles of choke flanges for rectangular waveguides are addressed in Section 3.1.4; in contrast, the chokes used in rotary joints are excited by circularly symmetric fields and need to be studied on the basis of the dominant TEM mode of coaxial lines. In most rotary joints, the TE_{10} mode in the feeding rectangular guide needs to be converted into the axially symmetric TM_{01} in the circular waveguide. The latter is then coupled via a second mode converter to the rectangular waveguide at the output. In fact, also the degenerate TE_{01} mode or the TE_{11} mode with circular polarization exhibit the required symmetry in a

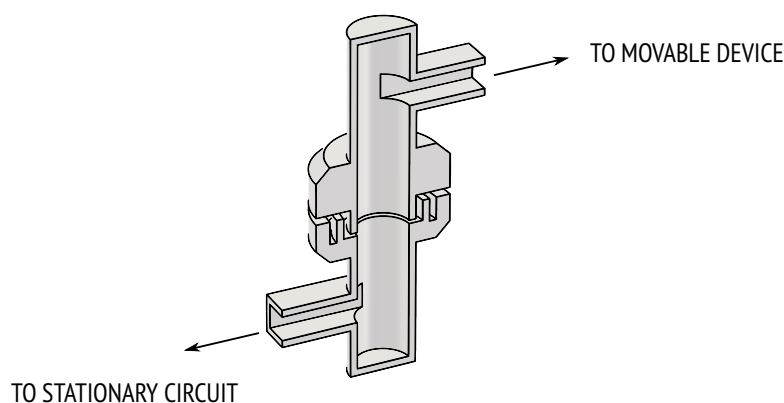


Figure 2.11: Cross-sectional view of a waveguide rotary joint.

circular waveguide, but for practical reasons the TM_{01} is most commonly used. The major challenge in this design arises from the fact that the dominant TE_{11} mode of the circular waveguide is asymmetric and, if excited simultaneously, will cause the transmission characteristics of the joint to vary with the rotation angle. Various mode converter solutions have been proposed to overcome this problem. A Ka-band rotary joint based on power dividers and coupling windows has been presented in [71]. The design requires precise tuning to a particular frequency; insertion losses of about 1 dB are reported. A rotary joint for Ku-band applications using coaxial waveguide transitions has been proposed in [72]. The insertion loss is below 0.65 dB over a fractional bandwidth of about 8%.

As shown in Fig. 2.7, rotary joints allow a compact integration of the feed with respect to the footprint of the focusing device, thus preventing aperture blockage by the support structure. When using radially symmetric lenses in combination with a rotary joint feed, the main beam can be scanned throughout an angle of 360° . In addition, waveguide rotary joints offer the advantages of mechanical ruggedness and higher power-handling capability compared to cable assemblies. The mode converters and choke section must be designed carefully in order to ensure broadband operation. The main drawback of this solution is that, due to the feeding from the vertical direction, the total height of the antenna is largely determined by the required waveguide structure, including the rotary joint, bends and additional matching sections. As a consequence, the advantage of a low-profile geometry is lost due to the feeding mechanism, rendering this approach inadequate for many applications.

2.4 Multiple-Feed-per-Beam Operation

The second reconfiguration technique studied in this work is based on the multiple-feed-per-beam (MFPB) concept. In this case, different feeds contribute to the synthesis of each beam, forming overlapping clusters that provide high crossover, and whose effective apertures are large enough to minimize spillover losses. In fact, the MFPB principle can be seen as a generalization of the beam overlap networks discussed in Section 2.2. In satellite communications, traditional feed clusters have been widely used for generating contoured beams with offset reflectors [73], and for the compensation of reflector surface distortion. Overlapping clusters, on the other hand, represent one of the two basic concepts for generating spot beam coverage with improved roll-off [74, 75]. Onboard geostationary satellites, typically four reflectors are used to provide the required beam overlap with single-feed-per-beam operation. In order to enable each reflector to be used on transmit and receive, feeds must be designed to produce a proper illumination in the Tx band and a certain under-illumination at Rx frequencies. Using multiple feeds per beam, overlapped multibeam coverage can be achieved using a single reflector. Due to the complexity of the feed structure, two separate reflectors are needed for Tx and Rx [75].

Multiple-feed-per-beam operation requires a complex beamforming network, consisting of couplers and phase shifter, that provides the feeds with proper phase and amplitude excitations. An overview of previous developments for satellite applications is given in [76]. A low-level BFN used on transmission routes the signals to the high-power amplifiers (HPA) that are connected to the feed elements. On reception, a low-level BFN distributes the signals received by the feed elements after they have been amplified by low-noise amplifiers. As a result, the insertion loss of the BFN has a small impact on the final gain (typically referenced to the output power of the amplifiers) or the signal-to-noise ratio of the antenna system. A high-level BFN used on transmission distributes the signals coming from the high-power amplifiers to the feed elements. On reception, a high-level BFN combines the signals received by the feed elements before they are passed through low-noise amplifiers. Therefore, network losses largely determine the efficiency of the beamforming device. One advantage of this configuration is that each cluster corresponds to one input port, i.e., the number of amplifiers required is equal to the number of beams, and not the number of feed elements as in low-level networks. To avoid high insertion losses in the divider/combiner network, the excitations of shared feed elements, used

to generate adjacent beams, need to be orthogonal. In a practical BFN, additional feed elements nearby the driven cluster are typically excited to a small extent [77].

The main advantage of MFPB systems is the significant reduction in antenna mass and volume since all beams can be formed from a single aperture. In addition, overlapping feeds offer a maximum of functionality, including nearly continuous scanning by means of beam switching and shaped beam synthesis.

2.5 Chapter Summary

This chapter has revisited the theoretical limitations of multibeam antennas, used to create multiple simultaneous beams or for beam scanning. Various solutions to the problem of orthogonality loss in quasi-optical beamformers have been discussed. Emphasis has been placed on two different techniques for improved wide-angle coverage, both implemented at feed level and particularly suited for continuous beamformers such as pillbox systems and parallel-plate waveguide lenses. The first corresponds to rapid mechanical scanning of a single beam. In this context, it has been demonstrated that for lens beamformers with linear aperture, a trade-off needs to be found between mechanical complexity of the feed system and scan performance. A review of the state of the art of mechanical scanning feeds has shown the limitations in terms of bandwidth, robustness and compact design of positioning systems based on coaxial lines and waveguides. The second approach refers to multiple-feed-per-beam operation, which allows for a higher degree of beam reconfigurability. Obviously, as the total number of feeds or the number of feeds per cluster increases, the complexity of the distribution network also increases. The design of compact low-loss beamforming networks for both direct radiating arrays and overlapping feed clusters has been subject of continuous research, but is not addressed in this work. Key to a fast and systematic co-design of quasi-optical system and feed cluster are accurate numerical models of the beamformer taking into account the receive problem.

CHAPTER 3

A Parallel-Plate Lens for Mechanical Wide-Angle Beam Steering

Mechanical beam scanning requires a rugged yet agile feed system, ensuring a minimum of radiation loss. Gap waveguides present a recent advance in millimeter-wave technologies, offering a number of desirable characteristics in view of these requirements. One major part of this work focuses on the utilization of gap waveguide technology for the design of a mechanically reconfigurable feed system. At the same time, efforts have been directed towards the development a novel type of continuous PPW lens with improved scanning performance. The combination of these two designs addresses the need for continuous beam scanning over a wide angular range.

In the first part of this chapter, the operating principle and unique properties of gap waveguides are discussed. Next, the analysis and design of the required electromagnetic bandgap (EBG) structure and of different gap waveguide components, used to build the proposed feed system, are described. The second main part of this chapter focuses on the design of a continuous parallel-plate waveguide lens with enhanced scan range. Approximate models and techniques for designing the quasi-optical system are discussed, while emphasis is placed on the involved design trade-offs due to mechanical constraints. The final structure, including the mechanical scanning feed system, is fine-tuned using full-wave simulations. Moreover, the manufacturing and experimental characterization of an all-metal prototype operating in the uplink Ka-band is described. Finally, further applications of the proposed feed system and possible avenues for advancement of the entire beamforming device are discussed.

3.1 Low-Profile Mechanical Feed System

The majority of previously developed mechanical feed systems is protected by patents and usually customized to one specific beamforming device. In conventional designs, the transition region between fixed and movable waveguide parts is fitted with specially developed choke structures [57, 78–80]. In the past decade, the high design flexibility of gap waveguides has promoted the development of various high-performance antennas and circuit components for millimeter-wave applications. Moreover, numerous scientific contributions over the past few years have made analysis and design techniques widely accessible. Gap waveguides combine the advantages of conventional waveguides such as high power-handling capability and low loss with the unique feature that no physical contact is needed between the two waveguide plates [81]. So far, this characteristic has been of interest mainly for manufacturing reasons, since high-precision welding, diffusion bonding or a large number of screws, typically required to ensure good electrical contact between waveguide parts at millimeter-wave frequencies, can be avoided. To some extent, the mechanical flexibility has been also exploited for the design of cyclically [82, 83] and constantly moving [66, 67] waveguide components.

3.1.1 Basic Principle and Advantages of Gap Waveguides

Gap waveguides are based on localized wave propagation between two metallic plates. In contrast to parallel-plate waveguides, one of the plates is fitted with a textured surface, usually a bed of nails as shown in Fig. 3.1(a), which is effectively a quarter-wavelength in height. Over a range of frequencies, the periodic structure acts as a high-impedance surface, also referred to as artificial magnetic conductor (AMC). Studying the source-free Maxwell's equations and enforcing the appropriate boundary conditions shown in Fig. 3.1(b), it is readily found that no solutions exist if the plate separation is smaller than a quarter-wavelength. Exploiting this parallel-plate cutoff, guiding structures such as ridges, grooves or microstrip lines are incorporated in order to control propagation between the plates. The provided stopband characteristic prevents leakage across the parallel-plate region, so that fields are localized to the guiding system. A ridge gap waveguide is formed by introducing a metallic ridge in between the textured surface, as shown in Fig. 3.2(a). The two-conductor guide supports a quasi-TEM mode within the provided stopband. The characteristic impedance

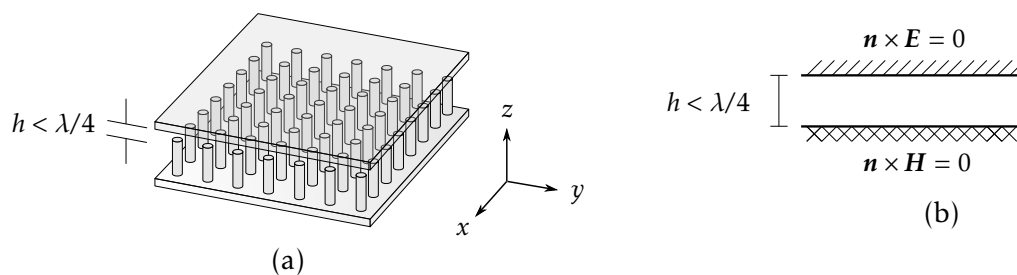


Figure 3.1: (a) Stopband structure, (b) equivalent boundary value problem.

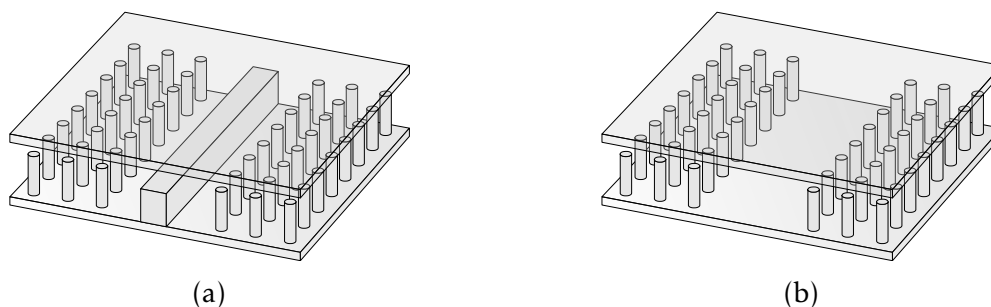


Figure 3.2: Basic structure of (a) ridge gap waveguides, (b) groove gap waveguides with vertical polarization.

of the dominant mode and the associated conductor loss are determined by the gap height and the width of the ridge; a wider ridge allows reduced losses but also lowers the cutoff frequency of the first higher-order mode supported by the conductor [84]. One advantage of ridge waveguides is the fact that transmission line discontinuities such as H -plane bends and T-junctions can be designed in a straightforward manner, i.e., by shaping the ridge similarly to the conductor of a microstrip line. Alternatively, waves may propagate inside a groove within the periodic structure as shown in Fig. 3.2(b). The modes supported by groove gap waveguides are essentially the TE and TM modes of conventional rectangular waveguides. Among all gap waveguide technologies studied so far, the groove-type implementation exhibits the lowest conductor loss, approximately 10 – 30% more than extruded rectangular waveguides and 30 – 55% less than ridge gap waveguides at V-band [85]. Moreover, groove gap waveguides can be designed to support horizontal polarization or dual polarization, suitable for use as a horn antenna. Although ridge gap waveguides have been used to build rotary phase shifters [66], it can be expected that the hollow structure of groove gap waveguides yields greater flexibility in the design of mechanically reconfigurable components. In view of this advantage, only the latter technology has been considered for the design of the feed system presented in this chapter.

3.1.2 Unit Cell Design for Ka-Band

The EBG structure plays a central role in the design of every gap waveguide component since it determines the bandwidth over which the desired mode can propagate. A variety of periodic structures suitable for this purpose has been studied, including circular or square metallic pins and mushroom-type surfaces. To find the configuration best suited to the given problem it is advisable to first weigh achievable performances against manufacturing complexity. For example, it has been shown in [86] that basic pin-bed structures offer about one octave bandwidth, while the stopband provided by mushroom EBG surfaces can be as large as two octaves. Additive manufacturing, molding and soldering processes allow the implementation of such more complex EBG without dielectric. However, bed-of-nail structures, particularly those formed by circular pins, are easy to realize using conventional machining processes such as turning and milling. Considering the advantage of reduced manufacturing cost and the requirements on bandwidth at Ka-band, the latter implementation of the AMC was selected. The dispersion characteristics of a pin-bed structure can be studied using the homogenization method described in [87]. Following this approach, the periodic structure is treated as a slab of a spatially and frequency dispersive medium. The derived permittivity model is valid in the limit of large λ . Moreover, if the metallic pins are densely packed so that the spacing p is much smaller than the length of the pins d , spatial dispersion becomes negligible and the structure can be characterized using an impedance boundary condition. This allows to study the reflection of plane waves incident from free-space onto the textured surface and the propagation of surface waves in the conventional manner. The propagation characteristics are affected substantially when a metallic plate is placed at a small distance h parallel to the pin structure. The resulting structure is a parallel-plate waveguide formed by a perfect electric conducting (PEC) surface and a reactance surface. Referring to the coordinate system in Fig. 3.1(a), the field distribution between the plates can be interpreted in terms of bouncing TM^z and TE^z waves. The transverse electric modes do not interact with the metallic pins, and the textured surface is therefore equivalent to a PEC plane. As a result, the corresponding dispersion relation is equivalent to that of a conventional parallel-plate waveguide, i.e., $k_z = \pi/(d + h)$ for the first solution. For TM waves, the dispersion equation can be derived from an equivalent resonant circuit, formed by the modal impedance seen looking from the top of the pin-bed structure toward the PEC plate above and those seen towards the ground plane

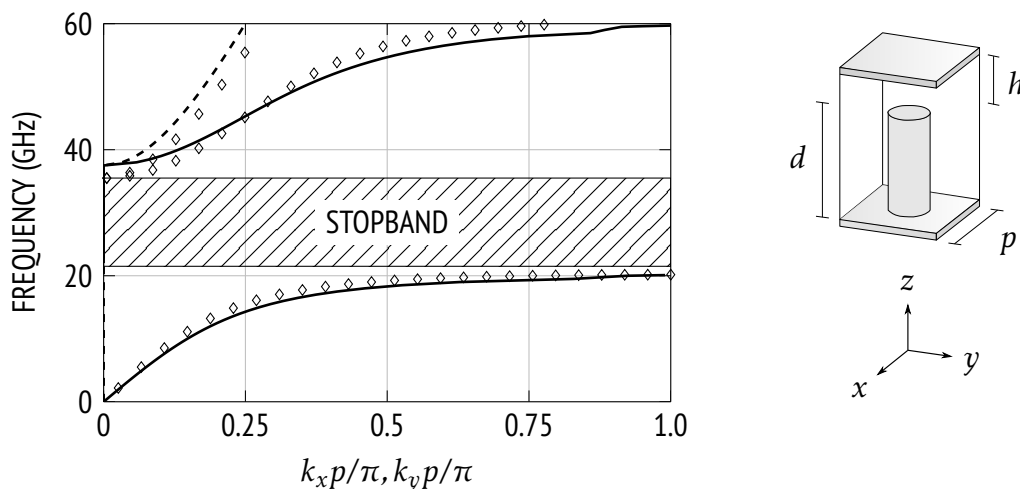


Figure 3.3: Calculated dispersion characteristic of TM (—), TE modes (--) and corresponding simulation results (\diamond) for a unit cell with $d = 3.5$ mm, $h = 0.5$ mm, $r = 0.2$ mm and $p = 0.8$ mm.

[88]. More specifically, it is found that for $\lambda > 4d$ the behavior of the surface impedance is inductive and the structure supports a TM surface wave which is closely bound to the lower plate when the density of pins is high. In the range $4d > \lambda > 2(d + h)$, the surface impedance is capacitive while k_z of the TM solution is real and greater than k , implying that waves are evanescent along the radial direction. This region corresponds to the stopband of the structure. For $2(d + h) > \lambda > 2d$, k_z is real and smaller than k , meaning that fast-wave propagation is supported between the plates. This upper frequency limit of the stopband is also marked by the onset of the first TE mode.

As a first step, the approximate analytical method described in [88] was used to design a pin surface for adequate parallel-plate cutoff at Ka-band. The computed dispersion diagram of the initial design is shown in Fig. 3.3. The results are in good agreement with those obtained using the Eigenmode solver of CST Microwave Studio, especially at lower frequencies where the pin periodicity is small with respect to the wavelength. The dispersion characteristic of the TM modes shows that the structure provides a stopband ranging from about 21.4 to 37.5 GHz. As mentioned earlier, the lower bound is associated to the frequency at which the behavior of the surface impedance changes from inductive ($\lambda > 4d$) to capacitive ($\lambda < 4d$). Likewise, there is an upper limit where the impedance changes from capacitive to inductive, thus supporting the propagation of TM surface waves. In addition, there is a second upper limit related to the plate

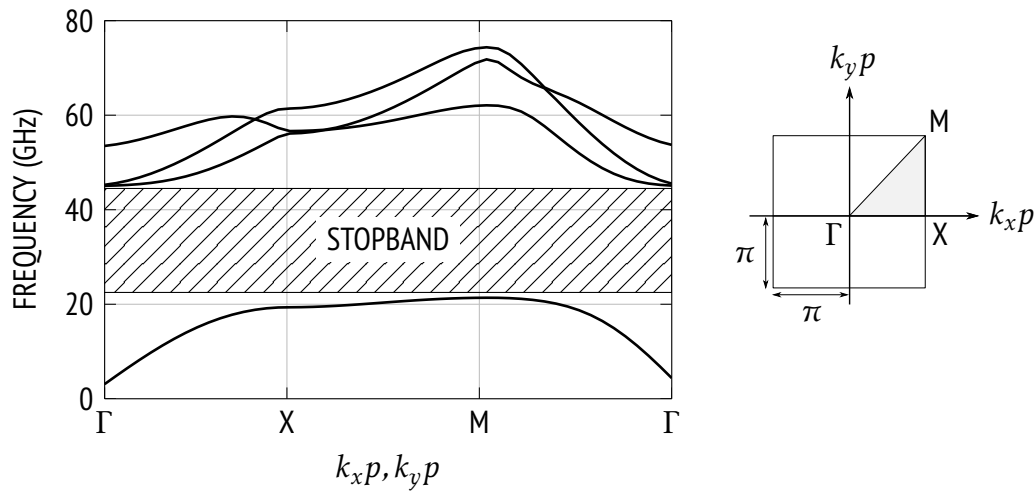


Figure 3.4: Simulated dispersion characteristic of an optimized unit cell with $d = 2.7$ mm, $h = 0.5$ mm, $r = 0.5$ mm and $p = 3.0$ mm.

spacing h beyond which, even for an ideal PMC condition on the lower surface, parallel-plate modes may propagate. As a result, small gap heights allow raising the upper cutoff limit; however, taking into account tolerances due to the movement of the waveguide plates, a trade-off value of $h = 0.5$ mm was selected.

The configuration of Fig. 3.3 uses pins of relatively small diameter and periodicity. Obviously, from a manufacturing point of view it would be desirable to avoid such fine structures. This would allow, for example, the use of a larger milling head thus accelerating the machining process. However, the homogenization technique described in [87] is only valid as long as the wavelength is much longer than the size of these features. Moreover, for less densely packed pins, the effects of spatial dispersion become significant, and the surface impedance model loses its validity. Considering these limitations, the optimization of the unit cell dimensions were carried out using full-wave simulations. The dispersion diagram of the final structure, considering the first four modes over the irreducible Brillouin zone, is plotted in Fig. 3.4. While the effect of the pin length d and gap height h are readily apparent from the analysis in [88], some insight can be gained through parametric studies regarding the radius and periodicity of the pins [86]. For example, it is found that the effective electrical length of the pins increases as the periodicity is increased, thus reducing the lower frequency limit. This explains why the stopband of the final configuration with $d = 2.7$ mm (theoretically forming an ideal PMC at about 27.8 GHz) ranges down to 22 GHz. The selected gap height of $h = 0.5$ mm implies an upper frequency

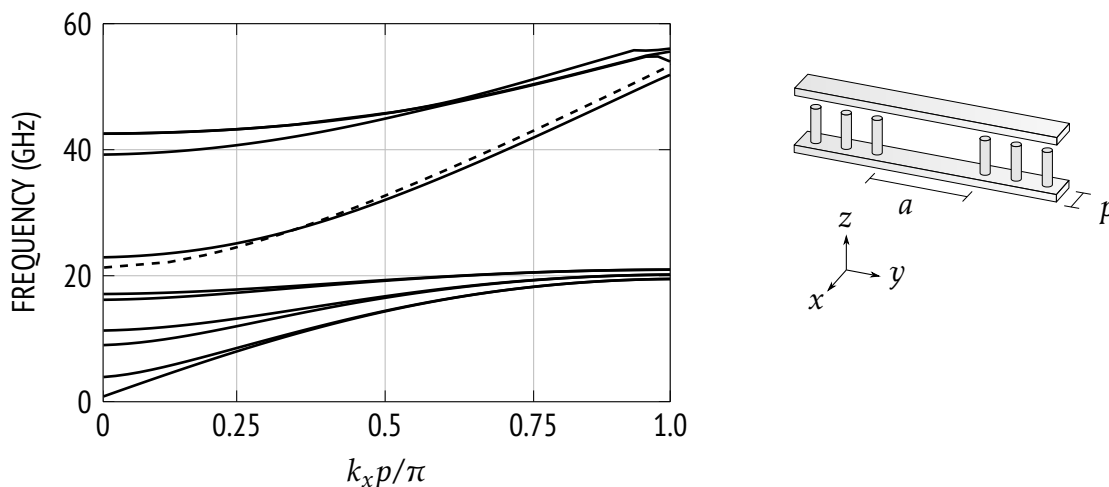


Figure 3.5: Simulated dispersion characteristic of a basic groove gap waveguide cell (—) and of TE_{10} mode in a WR-28 waveguide (--).

limit at 46.9GHz, i.e., where the distance between the plates ($d + h$) is equal to a half wavelength. This is in reasonable agreement with the cutoff frequencies of the second and third mode. It should be noted that a further increase in p gives rise to an additional mode supported by the pin structure. For large periodicities the cutoff frequency of this mode may fall below that of the parallel-plate modes, thus lowering the upper limit of the stopband [86].

The basic cell of the developed groove gap waveguide is shown in Fig. 3.5. The width of the groove is set to $a = 7.11$ mm, matching the dimensions of a WR-28 standard waveguide suitable for Ka-band operation (uplink). In the simulation, PMC boundary conditions are imposed on the lateral sidewalls to model an infinite PPW environment. The obtained dispersion diagram indicates a number of spurious modes propagating at frequencies below the stopband which are due to the cavities formed by the rows of pins. As expected, the dispersion characteristic of the mode supported by the groove is very close to that of the dominant mode in a conventional WR-28 guide.

3.1.3 Proposed Feed System

The proposed feed concept is based on distributing the textured surface reported in the previous section on two physically separated gap waveguide plates as illustrated in Fig. 3.6. The guiding structure is composed of two right-angled H -plane bends, a circular section of variable length between these and a sectoral horn. The pins forming the primary radiator and the inner sidewall of the

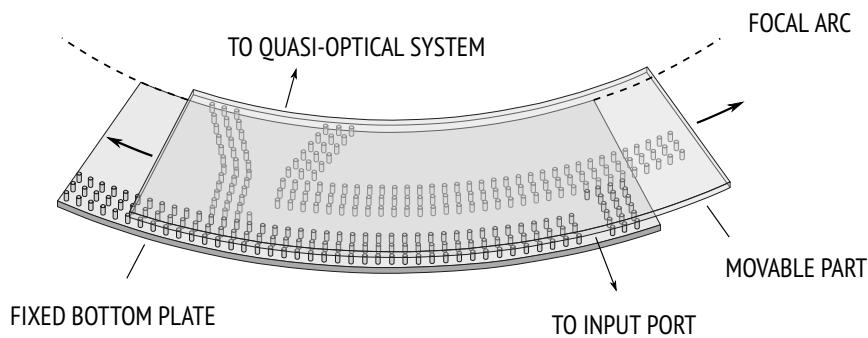


Figure 3.6: Perspective view of the proposed feed system.

circular gap waveguide section (i.e. toward the focal arc) are found on the upper plate (movable, shown transparent in Fig. 3.6). The inner radius of the structure is defined such that the phase center of the sectoral horn moves along the focal arc of the lens. The pins confining the input section and the outer sidewall are located on the stationary bottom plate. One drawback of this solution is that when used for feeding a lens, its overall size is proportional to both the focal distance and the angular scanning range. In contrast, the size of a rotary joint feed, as shown in 2.7, is independent of the latter. Due to the horizontal feeding, this structure offers the advantages of low profile and mechanical ruggedness. Moreover, complex mode converters, which are commonly employed in traditional rotary joints, are not needed.

3.1.4 Analysis and Design of Waveguide Building Blocks

The developed feed system involves a number of waveguide and gap waveguide components which largely determine the overall impedance bandwidth of the beamforming device. This section provides an overview of these building blocks along with basic guidelines that aid in the design process. Since groove gap waveguides operate essentially in the same way as conventional rectangular waveguides, common discontinuities can be treated in a similar manner. Equivalent circuit models and numerical techniques for analyzing the different types of components are discussed. Although some of the design features are specific to the developed feed network, the presented building blocks can be used in various ways for designing mechanically reconfigurable structures.

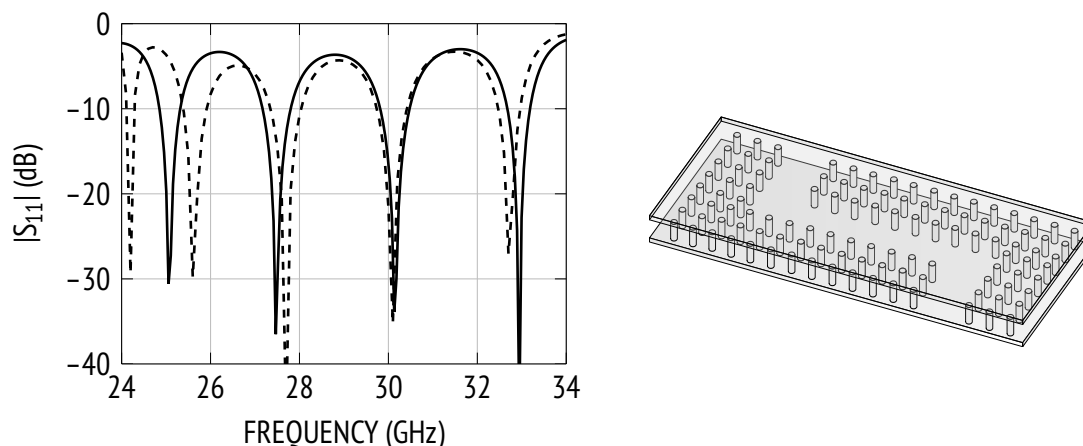


Figure 3.7: Simulated reflection coefficient of groove gap waveguide structure (—), calculation based on waveguide equivalent circuit model (--).

3.1.4.1 Movable *H*-Plane Corner

The proposed groove gap waveguide structure consists of two right-angle *H*-plane corners as illustrated in Fig. 3.7, effectively separated from each other by a guide section of varying length L . The simulated input reflection coefficient of the unmodified structure with $L = 30$ mm ($\approx 2\lambda_g$ at the center frequency) is shown in Fig. 3.7. The result is in good agreement with that predicted by the equivalent circuit model for a conventional waveguide [89, pp. 318–322]. The length of the waveguide section between the corners depends on the feed position and does obviously not affect the general level of return loss but rather determines the number of resonances. Considering these two points, the optimization of the structure was performed focusing on a single bend and by resorting to matching techniques that are well known for rectangular waveguide discontinuities.

A single waveguide corner may be viewed as pair of equal waveguides connected in a right angle to a square cavity. In the presence of such a discontinuity, the boundary conditions for the fields can only be satisfied by the complete set of eigenmodes supported by structure. A TE_{10} mode incident upon the junction will excite predominantly TE_{m0} and TM_{m1} modes. These higher order modes contribute, each to different extent, to magnetic and electric energy stored in close proximity to the corner, which is modeled as inductances and capacitances in equivalent circuit representation [89, pp. 318–322]. In the case of a sharp *H*-plane corner, the parasitic reactive components at the junction give rise to large reflections, resulting in a return loss of 9 dB at best. To minimize reflections over a wide range of frequencies while maintaining a compact structure, smooth

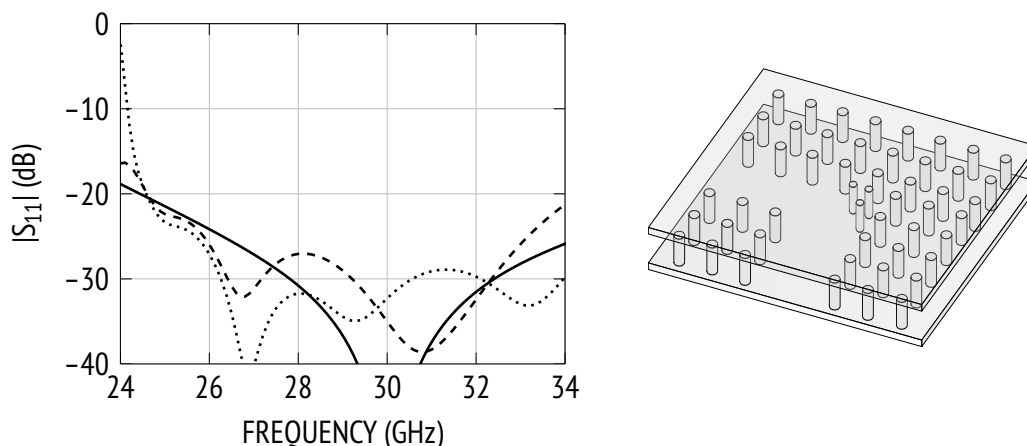


Figure 3.8: Simulated reflection coefficient of a groove gap waveguide H -plane corner compensated by one pin (---) and three pins (.....), of an optimized mitered WR-28 waveguide bend (—).

circular bends with small radius of curvature ($\lambda_g/2$) are commonly used. Due to the relative movement between the textured surfaces forming the elbow in the present structure, it turns out that this type of bend cannot be readily realized using discrete pins. In rectangular waveguides, a sharp bend can alternatively be compensated by mitering the corner; this provides similar performance and may be preferred for manufacturing reasons. In principle, a mitered bend is formed by combining two sharp H -plane corners which are spaced at a proper distance such that the reflections produced by each junction cancel each other at a fixed frequency. However, since higher order mode propagation between the two discontinuities cannot be neglected, the equivalent circuit parameters of a single corner are not sufficient for calculating the spacing [69, p. 204]. In the present case, such a bend has been approximated by inserting one or several pins close to the corner. The simulated input reflection coefficient of different configurations is plotted in Fig. 3.8. It can be seen that the overall performance of a groove gap waveguide corner compensated by discrete pins is comparable to that of a mitered WR-28 waveguide bend. The mode-matching technique described in [90] for rectangular waveguide corners can be used to study the effects of different design parameters, such as the number, diameter and positions of the pins. The designs related to Fig. 3.8 were obtained using full-wave simulations. In particular, the bend with three pins can be optimized such that a return loss of about 30 dB is achieved over the entire frequency band of interest.

3.1.4.2 Non-Contacting Choke Joint

The design of compact mechanically reconfigurable antennas is based on movable subcomponents, such as guiding structures or primary radiators. In addition to mechanical issues (e.g., adhesive wear) also design challenges from an electromagnetic point of view arise when employing movable parts. This is due to the fact that finite air gaps are formed between gliding surfaces which present a discontinuity in waveguide structures even if the gap is a small fraction of a wavelength in extent (e.g., $\lambda/20$). In the proposed feed system, shown in Fig. 3.6, a standard rectangular waveguide needs to be connected to the groove gap waveguide structure. Since the upper plate of the latter is rotated during scan, a motional joint is required. In fact, additional support structure could be provided to ensure a mechanical decoupling between movable and stationary external waveguide parts. A more compact solution, however, is to use a non-contacting flange. This specific problem has been the motivation for designing a reliable choke joint where no physical contact is needed. The basic operating principle of this type of transition, previous developments in this field and the proposed solution will be discussed in the following.

Problem

In the ideal case, shown in Fig. 3.9, a groove gap waveguide is fed horizontally by a rectangular waveguide having a width equal to that of the groove and a height equal to the distance between bottom and top plate. However, if one of the plates needs to be movable, the fixed rectangular waveguide leading to the transmitter/receiver cannot be connected to both plates. This means that all parts of the external feed network need to be mechanically decoupled from the moving structure. In the present case, the upper plate is movable, so that the bottom of the feed waveguide may be still connected to the lower plate. On the upper side, however, the feed needs to be physically separated from the groove gap waveguide, i.e., a certain gap needs to be provided between the aperture of the rectangular waveguide and the edge of the upper plate. An intuitive approach would be to reduce the dimensions of the feed waveguide such that it fits between the gap waveguide plates. One end of the waveguide would then be inserted into the groove and the other one connected to a standard waveguide via a tapered section. However, due to the finite wall thickness, the width and height of the waveguide would need to be reduced considerably to accomplish this. As a consequence, reflections occur at the junction of the two different guides. An

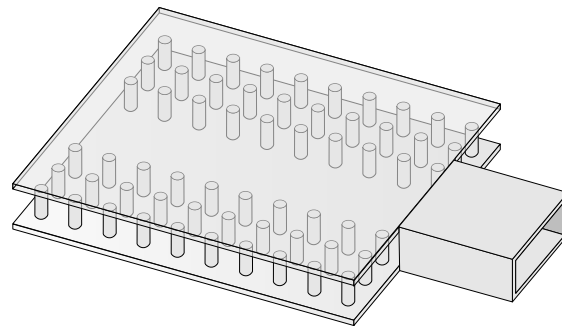


Figure 3.9: Ideal transition from rectangular to groove gap waveguide.

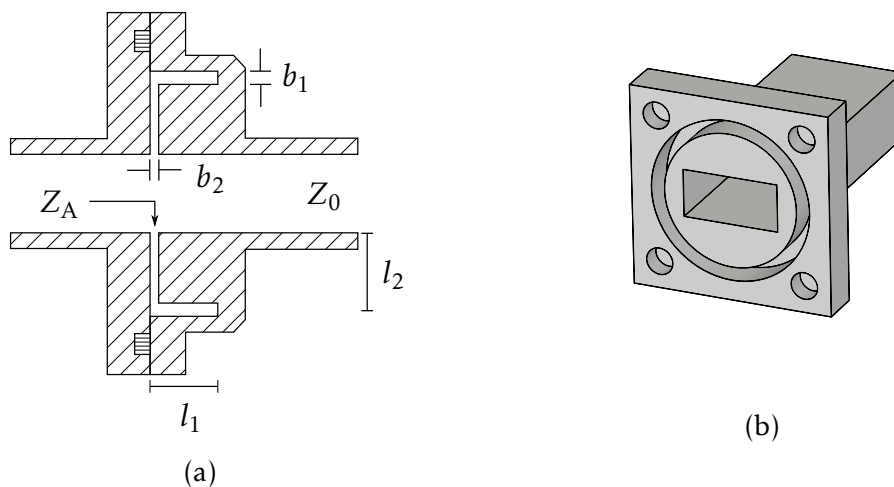


Figure 3.10: (a) Cross-sectional view of a conventional choke-flange coupling, (a) circular-groove choke flange.

alternative solution to this problem will be presented in the following.

Basic Principle of Choke Flanges

Choke flanges have been widely used for the connection of physically separable rectangular waveguide sections. A choke joint is formed when mating a choke flange with a cover flange as shown in Fig. 3.10(a). Generally, a finite gap between two flanges forms a discontinuity along all the waveguide walls. Considering the current distribution of the fundamental mode, a vertical slit in the narrow wall of the waveguide does not disturb the internal field distribution. In contrast, a transverse slot in the broad walls interrupts the current flow and therefore acts as a series load to the waveguide. Such discontinuity has a perturbing effect on the guided field distribution, which produces internal reflections and radiation. The effects of such a waveguide discontinuity can be minimized

by introducing a short-circuited half-wavelength stub at the interface. At the frequency of operation, the horizontal groove cut into the choke flange is one-quarter wavelength long and therefore transforms the short circuit at the right-hand end into an open circuit at the contact point of the flanges. Since the current is zero at this point, the branch may be broken. Hence, the finite load impedance introduced by the discontinuity is in series with the high (ideally infinite) impedance seen at the mouth of groove and has thus a negligible effect. The total impedance is then transformed back into a low impedance (ideally zero) by a second quarter-wave transformer formed by the vertical recess between the two flange surfaces. Hence, an effective short circuit is seen along the broad waveguide walls at the design frequency. For fabrication reasons, a circular groove as illustrated in Fig. 3.10(b) is most commonly used. The resulting rim around the waveguide aperture provides a quarter-wave transformer at the center of the broad waveguide walls [91, pp. 197–198], [92, pp. 120–121]. The effective length of the impedance transformer decreases continuously when moving away from the center, while the frequency at which the line is $\lambda_g/4$ long increases. It has been demonstrated in [82] that this effect leads to a larger bandwidth compared to that of choke flanges with rectangular groove. The distance between the narrow waveguide walls and the groove is small such that impedance transformation between these is negligible; however, this is not of great consequence, since the discontinuity has little effect there.

A simplified equivalent network that aids in the optimization of such joints is obtained by considering the choke as two separate rectangular arms, connected to the upper and lower waveguide wall, respectively [69, pp. 112–114]. Each arm is formed by an *E*-plane corner joining two waveguides of different height, one of which being short circuited. The reactance seen from point A, as illustrated in Fig. 3.10, is in series with the characteristic impedance of the main guide. The mismatch caused by the junction at frequencies other than the design frequency can then be studied using basic transmission line theory. As expected, reflection losses decrease as the gap b_2 becomes smaller. Moreover it is found that mismatch can be reduced by making the characteristic impedance of the groove large compared to that of the branch formed by the gap, i.e., by increasing b_1 [69, pp. 198–199].

State-of-the-Art Designs

Although the concept of choke flanges has been known for several decades, the

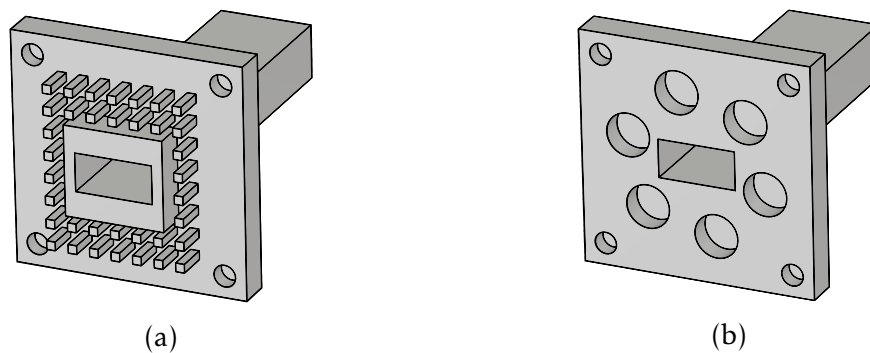


Figure 3.11: Choke flange based on (a) gap waveguide technology, (b) holey EBG structures.

development of novel high-performance waveguide interconnections has received increasing attention in the recent years. A contactless low-leakage flange based on the operating principle of gap waveguides for connecting WR3 waveguides has been first introduced in [82]. In the proposed transition, a textured surface on one of the flanges is used to create a parallel-plate cutoff condition at the interface, thus minimizing leakage from the discontinuity. One or several rows of pins forming the high-impedance surface are placed around the waveguide aperture, as illustrated in Fig. 3.11(a). In addition, the waveguide opening is surrounded by a rim having the same height as the pins; both rectangular and circular rim profiles have been investigated. An air gap of about $\lambda/20$ has been considered in the simulation, for which mismatch loss is kept below -20 dB over a fractional bandwidth of approximately 50%. A metalized SU8 polymer gap adapter based on the same concept and designed for a similar frequency band has been presented in [83]. Furthermore, a contactless flange adapter for WR15 waveguide interconnections has been proposed in [93]. The prototyped connector has been tested with gaps of about $\lambda/40$; the return loss is greater than 30 dB and insertion loss better than 0.1 dB over a fractional bandwidth of 40%. Moreover, flanges based on the concept of glide-symmetric holey electromagnetic bandgap structures (EBG) have been proposed in [94] for WR19 waveguide interconnections. In this case, the stopband characteristic inside the gap is achieved by introducing one row of glide-symmetric holes, as shown in Fig. 3.11(b), around the waveguide apertures of both flanges. Here, no further modifications are made on the flange surfaces for the purpose of impedance matching. A prototype consisting of a series connection of two such transitions has been tested with air gaps of up to $\lambda/70$. The measured return loss is greater than

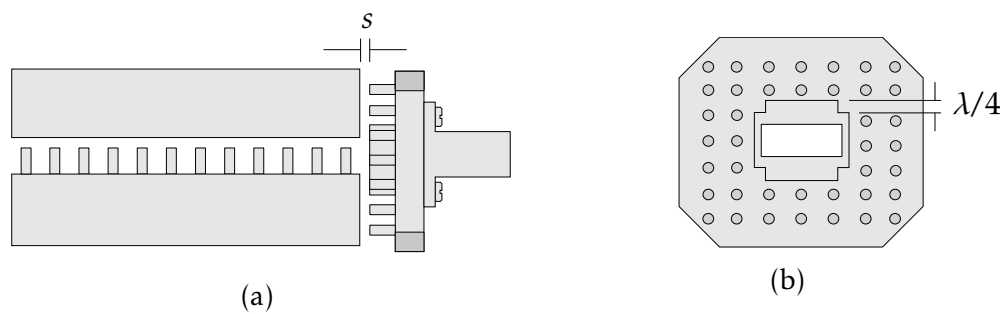


Figure 3.12: (a) Side view of a non-contacting choke coupling, (b) front view of the gap waveguide choke flange.

15 dB over the operating band.

It is important to note that all previously described non-contacting flanges have been developed to address the need for easily pluggable high-performance waveguide interconnections in measurement setups. Hence, the basic idea is to reduce the susceptibility to poor electrical contact as a result of instrumental or human errors. Although no uniform electrical contact may be required, a mechanical contact between the flanges is usually still provided to ensure a proper lateral alignment of the waveguide apertures, for example with mounting screws [83], [94] or magnets [93].

Developed Choke Flange

Among previous developments, the non-contacting flange adapters using gap waveguide technology as presented in [82] and [93] were identified as promising solutions. Due to their much lower manufacturing complexity, flanges based on glide-symmetric holey EBG structures are an attractive alternative. However, for the given problem such flanges are not suitable since glide symmetry is lost upon lateral displacement of the waveguide parts. Initially, the gap waveguide concept was adopted for the present case as illustrated in Fig. 3.12. The width and height of the aperture are equal to those of the groove, where the former has been set according to the WR-28 specifications. The choke flange can be fully separated from the groove gap waveguide or mounted firmly to the bottom plate, so that no air gap is found below the aperture. The pin-bed structure surrounding the aperture fulfills the same function as the textured surface confining the groove, i.e., it creates a parallel plate cut-off region in the air gap between the two waveguides, thus allowing propagation only in longitudinal direction and minimizing the leakage in transversal directions. The AMC design reported

in Section 3.1.2 can be readily reused for this purpose. Obviously, the top and bottom plate of the gap waveguide need to be of adequate thickness to act as a cover flange as illustrated in Fig. 3.12(a). A rim is placed around the waveguide opening, having the same height as the pins. As indicated in Fig. 3.12(b), the rim sections at the long sides of the waveguide are a quarter wavelength long to form together with the cover flange an impedance transformer that transforms an open circuit into a short circuit, thus minimizing reflections at the interface between the waveguides. To enhance the impedance bandwidth, the width of the shorter vertical rim sections is kept as small as possible. Further improvements can be achieved by optimizing the stepped corner. The simulated S parameters of the junction for a gap of $s = 0.5 \text{ mm} \approx \lambda/20$ at the center frequency (29.25 GHz) are shown in Fig. 3.14, where port 1 refers to the input of the choke flange. For comparison, the calculated reflection and transmission coefficient of a conventional choke flange, based on the simplified transmission line model described in [69], is shown. The reference model is tuned to the design frequency and forms a closed cavity so that in the absence of conductor loss $|S_{11}|^2 + |S_{21}|^2 = 1$. The designed flange provides a return loss greater than 20 dB over a fractional bandwidth of more than 30%. As in the symmetric equivalent circuit, $|S_{22}|$ of the simulated choke joint is essentially equal to $|S_{11}|$. Moreover, the low insertion loss confirms that the EBG structure, made of two concentric rows of pins, provides excellent shielding. To reduce manufacturing complexity, the pin-bed structure has eventually been replaced by an additional rectangular groove as shown in Fig. 3.13, providing an effective short circuit at the quarter-wavelength point of the inner choke. The position and width of the outer groove need to be selected carefully such that no standing waves are formed by the fields excited in the air-gap region [95]. The final dimensions are given in Fig. 3.13(b) and (c). The simulated S parameters of the developed choke joint are shown in Fig. 3.14. It should be recalled that the pin structure presents an isotropic impedance surface, therefore preventing wave propagation along any direction inside the radial waveguide formed by the gap. In contrast, the choke flange made of concentric grooves corresponds to a corrugated plane and therefore acts as a soft surface along x and y . However, the low insertion loss shows that despite this anisotropy, the final flange design provides sufficient parallel-plate mode suppression inside the gap. The performance parameters of the final design are summarized in Table 3.1 and compared with equivalent contact-free waveguide flanges.

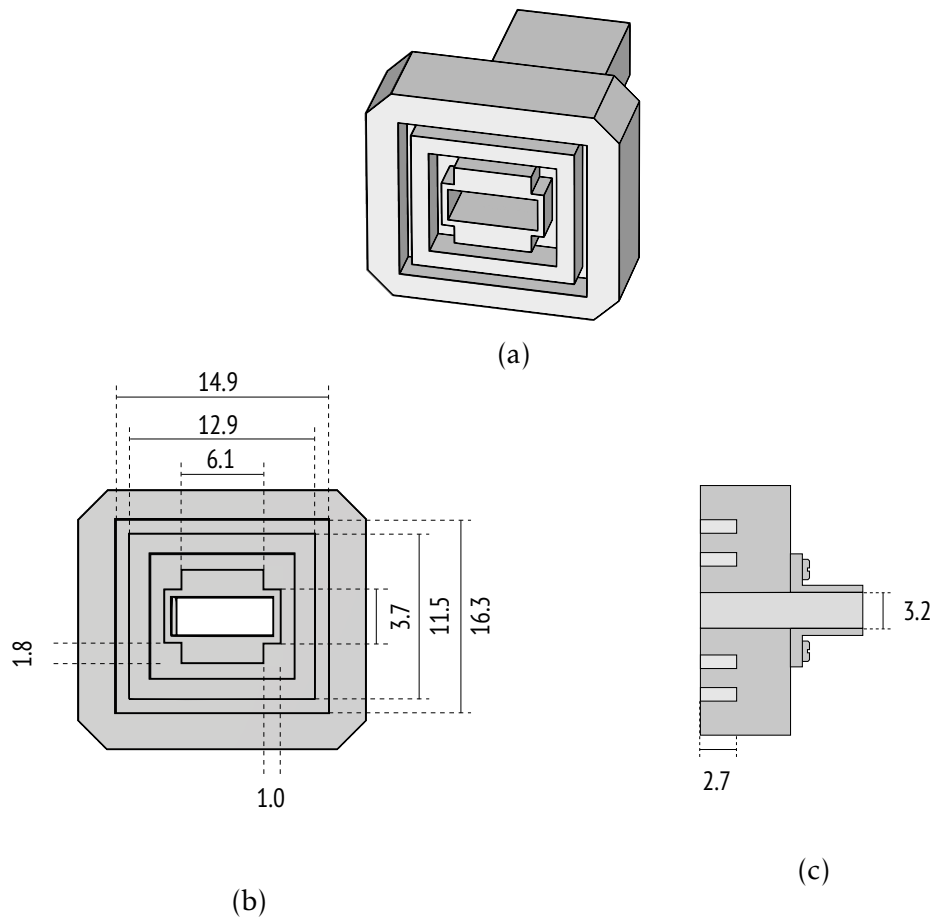


Figure 3.13: (a) Perspective view, (b) front view and (c) cross-sectional view of the proposed choke flange (all dimensions in mm).

Table 3.1: Comparison of non-contacting waveguide joints.

Reference	Type	Validation	Frequency band	Air gap ^a	Return Loss	Insertion Loss
[82]	Pin bed	Simulation	190–320 GHz	$\lambda/20$	20 dB	n.a.
[93]	Pin bed	Simulation	50–75 GHz	$\lambda/40$	30 dB	0.1 dB
[95]	Egg choke	Measurement ^b	8.5–11 GHz	$\lambda/30$	20 dB	0.1 dB
This work	Pin bed	Simulation	25–35 GHz	$\lambda/20$	20 dB	0.1 dB
This work	Rect. choke	Simulation	25–35 GHz	$\lambda/20$	20 dB	0.1 dB

^a Referring to the center frequency.

^b A variety of misalignments has been considered.

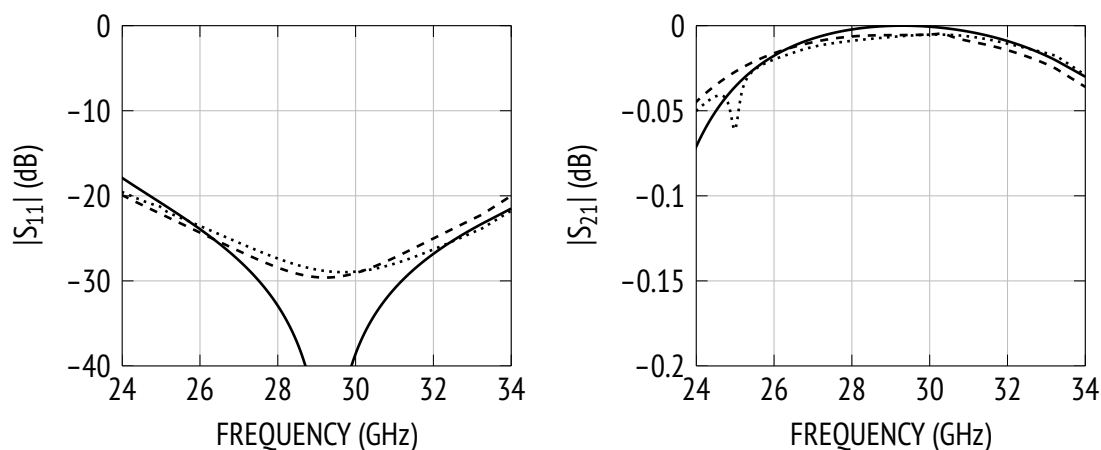


Figure 3.14: Simulated S parameters of a non-contacting gap waveguide joint (---) and of the proposed choke joint (....), calculation based on simplified equivalent circuit model for a circular choke joint (—).

3.1.4.3 Movable E -Plane Corner

As shown in Fig. 3.6, the proposed feed system is connected horizontally to a standard waveguide. One alternative approach that has been investigated consists in feeding the structure vertically as illustrated in Fig. 3.15. A similar design based on conventional waveguides has been presented in [78]. In the present case, a rectangular waveguide is connected to the stationary gap waveguide plate (here the upper one) while the textured surface defining the feed path lies on the movable plate. A number of pins placed behind the aperture act as a shorting wall so that all power coupled into the gap waveguide proceeds in the direction of the feed horn. As can be seen from the exploded-view drawing in Fig. 3.15, this pin structure is formed on the stationary plate such that the effective short circuit is at a fixed distance from the aperture. For proper mechanical operation, sufficient spacing between these pins and the ones delimiting the groove needs to be provided. If the width of the groove matches that of the waveguide, there is essentially no mode conversion and the resulting transition can be treated as a conventional E -plane bend if the shorting wall is placed directly behind the aperture. An incident TE_{10} mode will excite predominantly TE_{1n} and TM_{1n} modes in both waveguides. The simulated input reflection coefficient of the unmodified structure is shown in Fig. 3.15, where port 1 refers to the input of the standard waveguide. The width of the groove and the feed waveguide are equal to that of a WR-28 waveguide ($a = 7.11$ mm); the smaller dimension of the latter is set equal to the height of the groove ($d + h = 3.2$ mm).

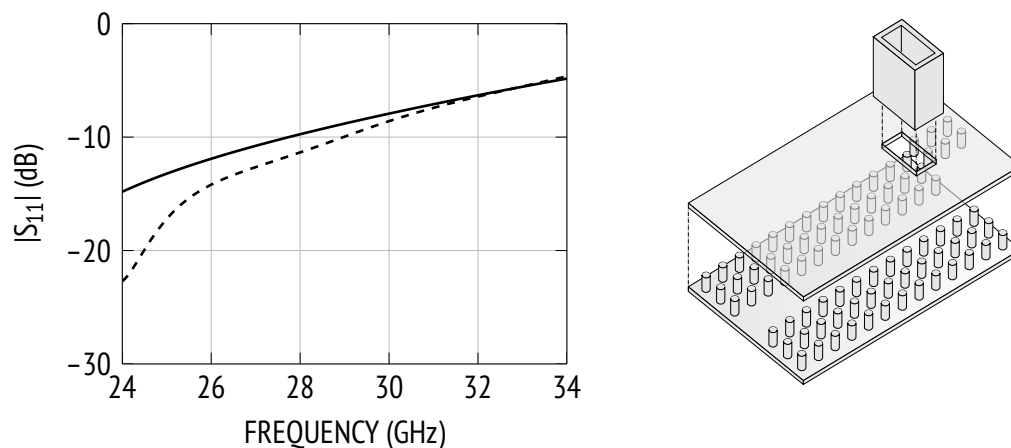


Figure 3.15: Simulated reflection coefficient of a vertical transition from rectangular to groove gap waveguide (—), calculation based on waveguide equivalent circuit model (--).

As expected, the result is in relatively close agreement with that predicted by the equivalent circuit model of a conventional right-angle *E*-plane bend [89, pp. 312–318]. Remaining differences are due to the fact that the dominant modes of the two guides show slightly different dispersion characteristics, as indicated in Fig. 3.5. As with the previously discussed transitions, the need for free-moving structures leads to limitations on the choice of compensation techniques. More specifically, matching elements need to be fixed with respect to the aperture and therefore attached to the upper plate. Since a sufficient clearance to the lower plate must be provided, common compensating structures such as circular, mitered or stepped bends are difficult to realize. Two wideband transitions from rectangular to groove gap waveguide have been proposed in [96], one of which being compatible with the given configuration. As illustrated in Fig. 3.16, the top plate of the groove gap waveguide is fitted with a small piece of rectangular conductor extending into the rectangular waveguide opening. Intuitively, this modification ensures that close to the center of the guide cross section, the electric field is less distorted when passing through the corner. The length, width and height of the conductor and its position with respect to the aperture are tuned to achieve the desired matching. These parameters were optimized for a WR-28 feed waveguide using full-wave simulations. The final dimensions are given in Fig. 3.16; the height of the conductor is 0.75 mm. As shown in Fig. 3.17, a return loss greater than 25 dB over a fractional bandwidth of 18% is achieved. Due to the loading by the conductor on the top plate, the groove behaves over a

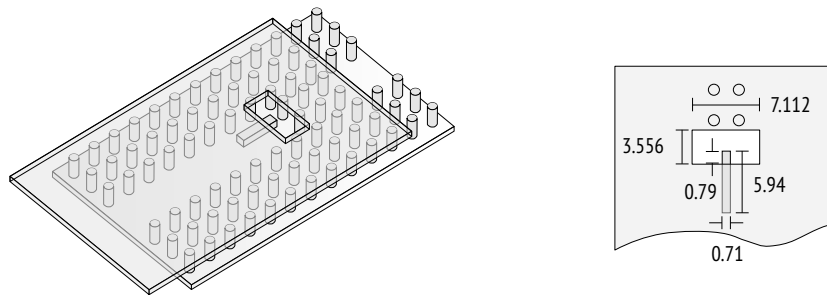


Figure 3.16: (a) Perspective view of a matched vertical transition from WR-28 waveguide to groove gap waveguide, (b) geometry of the top plate (all dimensions in mm).

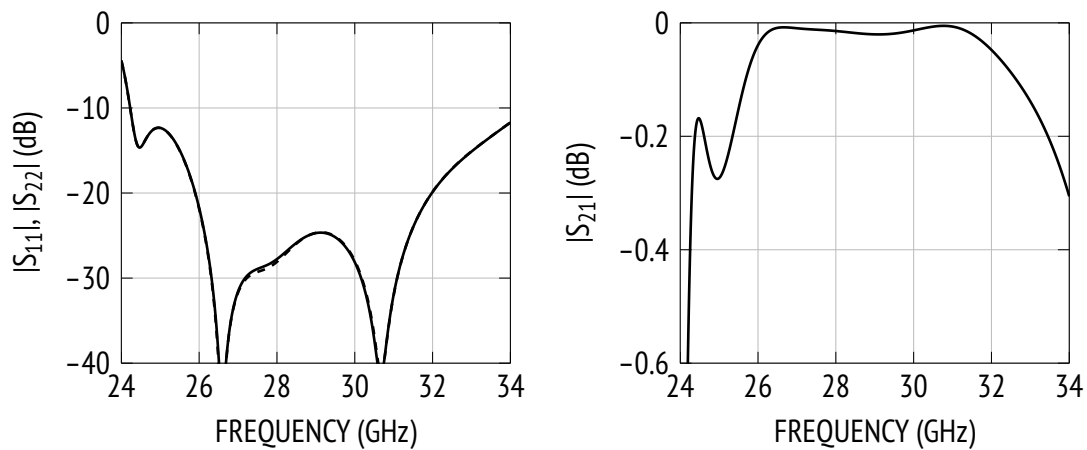


Figure 3.17: Simulated S parameters of an optimized transition from rectangular to groove gap waveguide.

short section as a ridge waveguide. Hence, the matching of the transition can be further improved by providing a smoother transition inside the groove; a stepped conductor can be used for this purpose.

This configuration offers the advantage of direct interconnection between the gap waveguide and external components, i.e., without requiring other motional joints. One drawback of vertical feeding is the fact that the required mechanical support may not be compatible with low-profile antenna designs. Moreover, the matching element and the pin-made shorting wall on the fixed plate are impractical to realize by subtractive manufacturing.

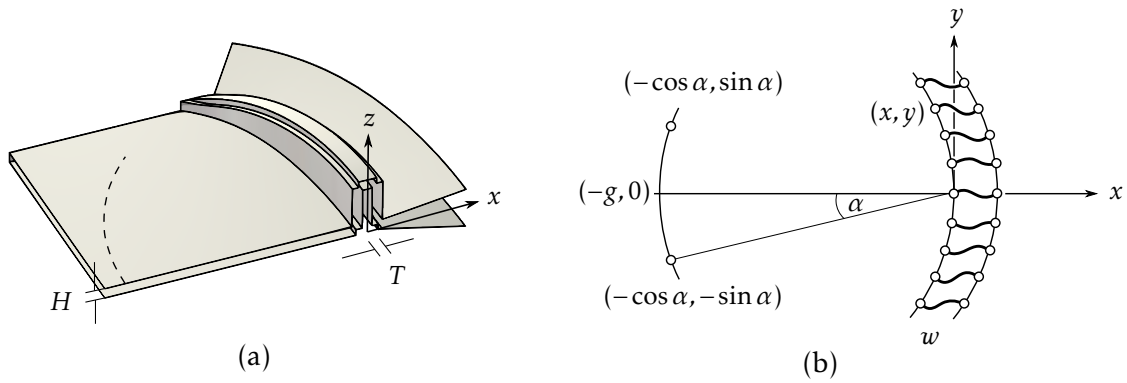


Figure 3.18: (a) Cross-sectional view of a continuous PPW lens, (b) constrained bifocal lens model.

3.2 Quasi-Optical Design

3.2.1 Basic Design Principles

Figure 3.18 shows a cross-sectional view of the developed lens beamformer, whose structure has already been described in Section 1.3.4. A deeper insight into the focusing behavior of the beamformer can be gained by treating it as a constrained lens which permits the definition of two independent path length conditions. Since the delay section is formed by a uniform guide, the continuous lens can be viewed as the *constant-refractive-index design* reported in [11], with the difference that inner and outer lens profile are identical and effectively collocated. The lens profiles are derived by imposing optical path length equality between a general ray and the central reference ray. This procedure is detailed in equations (1) through (14) in [38]. The available degrees of freedom allow the definition of two symmetrical off-axis focal points as depicted in Fig. 3.18(b). This leads to elliptical lens profiles given by

$$x = a_0 \left[\sqrt{1 - y^2} - 1 \right] \quad (3.1)$$

where $a_0 = \cos \alpha$. The coordinates (x, y) are normalized by the focal distance F so that $-d/2 \leq y \leq d/2$, where $d = D/F$. Furthermore, a simple expression describing the transmission line length can be obtained:

$$w = a_0 x. \quad (3.2)$$

The height profile of the vertical parallel-plate section is then given by

$$z = \frac{1}{2}[w - w_{\min}] \quad (3.3)$$

where the delay length w_{\min} at the edges of the lens ($y = \pm d/2$) is included so that positive values are obtained for z . Previous work has shown that the constrained lens model is not entirely adequate for the analysis and design of continuous PPW beamformers as it only approximates the propagation inside the vertical lens section. A ray-tracing procedure has been developed [38] to account for this effect, thus allowing an accurate prediction of the resulting radiation patterns. Moreover, due to its low computational cost, this method can be conveniently embedded into an optimization process. In this case, it is advantageous to represent the lens profiles by polynomial functions which provide additional degrees of freedom for retrieving the performance of the constrained lens model. The optimization procedure can be based on a phase-only model with the goal to minimize the RMS phase error for a range of feed positions. This approach results most likely in a non-focal design [34] which can differ considerably from the bifocal geometry. For designing the lens presented in this work, a pattern optimization process as described in [39] was used. In this way, the available degrees of freedom can be further exploited to also control the amplitude performance of the lens.

The first step in the design process is to define the diameter of the lens according to the required beamwidth. An initial reference focal length must be selected carefully by taking into account performance requirements and size limitations. In multiple-feed systems, a large F/D generally complicates the dimensioning and arrangement of primary radiators. Next, starting points and limits for the polynomial coefficients a_n need to be defined. The initial values can be set such that the polynomials approximate the lens shape described by (3.1) and (3.3). The parameter range should be specified such that strongly curved contours, where the ray-tracing method based on local application of Snell's law of reflection becomes inaccurate, are avoided. In the present model, even-order polynomials of order ten were used to define lens geometries as shown in Fig. 3.18. The inner lens and height profile are thus described by functions of the form

$$f(y) = \sum_{n=0}^5 a_n y^{2n}. \quad (3.4)$$

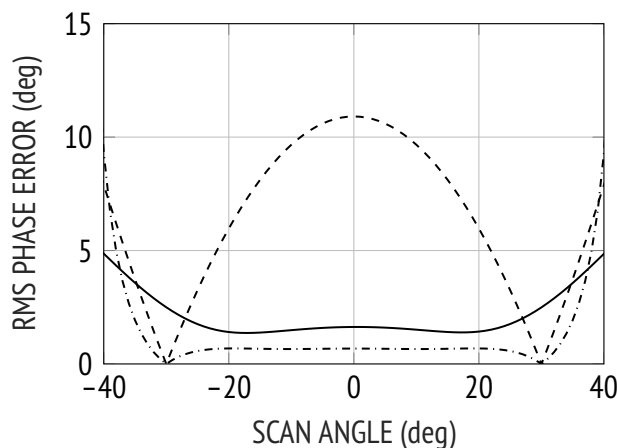


Figure 3.19: Normalized RMS phase error versus scan angle of a constrained bifocal lens with $g = 1.0$ (---), $g = 1.27$ (-.-), and of an optimized non-focal design (—) with $F/D = 0.7$.

While in multiple-feed designs the feed position for each scan angle could be used as an additional degree of freedom, the proposed feed system allows only one parameter, namely, the radius of the focal arc, to be used in the optimization process. As discussed in Section 2.3.1, the focal arc is centered at the vertex of the lens for reasons of amplitude performance. As with the Rotman lens, such a structural simplification limits the scan performance of the beamformer. The resulting penalty can be demonstrated by studying the RMS phase errors of a constrained lens reference model. The results presented in Fig. 3.19 refer to a lens with a moderate focal ratio of 0.7 and are normalized by F/λ . The two off-axis foci are found at an angular position of $\alpha = \pm 30^\circ$ and the focal arc is defined by the parameter g as in [38]. With the required configuration having $g = 1.0$, significant phase errors occur for the broadside case. By expanding the closed-form expression for the path length error into a power series, it can be shown that this effect can be overcome by refocusing the feed according to [11]

$$g = 1 + \alpha^2. \quad (3.5)$$

The four primary aberrations are given explicitly in Appendix B. This is verified by the low RMS error resulting for $g = 1.27$ with the design considered. However, as mentioned earlier, such a configuration is only relevant for stationary feed systems. It should be also noted that the curvature of the resulting focal arc is more pronounced, which may lead to practical difficulties [15]. Also shown in Fig. 3.19 is the RMS error of an optimized continuous PPW lens having the focal

arc centered on the apex of the inner lens contour. The results, calculated using the ray-tracing technique detailed in [38], confirm that for scan angles up to 30° , a low, nearly constant level of phase errors can be achieved with a non-focal design of moderate F/D .

3.2.2 Single-Ridge Lens with Moderate Scanning Range

The lens design referred to in Fig. 3.19 has been developed using a pattern-based optimization process, with the aim to validate the feed concept at Ka-band (uplink). The design frequency was fixed to $f_c = 29.25$ GHz with a free-space wavelength of $\lambda_0 = 10.26$ mm. The final design has a diameter of $D = 19.5\lambda \approx 200$ mm and a focal ratio of $F/D = 0.7$. It should be noted that in the absence of a perfect focus, F refers to the radius of the feed arc. The coefficients of the even-order polynomials representing the inner lens contour and the height profile are, in ascending order,

$$\begin{aligned} \mathbf{a}^x &= [a_0^x, a_1^x, a_2^x, a_3^x, a_4^x, a_5^x] = [0, -0.23, -0.2, -0.3, -0.2, 0.21] \\ \mathbf{a}^z &= [a_0^z, a_1^z, a_2^z, a_3^z, a_4^z, a_5^z] = [0, -0.227, 0.077, -0.55, 0.42, 0.4]. \end{aligned}$$

The normalized contours are thus given by

$$\begin{aligned} x &= \sum_{n=0}^5 a_n^x y^{2n} \\ z &= \sum_{n=0}^5 a_n^z y^{2n} - \min\left\{ \sum_{n=0}^5 a_n^z y^{2n} \right\}. \end{aligned}$$

The phase of the electric field along the front face of the lens aperture has been extracted from full-wave simulations in Ansoft HFSS for scan angles in the range $\phi_0 = [0 \dots 30^\circ]$. As can be seen from Fig. 3.20, a good agreement with the results from ray tracing is found over large parts of the aperture; the ideal phase profile is depicted for comparison. At the maximum scan angle, a slight deviation of the phase front can be seen at the aperture edge toward negative y (i.e., on the side where the feed is located). This is due to the limited accuracy of the ray-tracing method when angles made by incident rays with the normal vectors to the lens contours become large. In this case, the rays inside the vertical delay section experience significant lateral deflection but are still represented by straight lines; a more accurate description would be achieved with geodesic rays [30].

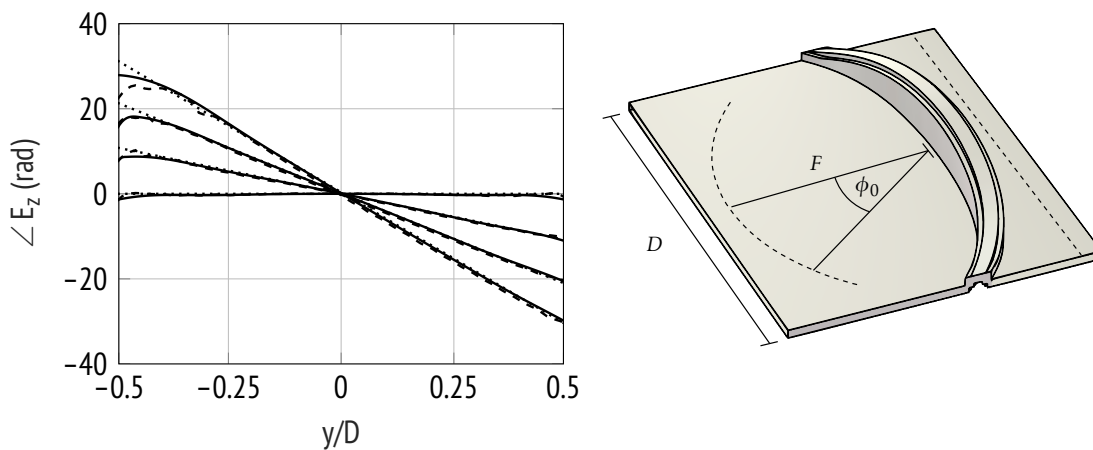


Figure 3.20: Calculated (—), simulated (---) and ideal (.....) phase front along the lens aperture.

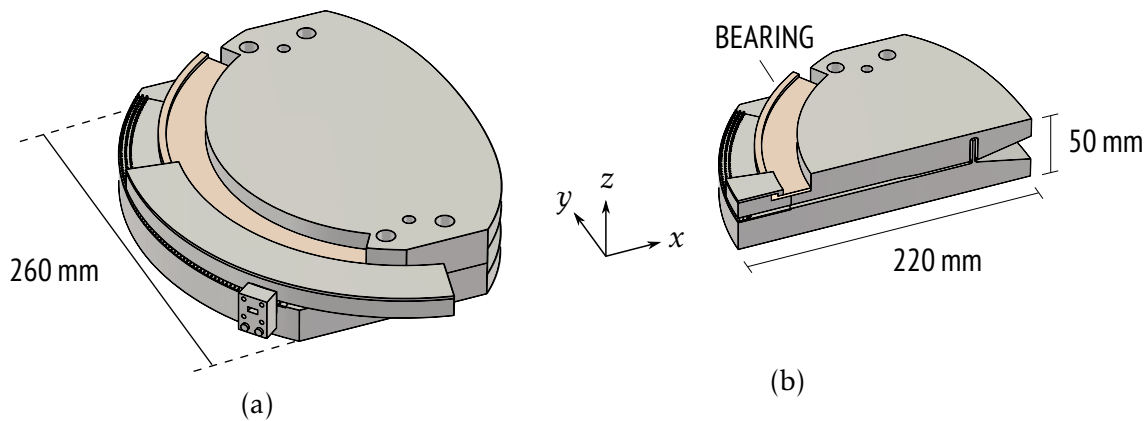


Figure 3.21: (a) All-metal implementation of single-ridge lens beamformer, (b) cross-sectional view.

The additional constraint that the feed arc must not be enclosed by the inner lens contours has been taken into account during the design process. This ensures that the feed can be rotated freely around the center of the lens. As illustrated in Fig. 3.21, the lens can be implemented using two complementary blocks [39]. In this case, the ridge is formed on the lower block while the upper one provides the cavity. The ridge in the final design has a thickness of $T = 2$ mm, which is equal to the height H of the PPW cavity. A linear taper along the focal region was used to interface the parallel-plate region with the groove gap waveguide of height $d + h = 3.2$ mm. Further, a flare with a length of $2.5\lambda \approx 25.65$ mm at the output leads to an aperture size of $25.35\lambda \times 2\lambda$. The lens is illuminated by an H -plane sectoral horn providing an edge taper of 20 dB. To provide a

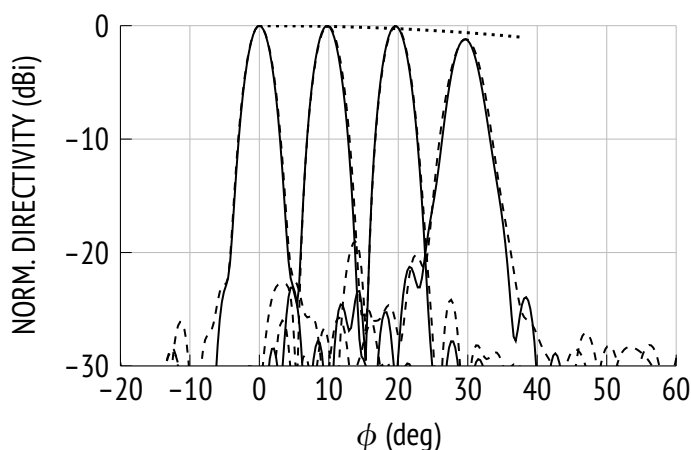


Figure 3.22: Calculated (—) and simulated (---) radiation patterns at the design frequency (29.25 GHz).

leakage-free low-friction transition from the feed system to the lens, the movable part is firmly mounted using a rotary bearing. The radiation patterns predicted by the ray tracing tool are shown in Fig. 3.22 for a range of feed positions. A very good agreement with the results from full-wave simulations in Ansoft HFSS is found. Differences in the sidelobe levels can be explained by the fact that an infinite PPW environment is assumed in the GO computation, i.e., internal reflections at the metallic sidewalls are not taken into account. Despite the mentioned constraints on the optical design, a good scanning performance is achieved with sidelobe levels below -17 dB and scan losses lower than 1.2 dB up to 30° and lower than 2 dB up to 35° .

3.2.3 Dual-Ridge Lens with Enhanced Scanning Range

As indicated in Fig. 3.19, the scan performance of each lens model deteriorates rapidly for scan angles beyond $\pm 35^\circ$. Obviously, this effect can be mitigated by increasing the focal length of the lens. Referring to the bifocal lens model, it can be shown that second-order aberrations decrease as $1/F$ and coma errors as $1/F^2$ [11]. The effect of these phase errors on uniform line source patterns are outlined in Appendix A. For the desired scan range of $\pm 50^\circ$ it appears that a ratio of $F/D \gg 1$ would be required in order to keep sidelobe levels well below -10 dB and scan losses within reasonable limits. Obviously, this necessitates a more directive feed to maintain a given edge illumination. In fact, there is no restriction on the size of the feed aperture in the proposed single-feed design.

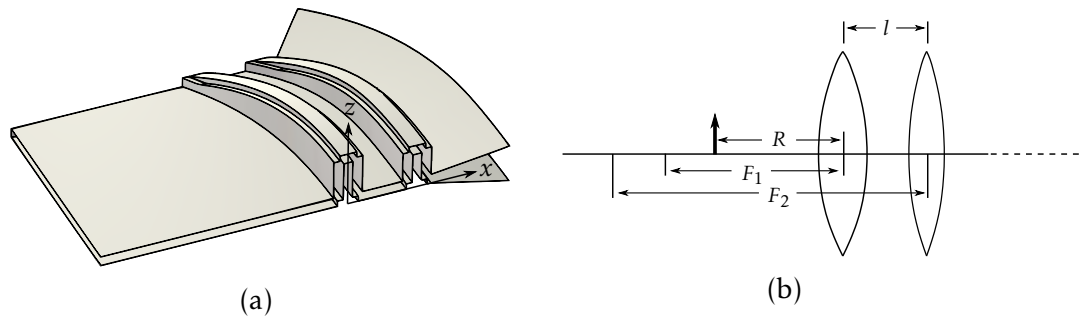


Figure 3.23: (a) Cross-sectional view of a dual-ridge lens, (b) first-order optics model.

However, the axial extent of the lens and the support required for the feed system become unreasonably large in such a design.

Instead, a second lens of equal diameter is introduced to increase the effective focal length of the quasi-optical system at the expense of slightly larger axial dimensions. The resulting structure can be treated as a system of two thin lenses [97, pp. 174–175] as shown in Fig. 3.23(b), where R denotes the position of the feed. Since on transmit, the feed is placed at a distance $R < F_1$ from the origin, i.e., in between the first lens and its focal point, a virtual image is formed as illustrated in Fig. 3.24. To transform the fields generated by the feed into a plane wave, the second lens is designed such that its maximum-field locus (described by F_2 at broadside) coincides with the virtual image positions. An approximate dimensioning process based on first-order optics is described in Appendix C. The focal surfaces of the two separate lenses resulting from plane-wave incidence at angles in the range $[-30^\circ, 30^\circ]$ are plotted in Fig. 3.25. For illustration also the lens contours and the imposed feed arc are depicted.

The optimized design has a diameter of $D = 20.5\lambda \approx 210\text{ mm}$ and a feed arc given by $R/D = 0.7$. As shown in Fig. 3.25, the focal ratios of the two individual lenses are $F_1/D \approx 1.2$ and $F_2/D \approx 1.66$. The distance between the two lenses, measured between the inner lens contours at $y = 0$, is $l = 19.5\lambda = 20\text{ mm}$. The coefficients of the polynomials representing the inner contour and ridge profile of the first lens are, in ascending order,

$$\mathbf{a}^{x1} = [0, -0.23, -0.34, 0.06, 0, 0]$$

$$\mathbf{a}^{z1} = [0, -0.118, -0.04, 0, 0.05, 0]$$

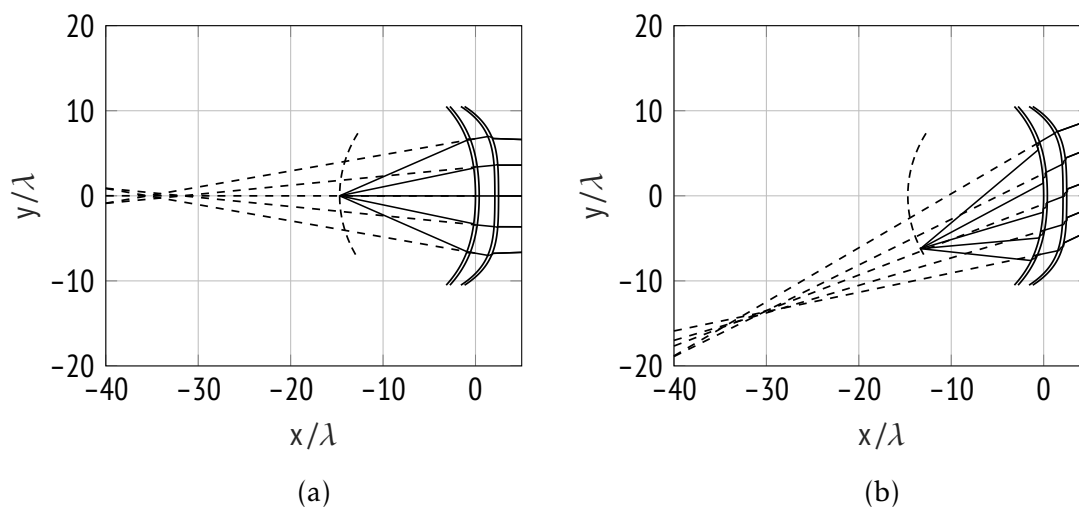


Figure 3.24: Rays passing through a dual-lens system in transmission (—) and rays describing the virtual image formation (--) for (a) $\phi_0 = 0^\circ$, (b) $\phi_0 = 25^\circ$.

and of the second lens

$$\mathbf{a}^{x_2} = [0, -0.05, -0.63, -0.18, -0.03, 0]$$

$$\mathbf{a}^{z_2} = [0, -0.099, 0, 0.03, 0, 0].$$

The corresponding normalized lens contours are defined as in (3.7). Also in this case, a pattern-based optimization process was used at the final design stage. The resulting RMS phase error is shown in Fig. 3.26. As can be seen, the phase error is significantly reduced at scan angles beyond 40° when compared to the single ridge design. However, two remarks should be made this point. First, as seen from the comparison with full-wave simulations in the previous section, the limited region of validity of the ray-tracing technique becomes apparent at large scan angles. As a result, small errors are expected to occur when determining the phase profile for extreme angles. Second, the RMS error of the final dual-ridge design suggests that even up to 60° , good scanning performance is achieved. However, for such scan angles, the feed lies relatively close to the edge of the inner lens contour leading to poor illumination. Geometrical optics (GO) and full-wave simulations showed that due to the highly asymmetric amplitude distribution, no useful patterns can be produced at this angular range. The phase of the electric field along a straight line in front of the lens aperture is plotted in Fig. 3.27 for scan angles in the range $\phi_0 = [0 \dots 50^\circ]$. Furthermore, the

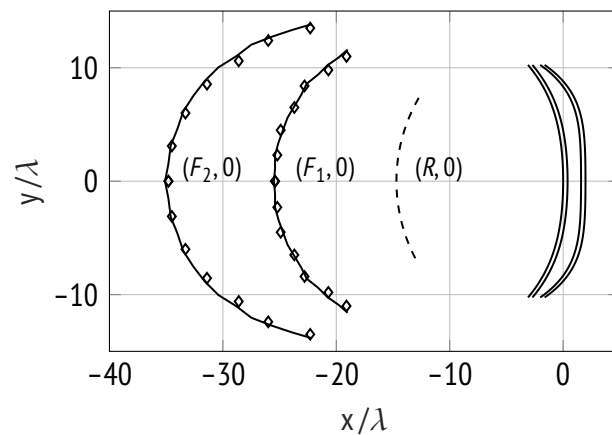


Figure 3.25: Calculated (—) and simulated (\diamond) focal surfaces for $\phi_i = [-30\dots30^\circ]$, imposed focal arc (--).

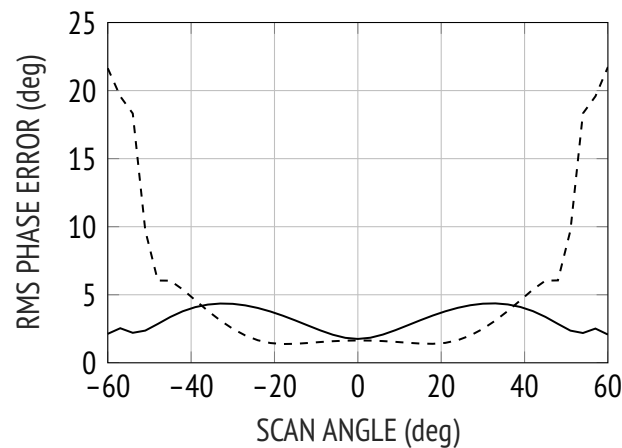


Figure 3.26: Normalized RMS phase error versus scan angle of an optimized dual-ridge (—) and single-ridge design (--).

calculated radiation patterns for the same range of scan angles is plotted in 3.28. A feed providing an edge taper of 20 dB is considered. The predicted scan loss is about 2.5 dB at 50° and sidelobe levels are below -17 dB over the entire scan range.

3.3 Antenna Manufacturing and Assembly

The final structure is shown in Fig. 3.29. The lens sections and radiating aperture were rotated by 90° compared to the single-ridge implementation shown in Fig. 3.21. The modification of the aperture was necessary in order to eliminate

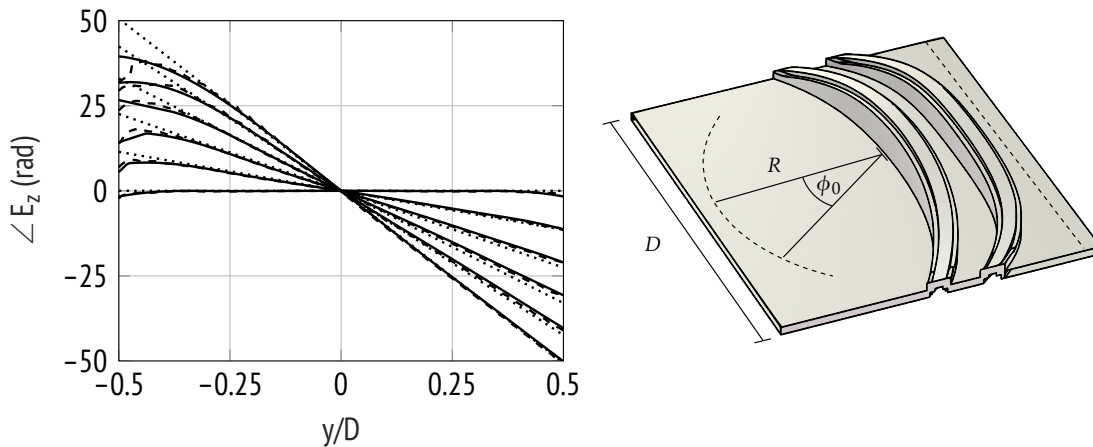


Figure 3.27: Calculated (—), simulated (--) and ideal (....) phase front along the lens aperture.

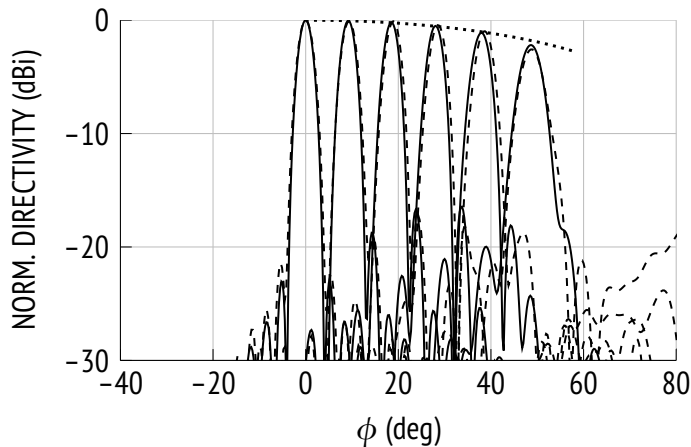


Figure 3.28: Calculated (—) and simulated (--) radiation patterns at the design frequency (29.25 GHz).

aperture blockage by the movable gap waveguide part at large positive scan angles. It should be noted that a similar configuration would be obtained when using the lens beamformer to excite a parallel-fed continuous transverse stub array [9]. The introduction of a 90° -bend between feed system and lens as well as between lens and flare were tested. A clear benefit of the latter configuration is its lower profile. However, quasi-plane waves generated at the output surface of the lens will be reflected by the PPW sidewalls that are required to form the bend, resulting in pattern degradation for large scan angles. To overcome this problem, the entire parallel-plate region at the output would need to be oversized by flaring the sidewalls according to the maximum scanning angle. Instead, the

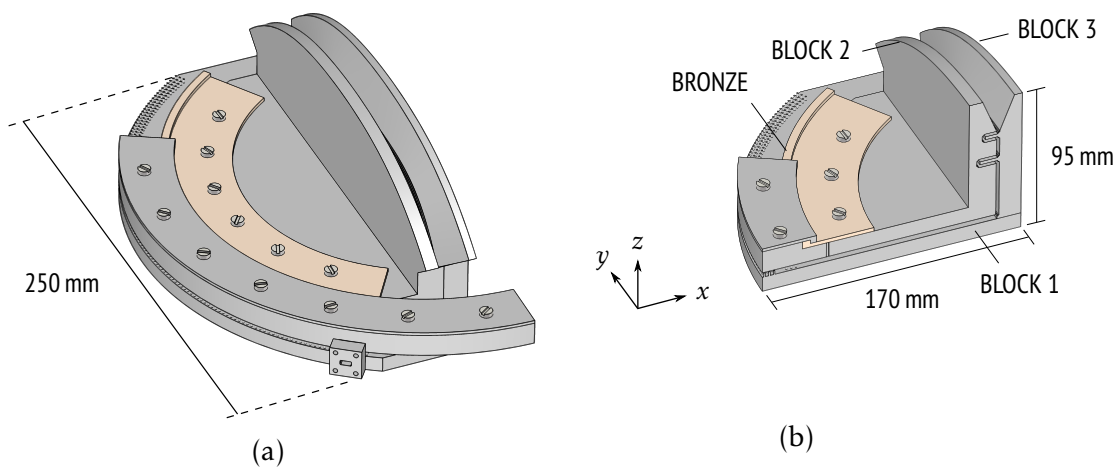


Figure 3.29: (a) All-metal implementation of dual-ridge lens beamformer, (b) cross-sectional view.

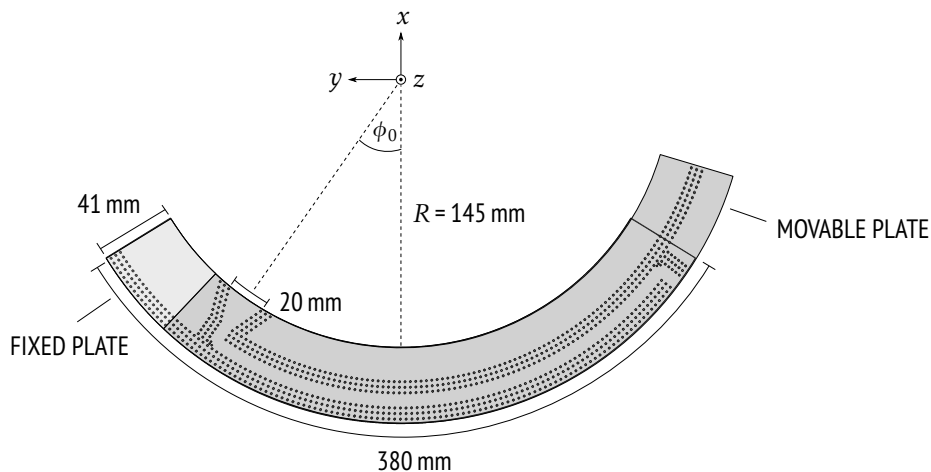


Figure 3.30: Top view of the final gap waveguide feed structure.

bend was inserted in the focal region, resulting in a higher profile but avoiding the use of an oversized aperture. Since scanning is demonstrated in the H plane (yz plane), no efforts have been made to optimize the flare at the output with respect to the pattern in the orthogonal plane. The horn dimension along the E plane (xz plane) is $2\lambda \approx 20.5$ mm and the flare length $2.5\lambda \approx 25.65$ mm. Full-wave simulations showed that this is large enough for scattering from the base block to become negligible, leading to an almost symmetric E -plane pattern. An improvement in gain could be obtained using a shaped flare [33]. The gap waveguide structure is shown in Fig. 3.30. The width of the groove is 7.11 mm from the input to the throat of the sectoral horn. The latter is designed to provide an edge taper of 20 dB. The length of the curved gap waveguide (measured along

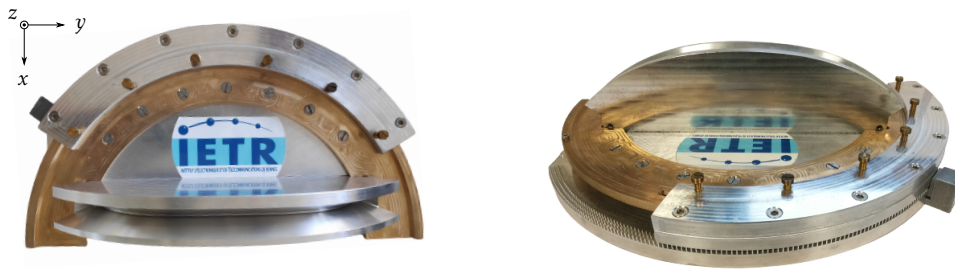


Figure 3.31: Top and back view of the prototype lens beamformer.

the center of the groove) ranges from 8 mm ($\phi_0 = 50^\circ$) to 310 mm ($\phi_0 = -50^\circ$). The simulated attenuation due to conductor and radiation loss for a groove gap waveguide in aluminum Alloy 5083 H111 ($\sigma = 1.72 \times 10^7$ S/m) is 0.018 dB/cm at 29.25 GHz. This would imply an insertion loss of about 0.01 dB and 0.56 dB, respectively, for the two extreme feed positions.

The structure was manufactured in bare aluminum. First, the three main blocks shown in Fig. 3.29(b) were cut to size using a water jet. The waveguide features, including cavities and ridges forming the lens and the textured surface in the feed system were made by CNC milling. The machining of the ridges and cavities on the milling machine naturally leads to rounded corners and pockets with a radius equal to that of the milling cutter. A reasonable corner radius of 0.5 mm was taken into account in the full-wave simulation. In general, more careful consideration must be given to the maximum depth of the lens cavities. In the final dual-ridge design, the maximum depths of the two cavities are about 12.5 mm and 9.0 mm, which is not critical from a manufacturing point of view. However, single-ridge designs with generally deeper cavity require longer milling cutters which are more likely to chatter as the tool moves across fillets. The lens was assembled by bolting the blocks together. A small gap needs to be provided between the movable feed part and block 2. Instead of an additional choke, a bronze bearing was placed between the two parts, preventing leakage from the gap. The bearing material is easy to machine and offers high resistance to friction and wear. The non-contacting flange, shown in Fig. 3.32, was made by 3D printing using an aluminum alloy powder. It should be noted that no surface treatment was applied. A smooth surface is achieved at the input side (shown in the back view of Fig. 3.32), corresponding to the lowest printing layer.

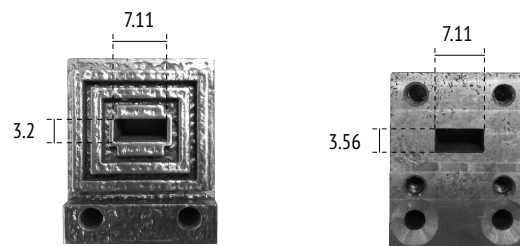


Figure 3.32: Front and back view of 3D printed non-contacting choke flange.

3.4 Experimental Results

3.4.1 Return Loss

The simulated and measured input reflection coefficient are shown in Figs. 3.33 and 3.34, respectively, for a range of feed positions. Simulations predict a return loss greater than 15 dB for all feed positions within the frequency band of interest. The measured S_{11} is somewhat higher but remains below -12 dB. This difference is attributed to fabrication tolerances of the 3D printed choke flange. It can be seen that in both cases, the maximum level of mismatch does not vary significantly with the feed position. The reactance introduced by the two groove gap waveguide corners is transformed differently depending on the length of the guide between these, resulting in a number of resonances that increases as the feed moves from $\phi_0 = 50^\circ$ toward -50° .

3.4.2 Radiation Performance at Broadside

The prototype was measured in the compact antenna test range of IETR. The measurement setup is shown in Fig. 3.35. Each angular feed position was adjusted using a prefabricated angle gauge as shown in Fig. 3.35(c). The movable plate was fastened with pressure screws. The broadside radiation pattern at the design frequency in the two principal planes is plotted in Fig. 3.36. A very good agreement between measurement and simulation is seen for the main beam and near-in sidelobes. The measured peak directivity is about 25 dB and the cross polarization levels are below -35 dB (peak-to-peak) in both planes. Since the structure surrounding the aperture is not symmetric, a slight asymmetry is observed in both planes. The sidelobe level in the E plane is about -13 dB, as expected for a uniform distribution. The effect of placing an additional absorber on the base block of the antenna as shown in Fig. 3.35(b) can be seen from the E -plane pattern in the range $-90^\circ < \theta < 0^\circ$. The dotted line corresponds to the

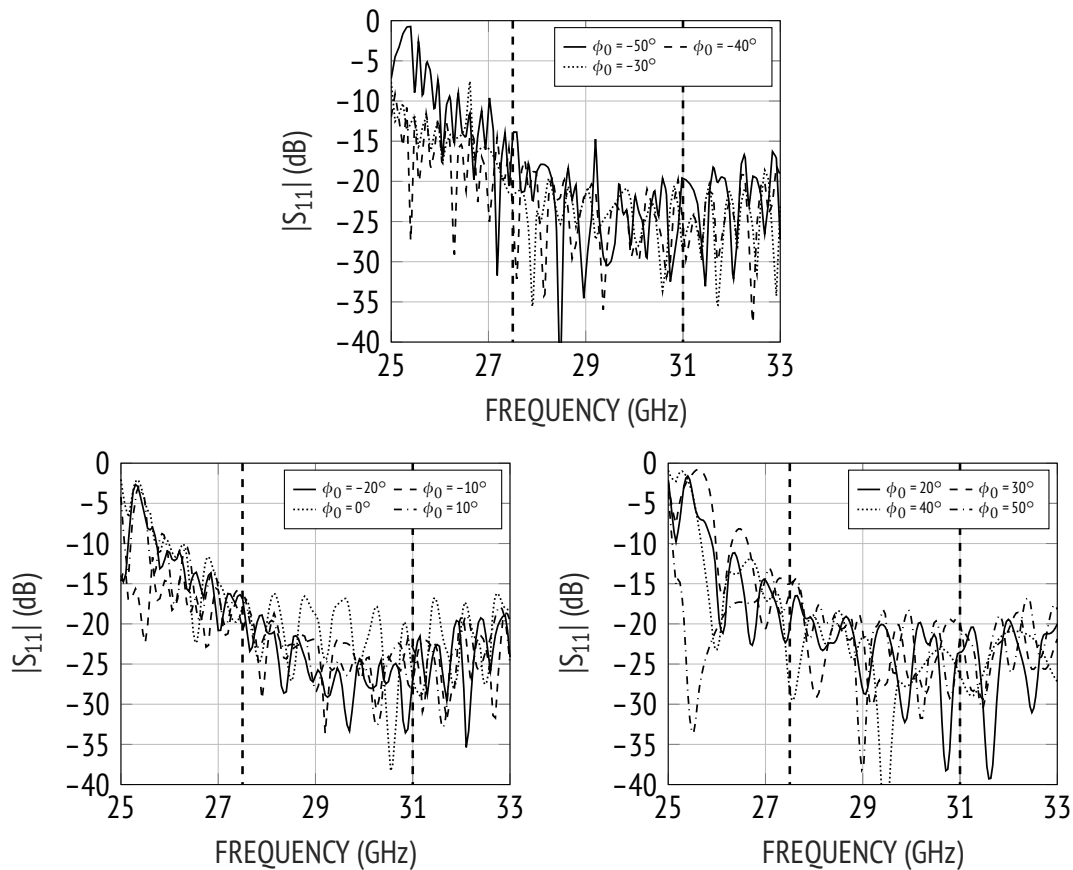


Figure 3.33: Simulated input reflection coefficient for various feed positions.

configuration without absorber as shown in Fig. 3.35(a).

3.4.3 Scanning Performance

The measured H -plane radiation patterns are shown in Fig. 3.37 for a range of feed positions. The results are in very good agreement with simulations in terms of pointing angle, beamwidth and gain loss. At the center frequency, a cosine variation of gain is obtained up to a scan angle of $\pm 30^\circ$ as in [39]. The measured scan loss is 2.7 dB and 3.3 dB for beams pointing at 50° and -50° , respectively. The asymmetry in gain loss is mainly due to the increased insertion loss in the gap waveguide, as explained in Section 3.3. Somewhat higher losses of 3.1 dB and 3.6 dB, respectively, occur at the lower end of the frequency band.

The H -plane radiation patterns of the antenna were measured in the entire uplink Ka-band and are plotted in Fig. 3.38 for various feed positions in the range $\phi_0 \leq 0^\circ$. The scanning angle is stable over the entire frequency range,

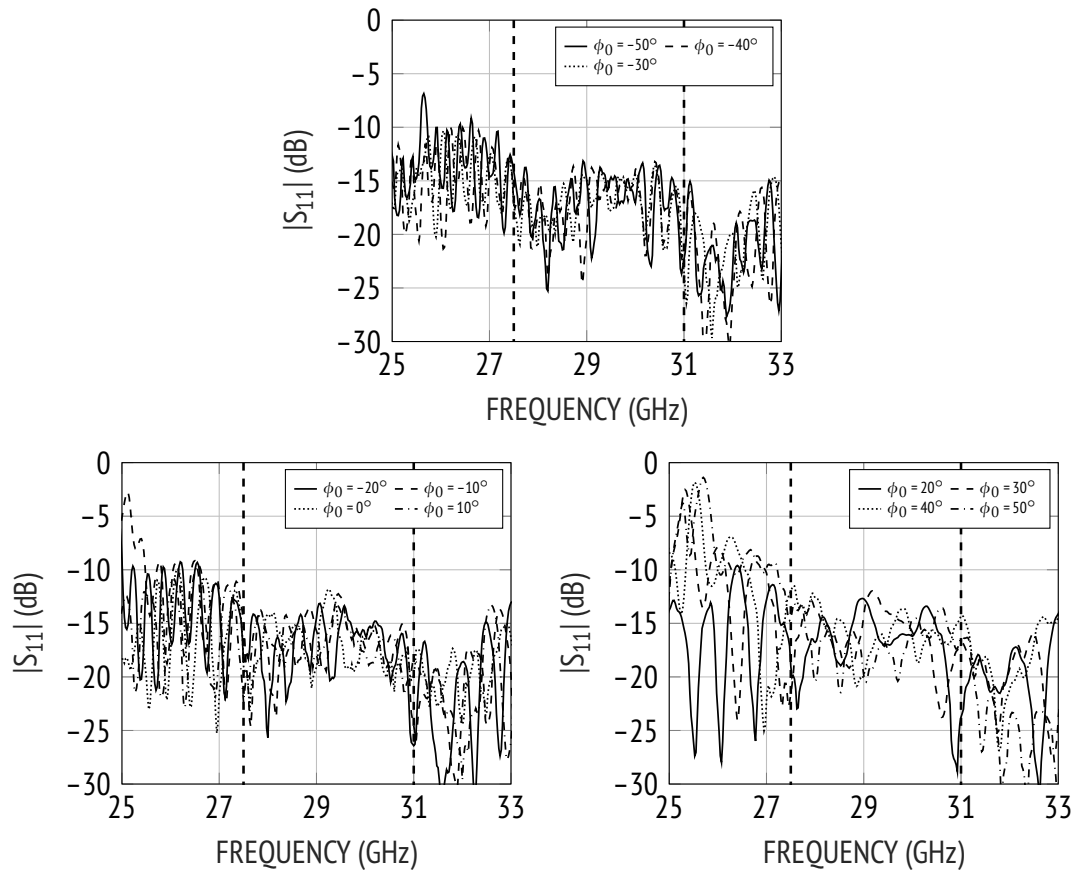


Figure 3.34: Measured input reflection coefficient for various feed positions.

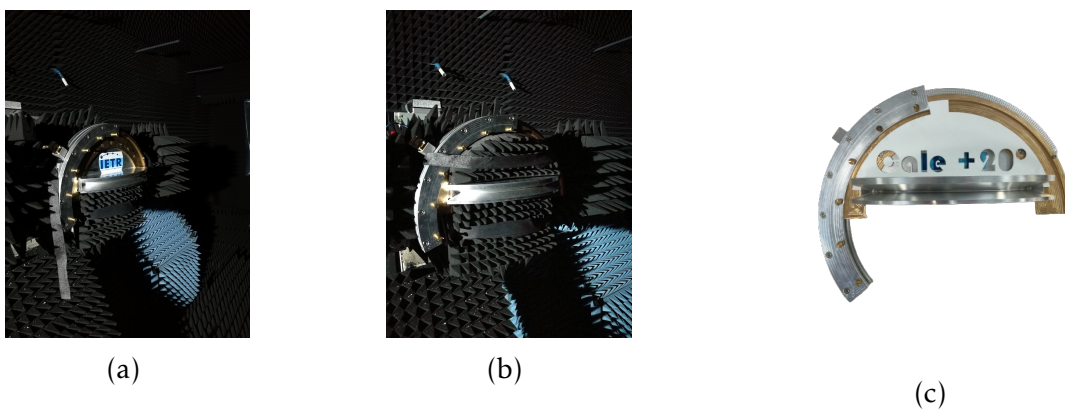


Figure 3.35: Measurement setup in the compact antenna test range (a) without and (b) with additional absorber. (c) Angular adjustment of the feed position.

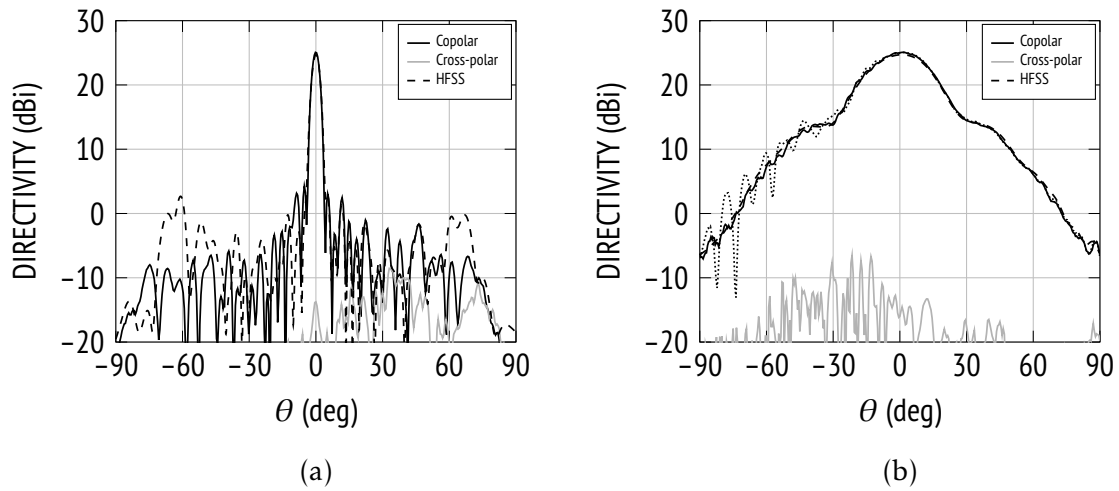


Figure 3.36: Broadside radiation pattern at 29.25 GHz in the (a) H plane and (b) E plane.

and the beamwidths have small variation. The extracted beam pointing angles, sidelobe levels and beamwidths are plotted in Fig. 3.39 as a function of frequency for the other half of the measured feed positions ($\phi_0 \geq 0^\circ$). It should be noted that the reported values do not necessarily refer to the first sidelobe. Within the frequency range 27.5 – 31 GHz, sidelobe levels are below -12 dB for all feed positions.

The peak directivity extracted from 3D radiation pattern measurements are shown in Fig. 3.40(a) for three different feed positions. At 29.25 GHz, the peak gain at broadside equals 24 dB, corresponding to a radiation efficiency of 86%. Due to the insertion loss of the gap waveguide slightly lower efficiencies are observed for $\phi_0 < 0$ and slightly higher ones for $\phi_0 > 0$. Figure 3.41 shows the 3D radiation patterns measured at the center frequency. The sine-space coordinates are defined as $u = \sin \theta \cos \phi$, $v = \sin \theta \sin \phi$ with θ being the polar and ϕ the azimuth angle in the coordinate system defined in Figs. 3.29 through 3.31.

3.5 Comparison with State-of-the-Art Solutions and Discussion

Table 3.2 summarizes the achieved performances of the developed single- and dual-lens beamformer. A comparison with other mechanically scanned millimeter-wave antennas is provided. Although the final design does not produce useful patterns beyond $\pm 50^\circ$, the performance in terms of scan loss and sidelobe

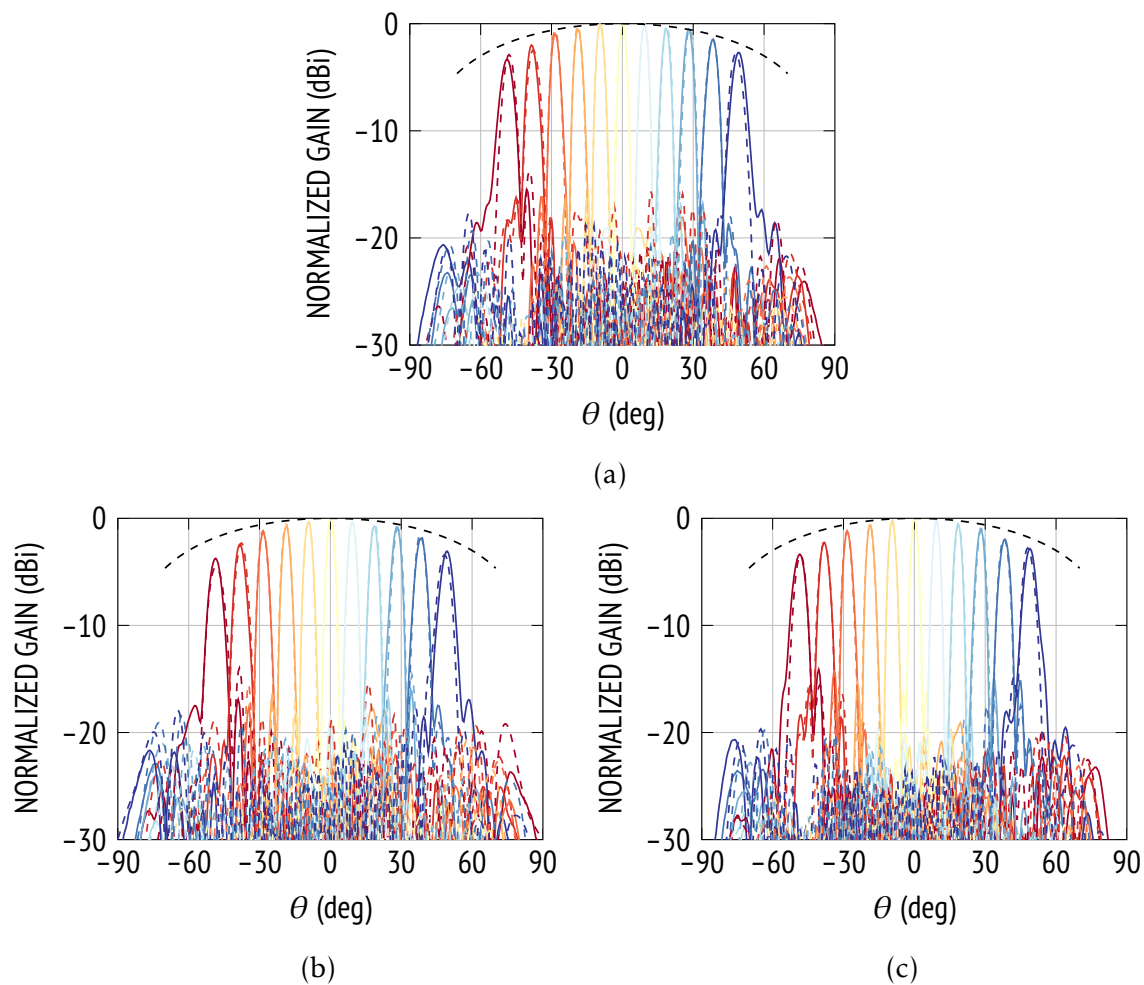


Figure 3.37: Measured (—) and simulated (--) H -plane radiation patterns for $\phi_0 = [-50^\circ, -40^\circ, \dots, 50^\circ]$ at (a) 29.25 GHz, (b) 27.5 GHz and (c) 31 GHz.

levels is within this range superior to that of related solutions. The designs presented in [6, 9, 62] are similar to the proposed system in that they also employ movable horns or equivalent feed elements. However, these feed systems have been developed for measurement rather than operational environment. In contrast, the feed system presented in this chapter can be directly connected to a transmitter/receiver via a standard waveguide and its rugged all-metal design makes it an attractive solution for harsh environments. Further potential of the quasi-optical system and the feed structure will be discussed in the following. As described in Sections 2.3.1 and 3.2.2, the phase and amplitude performance of lenses with linear aperture is compromised when using a single movable feed. For example, the multiple-beam design presented in [39] offers excellent

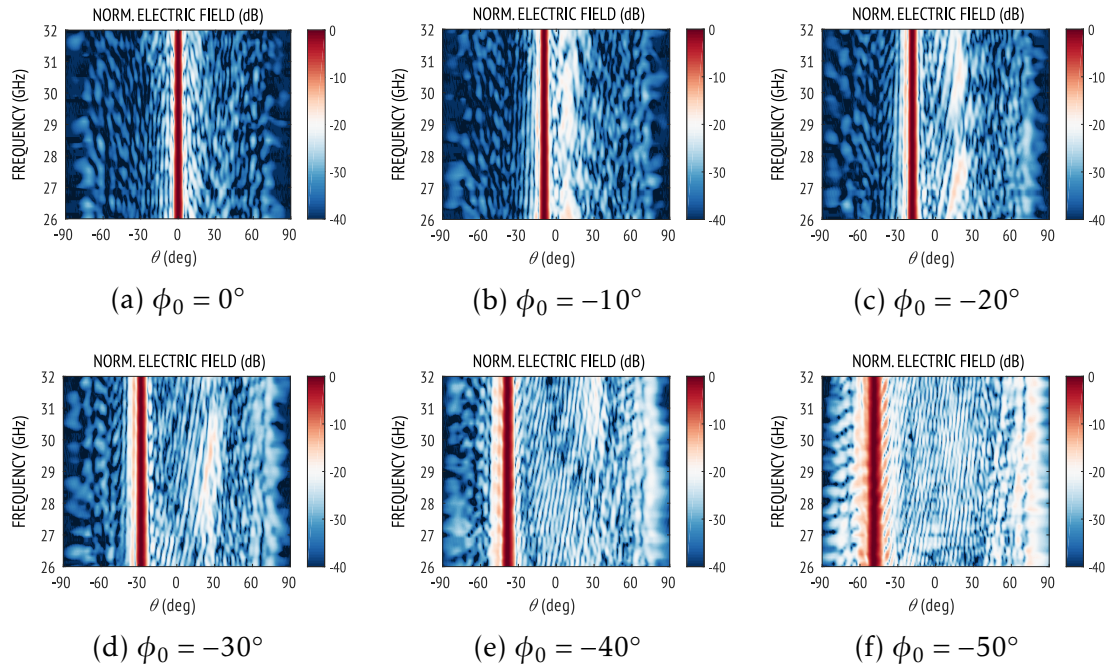


Figure 3.38: Measured H -plane radiation pattern as a function of frequency for various feed angular positions.

Table 3.2: Comparison of mechanical scanning antenna designs.

Reference	Type	Impedance bandwidth ^a	Size	Max. gain ^b	Scan range	Scan loss ^b	Max. SLL ^b
[6]	Parabolic pillbox	24 – 24.5 GHz	$13.5\lambda \times 15\lambda \times 0.1\lambda$	22 dBi	$\pm 35^\circ / 5.8$ BW	2 dB	-12 dB
[9]	Parabolic pillbox	> 26.5 – 31 GHz	$25\lambda \times 17\lambda \times 4.5\lambda$	29 dBi	$\pm 40^\circ / 6.7$ BW	2 dB	-11 dB
[62]	Modified Luneburg lens	29.5 – 32.5 GHz	$\approx 11.5\lambda \times 10\lambda \times 0.8\lambda$	15 dBi	$\pm 35^\circ$	3 dB	-10.5 dB
[66]	Rotary phase shifter	75 – 76.5 GHz	$15.7\lambda \times 15.7\lambda \times 6.4\lambda$	34 dBi	$\pm 18^\circ$	1.3 dB	-13 dB
[67]	Rotary phase shifter	57 – 65 GHz	$(8.8\lambda)^2 \pi \times 1.9\lambda$	29.3 dBi	$\pm 54^\circ$	4.3 dB	-15 dB
[98]	CTS + rotary line source	15.35 – 15.75 GHz	n.a.	31 dBi	$\pm 30^\circ / 6.8$ BW	0.5 dB	-15.4 dB
This work ^c	Continuous PPW lens	> 26 – 33 GHz	$25.4\lambda \times 21.5\lambda \times 4.9\lambda$	25.7 dBi	$\pm 35^\circ / 10.3$ BW	2.0 dB	-17 dB
This work	Continuous PPW lens	> 27.5 – 31 GHz	$26.7\lambda \times 15.9\lambda \times 9.7\lambda$	24 dBi	$\pm 49^\circ / 14$ BW	2.7/3.3 dB	-12.2 dB

^a Referring to the frequency range within which the return loss is greater than 10 dB for all scan positions.

^b Referring to the design frequency and the pattern in the plane of scan.

^c Only full-wave simulation results for a lens made of aluminum are considered.

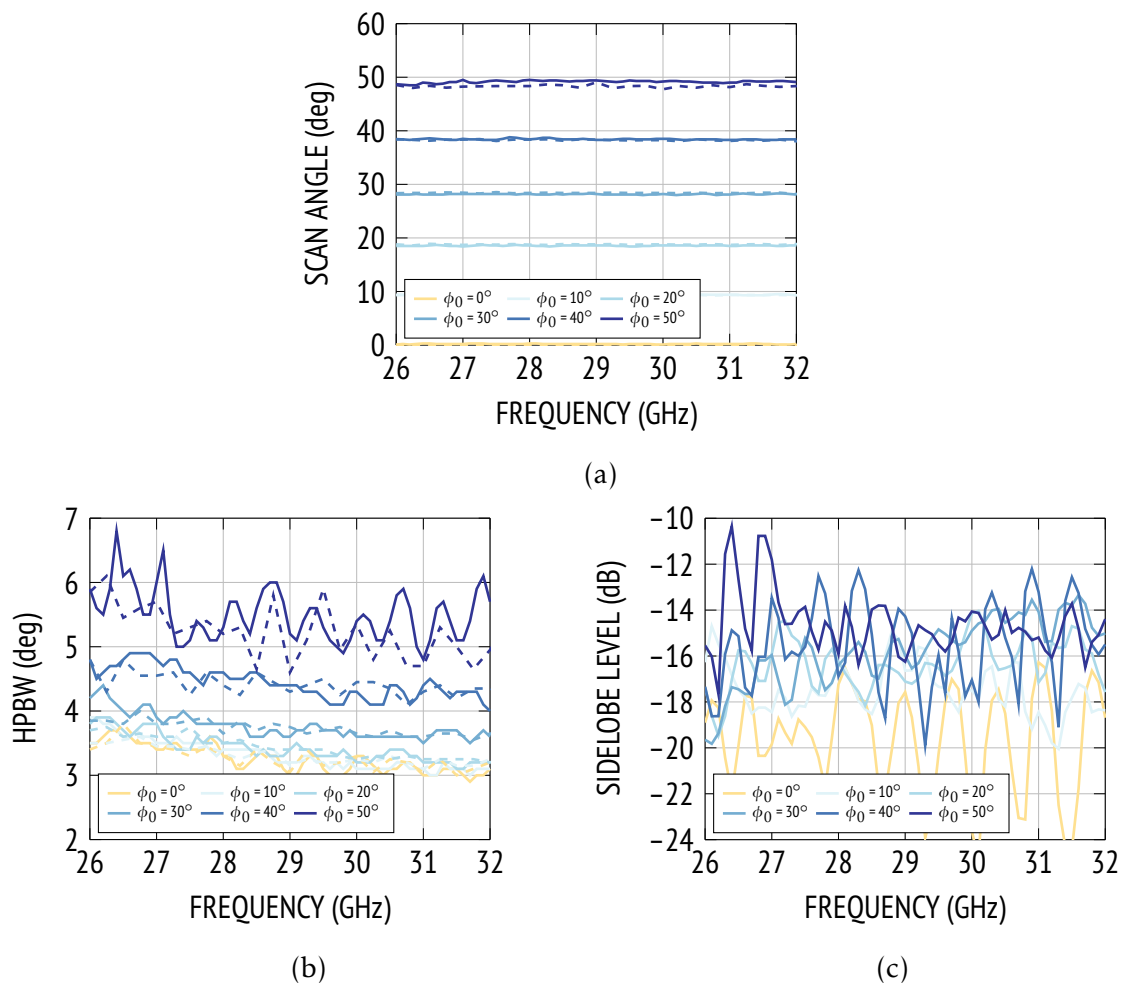


Figure 3.39: Measured (—) and simulated (--) (a) scan angle and (b) half-power beamwidth, (c) measured maximum sidelobe level in the H plane as a function of frequency.

scanning performance over a field of view of $\pm 31.5^\circ$ with scan loss lower than 0.7 dB, while the mechanical scanning lens incurs a scan loss of about 1.2 dB. As a consequence, appreciable improvement can be expected for a dual-ridge lens using multiple fixed feeds. In particular, non-circular feed curves and the freedom to rotate feeds about their axis allow a better control of the amplitude performance at extreme scan angles. Further studies are needed to assess the effect of internal reflections on the radiation pattern; iterative techniques [99] can be used for this purpose. Significant improvements in sidelobe level can be achieved with properly shaped and absorbing sidewalls [16, 17] or by employing dummy ports [18, 19].

The developed feed structure can be used for various quasi-optical systems

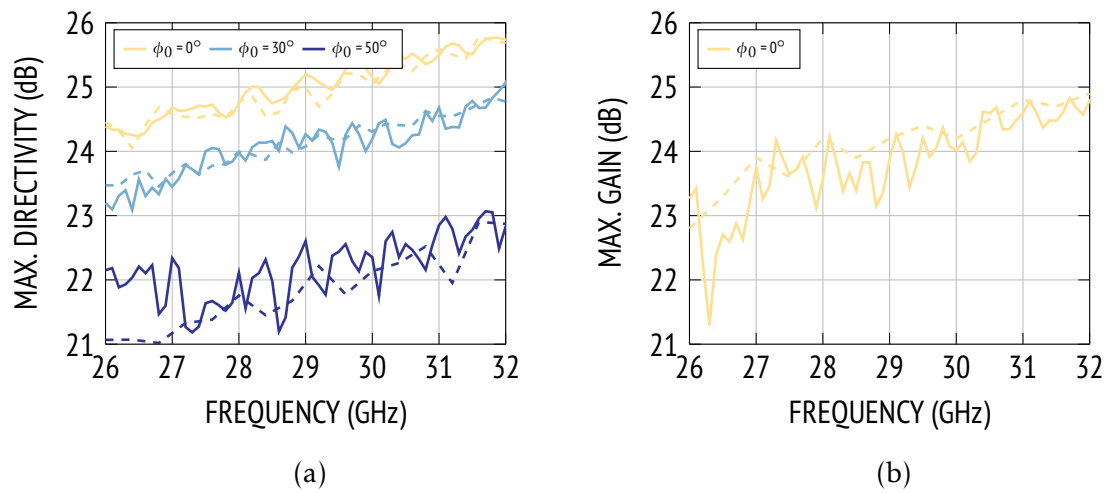


Figure 3.40: (a) Measured (—) and simulated (---) maximum directivity, (b) maximum gain.

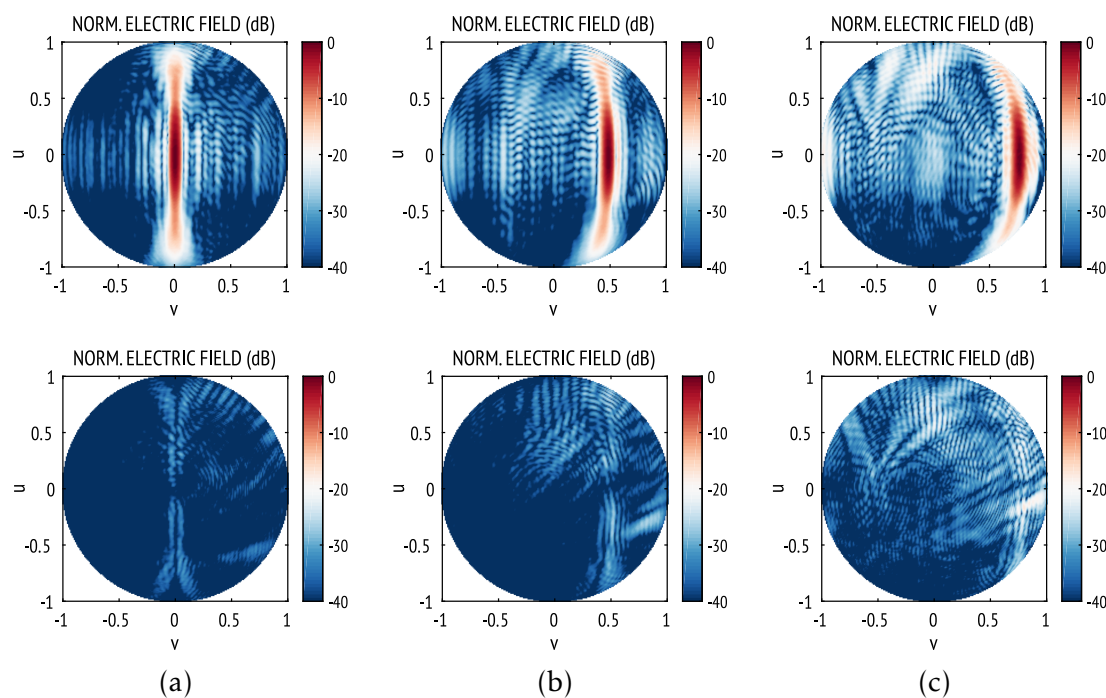


Figure 3.41: Measured 3D co- and cross-polarized pattern at 29.25 GHz for (a) $\phi_0 = 0^\circ$, (b) $\phi_0 = 30^\circ$ and (c) $\phi_0 = 50^\circ$.

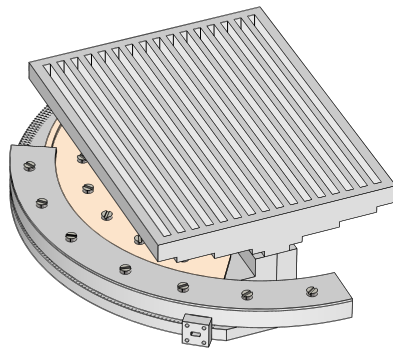


Figure 3.42: Perspective view of a mechanical scanning lens beamformer with CTS array.

with circular feed contour, such as constrained and geodesic lenses or circular pillboxes. Moreover, the concept can readily be extended to lateral feed displacement, as required for parabolic pillbox reflectors [78]. One advantage of the proposed solution over conventional rotary joint feeds is its low profile. However, the footprint of the feed system increases with the scan range. As a result, aperture blockage by movable parts becomes a problem at one edge of the coverage range. This mainly concerns lenses with circular feed contour and linear aperture. The lens beamformer presented in this section was validated using a plane flare as in [39]. In this configuration, the radiating aperture is rotated by 90° and the low-profile geometry of the feed and the quasi-optical systems is lost. Hence, the physical aperture area is relatively small compared to the footprint of the antenna, especially when considering the entire feed motion path. An attractive solution, utilizing the available space more efficiently, would be to interface the beamforming device with a continuous transverse stub array [9, 40] as illustrated in Fig. 3.42. In such a configuration, a peak gain of 30 dB or higher, as typically required for satellite terminal antennas, can be achieved while maintaining broadband performance.

3.6 Chapter Summary

In summary, a lens beamformer for continuous scanning over a wide angular range of $\pm 50^\circ$ was presented. A novel mechanical feed system, relying on the non-contact characteristic of gap waveguides, was developed. First, the feed structure was combined with a conventional continuous PPW lens for mechanical scanning over a moderate range of angles. The simulated gain loss at the design frequency

(29.25 GHz) is lower than 1.2/2.0 dB when scanning out to 30/35°. Further, the design of a dual-lens system with enhanced field of view was described. Geometrical optics and full-wave simulations predicted a maximum scan loss of 2.5 dB and sidelobe levels lower than -17 dB over a scanning range of $\pm 50^\circ$ or ± 14 beamwidths. An all-metal prototype was manufactured to validate the proposed combination of lens beamformer and gap waveguide feed system at Ka-band. Measurements showed a scan loss of 2.7 dB and 3.3 dB at the center frequency when scanning out to 50° and -50° , respectively. The worst-case sidelobes are -12 dB within the 27.5–31 GHz band. The estimated radiation efficiency ranges from 78 to 91%, depending on the feed position.

A previously developed ray-tracing tool was used to design the lens beamformer presented in this chapter. For a mechanical scanning design using a single constrained feed, the computational cost of the optimization process is reduced. The following chapter presents an extension of this method which is particularly useful for the synthesis of focal arrays involving a large number of design parameters.

CHAPTER 4

Analysis of Integrated Quasi-Optical Beamformers

As discussed in Section 1.3, the design procedure for quasi-optical systems with beam scanning capability typically relies on ray tracing. In this case, the problem is formulated through path length conditions and performance is evaluated in transmission based on the phase distribution on the aperture. If closed-form expressions for the path length errors in a fixed quasi-optical system can be derived, the feed phase center locations for minimum phase error can be readily obtained [11, 13–15]. Alternatively, an optimization routine shaping both the feed contour and the quasi-optical system can be used to achieve minimum phase error over a wide range of scan angles [34]. The same approach can be adopted for the design of continuous beamformers such as reflectors and parallel-plate waveguide lenses, provided that an efficient numerical model for the transmit case is available [35, 38]. Using phase-only optimization, the remaining task generally consists in matching the feed pattern to the contour of the quasi-optical system to provide an optimum illumination. An alternative approach is to employ a pattern-based optimization process, taking into account the effects of illumination taper and spillover with an adequate feed model. In this case, the feed size is usually fixed and the feed locations and shape of the quasi-optical system are adjusted in each iteration after comparing the computed radiation pattern with the prescribed mask. Since key design parameters, such as beamwidth and sidelobe levels are directly monitored during optimization, this method is not limited to the classical minimum-scan loss design but also well suited for shaped beam synthesis. The main disadvantage of this design approach is that optimization becomes a time-consuming process as the number of beams increases. For example, the lens beamformer presented in Chapter 3 was designed using three optimization points, sufficient for defining the re-

quired circular feed contour. However, for lens designs with MFPB operation, the number of degrees of freedom at feed level is significantly higher, making direct optimization prohibitive. As will be shown in this chapter, the analysis of quasi-optical systems in reception provides deterministic methods which greatly facilitate the design of such feed configurations.

In the first part of this chapter, a short overview of numerical techniques for the analysis of quasi-optical systems and their limitations is given. Approximate models for pillbox reflectors, Rotman lenses and continuous PPW lenses are presented, with emphasis on the receiving case. Further, the use of reciprocity for characterizing the coupling between focal-region fields and relevant feed distributions is discussed. The study of basic feed characteristics and the derivation of maximum scan-gain contours using the developed numerical procedure is described first. The approach is then extended to arbitrary incident fields and used for the design and characterization of overlapping feed clusters.

4.1 Overview of Relevant High-Frequency Techniques

Since the studied beamformers are typically more than a few wavelengths in extent, an efficient analysis requires the use of asymptotic high-frequency methods. Geometrical optics is widely used for determining the wave propagation associated with incident and scattered fields in antenna and scattering problems. In this case, the transport of energy by electromagnetic fields in an isotropic medium is assumed to take place along curved ray paths which are everywhere normal to the wavefronts. A formal way for establishing the connection between wavefronts and rays, leading to the geometrical optics field description, is the asymptotic expansion of solutions to Maxwell's equations [100]. At the interface between two different media, only the incident fields and the fields scattered toward specular directions can be described by geometrical optics; the latter are determined by Snell's laws of reflection and refraction. Geometrical optics and its extension to include diffracted rays are field-based techniques, which generally do not require the evaluation of radiation integrals for solving complex scattering scenarios. The amplitude variation of the geometrical optics field is determined by the principle of energy conservation in a tube of rays. Geometrical optics is commonly used for the analysis of quasi-optical systems in transmission. The standard method of analyzing reflector antennas is to use ray tracing to find

amplitude, phase and polarization of the field on the aperture plane and then determine the far-field radiation pattern using fast Fourier transform algorithms. Similarly, rays representing an incoming wave can be traced to the focal region of the quasi-optical system. Receive-mode analyses of paraboloidal reflectors based on geometrical optics have been carried out in [101, 102] for the determination of optimum feed distributions. However, it is well known that due to the singularities of ray optics, the classical GO field description breaks down at focal points where an infinite number of rays converge, or on caustic surfaces to which all rays are tangent. Infinite field intensities are predicted while the scattered field vanishes in a zone delimited by the caustic curve. Hence, the ray-optical approximation fails to provide a reasonable description of the focal-region field intensity in receiving quasi-optical systems [60]. To overcome this limitation, GO can be combined with a Fourier optics (FO) spectral field representation [103]. In this approach, geometrical optics is used to determine the scattered fields on an equivalent sphere centered at the focus of the quasi-optical system. The fields at any point in the image space could then be found from the equivalent currents on the specified sphere using Love's equivalence principle. Instead, using some geometrical approximations, the corresponding radiation integral can be transformed into a plane-wave spectrum representation, which provides a computationally efficient and accurate description of the received fields in a limited region of the focal plane.

Physical optics is a current-based method used extensively in electromagnetic scattering problems, and is also well-established for the analysis of antennas in reception [60, 104, 105]. High-frequency problems for which the physical optics solution becomes superior to that provided by geometrical optics are discussed in [106]. The total physical optics fields ($\mathbf{E}_{\text{tot}}, \mathbf{H}_{\text{tot}}$) generated by a source in the presence of an arbitrarily shaped object can be determined by the superposition of incident fields ($\mathbf{E}_i, \mathbf{H}_i$) and scattered fields ($\mathbf{E}_s, \mathbf{H}_s$). By definition, the incident field emanating from the source exists everywhere in space as if no scatterer was present; this differs from the geometrical optics approximation, where the wave function is discontinuous across the reflection and shadow boundaries. The scattered fields are obtained by integration of the field contributions from electric and magnetic current densities (\mathbf{J}, \mathbf{M}) established on the surface of the scatterer. Just as the actual source, these currents radiate the scattered fields as if

no obstacles were present. Moreover, they must satisfy the boundary conditions

$$\mathbf{J} = \hat{\mathbf{n}} \times \mathbf{H}_{\text{tot}} \quad (4.1a)$$

$$\mathbf{M} = -\hat{\mathbf{n}} \times \mathbf{E}_{\text{tot}} \quad (4.1b)$$

where $\hat{\mathbf{n}}$ is a unit vector normal to the surface. The method of physical optics is based on the assumption that scatterers are large compared to the wavelength and sufficiently far away from the sources, such that the incident field can be treated locally as a plane wave incident upon an infinite plane tangent to the scattering object. As a result, surface currents can be evaluated locally without the need for solving integral equations. In fact, this approximation is based on the geometrical optics field at the surface, which can be calculated using dyadic reflection and transmission coefficients derived from Fresnel's equations. In a pure reflection problem, involving only impenetrable surfaces, the scattered fields are equal to the reflected fields, and the total fields are the sum of incident and reflected fields. In a transmission problem, such as a dielectric lens, the surface is chosen such that only the transmitted fields are present at the boundary; the total fields are then equal to the transmitted fields. Usually, the resulting radiation or scattering integrals must be evaluated numerically. In fact, an asymptotic evaluation of the PO integral yields the geometrical optics fields due to stationary points which correspond to the points of specular reflection on the surface. As pointed out in [106], physical optics does not satisfy reciprocity except in the direction of specular scattering; however, it can be expected to provide a satisfactory approximation over the nearby region. This limitation can be attributed to the current approximation based on the GO fields. As a result, physical optics becomes inaccurate in regions where the scattering mechanism is not dominated by the geometrical optics currents, that is, for grazing angles of incidence, and for fields in the deep shadow region. The nonphysical discontinuity in surface current, due to the truncation of the incident fields at the shadow boundary, makes a spurious contribution to the radiation integral which may become numerically significant compared to the specular contribution. The quasi-optical systems studied in this work exhibit smooth contours with relatively large radii of curvature. Moreover, observation points generally lie in the caustic region, relatively far away from the edge of the illuminated surface. As will be shown in this chapter, the PO method provides in such cases a sufficiently accurate prediction of the received fields. The main

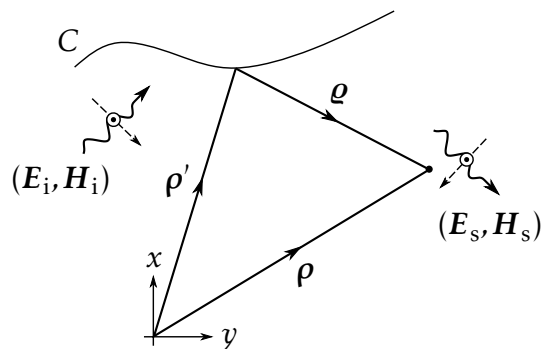


Figure 4.1: Schematic view of a two-dimensional scattering problem.

drawback of physical optics compared to the GO/FO approach is the higher computational effort associated with the evaluation of the radiation integral. However, since the structures of interest are of moderate size ($D < 30\lambda$) and can be treated as a two-dimensional problem, the resulting computation time is generally low. The application of GO and PO techniques in the analysis of different quasi-optical systems will be described in the following sections with emphasis on the receive case.

4.2 Modeling of Quasi-Optical Systems

Integrated quasi-optical systems can be realized in various ways, including shaped and layered dielectrics, reflectors, a set of transmission lines or shaped parallel-plate waveguides. Discrete delay lines and coupling elements, which are crucial in the design of multilayer structures, usually require separate analysis by means of equivalent circuit models [18]. Continuous parallel-plate structures are typically analyzed using ray-tracing techniques [25, 35, 38]. On the other hand, the focal region of most quasi-optical systems is formed by a parallel-plate cavity. As demonstrated in [6, 17, 51], the scattering and radiation in electrically large PPW structures can be adequately described by two-dimensional models. Therefore, this section is concerned with electromagnetic problems of the type shown in Fig. 4.1, assuming that only the fundamental mode is guided. As indicated, electromagnetic waves are polarized along the z axis and their propagation is confined to the xy plane. Furthermore, scatterers are defined by contours lying in the same plane, i.e., they can be assumed to be infinite in z direction.

4.2.1 Pillbox Reflector

Initial work on the receive-mode analysis of reflector antennas has been focused on the derivation of closed-form expressions for the scattered fields [104, 107]. For normal incidence, the obtained solutions provide a correction to the Airy diffraction pattern, which is valid only for large focal ratios common in optical systems. However, the derived expressions are typically limited to small angles of incidence or only valid in a limited area. As demonstrated in [60], the focal-region fields resulting from plane-wave incidence at an arbitrary angle can be studied rigorously using physical optics. In the two-dimensional case, the induced currents are approximated by the geometrical optics fields on the illuminated contour C which reduce to

$$\mathbf{J} = 2\hat{\mathbf{n}} \times \mathbf{H}_i. \quad (4.2)$$

The scattered fields at an arbitrary point $\boldsymbol{\rho}$ exterior to C are then given by [108]

$$\mathbf{E}_s(\boldsymbol{\rho}) = \frac{k\eta}{4} \int_C [\hat{\boldsymbol{\rho}} \times \hat{\boldsymbol{\rho}} \times \mathbf{J}(\boldsymbol{\rho}')] H_0^{(2)}(k\varrho) dl' \quad (4.3a)$$

$$\mathbf{H}_s(\boldsymbol{\rho}) = \frac{jk}{4} \int_C [\hat{\boldsymbol{\rho}} \times \mathbf{J}(\boldsymbol{\rho}')] H_1^{(2)}(k\varrho) dl' \quad (4.3b)$$

where $H_0^{(2)}$ and $H_1^{(2)}$ are the zero- and first-order Hankel functions of the second kind with $\varrho = |\boldsymbol{\rho} - \boldsymbol{\rho}'|$ as indicated in Fig. 4.1, and $\hat{\boldsymbol{\rho}}$ is a unit vector pointing from any point on the reflector toward the observation point; k and η are the propagation constant and intrinsic impedance of the medium. In this work, only parabolic reflectors with moderate F/D were investigated. The equivalent currents were therefore evaluated in a single step. For deep reflectors and large incident angles, further iterations may be required to account for interaction between these currents [99]. However, it has been shown in [104] that the contribution from secondary currents to the field in the caustic region is usually negligible. For electrically large reflectors, the spectral approach described in [105] may represent an attractive alternative to the evaluation of (4.3).

The geometry of the problem is depicted in Fig. 4.2. The computed electric field along the focal plane of two parabolic reflectors with equal diameter but different focal ratios is plotted in Fig. 4.3 and 4.4, respectively. The calculated results are compared with simulation results from CST Microwave Studio. It

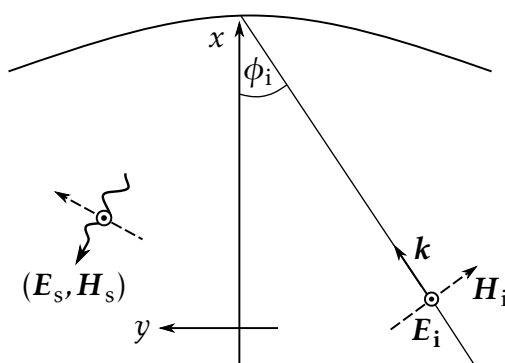


Figure 4.2: Schematic view of a receiving pillbox reflector.

can be seen that there is close agreement, even when the angle of incidence is increased and in regions of low intensity. Figure 4.5 shows the maximum-field locus of both reflectors resulting from a wide range of incident angles. Jumps in the contour occur when the field distribution exhibits a second, local maximum; taking the position between these two maxima would yield a smooth profile in 4.5(b). The contours indicate that for larger focal ratios, the axial distance of the maxima from the reflector decreases at larger scan angles, while an opposite tendency is observed for small F/D . This conclusion is also in accordance with the results reported in [60] for paraboloid reflectors.

4.2.2 Bootlace Lens

Assuming a single-layer configuration, the three most common implementations rely on coaxial lines coupled via probes to the parallel-plate cavity, microstrip lines, and vertically or horizontally polarized waveguides.

The first corresponds to the original Rotman lens design [13] and can be studied assuming that the array on the outer lens contour is formed by N isotropic receivers spaced a distance d apart. Further, the array elements are connected through lossless delay lines to their isotropic counterparts on the inner lens contour as shown in Fig. 4.6. As a result, the complex coefficients c_i defining the excitation of the omnidirectional current probes on the inner lens contour are found simply by multiplying the incident field by the phase factor e^{-jkW} , where W represents the electrical length of the delay lines. The focal-region fields are then found by superposition of weighted cylindrical waves emanating from the

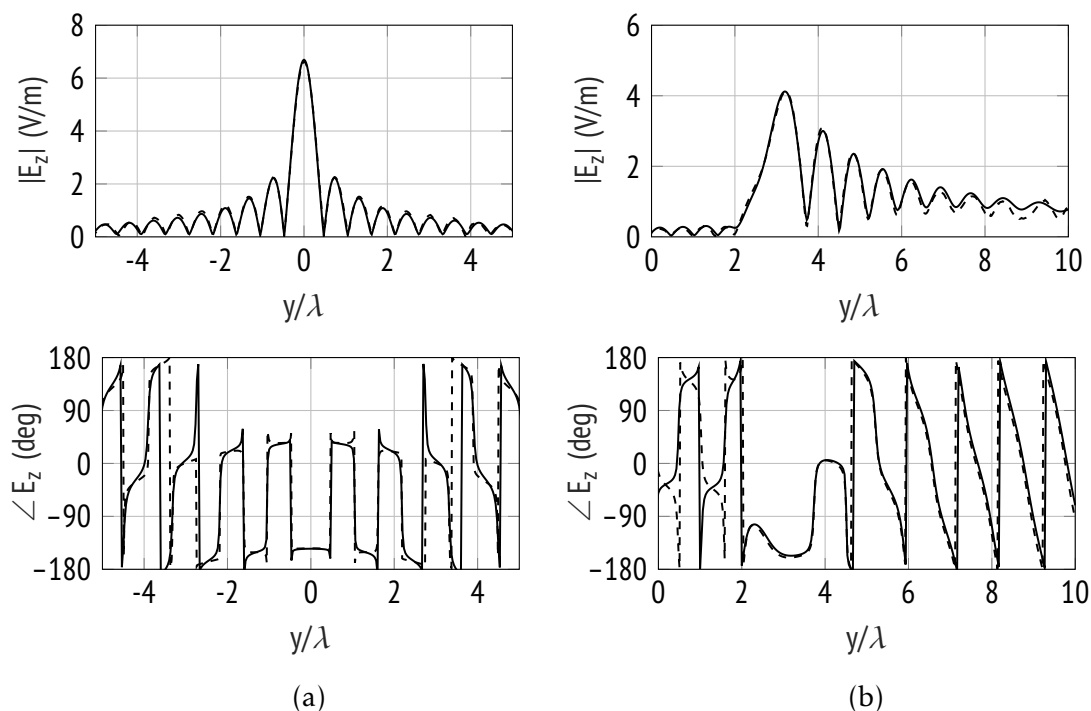


Figure 4.3: Calculated (—) and simulated (---) electric field along the focal plane of a reflector with $D = 20\lambda$, $F/D = 0.4$ for (a) $\phi_i = 0^\circ$, (b) $\phi_i = 20^\circ$.

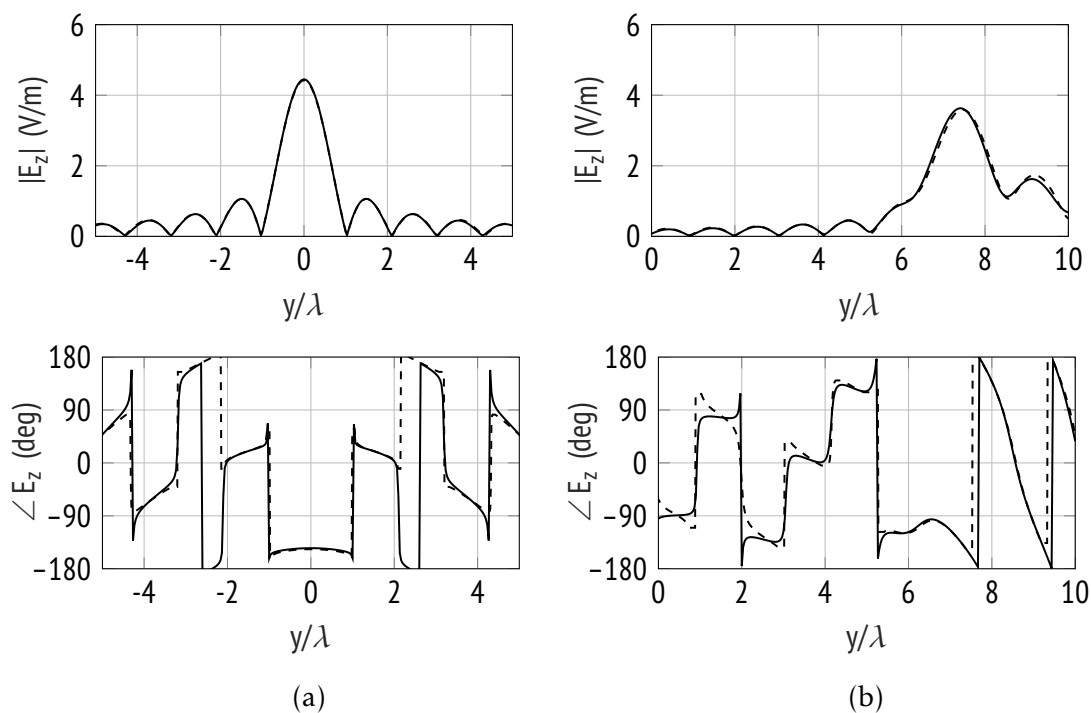


Figure 4.4: Calculated (—) and simulated (---) electric field along the focal plane of a reflector with $D = 20\lambda$, $F/D = 1.0$ for (a) $\phi_i = 0^\circ$, (b) $\phi_i = 20^\circ$.

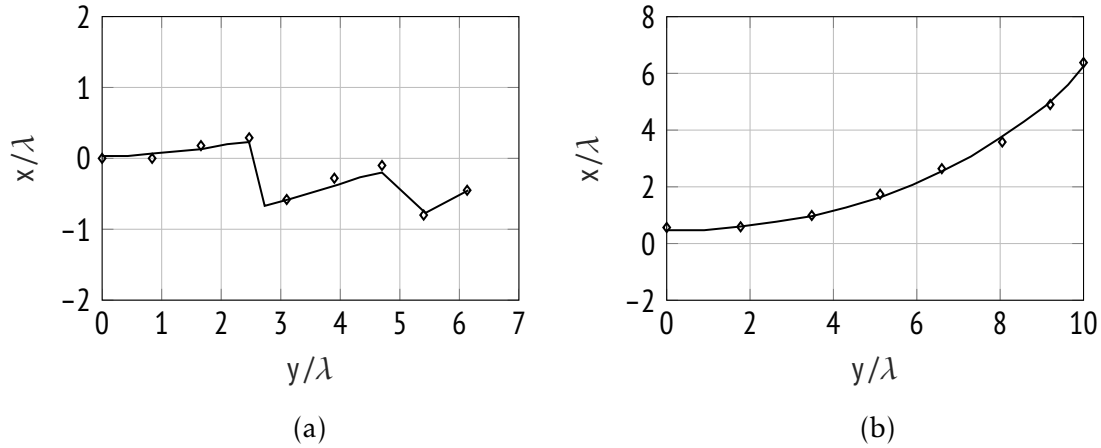


Figure 4.5: Calculated ($-$) and simulated (\diamond) maximum-field intensity points resulting from $\phi_i = [0\dots 40^\circ]$ for (a) $F/D = 0.4$, (b) $F/D = 1.0$.

probes, giving

$$\mathbf{E}_s(\boldsymbol{\rho}) = -\frac{k\eta}{4} \sum_{i=1}^N I_i H_0^{(2)}(k\rho_i) \quad (4.4a)$$

$$\mathbf{H}_s(\boldsymbol{\rho}) = -\frac{jk}{4} \sum_{i=1}^N I_i H_1^{(2)}(k\rho_i) \quad (4.4b)$$

where ρ_i is the distance between the i th probe and the observation point. Furthermore, I_i denotes the electric probe current which is related to c_i and whose amplitude can be obtained by invoking conservation of energy. In most cases, the probes do not radiate into unbounded space but are backed by a reflector. The field distribution for this case can then be found following the procedure outlined in the previous section with (4.4b) as the incident field. It is important to note that using (4.4), the mutual coupling between the probes is neglected. Integral equation methods can be used to fully account for electromagnetic interactions within the lens [51].

For constrained lenses implemented in microstrip or waveguide, two-dimensional aperture theory can be applied. Microstrip lines at the array port contour are modeled as apertures with uniform illumination, which is a reasonable approximation for tightly bound fields. For vertically polarized waveguides and sectoral horns with sufficiently small flare angle, a cosine distribution is assumed. As a result, closed-form expressions can be obtained for fields at a far-field observation point [16]. Also in this case, a more accurate description taking into account

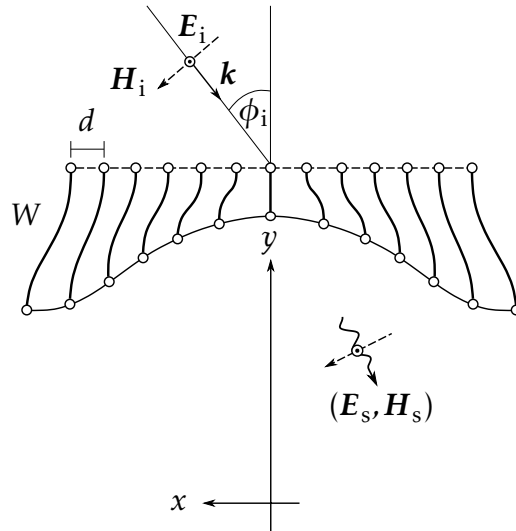


Figure 4.6: Schematic view of a receiving bootlace lens.

the coupling between nearby apertures can be achieved using integral equation techniques [17].

4.2.3 Continuous Parallel-Plate Waveguide Lens

Since scanning takes place in the H plane (xy plane), an ordinary PPW region is considered at the output of the lens. The geometry of the problem is shown in Fig. 4.2. The propagation inside the ridge can be determined using the geometrical optics technique detailed in [38]. Hence, the direction of rays entering the vertical lens section as illustrated in Fig. 4.8 is found applying Snell's law of reflection at a point P_1 on the outer lens contour. The same procedure is repeated two more times at points P_2 and P_3 , i.e., for the reflections at the top of the delay section, until the ray hits the inner lens contour at point P_4 . As indicated in Fig. 4.8, the E -plane corners are assumed to be compensated, such that all power incident upon the lens aperture is transmitted to the inner lens contour. It should be noted that the ray path depicted in Fig. 4.8 corresponds to the principal ray at normal incidence. In the general case, where the angle between the incident ray and the normal vector to the outer lens contour is nonzero, the points of reflection P_j have different y coordinates; more detailed illustrations can be found in [38].

As mentioned earlier, the ray-tracing technique is based on the assumption that rays follow straight lines inside the lens, rather than geodesic ones obeying Fermat's principle [30]. This approximation becomes worse for strongly curved

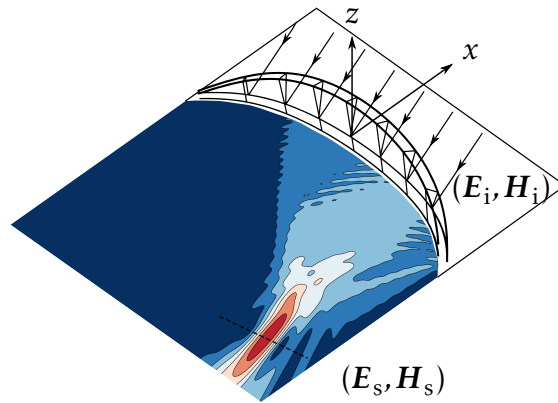


Figure 4.7: Schematic view of a receiving continuous PPW lens.

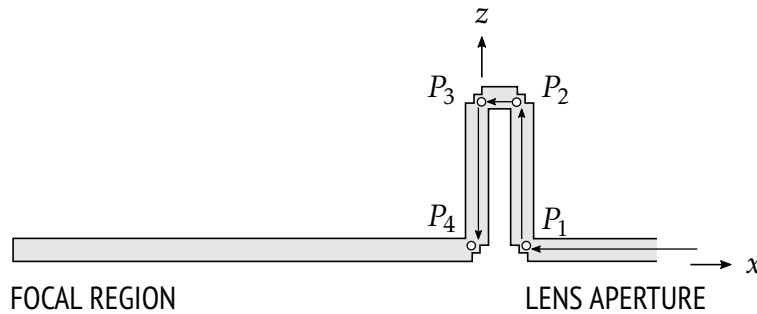


Figure 4.8: Simplified cross-sectional view of a receiving lens modeled by ray tracing.

lens contours or grazing angles of incidence. To validate this approach, a realistic lens design is considered with diameter $D = 20\lambda = 200\text{ mm}$ and $F/D = 0.7$. As in the previous chapter, the lens contour and height profile are described by tenth-order polynomials, whose coefficients were optimized for minimum RMS phase error over a moderate scan range of $\pm 35^\circ$:

$$\mathbf{a}^x = [0, -0.28, -0.165, -0.7, -0.16, 0.8]$$

$$\mathbf{a}^z = [0, -0.18, -0.14, -0.137, 0.62, -0.4].$$

The thickness of the ridge and the parallel-plate spacing are kept at $T = 2\text{ mm}$ and $H = 2\text{ mm}$, respectively. Figures 4.9 and 4.10 show the calculated tangential magnetic field along the inner lens contour, which is in good agreement with full-wave simulation results from Ansoft HFSS.

For reasons discussed in Section 4.1, further use of ray optics would fail to provide a reasonable description of the focal-region fields in the receiving problem. Instead, physical optics is used to determine these fields as scattering from

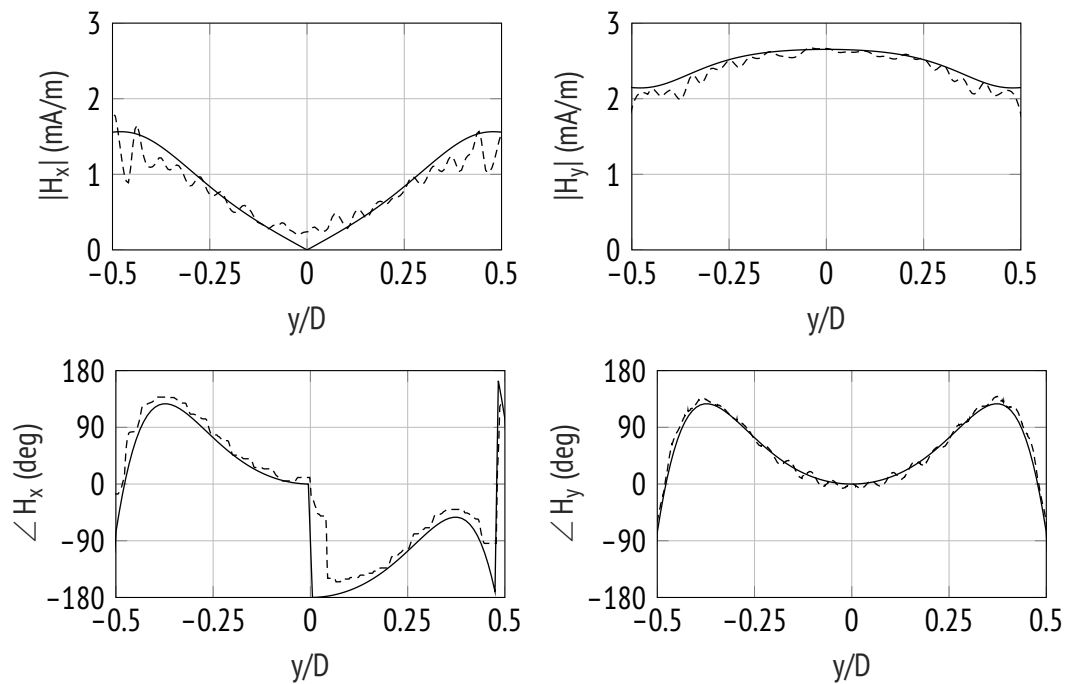


Figure 4.9: Calculated (—) and simulated (--) magnetic field along the inner lens contour for $\phi_i = 0^\circ$.

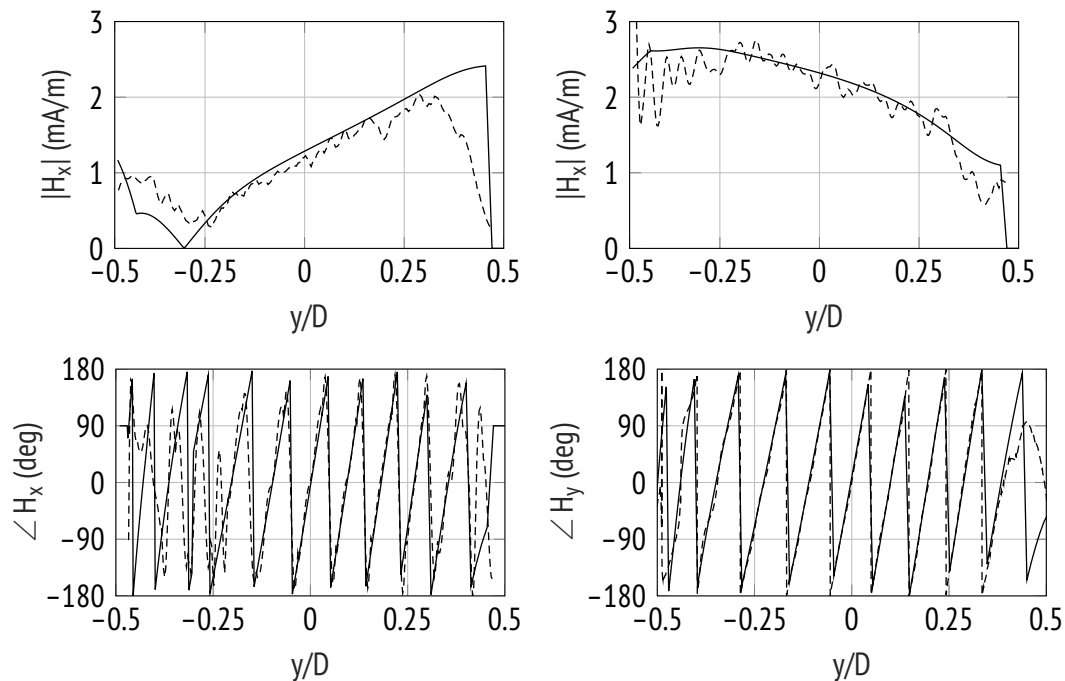


Figure 4.10: Calculated (—) and simulated (--) magnetic field along the inner lens contour for $\phi_i = 30^\circ$.

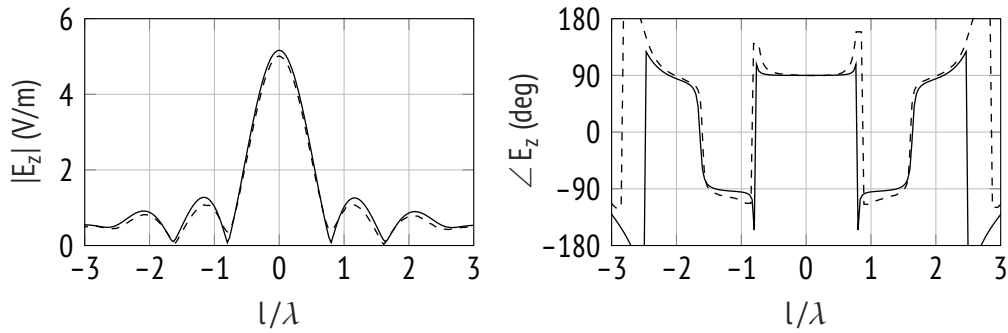


Figure 4.11: Calculated (—) and simulated (--) electric field in proximity of the focal-region maximum for $\phi_i = 0^\circ$.

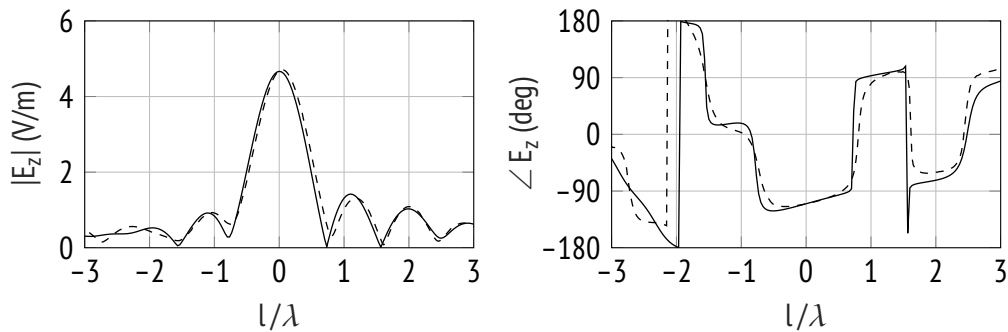


Figure 4.12: Calculated (—) and simulated (--) electric field in proximity of the focal-region maximum for $\phi_i = 30^\circ$.

equivalent currents \mathbf{J} on the inner lens contour. The electric field along a straight line passing through the focal-region maximum is shown in Figs. 4.11 and 4.12. For $\phi_i = 30^\circ$, the sampling line is tilted such that the normal vector to the line points toward the center of the lens; this is illustrated by the dashed line in Fig. 4.7. The resulting tilt angle is approximately equal to ϕ_i . The remaining phase slope around the center in Fig. 4.12 suggests that the phase front passing through the focal-region maximum is in fact not parallel to the sampling line but inclined at an angle smaller than ϕ_i . Furthermore, the field maxima defining the focal surface of the lens and the feed curve optimized for minimum RMS phase error are shown in Fig. 4.13 along with the lens contours.

4.3 Power Transfer Characterization

As demonstrated in [73, 107], the coupling between the received fields and an arbitrary feed distribution can be evaluated using the power transmission

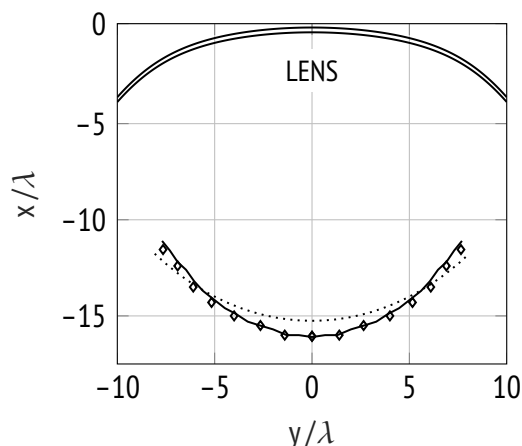


Figure 4.13: Calculated (—) and simulated (\diamond) maximum-field intensity points resulting from $\phi_i = [-35\dots35^\circ]$, feed curve optimized with a phase-only model (....).

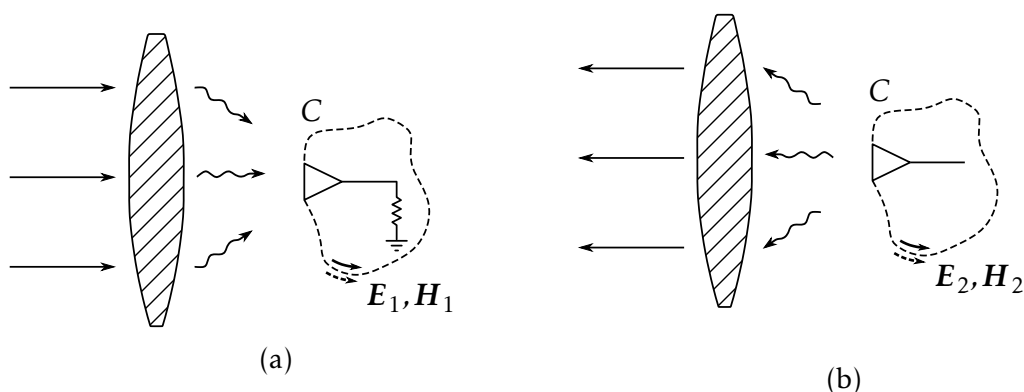


Figure 4.14: Power transfer in a quasi-optical system (a) from an incoming wave to a feed terminated with a matched load (receive mode), (b) from a radiating feed to an outgoing wave (transmit mode).

theorem introduced in [109]. The theorem was originally proposed to evaluate the power transfer between two antennas of arbitrary size, relative position and polarization. Its general formulation will be outlined briefly and the specific use for analyzing the coupling between focal-region fields and feed aperture fields will be discussed in more detail.

Consider two antennas 1 and 2 separated by a closed contour C , one radiating and the other one terminated with a matched load. With antenna 1 as transmitter and antenna 2 as receiver, the fields $(\mathbf{E}_1, \mathbf{H}_1)$ are created on C . Conversely, with antenna 2 radiating, the fields $(\mathbf{E}_2, \mathbf{H}_2)$ will exist on C . Considering the former scenario (with antenna 1 in the transmit mode), the efficiency of power transfer

between the two antennas corresponds to the ratio of power dissipated in the matched load terminating antenna 2 to the total power radiated by antenna 1. Making use of reciprocity, the transfer efficiency or T factor can be expressed as [109]

$$T = \frac{1}{16P_1P_2} \left| \oint_C [\mathbf{E}_1 \times \mathbf{H}_2 - \mathbf{E}_2 \times \mathbf{H}_1] \cdot \hat{\mathbf{n}} dl \right|^2 \quad (4.6)$$

where P_1 and P_2 denote the time-average powers radiated by antenna 1 and 2, respectively, and $\hat{\mathbf{n}}$ is the outward unit normal vector to C . If the antennas are placed at far-field distance, (4.6) reduces to the well-known Friis transmission formula expressed in terms of gains.

The theorem may be conveniently applied to analyze the power transfer from an incoming wave to an aperture antenna located in the focal region of a quasi-optical system. In this case, $(\mathbf{E}_1, \mathbf{H}_1)$ represent the fields intercepted and collimated by the beamformer which extend to the focal region and beyond, while $(\mathbf{E}_2, \mathbf{H}_2)$ are the fields produced by the aperture antenna in the transmit mode. The closed contour C may be chosen such that it includes the aperture as shown in Fig. 4.14. Furthermore, it is assumed that $(\mathbf{E}_2, \mathbf{H}_2)$ vanish on C outside the aperture. In fact, the reaction integral in (4.6) then needs to be performed only over the aperture. To analyze the performance of a receiving aperture with a given quasi-optical system, it is appropriate to define P_1 as the intercepted or collimated power rather than the total power contained in the incoming wave. Moreover, P_2 represents the power contained in the aperture fields of the feed. The transmission coefficient is maximized when the feed aperture fields are the complex conjugate of the focal region fields over the aperture S , that is, when $\mathbf{E}_2 = \mathbf{E}_1^*$ and $\mathbf{H}_2 = \mathbf{H}_1^*$. Equation (4.6) then reduces to [107]

$$T = \frac{1}{4P_1P_2} \left| \int \operatorname{Re} \{ \mathbf{E}_1 \times \mathbf{H}_1^* \} \cdot d\mathbf{S} \right|^2 \quad (4.7)$$

4.4 Single-Feed Study

As discussed in Chapter 2.1, the design of feed systems is often concerned with the inevitable trade-off between sidelobe levels and beam crossover. However, when taking the liberty of studying feeds individually, it is of primary interest to determine their optimum dimensions, position and orientation for achieving maximum gain or a certain pattern shape at a given scan angle. The numerical

results presented in the following were obtained using the power transmission theorem expressed in (4.6). The methods described in Section 4.2 were used to determine the focal-region distribution for a single incident plane wave. Given the wide use of flared H -plane sectoral horns in integrated quasi-optical beamformers [8, 13, 18, 39], a TE_{10} -mode aperture field distribution with quadratic phase error $k\delta$ [110] was assumed for the feeds, i.e.,

$$\mathbf{E}_2(y) = E_0 \cos(\pi y/a) e^{-jk\delta(y)} \hat{\mathbf{z}} \quad (4.8a)$$

$$\mathbf{H}_2(y) = -\frac{E_0}{\eta} \cos(\pi y/a) e^{-jk\delta(y)} \hat{\mathbf{y}} \quad (4.8b)$$

where a is the width of the horn aperture.

4.4.1 Pillbox Reflector

Two reflectors of diameter $D = 20\lambda$ with $F/D = 0.4$ and 1.0 were investigated. Figure 4.15 shows the maximum scan-gain contours of three different feeds for a scan range up to 40° . By reciprocity, the contour of the isotropic feed corresponds to the maximum-field locus shown in Fig. 4.5. It should be noted that the specified edge taper refers to the case where the feed is placed at the focal point of the reflector and that feed apertures are oriented parallel to the focal plane (y axis) up to this point. It can be seen that for lower F/D , the contours approach the Petzval surface of the reflector described by the equation [59]

$$x = -\frac{y^2}{2F}, \quad (4.9)$$

which corresponds to another parabola of half the focal distance with its vertex at the focal point of the reflector. For larger F/D the optimum feed contours lie closer to the focal plane as the illumination taper increases. Moreover, the optimum position of an on-axis isotropic feed does not exactly lie on the focal point but is slightly offset toward the parabola. This means that phase error losses due to defocusing are compensated by the decrease of spillover losses, i.e., a larger portion of the uniformly radiated power is intercepted by the reflector. The calculated transfer efficiency of several relevant feed types is shown in Fig. 4.16 as a function of the number of beamwidths scanned. The following configurations were considered:

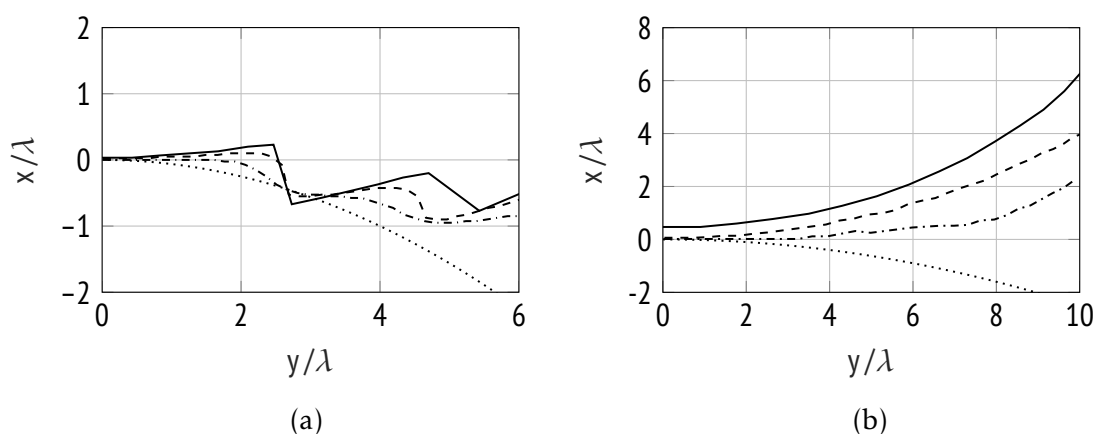


Figure 4.15: Comparison of Petzval surface (....) and maximum scan-gain contours of an isotropic feed (—) and feeds with 10 dB (--) and 20 dB edge taper (-.-) for (a) $F/D = 0.4$, (b) $F/D = 1.0$.

- Feed 1: 10 dB edge taper, aperture kept parallel to the focal plane, placed on the focal plane.
- Feed 2: 10 dB edge taper, aperture aiming at the vertex, placed on optimal contour.
- Feed 3: 10 dB edge taper, aperture kept parallel to the focal plane, placed on optimal contour.

As is well known, an edge taper of about 10 dB corresponds to the standard optimal illumination for central feeds, offering the best trade-off between taper and spillover efficiency [111, pp. 427–428]. For $D = 20\lambda$, this illumination yields a half-power beamwidth (HPBW) of 3° . Feed 1 is relevant to the case of a mechanical scanning pillbox system using a single movable feed. Feed 2 refers to the case of multiple fixed feeds, whose positions and orientations can be chosen almost independently. Feed 3 is shown for comparison. As expected, the 10-dB edge taper feed yields a transfer efficiency somewhat greater than 0.8 when placed at the focus; for the on-axis configuration T is synonymous with the more common term aperture efficiency. Furthermore, it can be seen that for lower F/D , the transfer efficiency cannot be significantly improved by axial displacement or rotation of the feed. Hence, the scan performance in a mechanical feed system is not compromised compared to the fixed-feed case. Due to the relatively flat scan contours, tilting the feed aperture may complicate the integration of multiple feeds. Figure 4.16(a) shows that for low F/D , a higher T is in fact obtained when keeping the feed aperture parallel to the focal plane. From a transmit viewpoint,

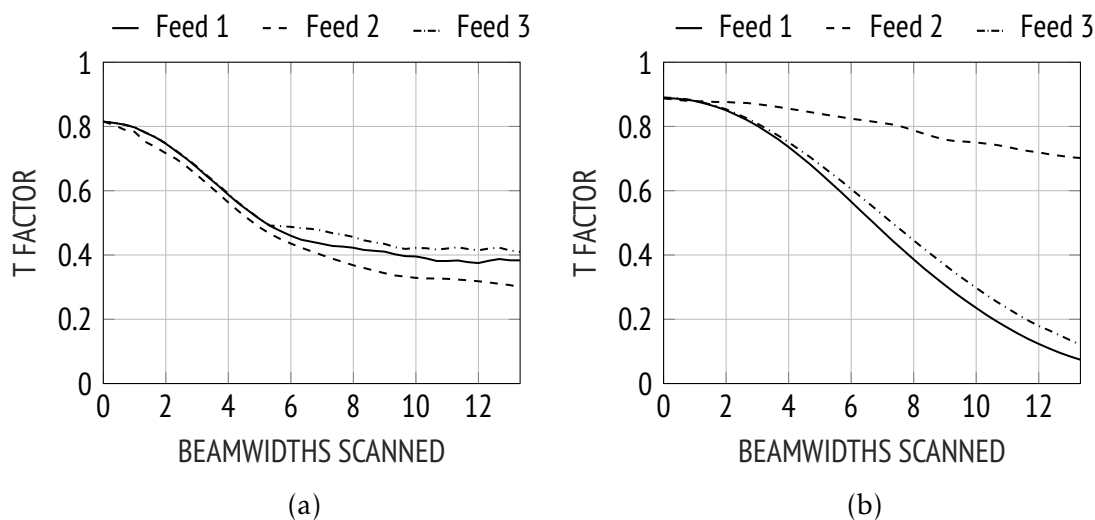


Figure 4.16: Maximum T factor with different feed configurations for (a) $F/D = 0.4$, (b) $F/D = 1.0$.

this may seem counterintuitive since reorienting the feed at larger scan angles reduces spillover losses and leads to a more symmetric illumination. Nevertheless, this result is in agreement with the conclusions in [60] and can be attributed to the fact that the equiphasic surfaces in the neighborhood of the focal-region maxima are essentially parallel to the focal plane. As seen from Fig. 4.16(b), for feeds placed along the focal plane of a reflector with larger F/D the transfer efficiency decreases rapidly as the angle of incidence is increased. From a receive perspective this is readily understood by noting that the focal-region maxima move toward the reflector as shown in Fig. 4.15(b). However, it can be seen that even when placing the aperture closer to the maximum (Feed 2), no significant improvement is achieved. Examining the focal-region distribution for large angles of incidence shows that the phase front passing through the maximum is inclined at an angle of about $-\phi_i$. As a consequence, T can be maximized by properly rotating the feed aperture. This effect is far more intuitively understood from a transmit viewpoint and purely geometrical considerations: for larger F/D the lateral displacement required for a certain scan angle increases, leading to asymmetric illumination and excessive spillover if the feed is not tilted toward the center of the reflector. Furthermore, a feed displaced by $D/2$ along the focal plane would produce a beam at about $\tan^{-1}(1/(2F/D)) \approx 27^\circ$ (neglecting the beam deviation factor). Larger scan angles can be achieved by reducing the axial distance to the reflector. Figure 4.16 also indicates the limited scanning performance of parabolic reflectors, especially for small F/D where the effect of

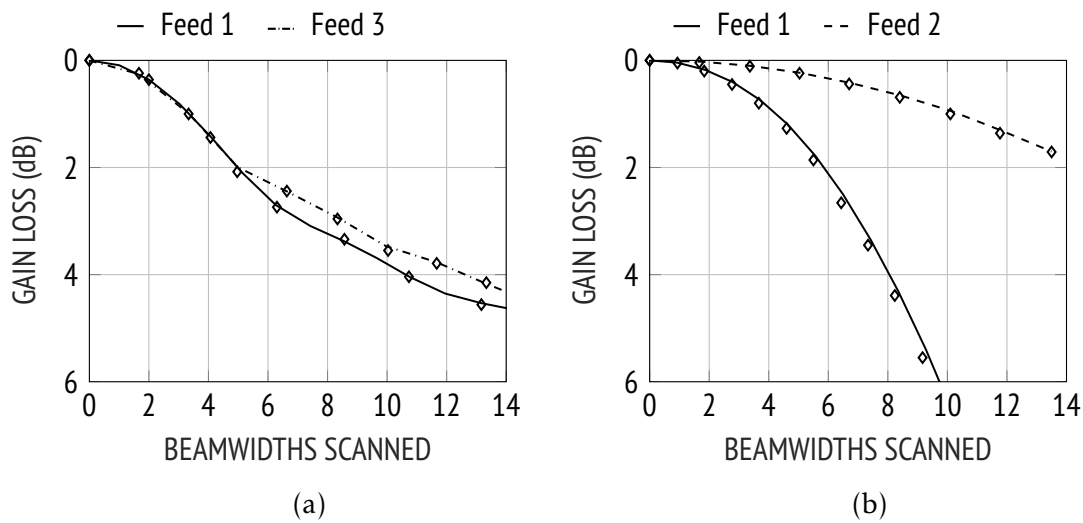


Figure 4.17: Calculated and simulated (\diamond) gain loss versus beamwidths scanned for (a) $F/D = 0.4$, (b) $F/D = 1.0$.

phase errors is more severe. This is also demonstrated by the gain loss shown in Fig. 4.17 for different feed configurations. It should be noted that the effect of aperture blockage has been neglected in the calculation of the corresponding radiation patterns; this is a reasonable approximation for double-layer pillbox systems.

4.4.2 Rotman Lens

A classical Rotman lens comprising $N = 41$ array elements spaced $d = \lambda/2$ apart ($D = 20\lambda$), with off-axis focal points at $\alpha = 30^\circ$ was investigated first. The ratio of off- to on-axis focal distance was set to the optimum value of $\beta = 0.88$, while F_1 was chosen such that $\zeta_{\max} = 0.6$ ($F/D \approx 0.83$). The basic lens model employing omnidirectional probes was considered. The computed maximum-field locus for angles of incidence up to $\pm 40^\circ$ is plotted in Fig. 4.18(a) with all coordinates normalized by the on-axis focal distance. It can be seen that in this optimal configuration, the contour nearly coincides with the focal arc defined in [13]. This result is to be expected with isotropic array ports where the received fields are dominated by the phase performance of the lens.

In addition, a lens design for extended scanning range was investigated. The angular position of the off-axis focal points was set to $\alpha = 60^\circ$ and a suboptimal value of $\beta = 1.0$ was selected such that inner lens profile and focal arc are properly arranged, i.e., without any of the contours being enclosed by the other.

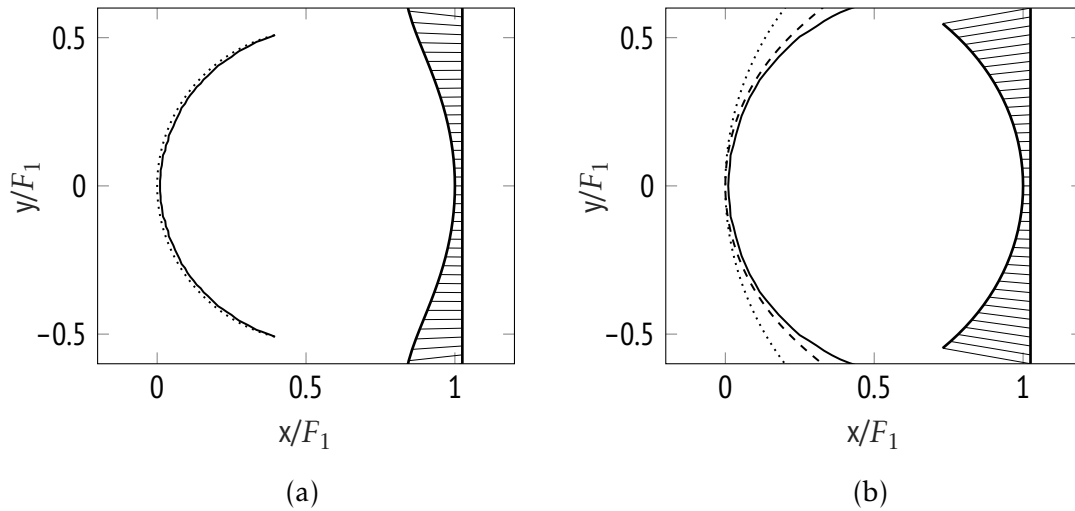


Figure 4.18: Original focal arc [13] (....), maximum-field locus (—) and improved focal curve [15] (--) of (a) original Rotman lens design, (b) lens design for enhanced scan range.

The maximum-field locus for angles of incidence up to $\pm 50^\circ$ is shown in Fig. 4.18(b). The calculated curve deviates significantly from the original focal arc [13]; a higher but still acceptable degree of curvature can be observed. As seen from the figure, a similar improved focal curve is obtained when following the analytical design procedure detailed in [15]. The shown curve has been derived by imposing zero phase error at array elements with index 5 and 36. The improvement over the original focal arc is demonstrated by the RMS phase error shown in Fig. 4.19. It can be seen that the determined maximum-field locus allows a significant reduction in phase error; however, best phase performance is achieved using the analytically derived feed curve. This suggests that, as with the reflector considered in the previous section, phase error losses due to defocusing can be compensated to a small extent by amplitude-related effects. The T factor for a 10-dB edge taper feed pointing toward the lens apex is shown in Fig. 4.20. For the scan angles considered here, the maximum-gain contour of the feed, not shown in Fig. 4.18(b), is practically coincident with the maximum-field locus. For simplicity, the effect of a reflector backing the probes on the field distribution was not considered in this study. However, P_1 used in (4.6) has been defined by the total power flow in negative x direction. It can be seen that at large scan angles, about 30% more power can be intercepted on the optimum contour when compared to the classical focal arc. The improvement is also apparent from the radiation patterns in Fig. 4.20(b). Since the two configurations are symmetric,

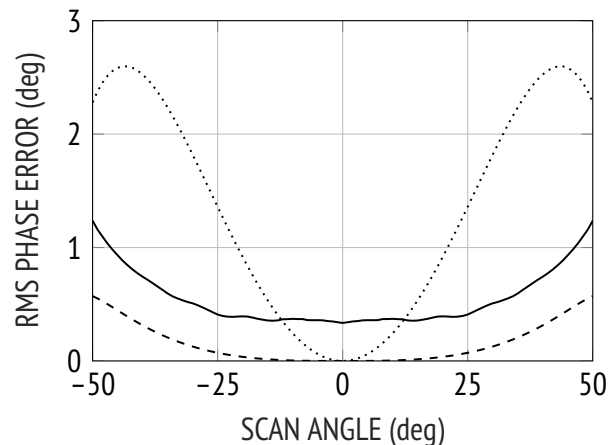


Figure 4.19: RMS phase error for original focal arc [13] (····), maximum-field locus (—) and improved focal curve [15] (---).

only half of the scanning range is plotted for each case. It can be seen that when scanning to 50° , a gain reduction of more than 4 dB and sidelobe levels as high as -8 dB are incurred with the original focal arc. The optimal feed curve results in gain losses lower than 2.4 dB and sidelobe levels below -12 dB.

4.5 Feed Cluster Synthesis

When considering a single incident plane wave as in the previous section, the resulting radiation patterns are naturally accompanied by relatively high sidelobes. Therefore, a more generalized approach is needed for most practical designs, where a set of pattern requirements has to be considered. This is typically accomplished by representing the radiated fields, associated with the desired beam pattern, as an angular spectrum of plane waves. One practical approach is to evaluate the spectrum asymptotically [112, pp. 22–27]. The singularity at the transition from the visible to the invisible region of the spectrum can be overcome using an adequate windowing function. In the case of a continuous PPW lens, ray tracing is then performed iteratively using the complex amplitudes of the plane-wave expansion to find the field distribution along the inner lens contour. As described previously, the contour maximizing T for a given feed could then be determined in a rigorous manner via reciprocity. This section, however, focuses on fixed feed arrangements used for the synthesis of overlapping clusters. An extension of the method described in Section 4.3 to the determination of optimal cluster excitations will be presented in the following.

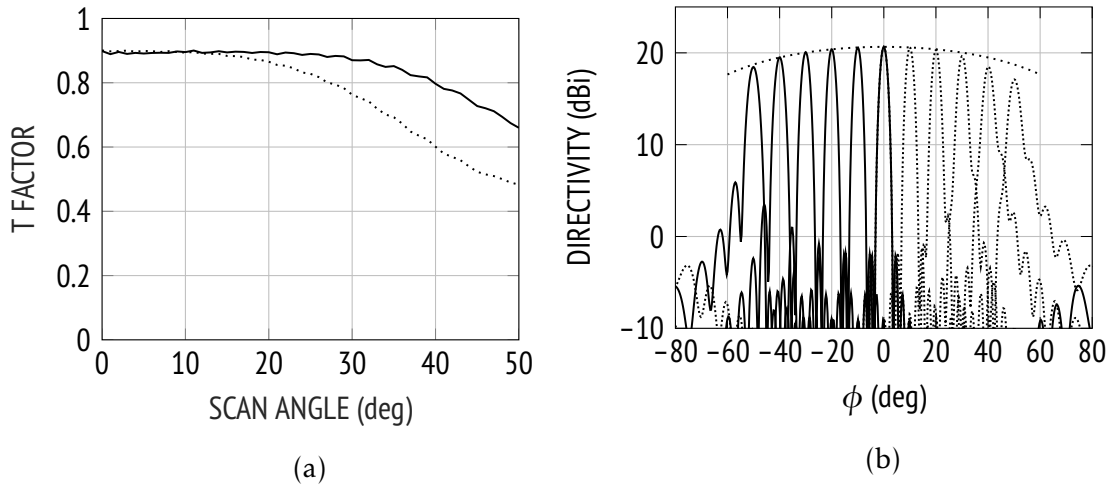


Figure 4.20: Comparison of original focal arc [13] (····) and optimal contour of 10-dB edge taper feed (—) in terms of (a) T factor, (b) radiation patterns.

4.5.1 Numerical Procedure

To determine the coupling between received fields and a cluster distribution, (4.6) needs to be evaluated for every feed element. With $(\mathbf{E}_r, \mathbf{H}_r)$ denoting the focal-region fields, the transfer efficiency can then be expressed as

$$T = \frac{|\sum_j c_j \alpha_j|^2}{4P_r [\sum_j |c_j|^2 \beta_j]} \quad (4.10)$$

with

$$\alpha_j = \int (\mathbf{E}_r \times \mathbf{H}_j - \mathbf{E}_j \times \mathbf{H}_r) \cdot d\mathbf{S}_j \quad (4.11)$$

and the time-average power

$$\beta_j = \text{Re} \left\{ \int (\mathbf{E}_j \times \mathbf{H}_j^*) \cdot d\mathbf{S}_j \right\} \quad (4.12)$$

associated with the fields $(\mathbf{E}_j, \mathbf{H}_j)$ on the feed aperture S_j . Furthermore, P_r is the total power contained in the received fields and c_j the complex weight of the j th feed. Equation (4.10) can be transformed into matrix notation

$$T = \frac{1}{4P_r} \frac{\mathbf{c}^H \underline{\underline{\mathbf{A}}} \mathbf{c}}{\mathbf{c}^H \underline{\underline{\mathbf{B}}} \mathbf{c}} \quad (4.13)$$

with $\underline{\underline{A}}$ being a Hermitian matrix given by

$$A_{jk} = \alpha_j^* \alpha_k \quad (4.14)$$

and $\underline{\underline{B}}$ being a diagonal matrix with

$$B_{jj} = \beta_j. \quad (4.15)$$

As demonstrated in [73], the excitation vector yielding maximum power transfer is given by

$$\mathbf{c} = \underline{\underline{B}}^{-\frac{1}{2}} \mathbf{d}_m \quad (4.16)$$

where \mathbf{d}_m is the eigenvector corresponding to the dominant eigenvalue of the matrix

$$\underline{\underline{D}} = \underline{\underline{B}}^{-\frac{1}{2}} \underline{\underline{A}} \underline{\underline{B}}^{-\frac{1}{2}}. \quad (4.17)$$

4.5.2 Cluster Example

The approach outlined above is used to synthesize overlapping feed clusters for the parallel-plate lens of Section 4.2.3. To allow for a quick comparison with full-wave simulations, the radiation pattern resulting from a cosine amplitude distribution along the aperture was considered. For a main beam at broadside, the visible spectrum can be expressed analytically by [113, p. 21]

$$F_z(k_y) \propto K \frac{\cos(k_y D/2)}{\pi^2 - (k_y D)^2} \quad (4.18)$$

where $k_y = k \sin \phi$ and K is a factor depending on the time-average power contained in the radiated fields. Using the weights of (4.18) to define the incident fields, the focal-region maximum moves about $\lambda/2$ toward the lens compared to the case of uniform illumination. The electric field along a straight line passing through the maximum is plotted in Fig. 4.21. The tapered illumination introduces a smooth aperture stop and, as expected, a broader focal-region pattern is obtained.

First, a single feed placed on the focal plane is considered. The transfer efficiency as a function of the feed size is shown in Fig. 4.22. A two-port simulation model is used to verify the calculated results. With port 1 representing the normally incident wave at the lens aperture and port 2 representing the feed

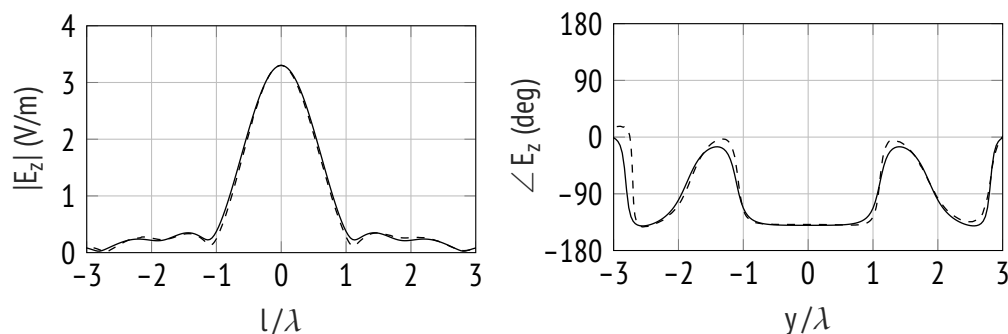


Figure 4.21: Calculated (—) and simulated (--) focal-region field for $\phi_i = 0^\circ$ with cosine illumination.

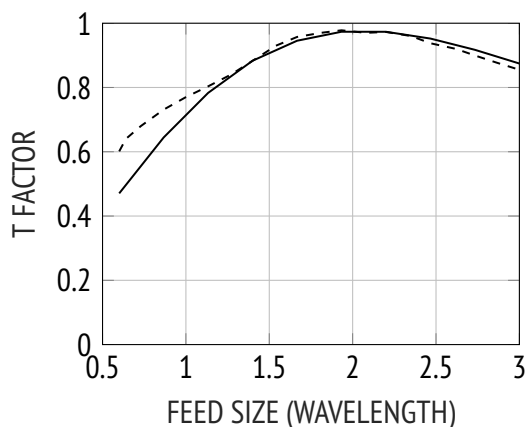


Figure 4.22: Calculated (—) and simulated transfer efficiency (--) versus feed size.

aperture, the simulated T factor is equivalent to $|S_{21}|^2$. As expected, the coupling is maximized for a feed size of 2λ , where the TE_{10} -mode aperture fields most effectively match the focal-region distribution of Fig. 4.21. For feeds larger than one wavelength, the calculated results agree well with full-wave simulations. However, a relative error of more than 15% occurs for apertures smaller than λ . This can be attributed to the assumption of vanishing fields outside the aperture with the feed in transmit mode. To illustrate this effect, Fig. 4.23 shows the simulated tangential fields along the aperture plane S for feeds of size 0.7λ and 2λ . It can be seen that for the smaller feed, the assumed magnetic field distribution differs significantly from the simulated one. This difference can be attributed to the diffraction at the aperture edges [113]. To verify the validity of the numerical procedure, the tangential fields over a sufficiently large portion of the aperture plane were extracted from full-wave simulations of an aperture

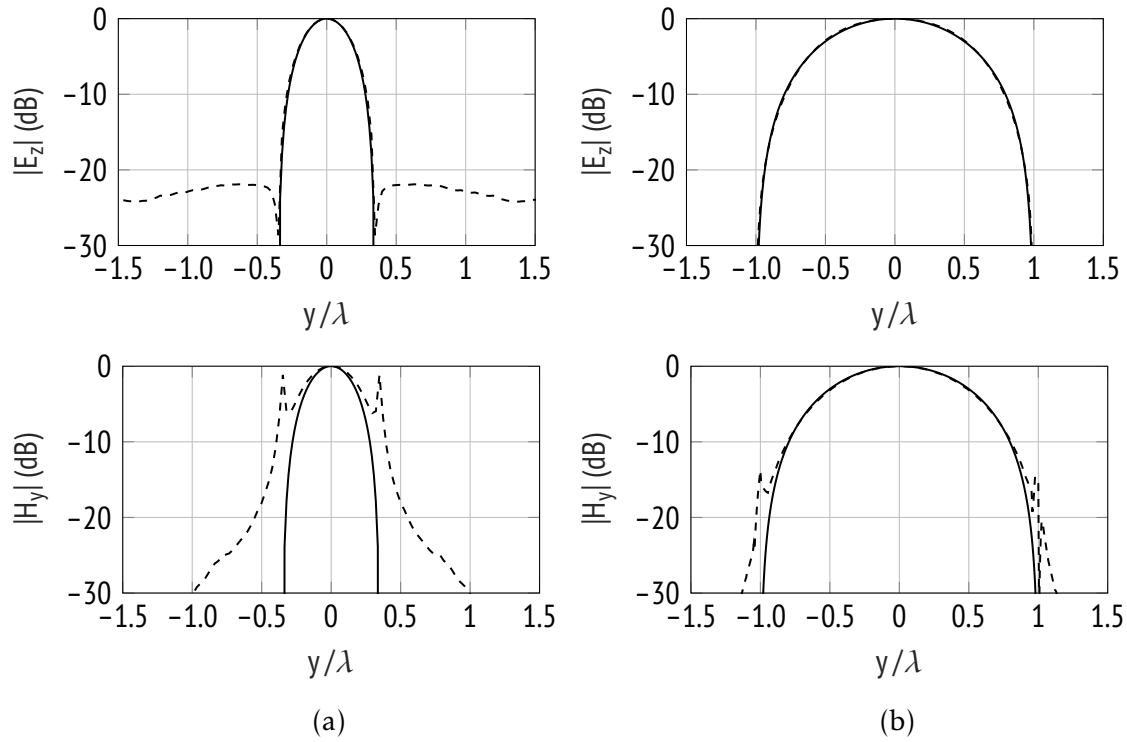


Figure 4.23: Comparison of the assumed field distribution (—) and the simulated tangential fields (--) on the aperture plane for a feed of (a) 0.7λ , (b) 2λ .

of 0.7λ in an infinite PPW environment. Using the imported fields to evaluate (4.10), the relative error with respect to the simulated transfer efficiency is less than 0.5%. In general, it can be expected that the fields transmitted by the feed inside the lens may differ from those transmitted into free space. However, since the E -plane corners inside the simulated delay section (see Fig. 4.8) are optimized and absorbing boundary conditions are employed at the sidewalls of the lens, the effect of internal reflections on the aperture plane distribution can be neglected.

Next, a cluster of feeds approximating the optimal feed distribution ($a_{\text{opt}} = 2\lambda$), is investigated. A trio of one-third apertures ($3 \times 0.67\lambda$), similar to the configuration reported in [49], is considered. It should be noted that in the present case, a pair of one-half apertures as presented in [49] does not provide adequate sampling. This is readily apparent from the primary pattern, exhibiting large secondary lobes that are only partly intercepted by the lens, while a significant part is lost as spillover. The assumed field distribution is shown in Fig. 4.24(b).

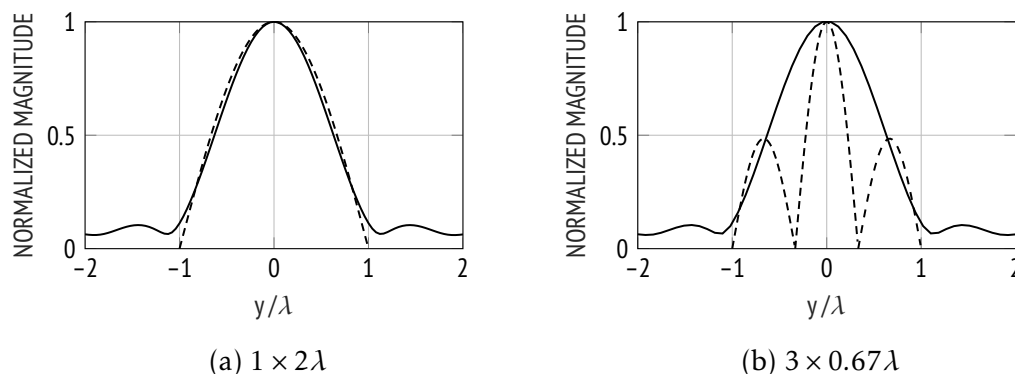


Figure 4.24: Magnitude of the received electric field (—) and the assumed amplitude distribution of the feed system (--).

The amplitude of the exterior feeds with respect to that of the central feed can be found using (4.16). Since the phase of the received field is approximately constant within $-\lambda < y < \lambda$ (see Fig. 4.21), the cluster elements are excited in-phase. It should be noted that in the present case, feeds of 0.67λ provide focal-plane sampling for complete coverage, with approximately -3 dB of beam crossover when excited individually [114]. Further, full-wave simulations of the feed cluster predict a mutual coupling below -24 dB for adjacent feeds of 0.67λ . The transfer efficiency associated with the different feed distributions and the received field is obtained using (4.13). The optimal cluster weights along with the resulting T factor are given in Table 4.1. For electrically small feed apertures, the discrepancy between calculated and simulated transfer efficiency is significant. As in the case of a single feed, this difference is due to the assumption of vanishing fields outside the feed apertures. The simulated cluster distribution is shown in Fig. 4.25 compared with the assumed field distribution for the calculated weights listed in Table 4.1. Also in this case, the deviation of the magnetic field magnitude is appreciable. As a result, the absolute value of the calculated transfer efficiency does not allow direct conclusions on the quality of the resulting radiation pattern. However, the derived complex weights agree reasonably well with the simulated ones. Figure 4.26 shows the resulting amplitude distribution along the inner lens contour for the calculated cluster weights. The normalized secondary patterns are plotted in Fig. 4.27 compared with the desired pattern of an in-phase aperture of $D = 20\lambda$ with cosine taper. The achieved radiation performances are summarized in Table 4.2. For the feed cluster, both the calculated weights and the ones extracted from full-wave simulations are considered. Simulation results show a difference of 0.15° in

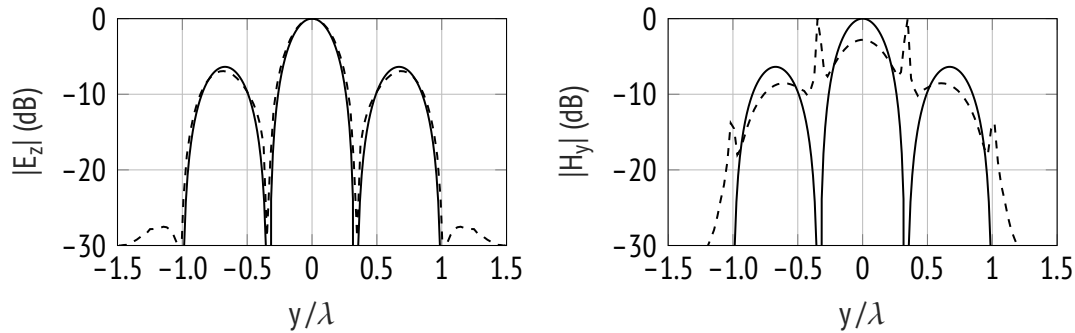


Figure 4.25: Comparison of the assumed field distribution (—) and the simulated tangential fields (--) on the aperture plane of a cluster with $3 \times 0.67\lambda$ elements.

Table 4.1: Maximum transfer efficiency and optimal cluster weights (calculated/simulated).

Feed	Amplitude $ c $	Phase $\angle c$	Transfer efficiency
$1 \times 2\lambda$	—	—	0.98/0.97
$3 \times 0.67\lambda$	$[0.48, 1, 0.48]/$ $[0.41, 1, 0.41]$	$[2^\circ, 0^\circ, 2^\circ]/$ $[3^\circ, 0^\circ, 3^\circ]$	0.76/0.91

beamwidth and 1 dB in sidelobe level for these excitations.

To synthesize feed clusters for a multiple-beam antenna, the above procedure is repeated for different incident fields, representing the desired radiation pattern at various scan angles, while considering an entire set of feeds placed along the focal curve. The above feed configurations are considered for a scan range of $\pm 35^\circ$. The feed contour is taken to be the one that maximizes T for a feed of 2λ and is therefore derived numerically. As with the Rotman lens of Section 4.4.2, this contour turns out to be practically coincident with the maximum-field locus. As shown in Section 2.1, the orthogonal spacing for a cosine illumination

Table 4.2: Comparison of pattern mask and synthesized patterns (calculated/simulated).

	HPBW ($^\circ$)	SLL (dB)	Spillover efficiency (%)
Pattern mask	3.44	-23	100
$1 \times 2\lambda$	3.34/3.45	-20.2/-21.2	99/99
$3 \times 0.67\lambda$ (calculated c)	3.60/3.69	-21.2/-21.6	98/99
(simulated c)	3.40/3.54	-20.6/-20.6	96/98

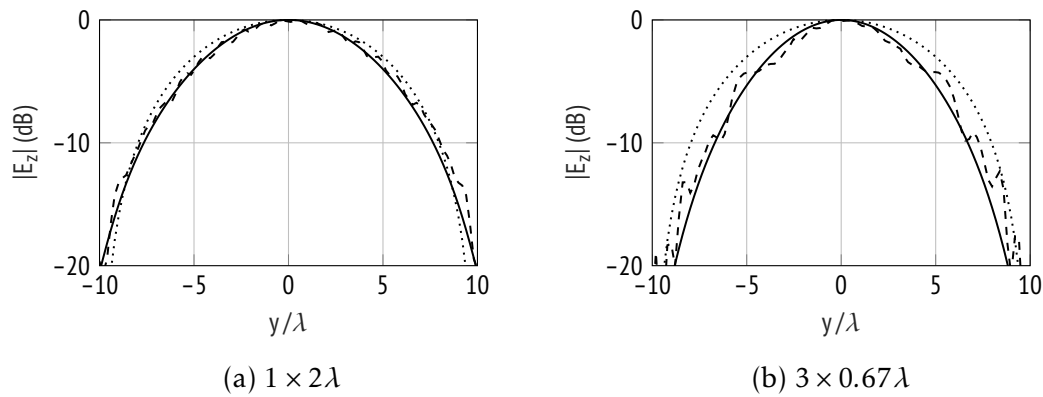


Figure 4.26: Calculated (—) and simulated (--) illumination of the inner lens contour, cosine illumination (....).

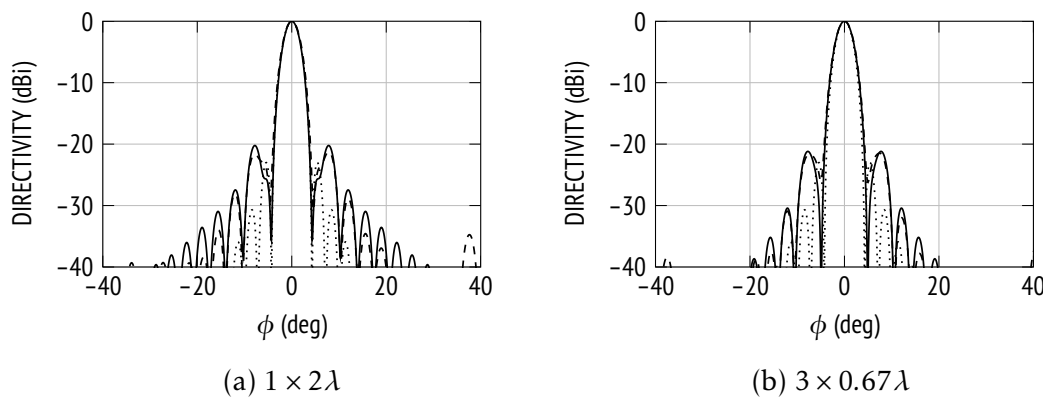


Figure 4.27: Comparison of calculated (—) and simulated (--) radiation pattern with prescribed pattern mask (....).

is $\Delta u = 2\lambda/D$, implying 11 independent beams over a scan range of $\pm 35^\circ$. Taking into account a finite spacing of $1.5 \text{ mm} = 0.15\lambda$ between the aperture edges, nine feeds of 2λ and 25 of 0.67λ can be accommodated on the feed curve within the given scan range. The resulting feed configurations are depicted in Fig. 4.28 along with the lens contours. The transfer efficiency characterizing the coupling between the received fields and the entire feed distribution is plotted in Fig. 4.29 as a function of the beam scan angle. As for the broadside case considered above, the absolute value of the calculated T factor at the different scan angles is expected to be in error for the cluster configuration. Nevertheless, the curves illustrate the gain ripple or beam crossover of the multibeam system, which is clearly visible for the configuration with feeds of 2λ . As the scan angle increases, the ripple decreases slightly; in transmission, this corresponds to the effect of beam broadening due to phase errors, leading to higher beam crossover. It can

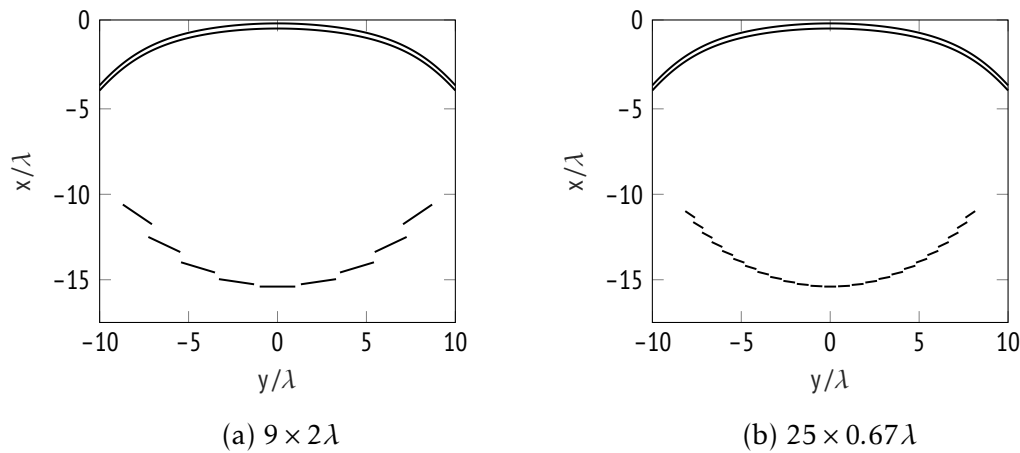


Figure 4.28: Schematic view of the studied feed configurations for a scan range of $\pm 35^\circ$.

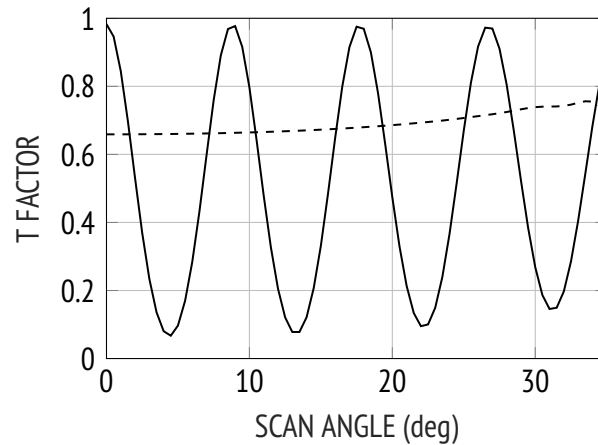


Figure 4.29: T factor versus scan angle for a feed system with 2λ - (—) and 0.67λ - apertures (....).

be seen that for feeds of 0.67λ , pattern stability is achieved over the entire field of view. In fact, the corresponding curve shows that at 30° , a better field match is achieved than at broadside. The multibeam configurations shown in Fig. 4.28 were simulated using Ansoft HFSS. The radiation patterns plotted in Fig. 4.30 were obtained using the complex weights derived from (4.16). The following remarks summarize these results:

- The radiation patterns plotted in Fig. 4.30(a) refer to the single-feed-per-beam configuration shown in Fig. 4.28(a). As expected, the crossover points of adjacent beams coincide with the T minima of the corresponding curve in Fig. 4.29.

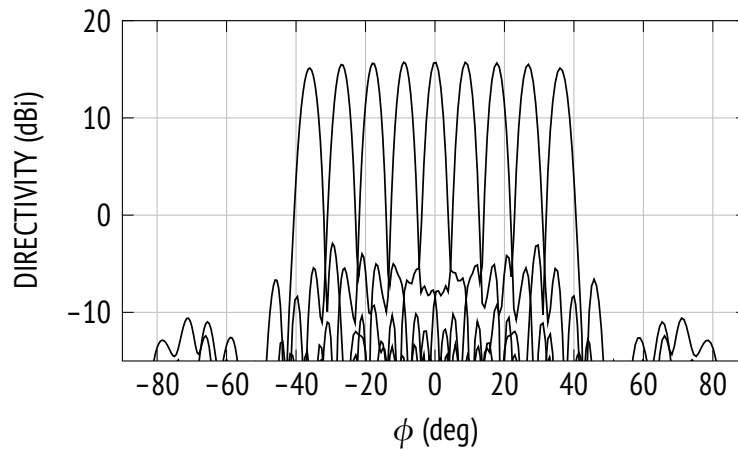
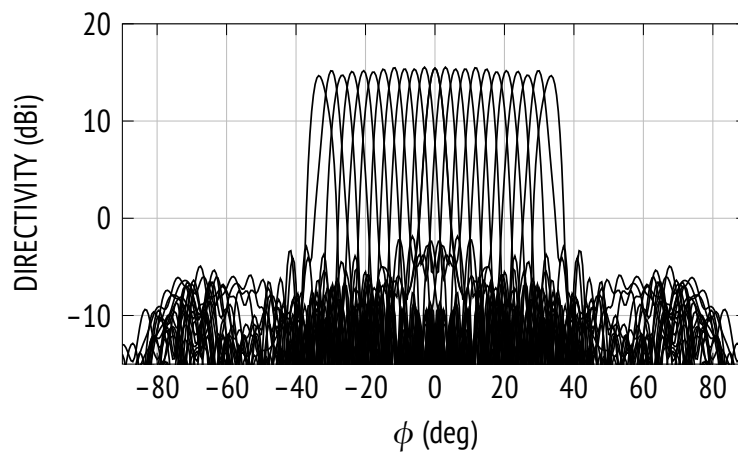
(a) $9 \times 2\lambda$ (b) $25 \times 0.67\lambda$

Figure 4.30: Simulated radiation patterns for (a) single-feed-per-beam excitation, (b) three-feeds-per-beam excitation.

- The radiation patterns shown in Fig. 4.30(c) were obtained using clusters with symmetrical amplitude weights. Each feed except for the two outermost is used as a beam port center, resulting in a total of 23 beams. The corresponding transfer efficiency suggests that similar patterns can be produced at intermediate scan angles, leading to asymmetric amplitude weights.

4.6 Chapter Summary

An overview of asymptotic high-frequency techniques commonly used for the analysis of quasi-optical systems in reception was given. Rigorous numerical models based on geometrical and physical optics for determining the received fields of pillbox reflectors, bootlace lenses and continuous parallel-plate waveguide lenses were presented. Furthermore, the use of reciprocity for characterizing the coupling between the focal-region distribution and realistic feed aperture fields was described.

The analysis of parabolic pillbox reflectors based on this approach led to the following conclusions:

- For reflectors with small F/D , the feed contours maximizing the power transfer generally lie close to the focal plane. Only for small angles of incidence and large feeds, these contours approach the Petzval surface of the reflector. Due to their shape, the contours are impractical for most multiple-feed configurations.

Higher efficiency is achieved when keeping the feed aperture parallel to the focal plane, unless the displacement is large enough for spillover loss to become significant. The improvement in transfer efficiency or peak gain is generally small (in the present case less than 0.04/0.3 dB) when placing feeds on the optimal contour rather than on the focal plane. As a result, nearly optimal scanning performance is achieved when using a simple mechanical feed.

- For reflectors with larger focal ratio, the contours producing maximum gain lie towards the reflector. For straight-ahead orientation, the contours approach the focal plane as the feed size increases. Due to the larger lateral displacement required for a certain scan angle, feeds need to be pointed toward the vertex of the reflector in order to maintain high efficiency. Mechanical scanning based on lateral displacement along the focal plane becomes inefficient beyond several beamwidths scanned. Scan loss is greatly reduced using the optimal contour of feeds aiming at the reflector. The scan contours are suitable for implementing efficient multiple-feed systems.

In the context of Rotman lenses, the method provides the following features:

- For lenses with optimal phase performance over a moderate scan range,

feed positions and orientations can be fine-tuned by taking into account amplitude effects. The improvement over the original focal arc is generally small, except for extreme scan angles where proper lens illumination becomes a challenge.

- For lens designs where the original focal arc does not yield optimal focusing performance, an improved feed curve can be rigorously derived. This approach is particularly useful in the design of lenses with enhanced scan range, where the optimal focal arc proposed in [13] is inconveniently arranged with respect to the lens contour. Using a simplified lens model it was shown that for a scan range of $\pm 50^\circ$, scan loss can be reduced by more than 1.5 dB.

The numerical approach has been extended to arbitrary incident fields, representing a desired radiation pattern, and cluster feed distributions. The analysis of a continuous PPW lens using this extension showed the following:

- For a fixed feed system, the method allows to determine the optimal cluster weights, i.e., the feed excitation for which the secondary pattern most effectively matches the prescribed pattern mask.
- For electrically small feeds ($< \lambda$), the assumption of vanishing fields on the aperture plane outside the aperture is no longer valid. For apertures smaller than λ the relative error between the calculated transfer efficiency and simulation results was up to 15%. However, the calculated cluster weights agree reasonably well with the weights extracted from full-wave simulations.

The techniques described in this chapter present a powerful and versatile tool for the analysis of integrated quasi-optical systems such as pillbox antennas and lenses implemented in parallel-plate waveguide. The reciprocity-based approach gives valuable insight into the mechanism of power transfer inside the beamformer and allows to evaluate the beam-scanning and beam-shaping capabilities by means of a single scalar quantity, referred to as transfer efficiency or T factor.

In the context of parallel-plate lenses, high-frequency models are typically developed for the transmit case [25, 35, 38]. When coupled with phase error- or pattern-based optimization algorithms, these models greatly facilitate the shaping procedure for designing quasi-optical systems with wide-angle focusing

properties. On the other hand, the developed procedure based on receive-mode analysis is particularly useful for the synthesis of advanced feed systems and thus key to the design of quasi-optical beamformers with enhanced pattern reconfigurability. The following chapter presents a practical lens design whose contours are shaped using an existing optimization procedure. The feed system for optimal scanning performance is then synthesized using the approach described in this chapter.

CHAPTER 5

A Multilayer PCB Lens Beamformer for Active Antenna Architectures

As described in Chapter 2.4, overlapping cluster feeds allow high-gain multiple-beam coverage while maintaining a compact radiating structure. The application of this feed concept to continuous PPW lenses is presented in this chapter. The design of a compact and efficient excitation network is an integral part of the development of practical MFPB systems. However, this work is focused on the design at antenna level, involving the quasi-optical system and the feed structure. Two novel aspects are demonstrated:

- The determination of optimal feed positions, orientations and cluster weights using the method outlined in Chapter 4.
- The implementation of a continuous PPW lens beamformer using a customized multilayer PCB manufacturing process.

In the first part of this chapter, the proposed PCB design concept and related constraints are discussed. The design procedure for the quasi-optical system and the feed structure are described. Two final designs, corresponding to single- and two-feed-per-beam operation, are reported.

5.1 Motivation

While various quasi-optical beamformers have been proposed over the past decade for satellite communications [9, 35, 39], recent initiatives such as Telesat and Starlink have selected active antenna architectures for their LEO megaconstellations, thereby following the approach of the MEO constellation O3b [115]. Nevertheless, active antennas pose several design challenges:

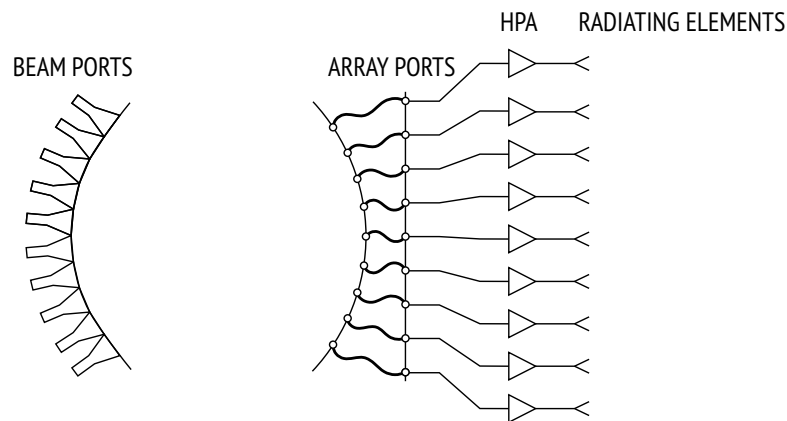


Figure 5.1: Schematic view of an active quasi-optical beamforming device.

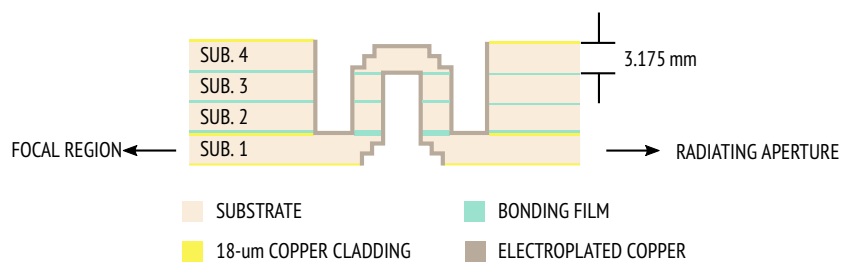
- The integration of solid-state power amplifiers and their thermal management when employing densely packed radiating elements.
- The gain loss at large scan angles and the compensation of pattern degradation due to mutual coupling between the radiating elements.
- The implementation of an analog beamformer for generating several dozen of reconfigurable beams from up to a few hundred radiating elements.

Due to the high power consumption of the processor unit for large bandwidths, fully digital beamforming is not well adapted to Ka-band space-segment antennas. On the other hand, traditional analog beamforming is limited by the cost and complexity of the hardware required for a certain number of radiating elements and beams. Low-loss PCB technologies such as substrate integrated waveguides allow the realization of quasi-optical beamformers and radiating structures that are compatible with an active antenna architecture. As shown in Fig. 5.1, the quasi-optical system acts in this case as a low-level beamforming network whose output ports are connected via high-power amplifiers to the radiating elements. Various PCB implementations have been proposed for quasi-optical beamformers, including pillbox systems [8, 47], Rotman [18, 19] and Luneburg lenses [27, 116]. Dual-layer pillbox systems are compatible with a low-cost PCB fabrication process: the reflector is realized by vias through both substrate layers, while coupling slots are etched on the metallization between these. However, the scanning range of previously developed pillbox beamformers is typically limited to about $\pm 35^\circ$ or 6–7 beamwidths, with scan losses in the order of 2 dB and maximum sidelobe levels of -12 dB [6, 8]. Similar scanning performance has been demonstrated with a multilayer Rotman lens using a slotted

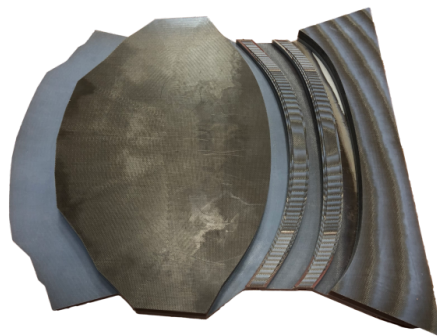
waveguide array at the output [18]. High-crossover low-sidelobe patterns have been demonstrated with a pillbox design using the split aperture decoupling method [47]. A cylindrical Luneburg lens implemented using standard PCB techniques has been presented in [116]. The gradient index profile is realized by drilling holes of varying diameter into a concentric arrangement of two different substrates. In this case, the lens is used to feed a linear slotted SIW array. The final structure provides an angular scanning range of $\pm 41^\circ$ with scan losses in the order of 2.5 dB. Another low-cost PCB design has been presented in [27]. The refractive index profile is achieved by etching a pattern of crossed transmission lines onto a copper-clad substrate with $\epsilon_r \approx 1$. The radiating aperture is formed by a flare made of metallized laminates. The proposed design offers a scanning range of $\pm 45^\circ$ with scan losses of about 1 dB. Coverage with 3-dB beam crossover has been demonstrated using a larger number of smaller feed elements. However, the resulting sidelobe levels are as high as -10 dB. Moreover, like with other radially symmetric designs, limited scanning performance must be expected when used for phasing a linear array. As a consequence, there is still a clear need for quasi-optical beamformers with enhanced scanning range ($> 50^\circ$) and small form factor, suitable for in-package antenna integration.

5.2 Proposed Design Concept

To enable the integration of receiver or transmitter circuits and radiating elements on the same substrate, a continuous PPW lens beamformer compatible with conventional PCB fabrication techniques is developed. A multilayer structure is adopted to implement the vertical delay sections. This is shown schematically in Fig. 5.2(a). An adhesive film is used to bond the substrate layers together. The lowest layer (Sub. 1) is copper cladded and used to realize the horizontal parallel-plate region. The shaped parallel-plate waveguide is formed by milling into the three upper substrate layers (Sub. 2, Sub. 3 and Sub. 4). First trials were made with a stack of PTFE slabs as shown in Fig. 5.2(b) using plasma and Tetra-Etch[®] surface treatment. The latter resulted in significantly better adhesion. Horizontal conducting plates are then formed by the metal cladding of the laminated substrates, while vertical conducting plates are created by electroplating of copper onto the exposed surfaces. The intermediate substrate layers (Sub. 2 and Sub. 3) are without metal cladding, while the upper surface of Sub. 4 is cladded. Outside the vertical delay section, Sub. 2 and Sub. 3 do not



(a)



(b)

Figure 5.2: (a) Schematic cross section of a PPW lens beamformer implemented in multilayer PCB technology. (b) machined PCB stack-up

serve as a waveguide. However, the layers can be left unmachined to reduce fabrication time and to provide mechanical support. Rogers RT/duroid 5880 with $\epsilon_r = 2.2$ and a loss tangent of $\tan \delta = 0.0009$ was found to be a suitable material for this purpose. A substrate thickness of $H = 3.175$ mm was chosen as it is the maximum thickness that is commercially available. The multilayer assembly was limited to four layers, resulting in a total height of 12.7 mm $\approx 0.8\lambda_0$ when using layers of equal thickness. One reason for this choice was to limit the fabrication complexity in this proof of concept. From an application perspective, a low profile is required for accommodation in an array of quasi-optical beamformers enabling pencil-beam scanning.

A thinner substrate could be used for the lower and upper layer (Sub. 1 and 4) which do not contribute to the vertical delay path. The minimum feasible thickness depends on the manufacturing tolerances and the features required to compensate the E -plane corners (see Fig. 5.2). The estimated attenuation α_d and α_c due to dielectric loss and conductor loss, respectively, of a TEM mode inside the parallel-plate waveguide [69, pp. 42–46] are plotted in Fig. 5.3, assuming a copper cladding with conductivity $\sigma = 5.8 \times 10^7$ S/m. The cutoff frequency of the

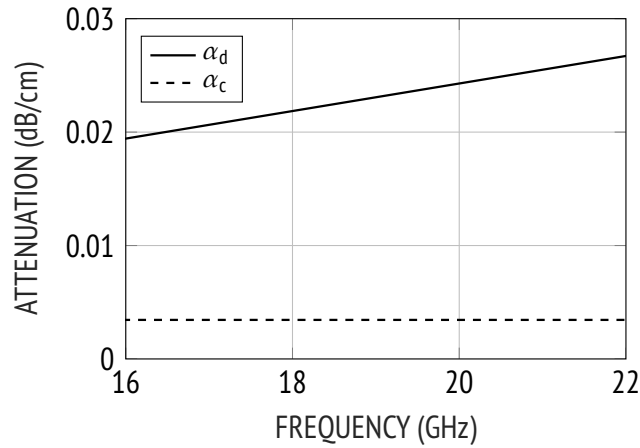


Figure 5.3: Estimated attenuation for the TEM mode of a parallel-plate waveguide in Rogers RT/duroid 5880 with thickness $H = 3.175$ mm.

first higher-order modes is 31.85 GHz, which is well above the frequency band of interest (17.3 – 20.2 GHz) and, in fact, also beyond the uplink band.

5.3 Quasi-Optical Design

As can be seen from (3.1) through (3.3), the normalized total height of a continuous PPW lens represented by the bifocal model is given by

$$z_{\max} = \frac{a_0^2}{2} \left[\sqrt{1 - \frac{1}{4(F/D)^2}} - 1 \right]. \quad (5.1)$$

The height-to-diameter ratio (not including the parallel-plate spacing) as a function of F/D is plotted in 5.4 for different off-axis focal point angular positions. It can be seen that for a moderate value of $F/D = 0.7$ as in [39], the ratio can be in the order of 7%. However, this is still relatively high compared to PCB designs [6, 8, 18, 27, 33, 47], where the total height is typically a small fraction of a wavelength. To overcome this problem, a dual-lens design as described in Section 3.2.3 is employed. In the previous case, this concept has been used to reduce phase aberrations over a wider angular range. As demonstrated in Section 3.25 and Appendix C, lenses with large focal length-to-diameter ratio are used, while the physical length of the beamformer (defined by the radius of the feed curve) is kept moderate. At the same time, this results in a lower profile when compared to the single-ridge design.

The procedure outlined in Appendix C was used as a starting point to define

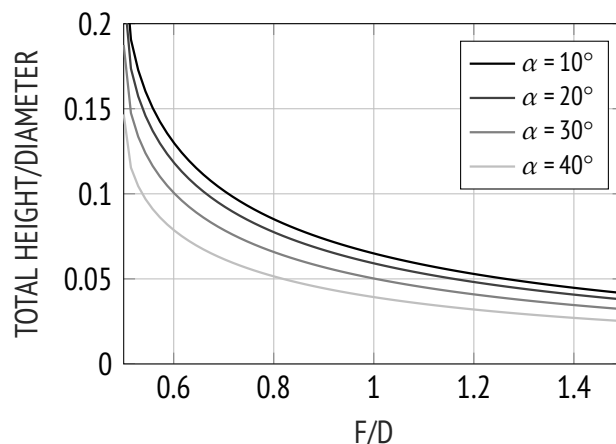


Figure 5.4: Height-to-diameter ratio versus focal ratio.

the focal ratios F_1/D and F_2/D , the distance between the two lenses l , and the ratio of on-axis feed position to diameter, in the following referred to as F/D . Next, a pattern optimization process, based on the ray-tracing model detailed in [38], was used to shape the lens contours and the feed curve. This was preferred over a phase-only optimization since proper lens illumination becomes critical at large scan angles. A series of optimizations, assuming a standard feed with 10-dB edge taper, were performed with the goal to minimize the beamwidth, scan loss and sidelobe levels of beams pointing at 0° , $\pm 20^\circ$ and $\pm 40^\circ$. Usually, the first step in this procedure is to fix the diameter of the lens according to the required H -plane beamwidth and a given edge taper. Here, the diameter was not specified a priori and the main constraint taken into account during the optimization was that the maximum height of the structure H_{\max} be smaller than 12.7 mm. The maximum scan angle was chosen with respect to the critical angle of the substrate-air interface, which will be discussed in more detail in Section 5.5. The design frequency was fixed to $f_c = 18.75$ GHz with a free-space wavelength of $\lambda_0 = 16$ mm. This resulted in a lens design with diameter $D = 10.7\lambda_0 = 15.9\lambda_d \approx 171$ mm and an on-axis feed position defined by $F/D = 0.74$. The spacing of the two lenses, measured between the inner lens contours at the center, is $l = 1.7\lambda_d = 18.3$ mm. The parallel-plate spacing is $H = 3.175$ mm and the thickness of the ridges $T = 4.5$ mm. The coefficients of the tenth-order polynomials representing the inner contour and ridge profiles of

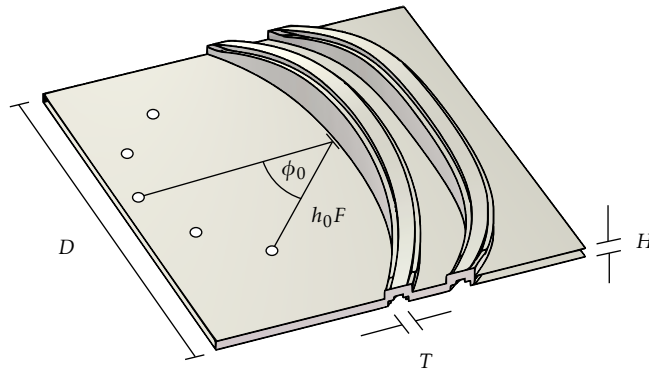


Figure 5.5: Perspective view of a dual-ridge lens with five optimized beam port positions.

the first lens are, in ascending order,

$$\mathbf{a}^{x_1} = [0, -0.32, -0.4, 0.05, 0.25, 0]$$

$$\mathbf{a}^{z_1} = [0, -0.114, -0.044, 0, 0.25, 0]$$

and of the second lens

$$\mathbf{a}^{x_2} = [0, -0.193, -0.06, -0.58, 0, 0]$$

$$\mathbf{a}^{z_2} = [0, -0.118, 0, 0.058, 0, 0].$$

The resulting height of the two lenses is 12.67 mm and 12.62 mm. This corresponds to a height-to-diameter ratio of about 3.7% when neglecting the parallel-plate spacing. Receive mode analysis shows that the focal ratios of the two individual lenses are approximately $F_1/D \approx 1.46$ and $F_2/D \approx 1.48$. The feed positions for the three optimized beams are defined by

$$\mathbf{h}_0 = [1, 0.99, 0.89]$$

$$\boldsymbol{\phi}_0 = [0^\circ, 21.4^\circ, 42.7^\circ]$$

where \mathbf{h}_0 is the normalized distance to the apex of the first lens and $\boldsymbol{\phi}_0$ the subtended angle as illustrated in Fig. 5.5(b). The radiation patterns corresponding to the three optimization points are plotted in Fig. 5.6. At this point, a lens of $D = 10.7\lambda_0$ with an edge taper of 10 dB radiating into free space is considered. The beamwidth and beam pointing angle are accurately predicted by ray tracing, while first sidelobe levels agree reasonably well with the simulation results. The calculated and simulated scan loss at 40° is about 1.5 dB, which is reasonably

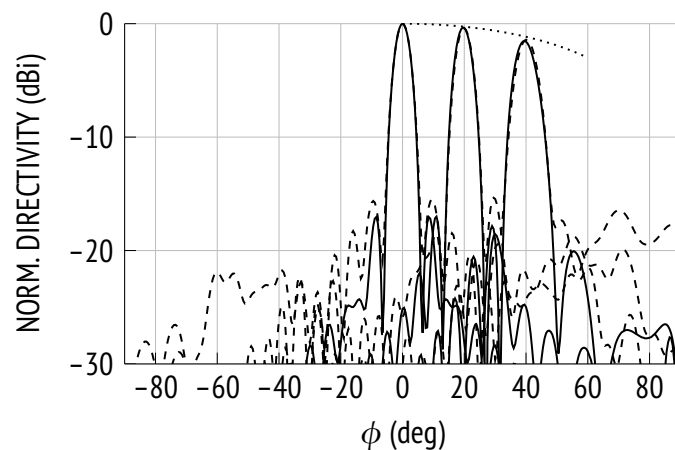


Figure 5.6: Calculated (—) and simulated (--) radiation patterns of single-ridge lens.

close to the cosine variation of 1.16 dB. It should be noted that the sidelobe level for an in-phase aperture would be about -20 dB. The predicted sidelobe level of -16 dB implies that the final lens design is not fully corrected for phase errors on axis.

5.4 Feed System Design

5.4.1 Beam Port Contour

The optimization process for shaping the lens contours provided a total of five feed positions, corresponding to scan angles of 0° , $\pm 20^\circ$ and $\pm 40^\circ$. The entire beam port contour could then be defined simply by interpolation of these points or by further optimization using only the feed positions as degrees of freedom. A more direct approach is to determine the feed contour from the focal-region distribution, as described in Section 4.4. The focal surface resulting from plane-wave incidence at angles $\phi_i = [-40\dots 40^\circ]$ is shown in Fig. 5.7. The calculated curve agrees well with the simulated results for all but the most extreme angles, where the focal-region maximum approaches the lens contours. Moreover, it can be seen that the optimized points lie relatively close to the calculated contour; remaining differences can be attributed to the fact that optimizations were carried out taking into account the beamwidth and sidelobe level, rather than the maximum gain. The contour could be further adjusted using the plane-wave expansion of a desired pattern and by conjugate matching for a given feed. For

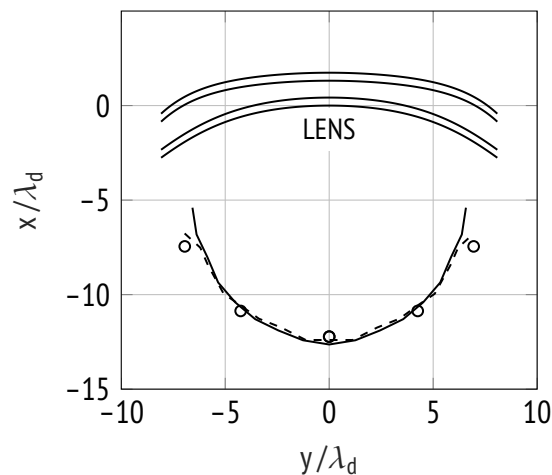


Figure 5.7: Calculated (—) and simulated (---) focal surface for $\phi_i = [-40\dots40^\circ]$, optimized feed positions (o).

simplicity, the maximum field locus shown in Fig. 5.7 was used as a starting point.

5.4.2 Feed Dimensioning

Two feed configurations are developed: a feed distribution for maximum gain that approaches the orthogonality condition, and a cluster distribution suitable for reproducing these reference beams with high crossover. A combination of receive- and transmit-mode analysis is used to determine the appropriate feed dimensions.

Single-Feed-per-Beam Configuration

The focal-plane field distribution for normal plane-wave incidence is shown in Fig. 5.8. A comparison with the results reported in Section 4.2.3 shows that the agreement between calculated and simulated results is still close for the two-lens configuration. The results suggest that the aperture efficiency is maximized when using a feed of size $a = 1.7\lambda_d \approx 2.3\lambda_d(F/D)$, which corresponds to an edge taper of 14 dB. The orthogonal spacing for this type of illumination is approximately $\Delta u = 1.8\lambda_d/D$ (see Fig. 2.3), implying 11 uncoupled beams over a scanning range of $\pm 40^\circ$. Taking into account practical constraints such as the finite wall thickness of the feeds, a total of nine feeds are placed over an angular range of $\pm 37.5^\circ$ in the first configuration. The beam crossover level as a function of the feed size is plotted in Fig. 5.9(a). The results refer to the configuration

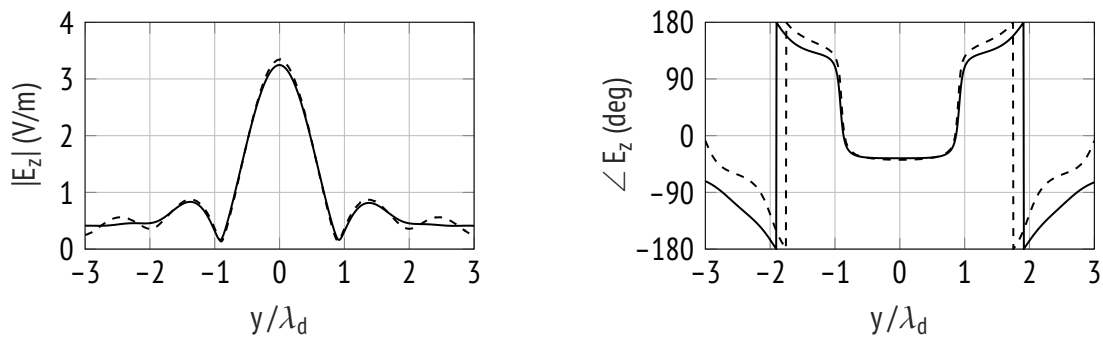


Figure 5.8: Calculated (—) and simulated (--) electric field in proximity of focal-region maximum for $\phi_i = 0^\circ$.

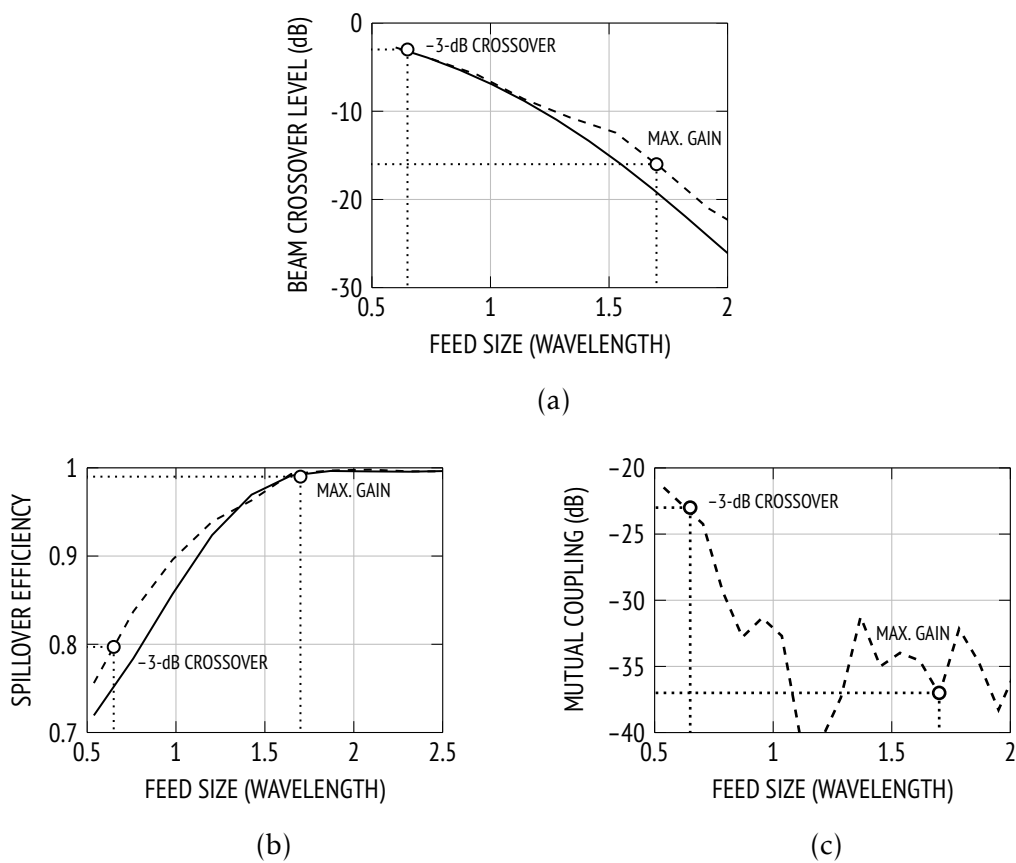


Figure 5.9: Calculated (—) and simulated (--) (a) beam crossover level, (b) spillover efficiency, and (c) mutual coupling versus feed size for single-feed-per-beam operation.

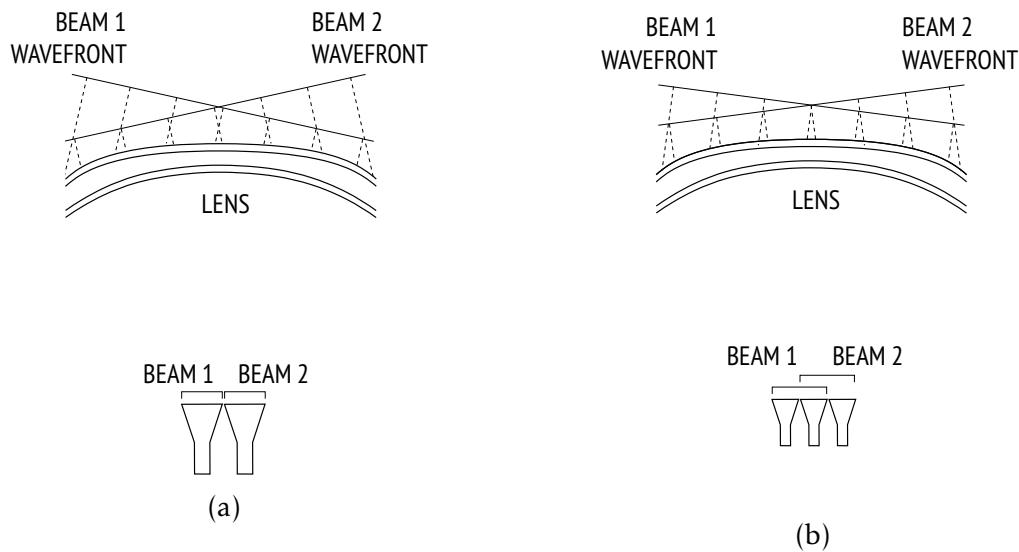


Figure 5.10: Schematic view of lens beamformer with (a) single-feed-per-beam operation, (b) two-feed-per-beam operation.

shown in Fig. 5.10(a), with two feeds placed symmetrically around the center. A spacing of $0.15\lambda_d$ between the apertures is assumed to account for the finite wall thickness of feeds implemented in SIW technology. For the chosen feed size of $1.7\lambda_d$, the predicted crossover is below -15 dB. The spillover efficiency is better than 97%. As expected for an orthogonal feed distribution, the mutual coupling between two adjacent apertures is very low (< -30 dB).

Multiple-Feed-per-Beam Configuration

The appropriate number of cluster elements and their size must be determined taking into account the fields to be sampled, the cutoff wavelength of the feed mode, the finite spacing between the apertures and the complexity of external circuitry. Here, the most basic form of cluster, consisting of two feed elements [16, 50], is used to match the field distribution shown in Fig. 5.8. The crossover level for a lens fed by overlapping pairs of feeds is shown in Fig. 5.11(a). The configuration is shown schematically in Fig. 5.10(b). It can be seen that a crossover greater than -2 dB is achieved for any feed aperture size. The general procedure for determining the optimal feed element size is to evaluate the field match between cluster distribution and focal-region fields. However, as demonstrated in Section 4.5, the approximation of the fields on the aperture plane becomes inaccurate for small feed elements and clusters consisting of such. Instead, the spillover loss is evaluated using two-dimensional aperture theory. It

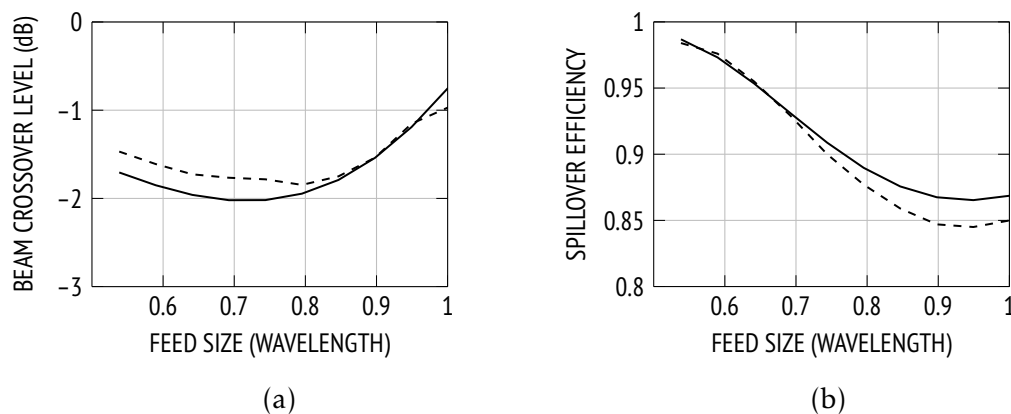


Figure 5.11: Calculated (—) and simulated (--) (a) beam crossover level and (b) spillover efficiency versus feed size for two-feed-per-beam operation.

should be noted that also in this approach, vanishing fields are assumed outside the feed apertures and mutual coupling is neglected. However, the calculated results, shown in Fig. 5.11(b), are in good agreement with the simulated data. The spillover losses are higher for larger feed elements due to the appearance of grating lobes. To ensure that the feeds operate well above cutoff, a width of $0.65\lambda_d$ is selected.

5.4.3 Input Transition

To interface the feed horns with $50\text{-}\Omega$ coaxial lines, a transition equivalent to the design presented in [117] was developed. The geometry of the input structure is shown in Fig. 5.12. An SMA end launch connector (Hirose HRM(G)-300-467B-1) is used to feed a grounded coplanar waveguide (GCPW) printed on the top of the lowest substrate layer. To ensure that the width of the trace at the board edge is smaller than the diameter of the insulator of the connector, the signal pad at the input was dimensioned according to recommendations in the datasheet of the connector. Due to the relatively high substrate thickness ($H = 3.175\text{ mm} \approx 0.3\lambda_d$), gaps smaller than $50\text{ }\mu\text{m}$ would be required to achieve a line impedance of $50\text{ }\Omega$ at the input of the GCPW. Since the available etching process allows a minimum gap of $100\text{ }\mu\text{m}$ between conductors, a line impedance greater than $50\text{ }\Omega$ needs to be accepted for the coplanar waveguide. A linear taper section and an additional impedance step of 1.85 mm is used to match the coplanar waveguide to an SIW of width 7.1 mm (center-to-center distance of the via rows), providing single-

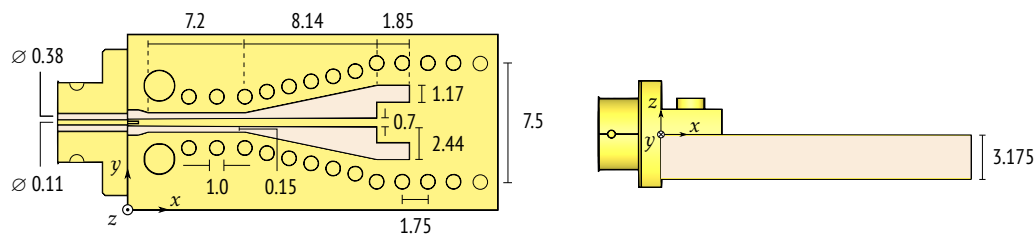


Figure 5.12: Top and side view of input transition (all dimensions in mm).

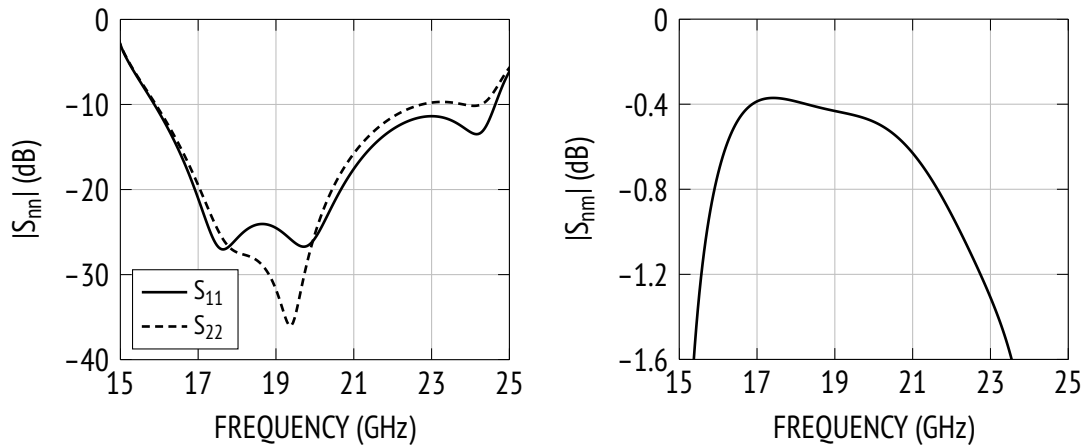


Figure 5.13: Simulated S parameters of optimized transition from SMA end launch connector (port 1) to SIW (port 2).

mode operation in the band from about 15 to 29 GHz. The positions of the vias surrounding the GCPW were optimized to reduce radiation due to parasitic parallel-plate modes. The simulated S parameters of the transition, including the 3D model of the connector provided by the manufacturer, are shown in Fig. 5.12. The return loss is greater than 10 dB in the band from 15.9 to 22.8 GHz and greater than 23 dB in the design band (17.3 – 20.2 GHz). The insertion loss is less than 0.5 dB over this frequency range. The latter is mainly due to leakage, corresponding to about 6% of the input power in the worst case.

5.5 Output Transition

According to Snell's law, the beam pointing angle ϕ_t in free space is related to the angle of incidence ϕ_i inside the dielectric by

$$\phi_t = \sin^{-1}(\sin \phi_i \sqrt{\epsilon_r}). \quad (5.5)$$

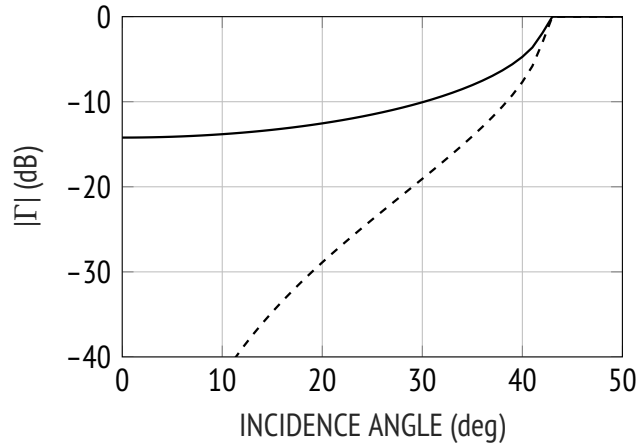


Figure 5.14: Reflection coefficient of a TE-polarized plane wave in Rogers RT/duroid 5880 obliquely incident upon a substrate-air interface with (--) and without (—) ideal quarter-wave matching layer.

Furthermore, the critical angle of the interface between the substrate and free space is given by

$$\phi_c = \sin^{-1}(1/\sqrt{\epsilon_r}) \approx 42.4^\circ. \quad (5.6)$$

Since the incident wave is TE-polarized with respect to the plane of incidence, the reflection and transmission coefficients are given by [97, pp. 40–43]

$$\Gamma = -\frac{\sin(\phi_i - \phi_t)}{\sin(\phi_i + \phi_t)} \quad (5.7a)$$

$$T = \frac{2 \sin \phi_t \cos \phi_i}{\sin(\phi_i + \phi_t)}. \quad (5.7b)$$

It should be noted that the square of the transmission coefficient corresponds to the transmitted energy flux per unit area. As a result, the conservation of energy in the given problem is stated by

$$R^2 + T^2 \frac{\cos \phi_t}{\sqrt{\epsilon_r} \cos \phi_i} = 1. \quad (5.8)$$

The calculated reflection coefficient [97, pp. 64–66] is shown in Fig. 5.14. When the main beam is broadside, about 4% of the incident power is reflected at the transition, while when scanning the main beam out to 60° (corresponding to an incidence angle of $\phi_i = 35.7^\circ$), about 17% is reflected. When using a quarter-wave matching layer of permittivity $\epsilon_m = \sqrt{\epsilon_r} \approx 1.48$ and thickness

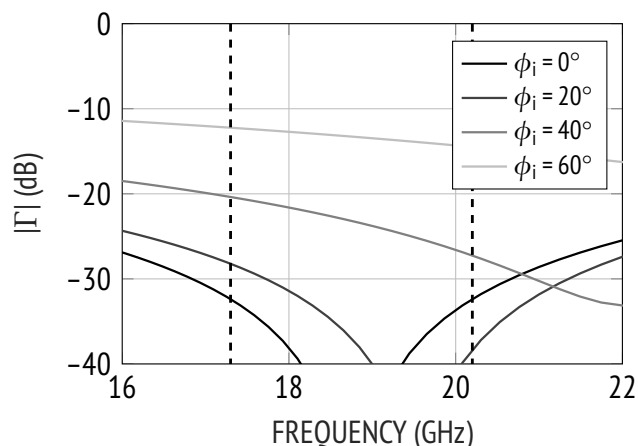


Figure 5.15: Reflection coefficient of a TE-polarized plane wave in Rogers RT/duroid 5880 obliquely incident upon a substrate-air interface with quarter-wave matching layer.

$L_m = \lambda_0 / (4\sqrt{\epsilon_m}) \approx 3.28$ mm, no power is reflected for a main beam at broadside and about 5% for a main beam pointing at 60° . The reflection coefficient of an interface with quarter-wave matching layer is plotted in Fig. 5.15 as a function of frequency for various scan angles; the corresponding incidence angles inside the substrate are $\phi_i = [0^\circ, 13.3^\circ, 25.7^\circ, 35.7^\circ]$. It can be seen that within the frequency band of interest, less than 6% of the incident power is reflected when scanning out to 60° .

To avoid the need for an additional medium, the effective permittivity at the interface can be varied gradually from ϵ_r to 1 in order to reduce reflections. This can be achieved by drilling one or several rows of holes, with properly chosen diameter and pitch, in the lowest substrate layer. Alternatively, a matched transition can be provided by tapering the substrate edge as proposed in [118]. For design and manufacturing reasons, the latter solution was selected. When using a linear taper as shown in Fig. 5.16, only one parameter, namely the taper length or chamfer angle, can be tuned. Simulations showed that for normal incidence, reflections are minimized when the taper length is equal to $L_m = \lambda_0 / (2\sqrt{\epsilon_m})$ or an integer multiple thereof, where $\epsilon_m = \sqrt{\epsilon_r}$.

In this proof of concept, an asymmetric pyramidal flare is used to interface the parallel-plate structure with free space. The geometry of the flare is shown in Fig. 5.18. The dimensions of the radiating aperture along the E plane (xz plane) is equal to the total thickness of the stack, i.e., 12.7 mm $\approx 0.8\lambda_0$. Full-wave simulations showed that a flare along the plane of scan (H plane) allows reduced

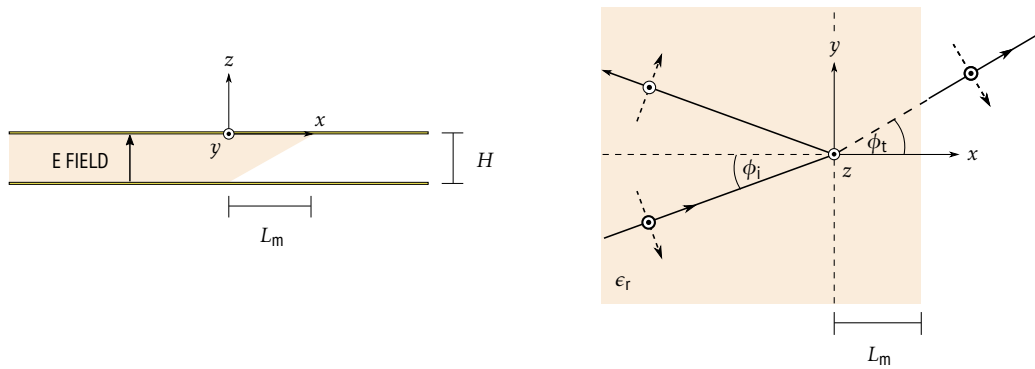


Figure 5.16: Side and top view of a chamfered substrate-air transition inside a parallel-plate waveguide.

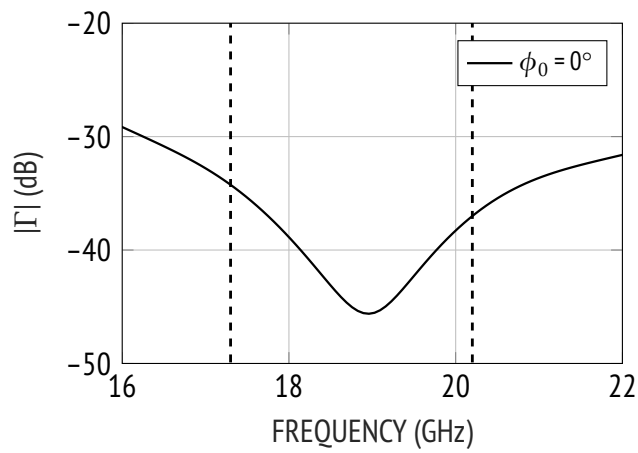


Figure 5.17: Simulated reflection coefficient of a TE-polarized plane wave incident upon optimized chamfered substrate-air transition.

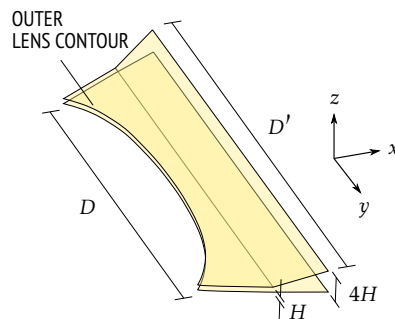


Figure 5.18: Perspective view of lens-flare interface.

scan losses as long as the flare angle is not significantly smaller than the angle of incidence at the transition from dielectric to air. On the other hand, the flare angle can be chosen to maximize the peak gain at broadside [110]. Hence, a trade-off needs to be found between these two performance criteria. The radiating horn employed in the final design has a flare length of $1.1\lambda_0 = 17.6\text{ mm}$ and a width of $D' = 13.8\lambda_0 \approx 220\text{ mm}$. Simulations of the one-dimensional E -plane model [29] show a return loss greater than 20 dB for normal incidence.

5.6 Final Designs and Simulation Results

5.6.1 Single-Feed-per-Beam Design

The final lens design is illustrated in Fig. 5.19. For clarity, the substrate layers above the focal region (Sub. 2, Sub. 3 and Sub. 4 in Fig. 5.2) are not shown. The flare length and width of the SIW sectoral horns (center-to-center distance between the vias at the aperture) are 18.5 mm. The latter corresponds to an effective aperture width of $1.7\lambda_d$ [119]. The phase centers of feeds 1 to 5 are located at points given by $h_0 = [0.94, 0.97, 0.99, 0.99, 1]$, $\phi_0 = [37.5^\circ, 27.5^\circ, 18^\circ, 9^\circ, 0^\circ]$ (see Fig. 5.5). The sidewalls of the lens are formed by a row of vias in the lowest substrate layer. As shown in Fig. 5.19(b), the stack is placed on a metallic plate which forms the lower E -plane wall of the flare at the output. The performance of the beamformer was simulated using Ansoft HFSS. A 3D model of the coaxial connectors was included in the simulations. The bonding film between the substrate layers was not taken into account at this stage.

5.6.1.1 Scattering Parameters

The simulated input reflection coefficients are shown in Fig. 5.20. Due to symmetry, only half of the off-axis feeds (corresponding to port 1 through 4) are considered. The return loss is greater than 12 dB in the 17.7–20.3 GHz band. Figure 5.21 shows the mutual coupling between the conjugate beam ports. The worst-case isolation within the band is about 14 dB for the two outermost ports. The coupling between non-conjugate ports is below -20 dB .

5.6.1.2 Radiation Performance

The simulated H -plane radiation patterns are shown in Fig. 5.22. It can be seen that the scan loss is approximately equal to the aperture size reduction in

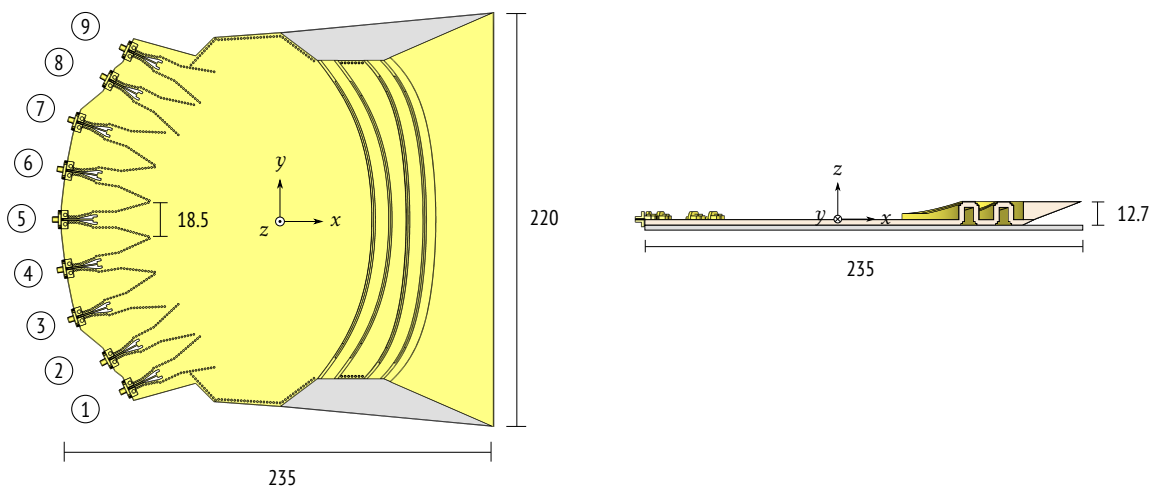


Figure 5.19: Top and cross-sectional view of PCB lens model with single-feed-per-beam excitation (all dimensions in mm).

the scan direction. At the design frequency, the peak gain for feed 1 is slightly higher than predicted by the cosine variation, despite the additional phase errors introduced by the lens and larger reflections at the chamfered dielectric-air transition. This is effect is due to the dimensioning of the flare in the H plane. A degradation of the main lobe in the pattern of feed 1 can be observed, especially at the upper and lower frequency. A simulation of the final structure without the connectors confirmed that this degradation is due to spurious radiation from the input transition.

The beam peaks are at $0^\circ, \pm 12.3^\circ, \pm 25.2^\circ, \pm 39.2^\circ$ and $\pm 59^\circ$ at the design frequency. It should be noted that the scan angles are somewhat smaller than $\sin^{-1}(\sin \phi_0 \sqrt{\epsilon_r})$, since the beam angle inside the dielectric is smaller than the feed position angle. Figure 5.23(a) shows the beam pointing angle as a function of frequency. As expected for a true-time delay beamformer, the scan angles are nearly frequency invariant. The maximum squint observed between 17.3 and 20.2 GHz is 2.4° for the extreme beam. The crossover level between the broadside beam and the adjacent beams is about -15 dB over the entire band. The maximum sidelobe levels are plotted in Fig. 5.23(b). The reported values do not necessarily refer to the first sidelobe. Within the frequency band of interest, sidelobe levels are less than -12 dB for all beam positions.

Figure 5.24(a) shows the realized peak gain as a function of frequency for the different beams. At the design frequency, the gain loss is about 2.2 dB for the beam at 59° . Within the operating frequency band, the maximum scan loss is 3.1 dB for this beam. The maximum gain variation over the frequency band is

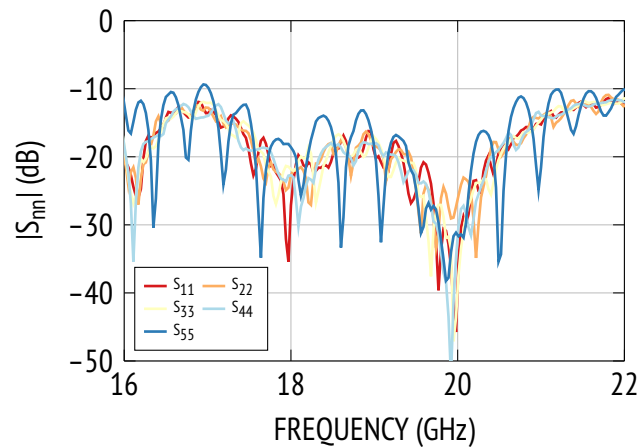


Figure 5.20: Simulated input reflection coefficient for the single-feed-per-beam configuration.

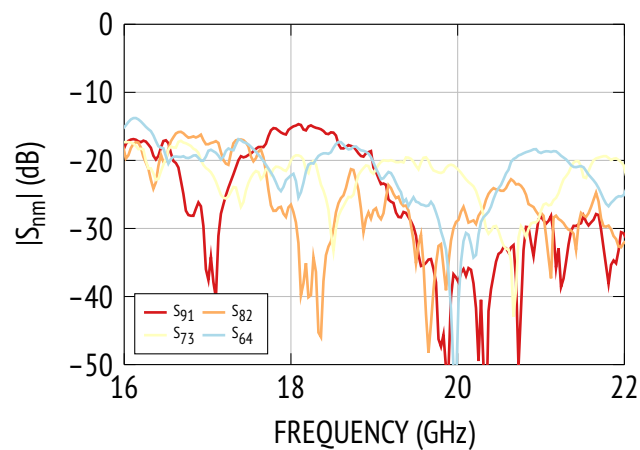


Figure 5.21: Simulated mutual coupling between conjugate input ports for the single-feed-per-beam configuration.

2.1 dB (feed 2 and 8).

The radiation efficiency for the broadside beam, plotted in Fig. 5.24(b), is higher than 81% over the band. At the design frequency, the total loss is 0.86 dB. The path length of the principal ray inside the PPW is about 185 mm, which implies a dielectric loss of 0.42 dB and a conductor loss of 0.06 dB at 18.75 GHz (see Fig. 5.3). The simulated insertion loss of the input transition is 0.42 dB. The estimated total loss (0.9 dB) is therefore in close agreement with the simulated value. Input reflections and port-to-port coupling reduce the peak realized gain by about 0.15 dB.

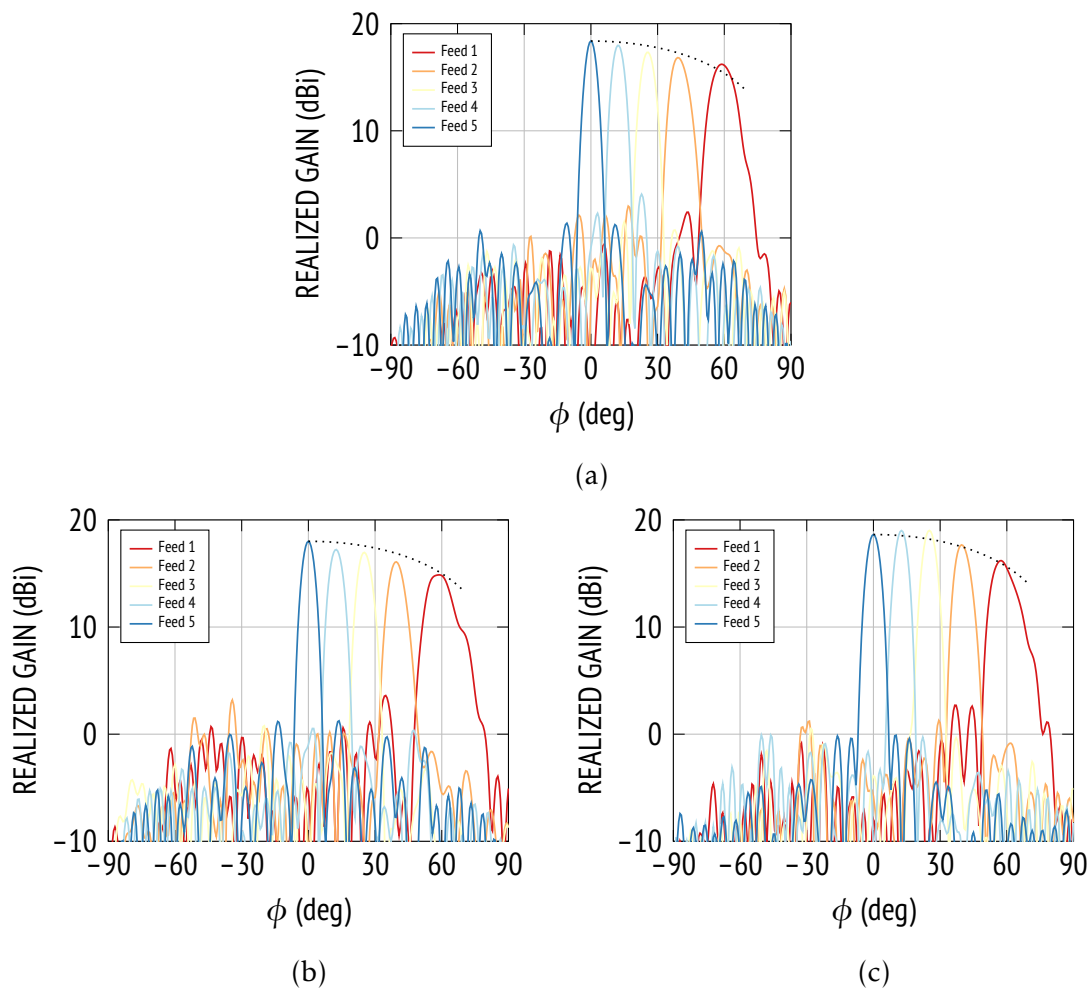


Figure 5.22: Simulated H -plane radiation pattern at (a) 18.75 GHz, (b) 17.3 GHz and (c) 20.2 GHz.

5.6.2 Multiple-Feed-per-Beam Design

The final lens design is shown in Fig. 5.19. The width of the SIW feeds (center-to-center distance between the vias at the aperture) is 7.5 mm, corresponding to an effective aperture width of $0.65\lambda_d$. The phase centers of feeds 1 to 10 are located at points given by $h_0 = [0.91, 0.92, 0.92, 0.93, 0.95, 0.96, 0.97, 0.97, 0.97, 0.97]$, $\phi_0 = [39.6^\circ, 34.9^\circ, 30.3^\circ, 25.8^\circ, 21.4^\circ, 17^\circ, 12.7^\circ, 8.5^\circ, 4.3^\circ, 0^\circ]$ (see Fig. 5.5). The input transition, the lens contours and the output transition are identical to the design presented in the previous section. During the final design process, simulations were carried out at three frequency points (17.3, 18.75 and 20.2 GHz). The results were evaluated in terms of the H -plane secondary pattern for the individual feeds, i.e., without the additional post-processing allowing for overlapping feeds.

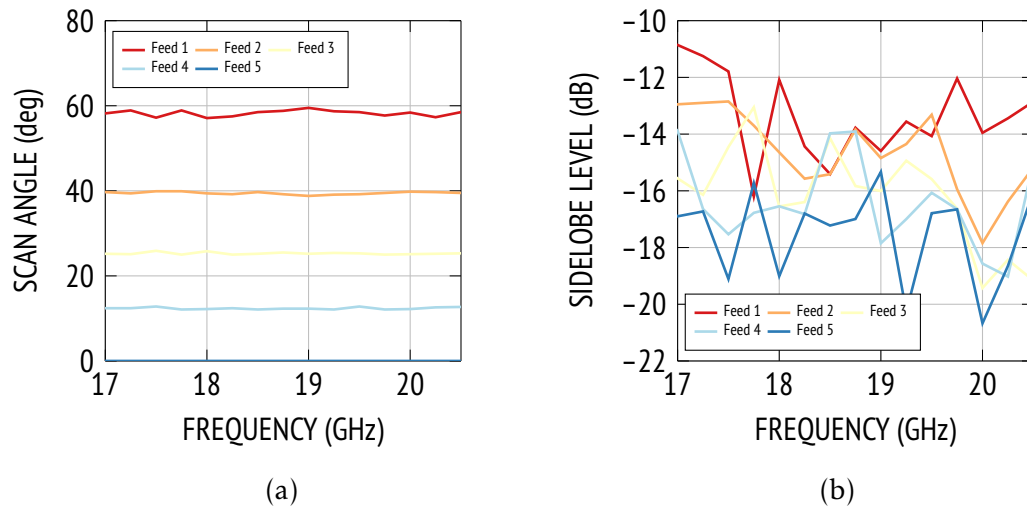


Figure 5.23: Simulated (a) scan angle and (b) sidelobe level in the H plane as a function of frequency.

Due to the high edge illumination (-4 dB), reflections at the metallic sidewalls have a significant effect on the radiation pattern. A parametric sweep based on two points was used to shape the sidewalls with the aim of improving the broadside gain while maintaining a cosine variation of gain for the scanned beams.

5.6.2.1 Scattering Parameters

Figure 5.20 shows the simulated input reflection coefficients for individually excited feeds. Due to symmetry, only half of the off-axis feeds (corresponding to port 1 through 10) are considered. The passive return loss is greater than 10 dB over most of the 17.3–20.2 GHz band for each port. As in the single-feed-per-beam design, slightly higher values are observed for the central feed (port 10). The mutual coupling between the conjugate beam ports is plotted in Figure 5.27. The worst-case isolation within the band is about 14 dB for the two outermost ports. The coupling between non-conjugate ports is below -17 dB.

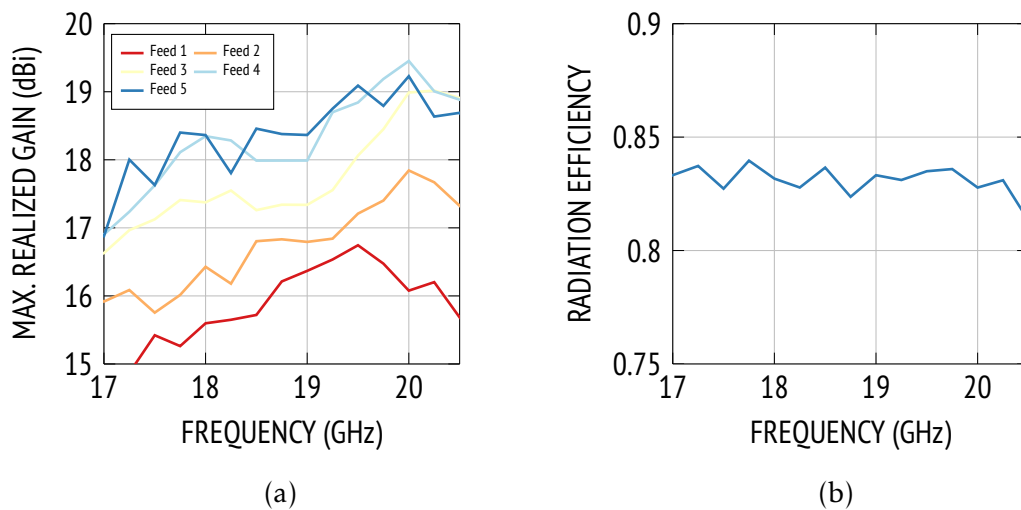


Figure 5.24: Simulated (a) realized gain, (b) radiation efficiency for the broadside beam as a function of frequency.

5.6.2.2 Radiation Performance

Figure 5.22 shows the simulated H -plane radiation patterns for individually excited feeds. At the design frequency, the peak gain at broadside is 17.7 dB, which is about 0.6 dB lower than for the case with feeds of $1.7\lambda_d$. The sidelobe levels are between -13.9 dB (feed 10) and -9.6 dB (feed 1 and feed 19). The crossover level between the broadside beam and the adjacent beams is -3.8 dB. The simulated H -plane radiation patterns for two-feed-per-beam excitation is shown in Fig. 5.29. The patterns were obtained by exciting the feed pairs with equal amplitude. The applied phase shifts was determined following the procedure outlined in Section 4.5. At the design frequency, the sidelobe levels are between -14 and -20 dB. The crossover level between the broadside beam and the adjacent beams is -2.2 dB. The peak realized gain for the beam closest to broadside (produced by feed 9 and 10) is 17.4 dB which is about 1 dB lower than for the broadside beam in the single-feed-per-beam design. This difference is partly due to the additional 0.4-dB insertion loss introduced by the second input transition and partly due to the suboptimal illumination leading to a wider beamwidth of 7° (about 5.5° in the single-feed-per-beam configuration).

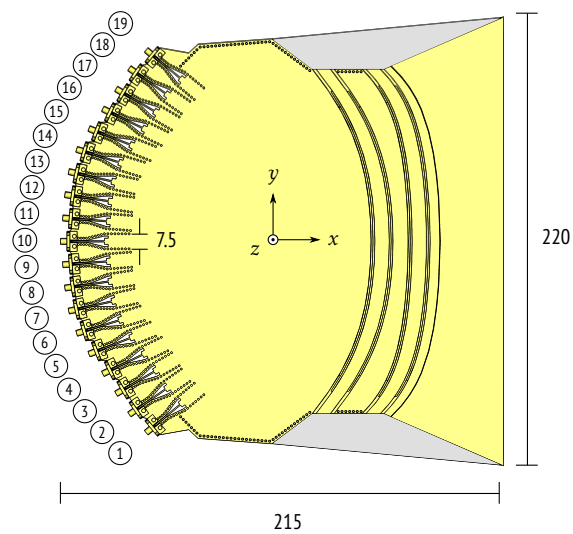


Figure 5.25: Top view of PCB lens model with multiple-feed-per-beam excitation (all dimensions in mm).

5.7 Comparison with State-of-the-Art Solutions and Discussion

Table 5.1 summarizes the simulated performances. A comparison with related low-profile designs is provided. It should be noted that the listed performance parameters refer to measured data. It can be seen that the field of view of previous solutions with linear aperture is typically limited to about 40° . The proposed design presents a significant improvement in this respect. The main limitation is the thickness of the lens, which scales with its diameter.

5.8 Chapter Summary

The design of a parallel-plate lens in PCB technology was presented. It was shown that the degrees of freedom in a two-lens system can be exploited to design a low-profile beamformer with good scanning performance over an angular range of $\pm 40^\circ$. Furthermore, it was demonstrated that useful patterns can be obtained over an enhanced field of view of $\pm 60^\circ/10.5$ beamwidths due to the refraction at the dielectric-air interface.

The design process of an orthogonal and an overlapping feed system was described. The determination of the beam port contour and the feed dimensioning were facilitated by the technique outlined in Chapter 4. To demonstrate the

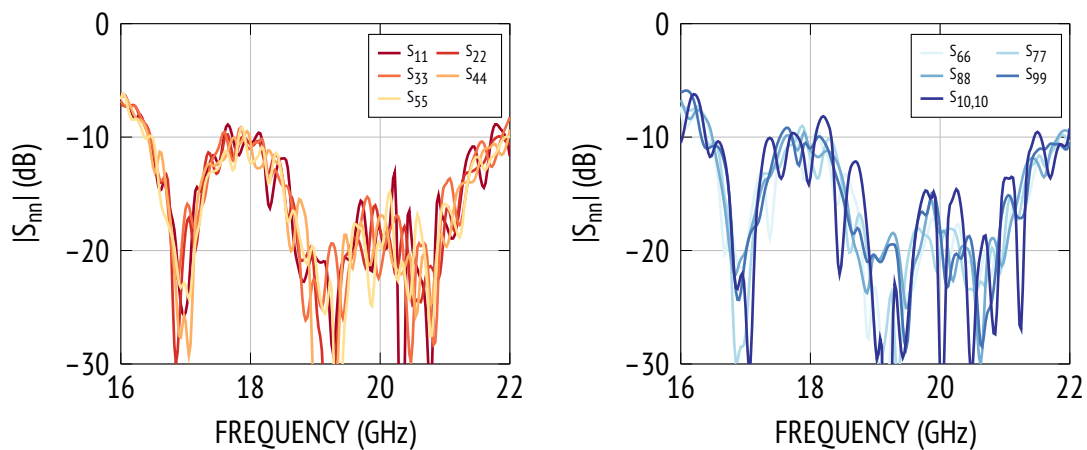


Figure 5.26: Simulated input reflection coefficient for the two-feed-per-beam configuration.

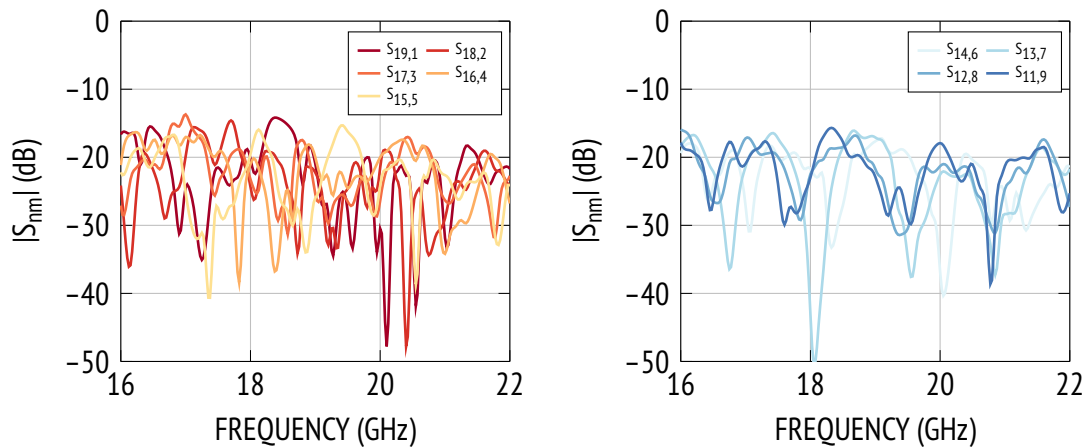


Figure 5.27: Simulated mutual coupling between conjugate input ports for the two-feed-per-beam configuration.

scanning performance, a plane flare was added to the lens beamformer.

Full-wave simulations of the single-feed-per-beam configuration with a diameter of $10.9\lambda_0$ and nine feeds showed a return loss greater than 12 dB and a worst-case port-to-port isolation of 14 dB in the 17.3–20.2 GHz band. Gain variations are smaller than 2.1 dB and sidelobe levels less than -12 dB for all beams. At the design frequency, the simulated scan loss is 2.2 dB for a beam pointing at 59° . The radiation efficiency is higher than 80%. For the two-feed-per-beam configuration with a total of 19 feeds, the passive return loss is greater 10 dB and the port-to-port isolation better than 14 dB. The gain loss at 57° is 2.4 dB and the beam crossover levels are higher than -2.2 dB.

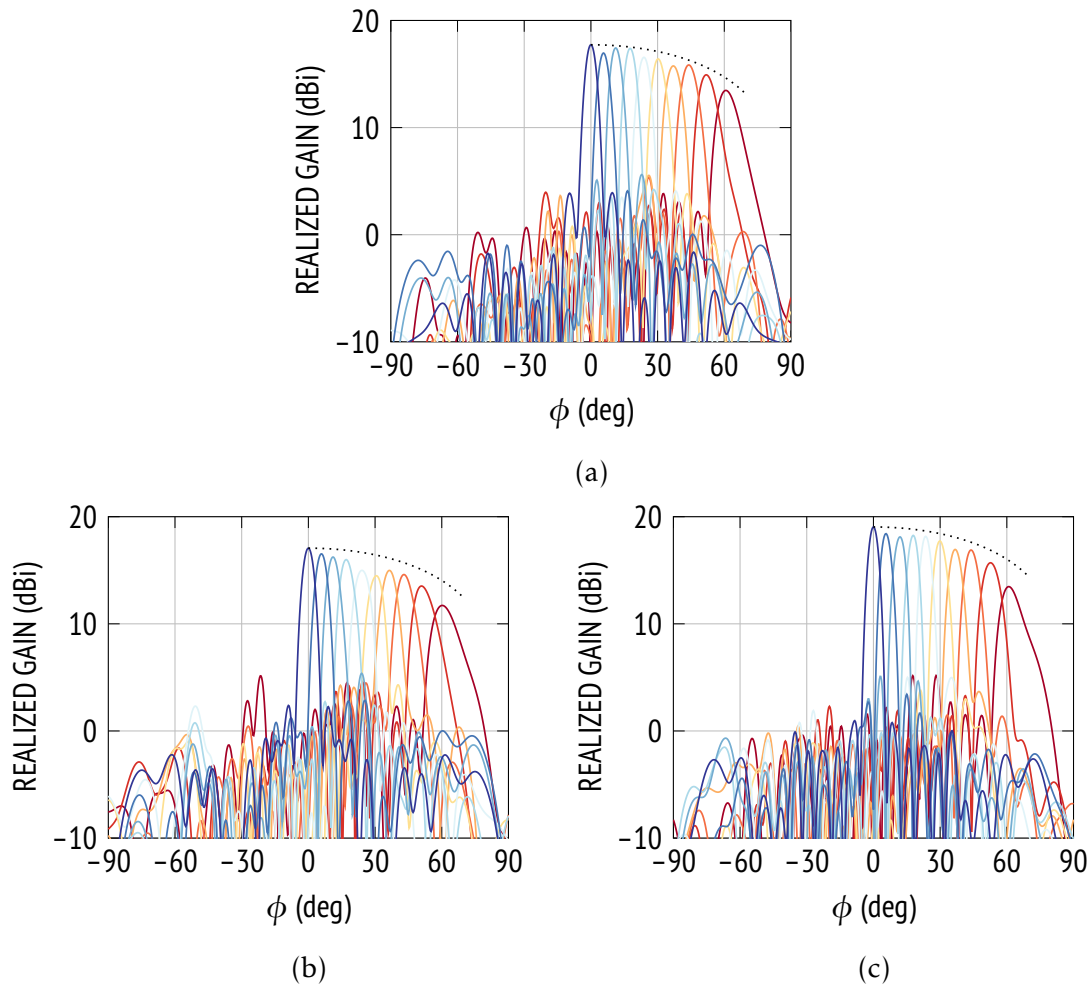


Figure 5.28: Simulated H -plane radiation pattern at (a) 18.75 GHz, (b) 17.3 GHz and (c) 20.2 GHz.

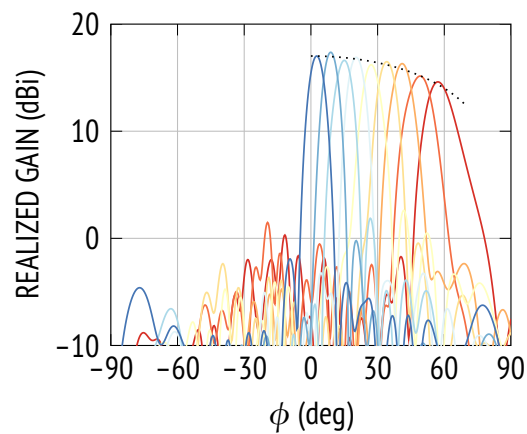


Figure 5.29: Simulated H -plane radiation pattern at 18.75 GHz for two-feed-per-beam excitation.

Table 5.1: Comparison of quasi-optical beamformers based on PCB technology.

Reference	Type	Impedance bandwidth ^a	Size ^b	Max. gain	Scan range	Scan loss ^b	Max. SLL ^b
[8]	Parabolic pillbox	23.5 – 25.75 GHz	$12\lambda \times 11.2\lambda \times 0.08\lambda$	n.a.	$\pm 30^\circ$	0.6 dB	-12.2 dB
[18]	Rotman lens	23.6 – 24.4 GHz	$10.5\lambda \times 8\lambda \times 0.12\lambda$	22.6 dBi	$\pm 33^\circ/4.2$ BW	1.65 dB	-15 dB
[27]	Luneburg lens	> 9 – 13 GHz	$(5.2\lambda)^2\pi \times 0.04\lambda$ ^c	51%	$\pm 45^\circ/10$ BW	1 dB	-13 dB
[116]	Luneburg lens + linear array	78.6 – 80.2 GHz	n.a.	12.3 dBi	$\pm 41^\circ/4$ BW	2.5 dB	-7 dB
This work ^d	Continuous PPW lens	17.3 – 20.2 GHz	$14.7\lambda \times 13.8\lambda \times 0.8\lambda$	18.5 dBi	$\pm 59^\circ/10$ BW	2.2 dB	-14 dB

^a Referring to the frequency range within which the return loss is greater than 10 dB for all beam ports.

^b Referring to the design frequency and/or the pattern in the plane of scan.

^c The size of the flare is not taken into account.

^d Only full-wave simulation results of the single-feed-per-beam configuration are considered.

Due to its large scanning range and compatibility with PCB manufacturing processes, the lens design is an attractive candidate for cost-effective active antenna configurations in LEO satellite networks. The presented design, fitted with a flared horn, can be stacked to provide electronically steerable spot beams. In such a configuration, the relatively high radiation efficiency of the system is a clear benefit. However, a further reduction in height (towards $\lambda_0/2$) is essential if a field of view of $\pm 60^\circ$ in the two orthogonal planes is targeted.

CHAPTER 6

Conclusion

This chapter summarizes the main contributions and most significant achievements presented in this work. The limitations and opportunities of the proposed analysis techniques and designs are discussed. Possible directions for future research are identified.

6.1 Summary and Discussion

The main objective of this research work was to investigate and develop quasi-optical systems with beam scanning and beam reconfiguration capabilities. Considering the complex link geometries in LEO/MEO satellite communications, the main focus was put on the requirements of wide field of view and continuous coverage. Among various quasi-optical designs, the concept of continuous parallel-plate lenses was selected as the most promising solution in terms of bandwidth, radiation efficiency, fabrication cost and complexity, and conformity with other parts of a satellite antenna system. This research work has led to the development of two novel lens designs operating in the uplink and downlink Ka-band, respectively. Furthermore, contributions have been made to the electromagnetic modeling of parallel-plate beamformers, which provide a valuable tool for the analysis and synthesis of advanced feed configurations.

6.1.1 Numerical Methods for the Analysis and Design of Parallel-Plate Beamformers

High-frequency models have been proposed for various quasi-optical systems implemented in parallel-plate waveguide technology. Typically, these models are based on transmit-mode analysis and, when coupled with an optimization

process in the secondary pattern space, can be used to efficiently design multi-beam antennas. However, this approach becomes impractical as the number of feeds and beams increases, especially when cluster feeds are employed on a beam port curve that is not restricted to a certain geometry. This work presented numerical models for the receiving problem, which enable a fast and rigorous characterization of arbitrary feed arrangements.

A comparison of asymptotic high-frequency methods for analyzing quasi-optical systems in reception was made. It was found that for the problems of interest, physical optics provides the best trade-off between accuracy and computation efficiency.

Two-dimensional models for receiving pillbox reflectors and constrained lenses were introduced. An accurate prediction of the entire focal-region distribution over a wide range of incidence angles ($> 30^\circ$, 10 beamwidths) was demonstrated for parabolic pillbox reflectors. The model presented for constrained lenses represents a starting point for the analysis of more practical designs. A more accurate description taking into account the mutual coupling between the array ports can be obtained using integral equation techniques. Furthermore, a procedure for analyzing continuous parallel-plate lenses in reception was proposed. The propagation between outer and inner lens contour is predicted using a previously proposed ray-tracing technique, while physical optics is used to determine the field distribution in the focal region. The model was validated through full-wave simulations using a commercial finite-element solver (Ansoft HFSS).

A method based on reciprocity for evaluating the coupling between the received fields and realistic feed aperture distributions was described. One advantage of this approach is that the interaction between the quasi-optical system and the feed can be fully characterized by means of a scalar quantity, referred to as transfer efficiency or T factor. This approach was used to determine the maximum scan-gain contour of parabolic pillbox reflectors. It was shown that for reflectors with low to moderate F/D , near-optimal scanning performance is achieved when employing feeds on the focal plane. This property is particularly advantageous for mechanical scanning antennas. Furthermore, it was shown that the method can be used to derive improved feed contours for Rotman lenses with suboptimal on-axis to off-axis focal ratio.

An extension of the numerical procedure to the synthesis of feed clusters was presented. It was found that for small feed apertures ($< \lambda$), the assumption of

vanishing fields on the aperture plane is no longer valid, causing a noticeable discrepancy between the calculated and simulated transfer efficiency. However, full-wave simulations of a continuous PPW lens showed that the associated cluster weights yield secondary patterns that are in good agreement.

6.1.2 Continuous Parallel-Plate Waveguide Lens for Mechanical Wide-Angle Beam Steering

The primary goal of this work was to develop a mechanism for continuous beam steering that is compatible with parallel-plate lenses. Here, a novel feed system based on the non-contact characteristic of gap waveguides was proposed. The main advantages of this design over flexible coaxial cables and rotary waveguide joints are its wide bandwidth, low profile and mechanical ruggedness.

An approximate analytical approach and full-wave simulations were used to design and optimize the EBG structure of a groove gap waveguide operating in the uplink Ka-band. The final design provides a stopband of about one octave (22–45 GHz). A non-contacting choke flange for connecting the feed system to a standard waveguide was developed, thus avoiding the need for additional support structure. Simulations of the proposed choke joint demonstrated a return loss greater than 20 dB and an insertion loss less than 0.1 dB in the 25–35 GHz band for a gap of $\lambda_0/20$, which is comparable with state-of-the-art designs.

A previously developed optimization routine based on ray tracing was used to fit the contours of a parallel-plate lens to a focal arc that is compatible with the mechanical design of the feed system. Simulations of the resulting structure at the design frequency (29.25 GHz) showed a scan loss of 2 dB at 35° and sidelobes below –17 dB within the entire field of view. To extend the scanning range up to $\pm 50^\circ$, a system of two parallel-plate lenses was developed. An all-metal prototype, comprising the final dual-lens design and the gap waveguide feed system, was successfully manufactured and measured. Measurements showed a scan loss of 2.7/3.3 dB at the center frequency when scanning out to $\pm 50^\circ$. The return loss is greater than 12 dB in the 27.5–31 GHz for all measured feed positions.

The integration of the feed system into the lens required structural modifications, such as a circular feed motion path and a rotation of the lens and radiating aperture by 90°, limiting its scanning performance and conformity compared to

multiple-beam designs. On the other hand, the developed feed concept can be adopted for a wide range of quasi-optical systems requiring rapid translational or rotational feed displacement.

6.1.3 Lens Beamformer in Multilayer PCB Technology using Overlapping Feed Clusters

Another main objective of this work was to develop a solution to the problem of high-crossover low-sidelobe patterns. Previous quasi-optical beamformers rely on the split aperture decoupling method at the expense of increased size and cost. In this thesis, a parallel-plate lens employing overlapping feed clusters was proposed. The design process was limited to the focal array, quasi-optical system and radiating part; the design of a network providing the desired excitations was not addressed in this work. A novel cost-effective implementation of the lens in multilayer PCB technology was proposed. A proof-of-concept design for Ka-band (downlink) operation was presented. The techniques presented in Chapter 4 were used to optimize the feed curve and to determine the complex cluster weights. The final structure employs 19 feeds for a total of 18 beams and a linear flare at the output. Simulations at the design frequency showed a gain loss of 2.4 dB at 58° , a beam crossover level of -2.2 dB and a radiation efficiency of about 81%.

Due to its reduced profile, linear aperture and high scanning performance, the design presents an attractive solution for highly integrated active antennas with stringent coverage requirements.

6.2 Future Directions

The numerical models presented in Chapter 4 were based on the assumption of an infinite parallel-plate environment. In a practical design where no absorbing material or dummy ports are used, the internal field distribution is affected by reflections at the metallic sidewalls, especially for large scan angles. Iterative physical optics could be used for a more rigorous analysis of pillbox reflectors and continuous PPW lenses taking into account this effect. At feed level, edge diffraction must be considered to allow for an accurate characterization of electrically small apertures and cluster feeds.

Further investigation is needed to determine the compatibility of the gap wave-

uide feed presented in Chapter 3 with other quasi-optical beamformers. All-metal implementations of pillbox couplers, lenses based on artificial dielectrics and geodesic lenses appear to be the most promising solutions. Parallel-plate designs in which the low profile of the feed system is maintained are of interest for stacked arrangements with corporate feeding. The resulting array of beamformers would offer hybrid electro-mechanical beam scanning in two orthogonal planes. Furthermore, the proposed beamformer can be integrated with a continuous transverse stub array to realize high-gain antennas with wide-angle steering capability.

The lens beamformer described in Chapter 5 must be constructed and measured to validate the proposed functional and technological concept. The structure was developed with the goal to provide stable radiation patterns with high-crossover over a field of view of $\pm 60^\circ$. In future work, lens and focal array can be designed to implement an isoflux gain profile.

Appendix A

Effects of Primary Aberrations on the Radiation Pattern of a Line Source

In antenna problems, the term *aberration* is used to describe the departure of the phase of a wavefront from a certain reference. Following the principle of geometrical optics, rays can be traced from the phase center of a feed to the aperture plane. The difference in path length between any arbitrary ray and a reference ray, in most cases the ray passing through the center of the aperture, can be defined as ΔL . The related phase aberration can then be written as

$$\Delta\psi = k\Delta L. \quad (\text{A.1})$$

Assuming rotational symmetry, the path length error across the aperture plane can be represented by a function of cylindrical coordinates (ρ, ϕ) . To provide a more illustrative representation of the different types of phase aberrations, the function $\Delta L(\rho, \phi)$ can be expanded into a power series with arguments ρ and $\cos\phi$. This leads to a representation of the wavefront aberration function in terms of so called Zernike polynomials, i.e., the aberration surface is described by a set elementary functions orthonormal on a unit circle [97, pp. 527–532]:

$$\Delta L(\rho, \phi) = S_1\rho \cos\phi + S_2\rho^2 + S_3\rho^2 \cos(2\phi) + S_4\rho^3 \cos(\phi) + S_5\rho^4, \quad (\text{A.2})$$

where only the five lowest-order terms of the power series have been retained. These terms represent the five primary aberrations, also known as Seidel aberrations. They are identified as distortion, curvature of field, astigmatism, coma and spherical aberration. To better understand the effect of these phase terms on the radiation from the aperture plane, the problem can be reduced to two dimensions. In this case, the aperture field is described by a line distribution,

and the error function therefore simplifies to

$$\Delta L(\rho, \phi) = S_1 x + S_2 x^2 + S_3 x^3 + S_4 x^4. \quad (\text{A.3})$$

The term representing field curvature and astigmatism degenerate into one single term since $\phi = 0$, so that the five primary aberrations reduce to linear, quadratic, cubic and quartic errors. Following the analysis in [111, pp. 186–192] for a two-dimensional aperture of width D with a uniform field distribution along y , the far-field pattern in the plane $y = 0$ can be described by

$$F(\theta) = \int_{-D/2}^{D/2} f(x') e^{jk \sin \theta x'} dx' \quad (\text{A.4})$$

where $f(x)$ denotes the distribution over the aperture. Introducing the new variables $\tilde{x} = 2x'/D$ and $u = (\pi D/\lambda) \sin \theta$, the above expression reduces to

$$F(\theta) = \frac{D}{2} \int_{-1}^1 f(\tilde{x}) e^{ju\tilde{x}} d\tilde{x} \quad (\text{A.5})$$

Assuming that the phase distribution only varies along the x direction, the pattern function can be expressed as

$$F(u) = \frac{D}{2} \int_{-1}^1 A(\tilde{x}) e^{j[u\tilde{x} - \psi(\tilde{x})]} d\tilde{x} \quad (\text{A.6})$$

where $A(\tilde{x})$ represents the amplitude and $\psi(\tilde{x})$ the phase distribution across the aperture.

Linear Phase Error

Including the first-order error term in the phase function leads to a pattern given by

$$F(u) = \frac{D}{2} \int_{-1}^1 A(\tilde{x}) e^{j(u - kS_1)\tilde{x}} d\tilde{x} \quad (\text{A.7})$$

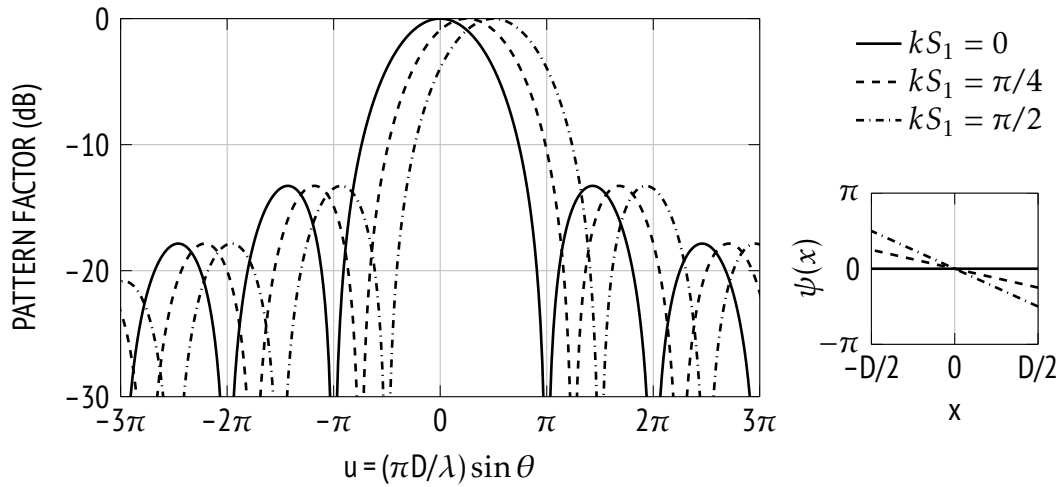


Figure A.1: Effect of linear phase error on radiation pattern.

The introduced phase error does not disturb the pattern shape but shifts the beam maximum to an off-axis angle

$$\theta_0 = \sin^{-1} \left(\frac{2S_1}{D} \right) \quad (\text{A.8})$$

or $u_0 = kS_1$. A phase error coefficient of $kS_1 = \pi/4$ implies that the phase ψ at the edge of the aperture is equal to $\pi/4$. The beam squint is accompanied by a decrease in gain as the dimension of the projected aperture is reduced by a factor of $\cos \theta_0$. The radiation pattern of a uniformly illuminated aperture with linear phase variation is shown in Fig. A.1.

Quadratic Phase Error

Second-order aberrations give rise to a pattern described by

$$F(u) = \frac{D}{2} \int_{-1}^1 A(\tilde{x}) e^{j(u\tilde{x} - kS_2\tilde{x}^2)} d\tilde{x} \quad (\text{A.9})$$

As can be seen from Fig. A.2, a quadratic phase error is mainly reflected in increased sidelobe levels, null filling between the sidelobes and decreased peak directivity. This effect on the pattern is symmetrical about $\theta = 0^\circ$ since the second-order term is symmetrical about $x = 0$. Moreover, it is found that the main lobe becomes bifurcated, having two symmetrical off-axis maxima, when S_2 becomes sufficiently large. Similar far-field patterns can be observed in

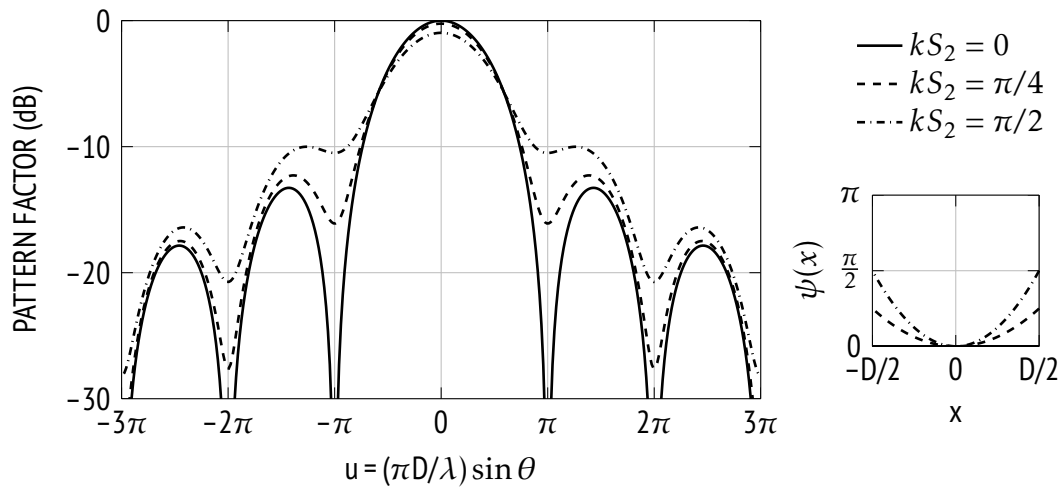


Figure A.2: Effect of quadratic phase error on radiation pattern.

the principal plane of sectoral horn antennas with large flare angles, where the constant phase contours reaching the aperture are rather cylindrical than plane. Moreover, the patterns shown in Fig. A.2 bear resemblance to the field distribution observed in the radiating near-zone of an antenna. This is due to the fact that plane apertures appear curved to observation points in close vicinity, which likewise leads to a Fresnel integral when evaluating the radiated fields.

Cubic Phase Error

Including the third-order error in the phase term leads to a radiation pattern given by

$$F(u) = \frac{D}{2} \int_{-1}^1 A(\tilde{x}) e^{j(u\tilde{x} - kS_3\tilde{x}^3)} d\tilde{x} \quad (\text{A.10})$$

The effect of cubic phase variation is a beam shift as in the case of a linear error. Moreover, the pattern becomes asymmetric with respect to the main lobe, that is, the sidelobes decrease on the side nearer to $\theta = 0$ and increase on the other side of the main lobe. As seen from Fig. A.3, the tilt of the main lobe is accompanied by a significant loss in gain at broadside. The gain loss and sidelobe level due to cubic phase errors are shown in Fig. A.5. It should be highlighted that the reduction in gain does not refer to the maxima of the tilted beams but to the gain drop at broadside.

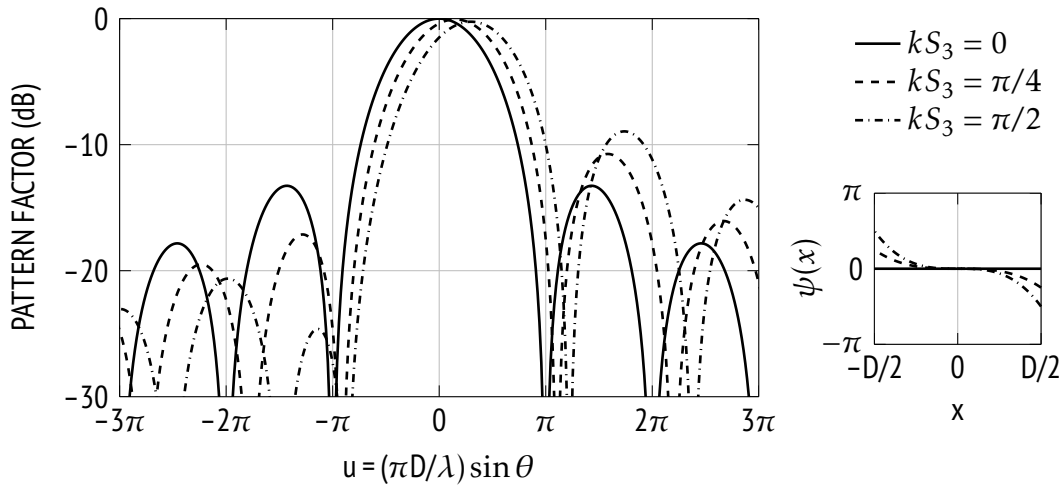


Figure A.3: Effect of cubic phase error on radiation pattern.

Quartic Phase Error

For quartic phase variation the radiation pattern becomes

$$F(u) = \frac{D}{2} \int_{-1}^1 A(\tilde{x}) e^{j(u\tilde{x} - kS_4\tilde{x}^4)} d\tilde{x} \quad (\text{A.11})$$

The effect of fourth-order errors is similar to that of quadratic ones. However, it is clear from Fig. A.3 that the beam distortion is less pronounced since for the same peak error, the total error over the aperture is less. The gain loss and sidelobe level due to quartic errors are shown in Fig. A.5. It should be noted that for $S_4 > \pi/2$, the first side lobe is almost entirely absorbed into a broadened main lobe and can no longer be identified as secondary lobe.

Gain Calculation

The broadside gain of a two-dimensional aperture with symmetrical field distribution $f(\tilde{x})$ is given by

$$G_{\max} = \frac{\pi D}{\lambda} \frac{\left| \int_{-1}^1 f(\tilde{x}) d\tilde{x} \right|^2}{\int_{-1}^1 |f(\tilde{x})|^2 d\tilde{x}} \quad (\text{A.12})$$

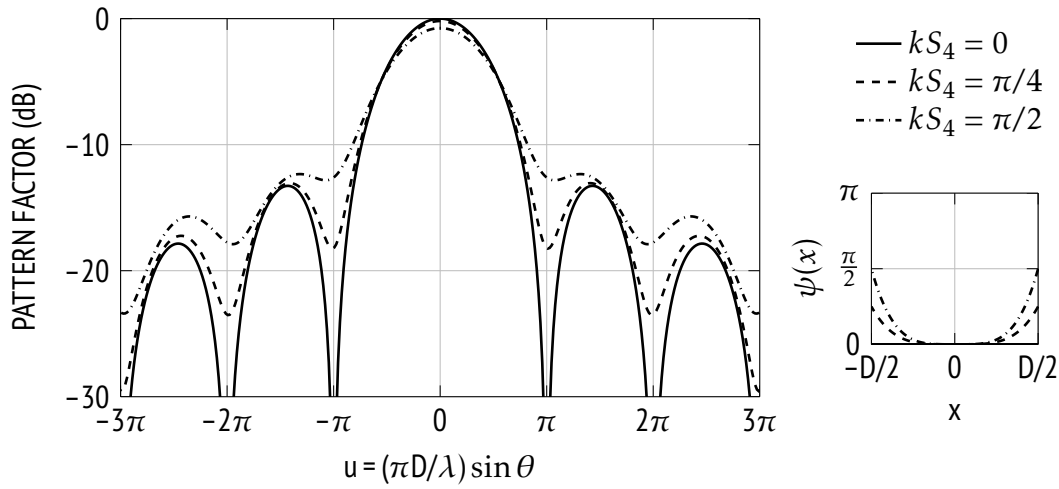


Figure A.4: Effect of quartic phase error on radiation pattern.

The gain loss can then be computed from

$$\text{Gain Loss} = \frac{\text{gain with phase error}}{\text{gain without phase error}} = \frac{\left| \int_{-1}^1 A(\tilde{x}) e^{-j\psi(\tilde{x})} d\tilde{x} \right|^2}{\left| \int_{-1}^1 A(\tilde{x}) d\tilde{x} \right|^2} \quad (\text{A.13})$$

Note that the above equation is only adequate for predicting the gain drop due second- and higher order phase errors. For linear phase variation, which in most cases is not considered as an actual error, the relevant reduction in gain is still equal to $\cos \theta_0$.

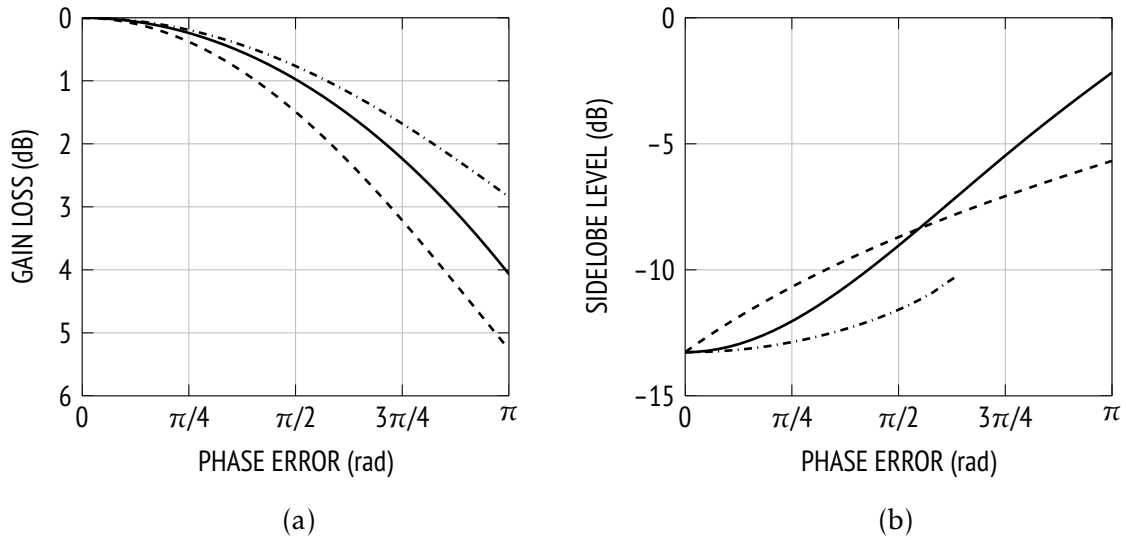


Figure A.5: Gain loss and sidelobe level due to quadratic (—), cubic (--) and quartic (---) phase error.

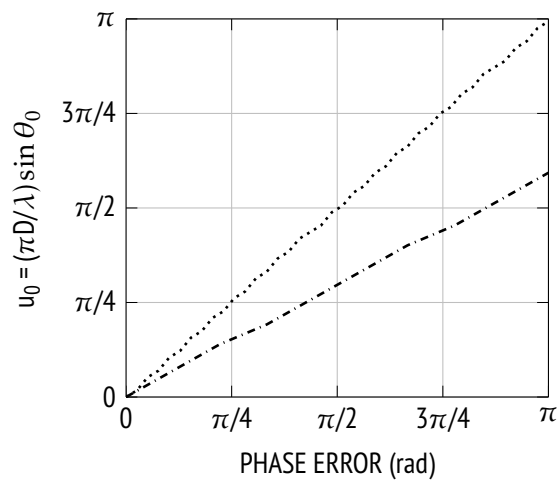


Figure A.6: Beam tilt due to linear (.....) and cubic (---) phase error.

156 A. Effects of Primary Aberrations on the Radiation Pattern of a Line Source

Appendix B

Phase Error Analysis of Bifocal Lens Model

The constrained lens model shown in Fig. B.1 is considered. The lens contour is determined by the path length conditions of the two focal points and given by [11]

$$X = -a_0 F \left[1 - \sqrt{1 - \frac{Y^2}{F^2}} \right] \approx -\frac{a_0}{2F} Y^2 - \frac{a_0}{8F^3} Y^4 - \dots \quad (\text{B.1})$$

It can be shown that the relative error of the series expansion up to the second term is smaller than 4.5% for $F/D \geq 0.7$.

With inner and outer lens contour being collocated the length of the transmission lines is

$$W = a_0 X. \quad (\text{B.2})$$

The path length error for a feed at an angular position ϕ on the focal arc with radius F centered at the vertex of the lens is

$$\Delta l = [F' + W + S] - [F + W_0] \quad (\text{B.3})$$

where S denotes the shortest distance between a point (X, Y) on the lens contour and the wavefront. Simple geometry shows that

$$S = -Yb - Xa \quad (\text{B.4})$$

with $a = \cos \phi$ and $b = \sin \phi$. The distance between the feed location and an arbitrary point on the lens contour is given by

$$F' = \sqrt{(X + aF)^2 + (Y + bF)^2}, \quad (\text{B.5})$$

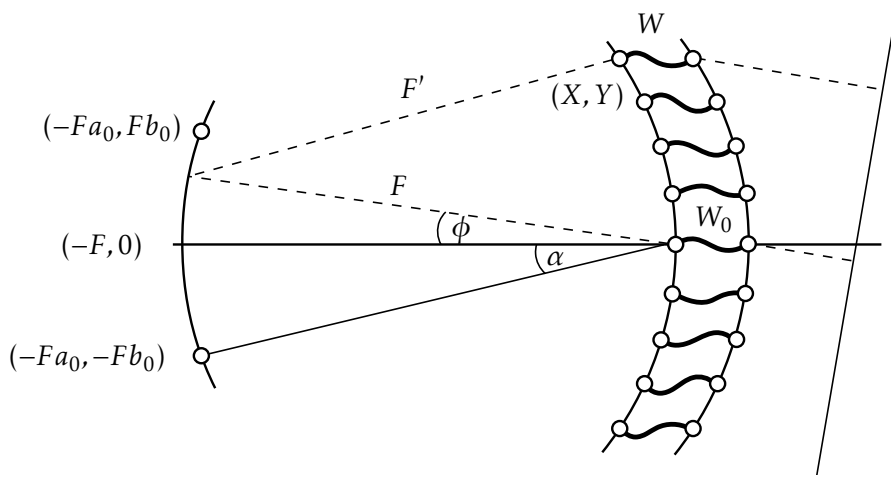


Figure B.1: Constrained bifocal model of a continuous PPW lens.

which can be rewritten as

$$F' = F \sqrt{1 + \frac{2bY}{F} + \frac{b_0^2 Y^2}{F^2} + \frac{2(a-a_0)X}{F}} \quad (\text{B.6})$$

Using the approximate formula of (B.1) and expanding (B.6) into a power series up to the fourth order gives

$$\begin{aligned} F' = & F + bY + \frac{1}{2F} [-aa_0 + a^2 + b_0^2 - b^2] Y^2 \\ & + \frac{b}{2F^2} [aa_0 + b^2 - 1] Y^3 \\ & + \frac{1}{8F^3} [-a^2 a_0^2 - a(-2a_0^3 + 6a_0 b^2 - 2a_0 b_0^2 + a_0) - a_0^4 + a_0^2(6b^2 - 2b_0^2 + 1) \\ & \quad - 5b^4 + 6b^2 b_0^2 - b_0^4] Y^4 \end{aligned} \quad (\text{B.7})$$

Substituting (B.6) along with (B.2) and (B.4) into (B.3) leads to

$$\begin{aligned} \Delta l = & \frac{1}{2F} [b_0^2 - b^2] Y^2 \\ & + \frac{b}{2F^2} [aa_0 + b^2 - 1] Y^3 \\ & + \frac{1}{8F^3} [-a^2 a_0^2 - a(-2a_0^3 + 6a_0 b^2 - 2a_0 b_0^2) - a_0^4 + a_0^2(6b^2 - 2b_0^2) \\ & \quad - 5b^4 + 6b^2 b_0^2 - b_0^4] Y^4 \end{aligned} \quad (\text{B.8})$$

Appendix C

Geometrical Optics Analysis of a Two-Lens System

A system formed by two centered thin lenses is considered. Since the optical system is supposed to act as a transmitting antenna, the goal is to form an image at infinity at the output. The lenses may be either converging or diverging and thus four configurations can be distinguished. Examining the different ray diagrams shows that an image at infinity cannot be formed by a real object when both lenses are diverging. Moreover, it can be shown that in the case where the first lens is diverging¹, the angle subtended by the final image (i.e., the beam pointing angle) is much smaller than the angle subtended by the object, implying a limited field of view. Hence, only the two configurations depicted in Fig. C.1 are considered. Referring to Fig. C.1(a) the image formation by the two lenses is described by

$$\frac{1}{\overline{O_1A'_1}} - \frac{1}{\overline{O_1A_1}} = \frac{1}{\overline{O_1F'_1}} \quad (\text{C.1a})$$

$$\frac{1}{\overline{O_2A'_2}} - \frac{1}{\overline{O_2A_2}} = \frac{1}{\overline{O_2F'_2}} \quad (\text{C.1b})$$

where distances measured to the left of the origins are negative. Furthermore, the linear magnification of the first lens is given by

$$M_1 = \frac{\overline{A'_1B'_1}}{\overline{A_1B_1}} = \frac{\overline{O_1A'_1}}{\overline{O_1A_1}}. \quad (\text{C.2})$$

¹On receive, this configuration is equivalent to a Galilean telescope.

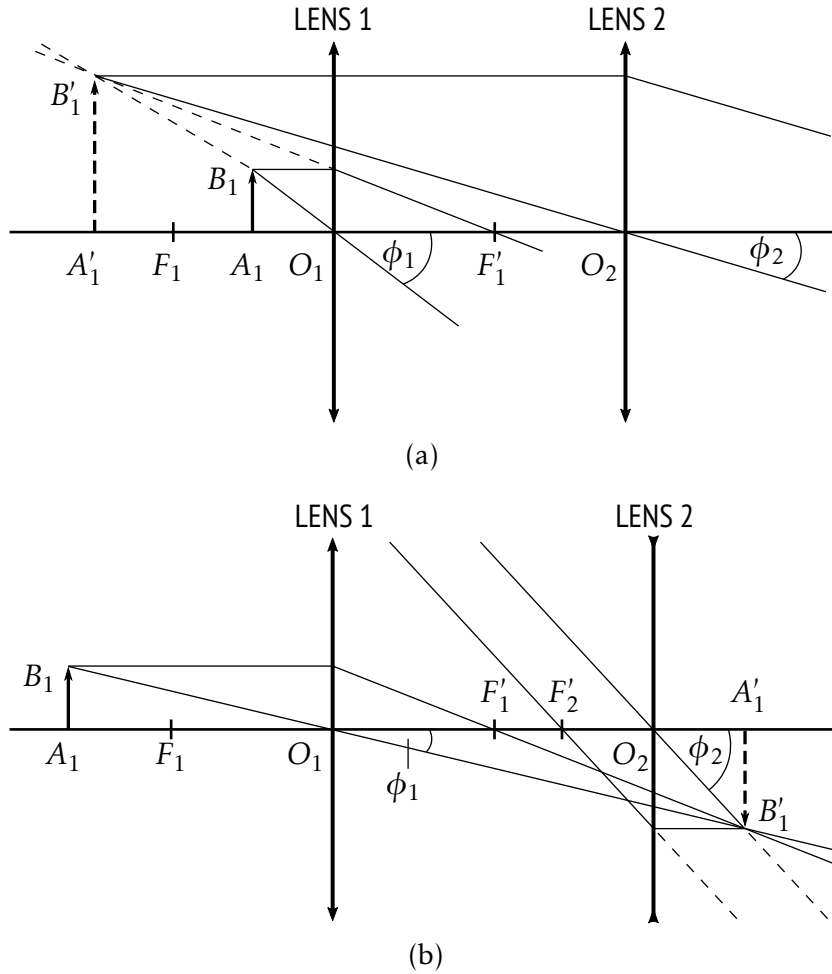


Figure C.1: Image formation in a system formed by (a) two converging lenses, (b) one converging and one diverging lens.

The angles subtended by object and image can be written as

$$\tan \phi_1 = \frac{\overline{A_1 B_1}}{\overline{O_1 A_1}} = \frac{\overline{A_1' B_1'}}{\overline{O_1 A_1'}} \quad (\text{C.3a})$$

$$\tan \phi_2 = \frac{\overline{A_1' B_1'}}{\overline{O_2 A_1'}} = \frac{\overline{A_1' B_1'}}{\overline{O_2 F_2'}}. \quad (\text{C.3b})$$

Solving (C.2) for $\overline{A_1' B_1'}$ and (C.1a) for $\overline{O_1 A_1'}$, and substituting both expressions into (C.3b) gives

$$\tan \phi_2 = \frac{\overline{A_1 B_1}}{f_2} \frac{f_1}{f_2 [f_1 + \overline{O_1 A_1}]} \quad (\text{C.4})$$

with $f_1 = \overline{O_1F'_1}$ and $f_2 = \overline{O_2F'_2}$.

Letting $\overline{O_1A_1} = -gf_1$, where $g = 1$ refers to an object on the focal plane of the first lens, (C.4) can be rewritten as

$$\tan \phi_2 = \frac{\overline{A_1B_1}}{f_2(1-g)}. \quad (\text{C.5})$$

Moreover, the distance between the two lenses can be expressed as

$$l = \overline{O_1A'_1} - \overline{O_2A'_1}. \quad (\text{C.6})$$

To form an image at infinity, the distance of the virtual image from the second lens must equal its focal distance, i.e., $-\overline{O_2A'_1} = f_2$. Thus,

$$f_2 = l - \overline{O_1A'_1}. \quad (\text{C.7})$$

It can be shown that

$$\overline{O_1A'_1} = \frac{gf_1}{g-1} \quad (\text{C.8})$$

which by substitution into (C.7) leads to the required focal distance

$$f_2 = l + \frac{gf_1}{1-g} \quad (\text{C.9})$$

for a desired object distance g . The angular magnification is then given by

$$\frac{\tan \phi_1}{\tan \phi_2} = \frac{\overline{A_1B_1}}{\overline{O_1A_1}} \frac{f_2(1-g)}{\overline{A_1B_1}} = 1 + \frac{(1-g)l}{gf_1}. \quad (\text{C.10})$$

Assuming a maximum lateral feed displacement of $\overline{A_1B_1} = D/2$, the scan angle predicted by (C.5) using (C.9) is

$$\phi_{2(\max)} = \tan^{-1} \frac{D/2}{(1-g)l + gf_1}. \quad (\text{C.11})$$

Based on (C.9) and (C.10) the two configurations from Fig. C.1 can be recognized:

1. For $g < 1$ (i.e., the feed is placed between the first lens and its focal plane), $f_2 > 0$, which corresponds to a converging lens. Further, $\tan \phi_1 > \tan \phi_2$ or $\phi_1 > \phi_2$.
2. For $g > 1$ (i.e., the feed is placed behind the focal plane of the first lens)

and $l < \overline{O_1A'_1}$, $f_2 < 0$, which corresponds to a diverging lens. Further, $\tan \phi_1 < \tan \phi_2$ or $\phi_1 < \phi_2$.

The second configuration appears promising in that it provides a beam pointing angle larger than the feed position angle. However, $g > 1$ leads to a larger axial dimension, and thus to a smaller α_1 for $\overline{A_1B_1} = D/2$. Parametric studies show that for most practical values of f_1/D , g and l , the magnification is not sufficient to achieve the required exit angle.

The system formed by two converging lenses offers a wider field of view with a more compact design and was therefore the preferred solution.

Bibliography

- [1] I. Philbeck, "Connecting the unconnected: working together to achieve Connect 2020 agenda targets," International Telecommunication Union (ITU), Davos, Switzerland, 2017.
- [2] M. Kretschmer, "Connecting the unconnected: tackling the challenge of cost-effective broadband internet in rural areas," Fraunhofer Institute for Applied Information Technology (FIT), 2019.
- [3] G. Maral and M. Bousquet, *Satellite Communications Systems: Systems, Techniques and Technology*, 5th ed. Chichester: John Wiley & Sons, 2009.
- [4] J. Blass, "Multidirectional antenna – a new approach to stacked beams," in *IRE Int. Conv. Rec.*, pt. 1, 1960, pp. 48–50.
- [5] J. Butler and R. Lowe, "Beam-forming matrix simplifies design of electronically scanned antennas," *Electron. Design*, pp. 170–173, Apr. 1961.
- [6] E. Gandini, M. Ettorre, M. Casaletti, K. Tekkouk, L. Le Coq, and R. Sauleau, "SIW slotted waveguide array with pillbox transition for mechanical beam scanning," *IEEE Antennas Wireless Propag. Lett.*, vol. 11, pp. 1572–1575, 2012.
- [7] W. Rotman, "Wide-angle scanning with microwave double-layer pillboxes," *IEEE Trans. Antennas Propag.*, vol. 6, no. 1, pp. 96–105, Jan. 1958.
- [8] M. Ettorre, R. Sauleau, and L. Le Coq, "Multi-beam multi-layer leaky-wave SIW pillbox antenna for millimeter-wave applications," *IEEE Trans. Antennas Propag.*, vol. 59, no. 4, pp. 1093–1100, Apr. 2011.
- [9] M. Ettorre, F. Foglia Manzillo, M. Casaletti, R. Sauleau, L. Le Coq, and N. Capet, "Continuous transverse stub array for Ka-band applications," *IEEE Trans. Antennas Propag.*, vol. 63, no. 11, pp. 4792–4800, Nov. 2015.
- [10] W. E. Kock, "Metal-lens antennas," *Proc. IRE*, vol. 34, no. 11, pp. 828–836, Nov. 1946.

-
- [11] J. Ruze, "Wide-angle metal-plate optics," *Proc. IRE*, vol. 38, no. 1, pp. 53–59, Jan. 1950.
- [12] H. Gent, "The bootlace aerial," *Roy. Radar Establishment Jour.*, pp. 47–57, 1957.
- [13] W. Rotman and R. Turner, "Wide-angle microwave lens for line source applications," *IEEE Trans. Antennas Propag.*, vol. 11, no. 6, pp. 623–632, Nov. 1963.
- [14] T. Katagi, S. Mano, and S.-I. Sato, "An improved design method of Rotman lens antennas," *IEEE Trans. Antennas Propag.*, vol. 32, no. 5, pp. 524–527, May 1984.
- [15] N. J. G. Fonseca, "A focal curve design method for Rotman lenses with wider angular scanning range," *IEEE Antennas Wireless Propag. Lett.*, vol. 16, pp. 54–57, 2017.
- [16] M. S. Smith and A. K. S. Fong, "Amplitude performance of Ruze and Rotman lenses," *Radio Electron. Eng.*, vol. 53, no. 9, pp. 329–336, Sep. 1983.
- [17] A. F. Peterson and E. O. Rausch, "Scattering matrix integral equation analysis for the design of a waveguide Rotman lens," *IEEE Trans. Antennas Propag.*, vol. 47, no. 5, pp. 870–878, May 1999.
- [18] K. Tekkouk, M. Ettorre, L. Le Coq, and R. Sauleau, "Multibeam SIW slotted waveguide antenna system fed by a compact dual-layer Rotman lens," *IEEE Trans. Antennas Propag.*, vol. 64, no. 2, pp. 504–514, Feb. 2016.
- [19] Y. Liu, H. Yang, Z. Jin, F. Zhao, and J. Zhu, "Compact Rotman lens-fed slot array antenna with low sidelobes," *IET Microw., Antennas & Propag.*, vol. 12, no. 5, pp. 656–661, Apr. 2018.
- [20] R. E. Clapp, "Extending the R-2R Lens to 360°," *IEEE Trans. Antennas Propag.*, vol. 32, no. 7, pp. 661–671, Jul. 1984.
- [21] L. C. Gunderson, "An electromagnetic analysis of a cylindrical homogeneous lens," *IEEE Trans. Antennas Propag.*, vol. 20, no. 4, pp. 476–479, Jul. 1972.
- [22] A. S. Gutman, "Modified Luneburg lens," *Jour. Appl. Phys.*, vol. 25, no. 7, pp. 855–859, Jul. 1957.

- [23] H. Mosallaei and Y. Rahmat-Samii, "Nonuniform Luneburg and two-shell lens antennas: radiation characteristics and design optimization," *IEEE Trans. Antennas Propag.*, vol. 49, no. 1, pp. 60–69, Jan. 2001.
- [24] G. Peeler and D. Archer, "A two-dimensional microwave Luneberg lens," *IRE Trans. Antennas Propag.*, vol. 1, no. 1, pp. 12–23, Jul. 1953.
- [25] C. Hua, X. Wu, N. Yang, and W. Wu, "Air-filled parallel-plate cylindrical modified Luneberg lens antenna for multiple-beam scanning at millimeter-wave frequencies," *IEEE Trans. Microw. Theory Techn.*, vol. 61, no. 1, pp. 436–443, Jan. 2013.
- [26] L. Xue and V. Fusco, "Patch-fed planar dielectric slab waveguide Luneburg lens," *IET Microw., Antennas & Propag.*, vol. 2, no. 2, pp. 109–114, Mar. 2008.
- [27] C. Pfeiffer and A. Grbic, "Printed, broadband Luneburg lens antenna," *IEEE Trans. Antennas Propag.*, vol. 58, no. 9, pp. 3055–3059, Sep. 2010.
- [28] C. D. Diallo, E. Girard, H. Legay, and R. Sauleau, "All-metal Ku-band Luneburg lens antenna based on variable parallel plate spacing fakir bed of nails," in *Proc. 11th Eur. Conf. Antennas Propag. (EuCAP)*, Mar. 2017, pp. 1401–1404.
- [29] O. Quevedo-Teruel, J. Miao, M. Mattsson, A. Algaba-Brazalez, M. Johansson, and L. Manholm, "Glide-symmetric fully metallic Luneburg lens for 5G communications at Ka-band," *IEEE Antennas Wireless Propag. Lett.*, vol. 17, no. 9, pp. 1588–1592, Sep. 2018.
- [30] S. B. Myers, "Parallel plate optics for rapid scanning," *Jour. Appl. Phys.*, vol. 18, pp. 221–229, Feb. 1947.
- [31] R. F. Rinehart, "A family of designs for rapid scanning radar antennas," *Proc. IRE*, vol. 40, no. 6, pp. 686–688, Jun. 1952.
- [32] K. S. Kunz, "Propagation of microwaves between a parallel pair of doubly curved conducting surfaces," *Jour. Appl. Phys.*, vol. 25, no. 5, pp. 642–653, May 1954.
- [33] Q. Liao, N. J. G. Fonseca, and O. Quevedo-Teruel, "Compact multibeam fully metallic geodesic Luneburg lens antenna based on non-Euclidean transformation optics," *IEEE Trans. Antennas Propag.*, vol. 66, no. 12, pp. 7383–7388, Dec. 2018.

- [34] J. Dong, A. I. Zaghoul, and R. Rotman, "Phase-error performance of multi-focal and non-focal two-dimensional Rotman lens designs," *IET Microw., Antennas & Propag.*, vol. 4, no. 12, pp. 2097–2103, Dec. 2010.
- [35] N. J. G. Fonseca, Q. Liao, and O. Quevedo-Teruel, "Equivalent planar lens ray-tracing model to design modulated geodesic lenses using non-Euclidian transformation optics," *IEEE Trans. Antennas Propag.*, vol. 68, no. 5, pp. 3410–3422, May 2020.
- [36] J. L. McFarland, "Catenary geodesic lens antenna," U.S. Patent 3 383 691, May 14, 1968.
- [37] H. Legay, S. Tubau, E. Girard, J.-P. Fraysse, R. Chiniard, C. Diallo, R. Sauleau, M. Ettorre, and N. Fonseca, "Multiple beam antenna based on a parallel plate waveguide continuous delay lens beamformer," in *Proc. Int. Symp. Antennas Propag.*, Oct. 2016, pp. 118–119.
- [38] F. Doucet, N. J. G. Fonseca, E. Girard, H. Legay, and R. Sauleau, "Analytical model and study of continuous parallel plate waveguide lens-like multiple-beam antennas," *IEEE Trans. Antennas Propag.*, vol. 66, no. 9, pp. 4426–4436, Sep. 2018.
- [39] F. Doucet, N. J. G. Fonseca, E. Girard, X. Morvan, L. Le Coq, H. Legay, and R. Sauleau, "Shaped continuous parallel plate delay lens with enhanced scanning performance," *IEEE Trans. Antennas Propag.*, vol. 67, no. 11, pp. 6695–6704, Nov. 2019.
- [40] H. Legay, S. Tubau, J.-P. Fraysse, E. Girard, M. Ettorre, R. Sauleau, and N. Fonseca, "Quasi-optical beamformer with lens and planar antenna comprising such a beamformer," U.S. Patent 10 135 150, Nov. 20, 2018.
- [41] M. P. DeLisio and R. A. York, "Quasi-optical and spatial power combining," *IEEE Trans. Microw. Theory Techn.*, vol. 50, no. 3, pp. 929–936, Mar. 2002.
- [42] F. F. Manzillo, M. Ettorre, R. Sauleau, and A. Grbic, "Systematic design of a class of wideband circular polarizers using dispersion engineering," in *Proc. 11th Eur. Conf. Antennas Propag. (EuCAP)*, Mar. 2017, pp. 1279–1281.

- [43] N. Bartolomei, M. Garcia-Vigueras, F. Doucet, D. Blanco, E. Girard, R. Sauleau, and M. Ettore, "Circularly polarized parallel plate waveguide multiple-beam lens-like antenna for Satcom applications," in *Proc. 13th Eur. Conf. Antennas Propag. (EuCAP)*, Mar. 2019.
- [44] J. L. Allen, "A theoretical limitation on the formation of lossless multiple beams in linear arrays," *IRE Trans. Antennas Propag.*, vol. 9, no. 4, pp. 350–352, Jul. 1961.
- [45] W. D. White, "Pattern limitations in multiple-beam antennas," *IRE Trans. Antennas Propag.*, vol. 10, no. 4, pp. 430–436, Jul. 1962.
- [46] S. Stein, "On cross coupling in multiple-beam antennas," *IRE Trans. Antennas Propag.*, vol. 10, no. 5, pp. 548–557, Sep. 1962.
- [47] K. Tekkouk, M. Ettore, E. Gandini, and R. Sauleau, "Multibeam pillbox antenna with low sidelobe level and high-beam crossover in SIW technology using the split aperture decoupling method," *IEEE Trans. Antennas Propag.*, vol. 63, no. 11, pp. 5209–5215, Nov. 2015.
- [48] E. C. DuFort, "Optimum low sidelobe high crossover multiple beam antennas," *IEEE Trans. Antennas Propag.*, vol. 33, no. 9, pp. 946–954, Sep. 1985.
- [49] M. S. Smith, "Amplitude performance of Ruze and Rotman lenses," *Jour. Inst. Electron. Radio Eng.*, vol. 55, no. 1, pp. 33–36, Jsn. 1983.
- [50] T. Potelon, M. Ettore, T. Bateman, J. Francey, and R. Sauleau, "Broadband passive two-feed-per-beam pillbox architecture for high beam crossover level," *IEEE Trans. Antennas Propag.*, vol. 68, no. 1, pp. 575–580, Jan. 2020.
- [51] E. Gandini, M. Ettore, R. Sauleau, and A. Neto, "Mutual coupling reduction of Fabry-Perot SIW feeds using a double partially reflecting pin-made grid configuration," *IEEE Antennas Wireless Propag. Lett.*, vol. 10, pp. 647–650, 2011.
- [52] P. Balling, C. Mangenot, and A. G. Roederer, "Shaped single-feed-per-beam multibeam reflector antenna," in *Proc. 1st Eur. Conf. Antennas Propag. (EuCAP)*, Nov. 2006.
- [53] C. C. Han and Y. Hwang, "Satellite antennas," in *Antenna Handbook Volume III: Applications*, Y. T. Lo and S. W. Lee, Eds., New York: Van Nostrand Reinhold, 1993, pp. 21.38–21.43.

-
- [54] J. S. Foster, "Electromagnetic energy phase shifting device," U.S. Patent 2 832 936, Apr. 29, 1958.
- [55] H. Iams, "Focusing device for centimeter waves," U.S. Patent 2 576 181, Nov. 27, 1951.
- [56] W. C. Wilkinson, "Scanning antenna system," U.S. Patent 2 576 182, Nov. 27, 1951.
- [57] D. Ferrante and R. Richard, "Microwave scanning apparatus employing feed horn coupled to spaced lens by coaxial transmission lines," U.S. Patent 3 230 535, Jan. 18, 1966.
- [58] W. A. Hanson, "In their own words: OneWeb's internet constellation as described in their FCC Form 312 application," *New Space*, vol. 4, no. 3, pp. 153–167, Sep. 2016.
- [59] J. Ruze, "Lateral-feed displacement in a paraboloid," *IEEE Trans. Antennas Propag.*, vol. 13, no. 5, pp. 660–665, Sep. 1965.
- [60] W. V. T. Rusch and A. Ludwig, "Determination of the maximum scan-gain contours of a beam-scanning paraboloid and their relation to the Petzval surface," *IEEE Trans. Antennas Propag.*, vol. 21, no. 2, pp. 141–147, Mar. 1973.
- [61] O. Quevedo-Teruel, W. Tang, and Y. Hao, "Isotropic and nondispersive planar fed Luneburg lens from Hamiltonian transformation optics," *Opt. Lett.*, vol. 37, no. 23, pp. 4850–4852, Sep. 2012.
- [62] H. B. Molina, J. G. Marin, and J. Hesselbarth, "Modified planar Luneburg lens millimetre-wave antenna for wide-angle beam scan having feed locations on a straight line," *IET Microw., Antennas & Propag.*, vol. 11, no. 10, pp. 1462–1468, Aug. 2017.
- [63] R. C. Hansen, "Design trades for Rotman lenses," *IEEE Trans. Antennas Propag.*, vol. 39, no. 4, pp. 464–472, Apr. 1991.
- [64] S. G. Hay, J. W. Archer, G. P. Timms, and S. L. Smith, "A beam-scanning dual-polarized fan-beam antenna suitable for millimeter wavelengths," *IEEE Trans. Antennas Propag.*, vol. 53, no. 8, pp. 2516–2524, Aug. 2005.
- [65] S. G. Hay, S. L. Smith, G. P. Timms, and J. W. Archer, "Three-shaped-reflector beam-scanning pillbox antenna suitable for mm wavelengths," *IEEE Trans. Antennas Propag.*, vol. 59, no. 7, pp. 2495–2501, Jul. 2011.

- [66] H. Kirino and K. Ogawa, "A 76 GHz multi-layered phased array antenna using a non-metal contact metamaterial waveguide," *IEEE Trans. Antennas Propag.*, vol. 60, no. 2, pp. 840–853, Feb. 2012.
- [67] K. Tekkouk, J. Hirokawa, R. Sauleau, and M. Ando, "Wideband and large coverage continuous beam steering antenna in the 60-GHz band," *IEEE Trans. Antennas Propag.*, vol. 65, no. 9, pp. 4418–4426, Sep. 2017.
- [68] S. Prinack, "Lessons learned to avoid coax cable failure in moving mechanical mechanisms," in *Proc. 41st Aerospace Mech. Symp.*, May 2012, pp. 211–222.
- [69] G. L. Ragan, *Microwave Transmission Circuits*. New York: McGraw-Hill, 1948.
- [70] R. E. Collin, *Field Theory of Guided Waves*. New York: IEEE Press, 1991.
- [71] D. G. D. Mesquita and A. G. Bailey, "A symmetrically excited microwave rotary joint," *IEEE Trans. Microw. Theory Techn.*, vol. 18, no. 9, pp. 654–656, Sep. 1970.
- [72] M. Tayyab Azim, J. Park, and S.-O. Park, "Contactless linear rotary joint at Ku-band," *IEEE Microw. Wireless Comp. Lett.*, vol. 29, no. 6, pp. 373–375, Jun. 2019.
- [73] V. Courtonne, T. Dusseux, and P. Brunet, "Feed cluster synthesis from focal field distribution," in *Proc. IEEE Int. Symp. Antennas Propag.*, Jun. 1992, pp. 20–23.
- [74] K. S. Rao, G. A. Morin, M. Q. Tang, S. Richard, and K. K. Chan, "Development of a 45 GHz multiple-beam antenna for military satellite communications," *IEEE Trans. Antennas Propag.*, vol. 43, no. 10, pp. 1036–1046, Oct. 1995.
- [75] M. Schneider, C. Hartwanger, and H. Wolf, "Antennas for multiple spot beam satellites," *CEAS Space Jour.*, vol. 2, pp. 59–66, Aug. 2011.
- [76] P. Angeletti and M. Lisi, "Multimode beamforming networks for space applications," *IEEE Antennas Propagag. Mag.*, vol. 56, no. 1, pp. 62–78, May 2014.
- [77] E. Amyotte and L. M. Camelo, "Antennas for Satellite Communications," in *Space Antenna Handbook*, W. A. Imbriale, S. Gao, and L. Boccia, Eds., Chichester: John Wiley & Sons, 2012, Ch. 12.

- [78] T. Takenoshita, "Primary radiator, phase shifter, and beam scanning antenna," U.S. Patent 6 597 322, Jul. 22, 2003.
- [79] J. M. Howell, "Mechanical scanning feed assembly for a spherical lens antenna," U.S. Patent 7 301 504, Nov. 27, 2007.
- [80] A. Mirkamali, R. Deban, F. Siaka, and J.-J. Laurin, "Fast and low-cost beam steering using an agile mechanical feed system for exciting circular arrays," *IET Microw., Antennas & Propag.*, vol. 10, no. 4, pp. 378–384, Mar. 2016.
- [81] P.-S. Kildal, E. Alfonso, A. Valero-Nogueira, and E. Rajo-Iglesias, "Local metamaterial-based waveguides in gaps between parallel metal plates," *IEEE Antennas Wireless Propag. Lett.*, vol. 8, pp. 84–87, 2009.
- [82] E. Pucci and P.-S. Kildal, "Contactless non-leaking waveguide flange realized by bed of nails for millimeter wave applications," in *Proc. 1st Eur. Conf. Antennas Propag. (EuCAP)*, Mar. 2012, pp. 3533–3536.
- [83] S. Rahiminejad, E. Pucci, V. Vassilev, P.-S. Kildal, S. Haasl, and P. Enoksson, "Polymer gap adapter for contactless, robust, and fast measurements at 220–325 GHz," *Jour. Microelectromech. Syst.*, vol. 25, no. 1, pp. 160–169, Feb. 2016.
- [84] A. Polemi and S. Maci, "Closed form expressions for the modal dispersion equations and for the characteristic impedance of a metamaterial-based gap waveguide," *IET Microw., Antennas & Propag.*, vol. 4, no. 8, pp. 1073–1080, Aug. 2010.
- [85] A. U. Zaman and P.-S. Kildal, "Gap Waveguides," in *Handbook of Antenna Technologies*, Z. N. Chen, Ed., Singapore: Springer.
- [86] E. Rajo-Iglesias and P.-S. Kildal, "Numerical studies of bandwidth of parallel-plate cut-off realised by a bed of nails, corrugations and mushroom-type electromagnetic bandgap for use in gap waveguides," *IET Microw., Antennas & Propag.*, vol. 5, no. 3, pp. 282–289, Feb. 2011.
- [87] M. G. Silveirinha, C. A. Fernandes, and J. R. Costa, "Electromagnetic characterization of textured surfaces formed by metallic pins," *IEEE Trans. Antennas Propag.*, vol. 56, no. 2, pp. 405–415, Feb. 2008.

- [88] A. Polemi, S. Maci, and P.-S. Kildal, "Dispersion characteristics of a metamaterial-based parallel-plate ridge gap waveguide realized by bed of nails," *IEEE Trans. Antennas Propag.*, vol. 59, no. 3, pp. 904–912, Mar. 2011.
- [89] N. Marcuvitz, *Waveguide Handbook*. New York: McGraw-Hill, 1951.
- [90] S. Matsumoto, M. Ohshima, K. Fukata, T. Kawai, I. Ohta, M. Kishihara, K. Iio, and T. Kashiwa, "Compact H-plane waveguide corners with very wide bandwidth," in *Proc. IEEE MTT-S Int. Microw. Symp.*, Jun. 2016, pp. 900–902.
- [91] C. G. Montgomery, R. H. Dicke, and E. M. Purcell, *Principles of Microwave Circuits*. New York: McGraw-Hill, 1948.
- [92] D. M. Pozar, *Microwave Engineering*, 4th ed. Hoboken: John Wiley & Sons, 2011.
- [93] E. Alfonso, S. Carlred, S. Carlsson, and L.-I. Sjöqvist, "Contactless flange adapters for mm-wave measurements," in *Proc. 11th Eur. Conf. Antennas Propag. (EuCAP)*, Mar. 2017, pp. 1690–1693.
- [94] M. Ebrahimpouri, A. Algaba Brazalez, L. Manholm, and O. Quevedo-Teruel, "Using glide-symmetric holes to reduce leakage between waveguide flanges," *IEEE Microw. Wireless Comp. Lett.*, vol. 28, no. 6, pp. 473–475, 2018.
- [95] B. Pyne, R. Naruse, H. Saito, J. Hirokawa, V. Ravindra, and P. R. Akbar, "Robust contactless noncircular choke flange for wideband waveguide applications," *IEEE Trans. Microw. Theory Techn.*, vol. 67, no. 3, pp. 861–867, Mar. 2019.
- [96] A. Farahbakhsh, D. Zarifi, and A. U. Zaman, "60-GHz groove gap waveguide based wideband H-plane power dividers and transitions: for use in high-gain slot array antenna," *IEEE Trans. Microw. Theory Techn.*, vol. 65, no. 11, pp. 4111–4121, Nov. 2017.
- [97] M. Born and E. Wolf, *Principles of Optics*, 7th ed. Cambridge: Cambridge University Press, 1999.
- [98] X. Lu, S. Gu, X. Wang, H. Liu, and W. Lu, "Beam-scanning continuous transverse stub antenna fed by ridged waveguide slot array," *IEEE Antennas Wireless Propag. Lett.*, vol. 16, pp. 1675–1678, Feb. 2017.

- [99] F. Obelleiro-Basteiro, J. L. Rodriguez, and R. J. Burkholder, "An iterative physical optics approach for analyzing the electromagnetic scattering by large open-ended cavities," *IEEE Trans. Antennas Propag.*, vol. 43, no. 4, pp. 356–361, Apr. 1995.
- [100] M. Kline, "An asymptotic solution of Maxwell's equations," *Comm. Pure Appl. Math.*, vol. 4, pp. 225–262, Aug. 1951.
- [101] C. J. Sletten, R. B. Mack, W. G. Mavroides, and H. M. Johanson, "Corrective line sources for paraboloids," *IRE Trans. Antennas Propag.*, vol. 6, no. 3, pp. 239–251, Jul. 1958.
- [102] V. Krichevsky and D. DiFonzo, "Optimum beam scanning in offset single and dual reflector antennas," *IEEE Trans. Antennas Propag.*, vol. 33, no. 2, pp. 179–188, Feb. 1985.
- [103] N. Llombart, S. O. Dabironezare, G. Carluccio, A. Freni, and A. Neto, "Reception power pattern of distributed absorbers in focal plane arrays: a Fourier optics analysis," *IEEE Trans. Antennas Propag.*, vol. 66, no. 11, pp. 5990–6002, Nov. 2018.
- [104] W. Watson, "The field distribution in the focal plane of a paraboloidal reflector," *IEEE Trans. Antennas Propag.*, vol. 12, no. 5, pp. 561–569, Sep. 1964.
- [105] A. Nagamune and P. H. Pathak, "An efficient plane wave spectral analysis to predict the focal region fields of parabolic reflector antennas for small and wide angle scanning," *IEEE Trans. Antennas Propag.*, vol. 38, no. 11, pp. 1746–1756, Nov. 1990.
- [106] R. Kouyoumjian, "Asymptotic high-frequency methods," *Proc. IEEE*, vol. 53, no. 8, pp. 864–876, Aug. 1965.
- [107] B. M. Thomas, "Matching focal-region fields with hybrid modes," *IEEE Trans. Antennas Propag.*, vol. 18, no. 3, May 1970.
- [108] P. H. Pathak, "Techniques for High-Frequency Problems," in *Antenna Handbook Volume I: Antenna Fundamentals and Mathematical Techniques*, Y. T. Lo and S. W. Lee, Eds., New York: Van Nostrand Reinhold, 1993, pp. 4.18–4.23.
- [109] M.-K. Hu, "Near-zone power transmission formulas," in *IRE Natl. Conv. Rec.* 6, pt. 8, 1958, pp. 128–135.

- [110] C. A. Balanis, "Horn Antennas," in *Antenna Handbook Volume II: Antenna Theory*, Y. T. Lo and S. W. Lee, Eds., New York: Van Nostrand Reinhold, 1993, pp. 8.20–8.21.
- [111] S. Silver, *Microwave Antenna Theory and Design*. New York: McGraw-Hill, 1949.
- [112] W. Yu, W. Li, A. Elsherbeni, and Y. Rahmat-Samii, *Advanced Computational Electromagnetic Methods and Applications*. Boston: Artech House, 2015.
- [113] E. V. Jull, *Aperture Antennas and Diffraction Theory*. Stevenage: Peter Peregrinus, 1981.
- [114] P. F. Goldsmith, C.-T. Hsieh, G. R. Huguenin, J. Kapitzky, and E. L. Moore, "Focal plane imaging systems for millimeter wavelengths," *IEEE Trans. Microw. Theory Techn.*, vol. 41, no. 10, pp. 1664–1675, Oct. 1993.
- [115] S. H. Blumenthal, "Medium earth orbit Ka band satellite communications system," in *Proc. IEEE Mil. Comm. Conf.*, Nov. 2013, pp. 273–277.
- [116] A. B. Numan, J.-F. Frigon, and J.-J. Laurin, "Printed W-band multibeam antenna with Luneburg lens-based beamforming network," *IEEE Trans. Antennas Propag.*, vol. 66, no. 10, pp. 5614–5619, Oct. 2018.
- [117] F. F. Manzillo, M. Ettorre, M. S. Lahti, K. T. Kautio, D. Lelaidier, E. Seguenot, and R. Sauleau, "A multilayer LTCC solution for integrating 5G access point antenna modules," *IEEE Trans. Microw. Theory Techn.*, vol. 64, no. 7, pp. 2272–2283, Jul. 2016.
- [118] T. Potelon, M. Ettorre, L. L. Coq, T. Bateman, J. Francey, D. Lelaidier, E. Seguenot, F. Devillers, and R. Sauleau, "A low-profile broadband 32-slot continuous transverse stub array for backhaul applications in E-band," *IEEE Trans. Antennas Propag.*, vol. 65, no. 12, pp. 6307–6316, Dec. 2017.
- [119] F. Xu and K. Wu, "Guided-wave and leakage characteristics of substrate integrated waveguide," *IEEE Trans. Microw. Theory Techn.*, vol. 53, no. 1, pp. 66–73, Jan. 2005.

List of Publications

Journal Papers

T. Ströber, H. Legay, G. Goussetis, and M. Ettorre, "Multiple-beam synthesis for continuous parallel-plate waveguide lenses," in preparation for submission to *IEEE Antennas Wireless Propag. Lett.*

T. Ströber, S. Tubau, E. Girard, H. Legay, G. Goussetis, and M. Ettorre, "Shaped parallel-plate waveguide lens for mechanical wide-angle beam steering," in preparation for submission to *IEEE Trans. Antennas Propag.*

T. Ströber, H. Legay, G. Goussetis, and M. Ettorre, "Multiple-beam parallel-plate waveguide lens in multilayer PCB technology," in preparation for submission to *IEEE Trans. Antennas Propag.*

Conference Papers

T. Ströber and M. Ettorre, "2D physical optics analysis of the focal region of parallel-plate waveguide lenses," in *Proc. IEEE Int. Symp. Antennas Propag.*, Atlanta, GA, USA, Jul. 7–12, 2019.

T. Ströber, S. Tubau, E. Girard, H. Legay, G. Goussetis, and M. Ettorre, "Parallel-plate waveguide lens for mechanical beam scanning using gap waveguide feed system," in *Proc. 14th Eur. Conf. Antennas Propag. (EuCAP)*, Copenhagen, Denmark, Mar. 15–20, 2020 (Convened Session).

T. Ströber, S. Tubau, H. Legay, G. Goussetis, and M. Ettorre, "A parallel-plate lens for mechanical wide-angle beam scanning," submitted to *15th Eur. Conf. Antennas Propag. (EuCAP)*, Düsseldorf, Germany, Mar. 22–26, 2021 (Convened Session).

About the author



Thomas Ströber was born on June 8, 1993 in Oberndorf bei Salzburg, Austria. He obtained the M.Sc. degree in electrical and computer engineering from the Technical University of Munich (TUM), Germany, in 2017. He carried out his six-month Master's thesis on antenna designs for UWB microwave imaging as a visiting research student at the University of Edinburgh.

In October 2017, he joined the Institut d'Electronique et des Technologies du NuméRique (IETR), Rennes, France, and the Institute of Sensors, Signals, and Systems, Heriot-Watt University, Edinburgh, United Kingdom. His Ph.D. research was carried out under the supervision of Dr. Mauro Ettore and Prof. George Goussetis. During his thesis, he spent 18 months with the Research & Technology Department at Thales Alenia Space, Toulouse, France. His Ph.D. activities were part of the REVOLVE project, funded by the European Commission's H2020 Marie Skłodowska-Curie Actions.

His research interests include quasi-optical beamformers, gap waveguide technology and asymptotic high-frequency techniques.

Titre: Modélisation et conception de formateurs de faisceaux quasi-optiques reconfigurables pour les futures constellations de satellites

Mot clés : antennes multifaisceaux, méthodes asymptotiques, optique de guide d'ondes à plans parallèles, systèmes quasi-optiques

Résumé : La nécessité d'avoir un large secteur angulaire et la possibilité d'utiliser des plus larges bandes de fréquence dans les futures constellations de satellites ont créé de nouveaux défis dans la conception d'antennes. De plus, des solutions à bas coût sont nécessaires. L'objectif de cette thèse est d'étudier et de développer des antennes quasi-optiques en bande millimétrique offrant des performances de balayage élevées et une reconfiguration du faisceau pour répondre aux besoins cités au-dessus. Des modèles asymptotiques pour l'analyse des formateurs de faisceaux en guide d'ondes à plans parallèles en réception sont présentés. Il est démontré que ces modèles permettent la conception efficace de systèmes d'alimentation avec des exigences strictes en termes de couverture. Deux nouveaux formateurs de faisceau fonctionnant en bande Ka sont présentés. Le premier est une lentille en guide d'ondes à plans parallèles comprenant un système d'alimentation en technologie gap waveguide qui permet un balayage mécanique rapide du faisceau. Le second correspond à un formateur de faisceaux à lentille réalisé en technologie PCB multicouche. L'outil numérique présenté est employé pour la synthèse des clusters superposés. Les deux solutions présentent des avancées importantes en termes de performances de balayage et réalisations faible coût.

Title: Reconfigurable Quasi-Optical Beamformers for Next-Generation Satellite Applications: Electromagnetic Modeling and Design

Keywords: gap waveguide technology, high-frequency techniques, multiple-beam antennas, parallel-plate optics, quasi-optical systems

Abstract: The requirements of wide field of view and the availability of larger bandwidths for emerging satellite constellations have opened new challenges in antenna design. At the same time, highly cost-effective solutions are needed. The main objective of this dissertation is to investigate and develop quasi-optical millimeter-wave antennas with enhanced beam scanning and beam reconfiguration capabilities that answer these needs. High-frequency models are developed for the analysis of different parallel-plate beamformers in reception. It is shown that these models can be used efficiently for the design of feed systems with stringent requirements on scanning range. Two novel lens beamformers, operating in the uplink and downlink Ka-band, respectively, are presented. The first is a shaped parallel-plate lens combined with a mechanical scanning feed based on gap waveguide technology. Equivalent circuit models which aid in the design of the feed structure are addressed. The resulting design and experimental results from an all-metal demonstrator are reported. The second corresponds to a lens beamformer implemented in multi-layer PCB technology. The developed numerical procedure is applied to the synthesis of overlapping feed clusters. Both designs represent significant advances in terms of scanning performance and low-cost implementation.